Design and Characterization of Acoustic Pulse Shape Memory Alloy Actuators

by

Joshua Michael Chambers

Bachelor of Mechanical Engineering (2003)
University of Minnesota

Submitted to the Department of Mechanical Engineering
in partial fulfillment of the requirements for the degree of

Master of Science in Mechanical Engineering

at the

MASSACHUSETTS INSTITUTE OF TECHNOLOGY

June 2005

Author .....
Department of Mechanical Engineering
February 28, 2005

Certified by .....
Steven R. Hall
Professor of Aeronautics and Astronautics
Thesis Supervisor

Read by .....
David L. Trumper

Accepted by .....
Lallit Anand
Chairman, Department Committee on Graduate Students

Design and Characterization of Acoustic Pulse Shape Memory Alloy Actuators

by

Joshua Michael Chambers

Submitted to the Department of Mechanical Engineering
on March 4, 2005, in partial fulfillment of the
requirements for the degree of
Master of Science in Mechanical Engineering

Abstract

Single crystal Ni–Mn–Ga ferromagnetic shape memory alloys (FSMAs) are active materials which produce strain when a magnetic field is applied. The large saturation strain (6%) of Ni–Mn–Ga, and material energy density comparable to piczoelectric ceramics make Ni–Mn–Ga an interesting active material. However, their usefulness is limited by the bulky electromagnet required to produce a magnetic field.

In this thesis, a novel actuation method is developed for shape memory alloys in their martensitic phase, whereby asymmetric acoustic pulses are used to drive twin boundary motion. Experimental actuators were developed using a combination of Ni-Mn-Ga FSMA single crystals and a piezoelectric stack actuator. In bi-directional actuation without load, strains of over 3% were achieved using repeated pulses (at 100 Hz) over a 30 s interval, while 1% strain was achieved in under 1 s. The maximum strains achieved are comparable to the strains achieved using bi-directional magnetic actuation, although the time required for actuation is longer. No-load actuation also showed a nearly linear relationship between the magnitude of the asymmetric stress pulse and the strain achieved during actuation, and a positive correlation between pulse repetition rate and output strain rate, up to at least 100 Hz. Acoustic actuation against a spring load showed a maximum output energy density for the actuator of about 1000 J/m^3, with a peak-to-peak stress and strain of 100 kPa and 2%, respectively.

Thesis Supervisor: Steven R. Hall
Title: Professor of Aeronautics and Astronautics

Acknowledgments

First, I would like to thank my advisor Prof. Steven Hall, who provided the opportunity, motivation, and guidance that made this work possible. His faith in my abilities and eagerness to explore new ideas helped make this project truly unique. Second, I would like to thank Bob O'Handley, who provided lab space and a lab group to work with, as well as providing invaluable assistance throughout the course of this work. Also, a special thanks to Prof. David Trumper for taking time out of his busy schedule to be a reader for this thesis.

I must profess an enormous debt of gratitude to my colleagues in the O'Handley group, for both their friendship and their assistance. Jorge Feuchtwanger and Brad Peterson, who introduced me to the lab, and allowed me to stay, even after my affinity for gravity was demonstrated. David Bono, for his electronics expertise and extraordinary collection of spare parts. Migeul Marioni, Marc Richard, Ratchatee Techapiesancharoenkij, and David Paul, for answering, or at least trying to answer, so many of my impossible questions. Kyungyeol Song, for the chance to see my own research from a different perspective. Jesse Simon, for the opportunity to pass on all that I have learned, and his work gathering and preparing the final sets of data used in this thesis.

Many thanks to the Edgerton Center, and the Edgerton Student Shop, whose machines were instrumental in the creation of many an apparatus. A very special thanks to Fred Cote, whose patience and experience were often the only thing that made my work in the shop productive. Also, thanks to the off-hour shop instructors, David Breslau, John McBean, and Andrew Heafitz.

I would like to thank Prof. Tom Eager for the use of his electronic discharge milling machine (EDM), and Don Galher for allowing the O'Handley group to expedite repairs whenever necessary.

I'm eternally grateful to Leslie Reagan and Joan Kravit, whose extraordinary administrative skills were always able to make mole hills out of mountains.

Of course, to all those I have met at MIT, who made my stay a little less technical and a little more enjoyable, James, Zil, Toby, Sam, Sara, Tai, Jiwoon, everyone from the 2003 MIT-Germany trip and the ME soccer team, and anyone I just had a drink with one night. I thank you for every life lesson, every laugh and every smile.

And, to my family and friends back in Minnesota, I couldn't have done it without you. Finally, I would like to dedicate this work to my grandpa, Hilarius Tauer, who didn't believe in dinosaurs.

This work was sponsored by the Office of Navel Research, grant number ONR-MURI N00014-01-10758, monitored by Dr. Roshdy Barsoum and Dr. Jan Lindberg.

Contents

Chapter 1

Introduction

Ferromagnetic shape memory alloys (FSMAs) are a recently discovered area of active materials that have garnered much interest due to their high saturation strains, up to 10% [1], in orthorhombic Ni_2MnGa, and frequency response on the order of 1 kHz [2, 3]. The unique properties of FSMAs also make a new type of hybrid active material actuator possible. The extremely low twinning stresses, on the order of 1 MPa, required for magnetic actuation in FSMAs, make it possible to induce actuation using the transient stresses of an acoustic pulse. By generating a properly shaped acoustic pulse using a piezoelectric actuator it is possible to achieve the same actuation strains seen in magnetic actuation. This acoustic pulse actuation of SMAs is of interest because it is possible to create an acoustic pulse actuator that is nearly the same size as its active material components. In contrast, magnetic FSMA actuators require a bulky electromagnet that is typically 300 times the volume of the active material.

To fully understand acoustic pulse SMA actuation, we will first review the mechanisms at work in the classical shape memory effect and the use of SMAs as actuators. We then review FSMAs, whose extremely low twinning stress allow acoustic pulse actuation to be effective, and discuss the motivation behind developing acoustic pulse SMA actuation. Finally, a brief overview of the organization of this thesis is presented.

1.1 SMA Overview

Classical shape memory alloys actuate as they go through a diffusionless transformation between a low temperature, low symmetry phase referred to as martensite, and a high tem-

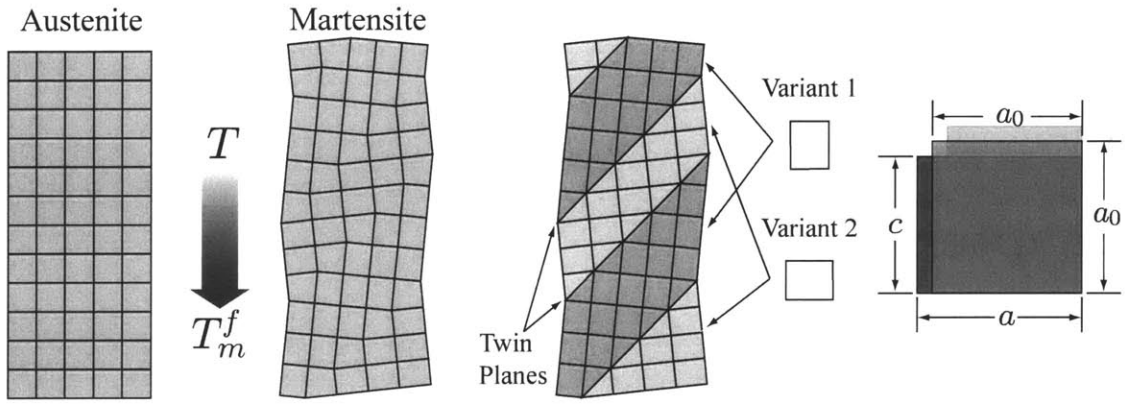

Figure 1-1: As the crystal cools from above the martensite start temperature (T_m^s) to below the martensite finish temperature (T_m^f), it transitions from austenite to martensite. In Ni–Ma–Ga, the austenitic phase is cubic with lattice constants a_0, and the martensitic phase is tetragonal with a short c-axis and longer a-axes.

perature, high symmetry phase known as austenite. In the low symmetry phase, it possible to have distinct portions of a single crystal with different orientations of the martensite crystal structure, referred to as variants. These variants often form in self-accommodating pairs [4], which are referred to as twin variants. The boundary between twin variants is referred to as a twin plain or twin boundary. Shifting of these boundaries allows low stress deformation of the low temperature phase, which is entirely reversible by returning to the high temperature phase. Figure 1-1 illustrates twin formation in an oriented single crystal. The diagram only depicts two variants in a two dimensional lattice, while in reality the crystal is three dimensional, and variants can form with three or more orientations. Ni–Mn–Ga, the most extensively studied FSMA, has a tetragonal martensite structure with a short c-axis. The orientation of the c-axis is used to define the orientation of the twin variants. The orientation of the c-axis is limited to one of the directions of three identical a-axes of the cubic parent phase.

As an SMA crystal cools past the temperature at which martensite formation starts (T_m^s), the low temperature phase will begin to form. Martensite formation will continue with temperature decrease until the crystal has fully transformed to martensite at temperature T_m^f (Fig. 1-2). Sections of the crystal will form the low temperature phase with variants facing different directions. Twin variant formation occurs in a manner that minimizes the elastic energy of the transformation product. A large enough external stress applied to

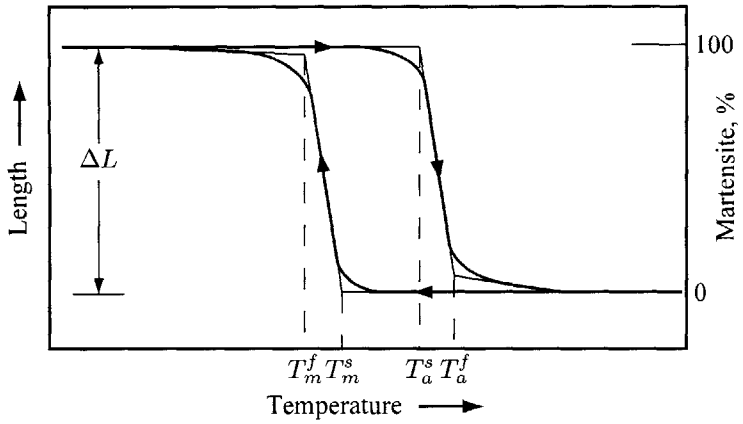

Figure 1-2: The transition from austenite to martensite occurs between the temperatures T_m^s and T_m^f, and the reverse transition occurs between T_a^s and T_a^f. From [4].

the crystal during transformation will cause the low symmetry phase to form with twin variants that best accommodate the stress (Fig. 1-3). If the c-axis is shorter than the a-axis in the low symmetry phase, and a compressive stress is applied along a {100} direction, it is possible to transform into a crystal with a single martensite variant.

Stresses applied to the crystal while it is in its low temperature phase can cause twin variant reorientation. This is usually accomplished by the movement of an existing twin boundary. Any stress that can be resolved as a shear along a twin boundary can cause the atoms near that boundary to slip from positions on the lattice of the first variant, to positions on the lattice of the second. As the atoms along the twin plain slip into new positions, the twin plain moves, increasing the quantity of one variant and decreasing the other, as shown in Figure 1-4. If none of the existing variants can expand to better accommodate an external stress, the stress may cause nucleation of a new twin boundary. Through these mechanisms of deformation, SMAs can accommodate up to 10% strain, which is fully recoverable. The deformations do not alter the original parent phase of the crystal. Thus, when the crystal is heated above its transformation temperature, it returns to its original shape as the variants revert to their original cubic shape.

One-way shape memory actuation consists simply of heating a shape memory alloy device to do work as the high temperature phase forms. The speed of this actuation is limited by the rate of heating and cooling that can be applied to the material. The maximum strain that can be achieved by thermal transformation is limited by the largest change in

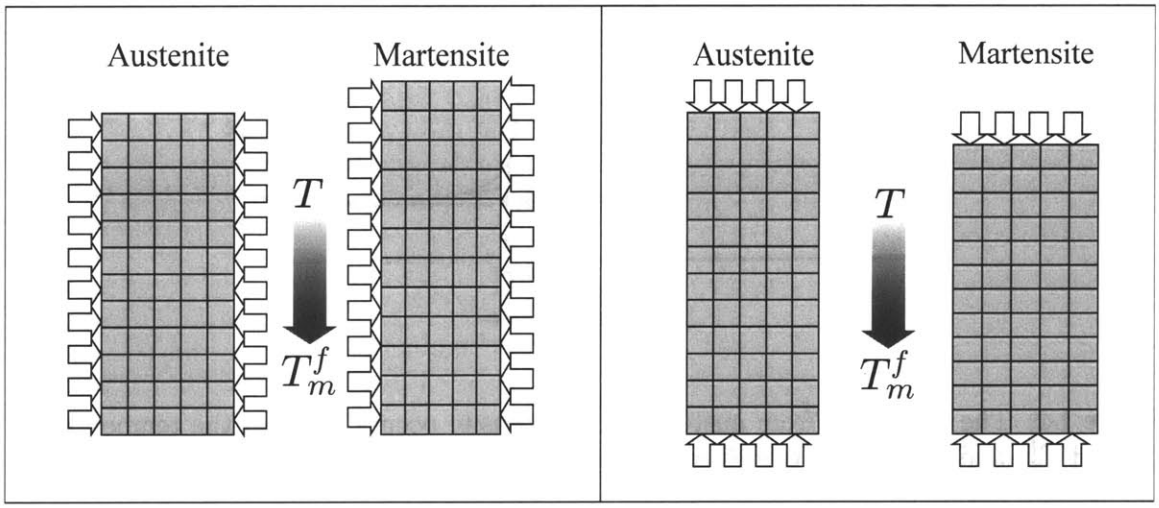

Figure 1-3: Austenite can be cooled under stress to form a single variant martensite crystal.

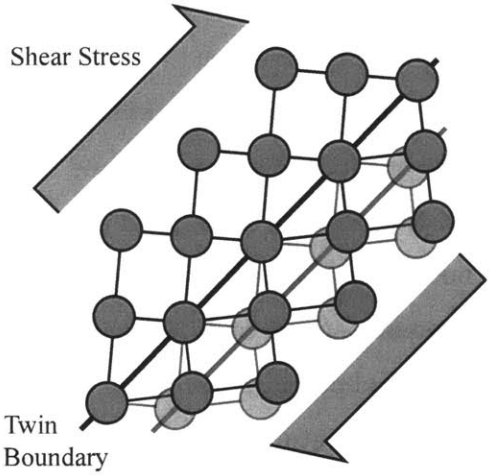

Figure 1-4: A shear stress along a twin boundary, larger than the threshold shear stress τ_0, will cause the twin boundary to move, growing one variant and shrinking the other.

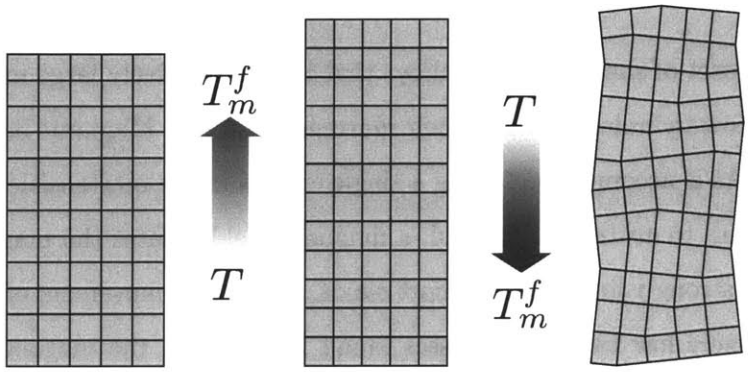

Figure 1-5: A one-way shape memory alloy actuator will not return to its original low temperature shape unless a restoring force is used to reshape it.

the lattice parameters during the martensite-austenite transformation. The maximum stress that can be generated by the martensite to austenite transformation is essentially limited only by the modulus and yield strength of the austenitic phase of the material. Upon cooling to the martensitic phase again, a one-way actuator will change to a third shape (Figure 1-5) potentially different from the original martensite and from the austenite. In a cyclic thermoelastic actuator, an external prestress does work on the SMA as it transforms to martensite, so that it returns to its original shape.

Two-way shape memory actuation is accomplished by first training an SMA material to have a preferred low temperature shape. This training is accomplished by thermally cycling the SMA while it is clamped in the desired low temperature position. This heat treatment helps develop dislocations that promote the formation of a specific variant structure at low temperature. The rate of this mode of actuation is limited by the rate at which the material can be heated and cooled. The strain is again limited by the difference in the crystallographic axis between the two phases. The stress that can be generated during the martensite-austenite transition is the same as during one-way shape memory actuation. However, the stress that can be generated during the transition to martensite is limited by the twinning stress of the low temperature phase. This stress is typically between 10 and 100 times smaller than the yield strength of the austenite. Two-way SMA actuators have a lifespan that is limited by the addition of new dislocations and the loss of the training effect in the low temperature phase [5].

1.2 FSMA Overview

FSMAs are a subset of shape memory alloys that have a relatively large magnetocrystalline anisotropy and low twinning stress in their martensitic phase. Magnetic field induced strain (MFIS) of FSMAs is accomplished using a single crystal in the martensitic phase, and never uses the transition to austenite. Instead, a magnetic field rotates the magnetization of the crystal, which is strongly linked to the short c-axis, and causes movement of twin boundaries. With the extremely low twinning stresses found Ni–Mn–Ga, the magnetic field can force the entire crystal from one variant to another. Figure 1-6 illustrates MFIS in an crystal with faces cut along the {100} planes. The illustrated actuation is nearly ideal, and is difficult to achieve with actual crystals. Murray et al. [6, 7] were the first to achieve strains near the theoretical limit in Ni–Mn–Ga. Murray observed one-time strains of nearly 6% in an oriented single crystal sample of off-stoichiometry Ni_2MnGa, which forms a tetragonal martensite. The theoretical limit for strain in this material can derived from the theoretical geometry of the lattice structure over a twin boundary. Figure 1-7 shows a theoretical unit cell deformed by a twin plane. From the figure it is obvious the the deformation is a pure shear, and the magnitude of the shear strain can be calculated as

$$\begin{aligned} \gamma_0 &\equiv b/d = \tan\Phi \\ \Phi &= 90^\circ - 2\beta \\ \tan\beta &= c/a \end{aligned} \quad . \tag{1.1}$$

Note that in a cubic system, $\beta = 45^\circ$ and the strain, γ_0, and Φ go to zero. In the tetragonal Ni_2MnGa system,

$$\begin{aligned} c/a &\approx 0.94 \\ \gamma_0 &\approx 0.062 \\ \epsilon_0 = \tfrac{a-c}{a} &\approx 0.06 \end{aligned} \quad . \tag{1.2}$$

Note the small disagreement between the shear strain and difference in axis lengths. This is due to the slight rotation of the second variant beyond 90° by the angle Φ. FSMA testing has focused mainly on longitudinal strain of rectangular parallelepiped crystals. If these crystals are fully actuated as shown in Figure 1-6 and the length is measured perpendicular to the end faces in both configurations, the measure strain will be exactly the difference between c and a. In actual devices, however, the end faces are often constrained, and the

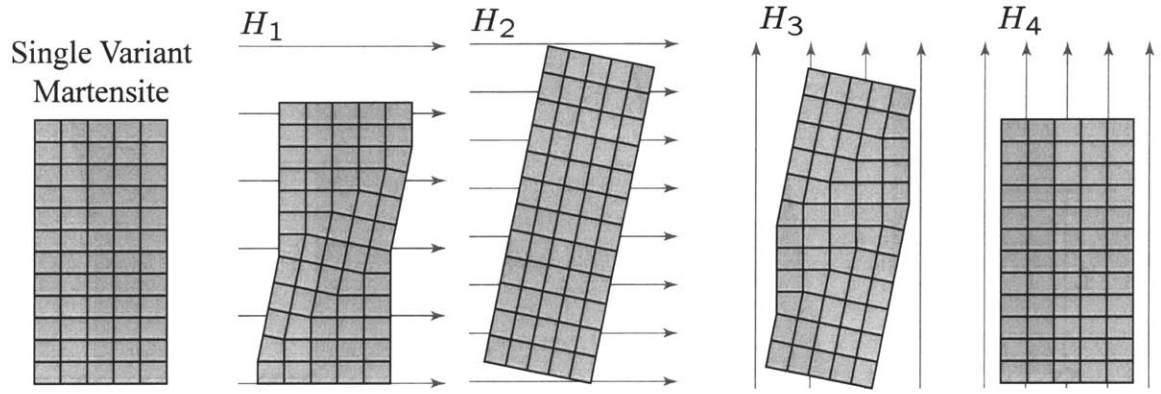

Figure 1-6: A small magnetic field (H_1) perpendicular to the short axis of the crystal will cause partial actuation. A larger field (H_2) will cause the entire crystal to switch to the second variant. This crystal is constrained from rotating or translating, but the faces are free to deform.

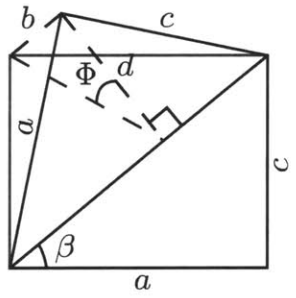

Figure 1-7: Schematic showing a distorted unit cell at a twin boundary. Movement of the twin boundary results from shearing the plane of atoms parallel and adjacent to it.

maximum theoretical strain cannot be achieved. Figure 1-8, shows a constrained crystal and the effective active length due to the constrains. Using the effective lengths shown, the maximum measured and theoretical longitudinal strains should differ by only a factor of $\cos(\Phi)$, or 0.998 in Ni–Mn–Ga. The strains reported herein will be relative to the entire length of the crystal, unless an effective length is explicitly defined.

Initial data collected by Ullakko et al. on single crystal Ni–Mn–Ga showed only a small fraction of the theoretical output strain [8]. The limiting factor was the lack of mobile twin boundaries and the absence of a coherent twin system in the crystal. Crystal composition is critical to achieving actuation, but even with the correct composition, special sample preparation is required to ensure mobile twin boundaries. A heat treatment was developed to

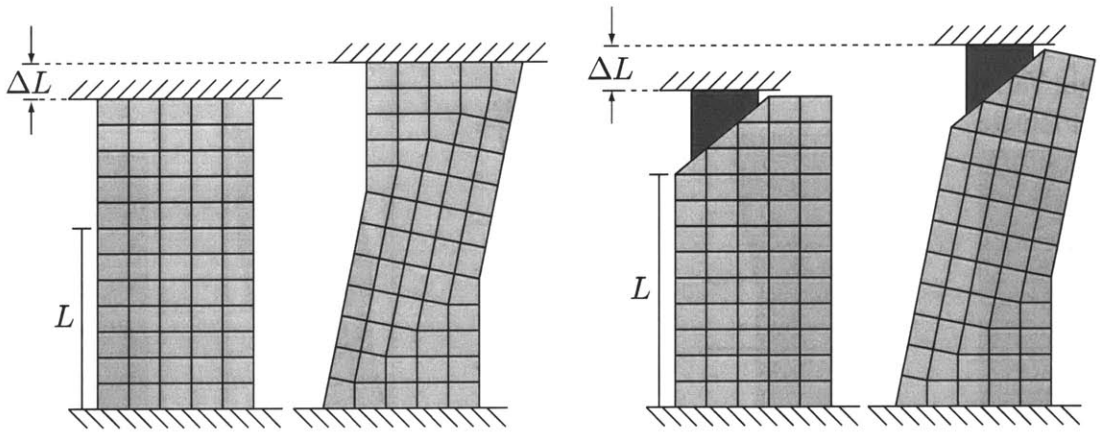

Figure 1-8: Effective actuation length for two different constraint sets. The constraints on either end of the crystal are free to translate relative to each other, but not rotate.

promote the development of a coherent twining system in a Ni–Mn–Ga crystal. The treatment involves first annealing the crystal, then placing the crystal under a large longitudinal stress before it has cooled below M_s. The crystal will then have a more coherent variant structure as it cools to room temperature. After cooling, a transverse stress is applied to nucleate a set of twin boundaries that will allow set of second variants to grow. After a favorable set of twin planes has been nucleated, the preferred orientation of the twin planes is semi-permanently established. A force much larger than the twinning stress is required to create new twin planes facing a different direction. The data collected by Murray et al., using a heat treated crystal [6] comes much closer to the theoretical limits of tetragonal Ni–Mn–Ga. A portion of the data is shown in Figure 1-9.

O'Handley [9] developed a widely accepted model that describes the stress on a twin boundary generated by an external magnetic field. The model assumes that the forces seen by the atoms along the twin boundary are generated by the combination of two energies, the Zeeman energy or magnetization energy, and the anisotropy energy. The Zeeman energy is given by

$$U_z = -\mu_0 M_s H \cos\theta \ , \tag{1.3}$$

where M_s is the saturation magnetization of Ni–Mn–Ga, H is the applied magnetic field, and θ is the angle of the magnetization vector relative to the applied field. Normally the magnetization points along the magnetic easy axis (c-axis) of the crystal, but an external

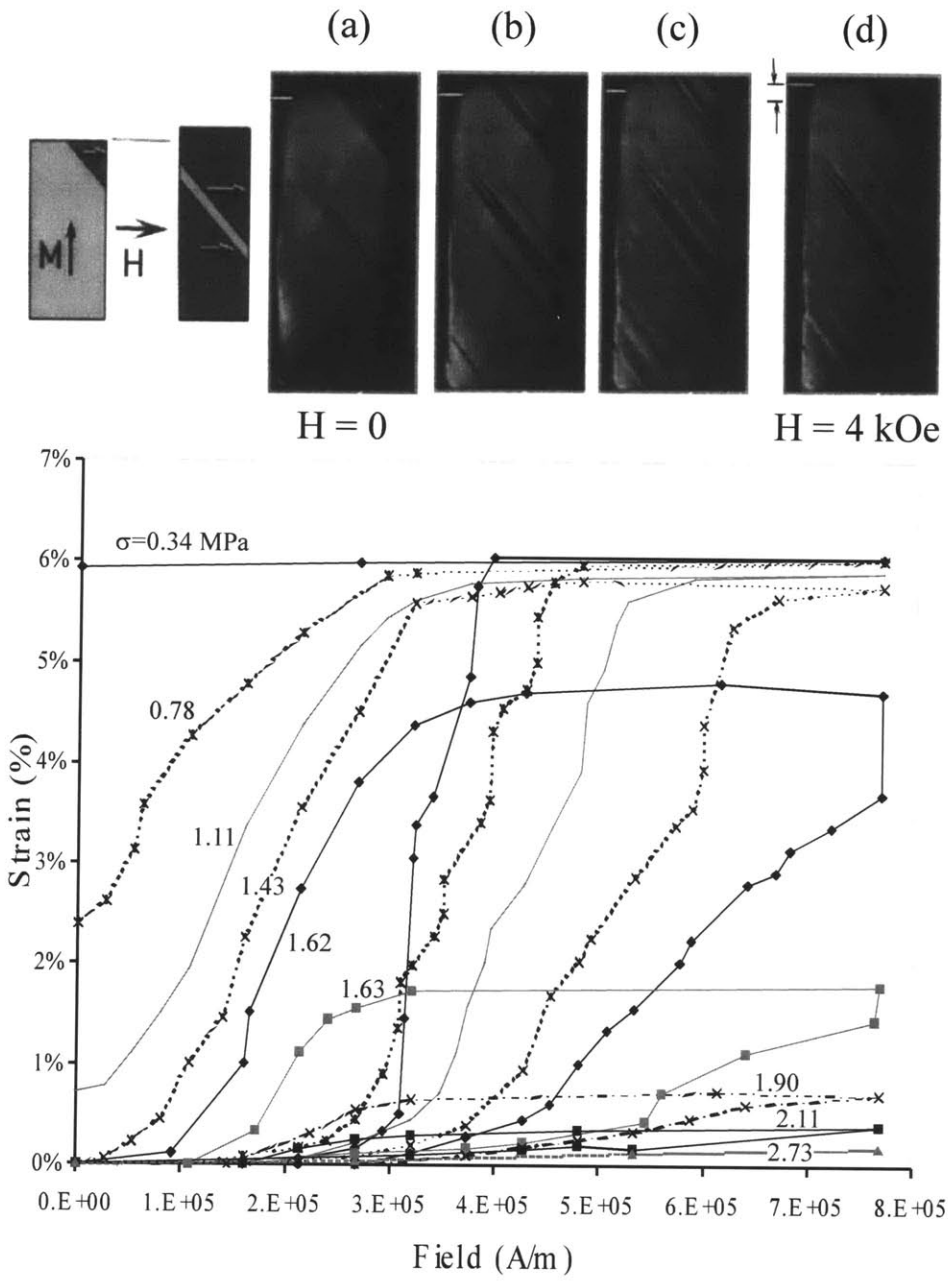

Figure 1-9: Quasistatic strain versus field for a Ni–Mn–Ga crystal actuating against a mechanical load. The loads consisted of various masses applied to the crystal actuating in the vertical direction. From [6].

field can rotate it away from that axis. The anisotropy energy is

$$U_k = -K_u(1 - \cos^2\theta) \ , \tag{1.4}$$

where K_u is the magnetocrystalline anisotropy and θ is again the angle of magnetization. The sum of these two energies gives the free energy in each variant of the crystal, and the difference in the free energies across a twin boundary give the driving force associated with the magnetic field [10] as

$$\Delta g = u_{\|} - u_{\perp} = \begin{cases} -K_u(2\eta - \eta^2) & \text{if} \quad \eta \leq 1 \\ -K_u & \text{if} \quad \eta > 1 \end{cases} \ , \tag{1.5}$$

where

$$\eta \equiv \frac{H}{H_a} = \frac{\mu_0 M_s H}{2K_u} \ , \tag{1.6}$$

and Δg is the Gibbs free energy difference between the variants, $u_{\|}$ and $u_{\perp}$ are the energy densities in the variants parallel and perpendicular to the magnetic field, respectively. The energy difference between the variants represents the maximum work that can be done by magnetic field induced stain, and thus the equivalent magnet stress at the twin boundaries can be written as

$$\tau_m = \Delta g / \gamma_0 \ . \tag{1.7}$$

The shear stress τ_m differs only slightly from the longitudinal stress σ_m output in an actuating crystal, and is given by

$$\sigma_m = \tau_m \tan\beta = \tau_m c/a = 0.94\,\tau_m \ . \tag{1.8}$$

The response of an FSMA actuator to this magnetic stress is related to its response to any quasi-static mechanical stress. An idealized mechanical stress-strain response is shown in Figure 1-10. Typical values for the properties labeled in the figure are shown in Table 1.1. Some of the material properties, especially T_m^s, σ_0 and C_{tb}, are highly dependent on composition. The later two properties also depend on defect structure, which is affected by heat treatment and actuation history. Crystals chosen for actuation experiments have very carefully controlled composition, and as mentioned earlier are subject to a controlled heat

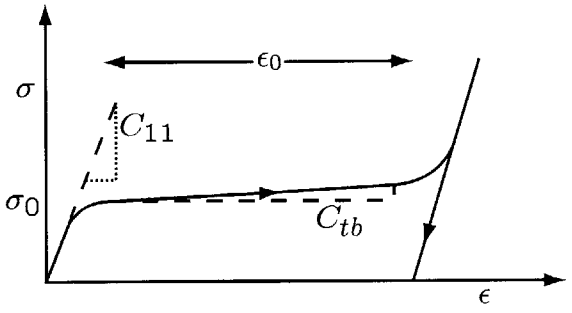

Figure 1-10: Idealized stress versus strain behavior of an Ni–Mn–Ga crystal. From [6].

treatment.

1.2.1 Magnetically Induced FSMA Actuation

The dynamic limits of magnetic FSMA actuation were studied in two distinctly different sets of experiments by Henry [11, 12, 3] and Marioni [10, 2, 13]. Henry's experiments focused on the cyclic actuation of an FSMA actuator up to frequencies of 500 Hz. Marioni's work utilized high speed magnetic pulses to study the phenomena that limit the actuation speed of an FSMA crystal.

There are two basic methods for accomplishing cyclic actuation of an FSMA actuation. First, the FSMA could be placed in a rotating magnetic field or a set of coils capable of generating magnetic fields perpendicular and parallel to the actuation direction. Second, a simple magnet with a single field direction can be used to actuate the FSMA against a prestress. Henry studied cyclic actuation against a prestress. A selection of his data, shown in Figure 1-11, indicated that the optimal prestress for such an actuator is roughly half the maximum magnetically induced stress output. The high frequency strain response of his actuator is shown in Figure 1-12. The frequency response limit that can be seen in Henry's data is not very indicative of the fundamental limit of Ni–Mn–Ga, but rather of Ni–Mn–Ga in a specific actuator with a specific power supply. The magnetic field generated by that specific electromagnet/power supply combination begins to drop off above 300 Hz.

Marioni's data, which examines the pure magnetic response of an isolated crystal, shows the fundamental limits of the magnetic driving force in Ni–Mn–Ga. Marioni used an air

Table 1.1: Accepted values for properties of active tetragonal Ni–Mn–Ga in the martensitic phase.

Material Property	Symbol	Value
Martensite Start Temperature	T_m^s	32°C ±30°C
Tetragonality	c/a	0.94
Twinning Shear Strain	ϵ_0	6.2 %
Twin Boundary Angle	β	43°
Saturation Magnetization	M_s	4.8×10^5 Am^{-1}
Magnetocrystalline Anisotropy Energy	K_u	1.9×10^5 Jm^{-3}
Threshold Magnetic Field for Actuation	H_0	$1.2 \times 10^5 \pm 0.2 \times 10^5$ Am^{-1}
Threshold Twinning Stress	σ_0	1 ± 0.5 MPa
Blocking Stress for Magnetic Actuation	σ_M	3.1 Mpa
Twinning Stiffness	C_{tb}	30 ± 20 MPa
Elastic Stiffness (c-axis)	C_{33}	28 GPa
Elastic Stiffness (a-axis)	C_{11}	30 GPa
Mass Density	ρ	8.1×10^3 kgm^{-3}

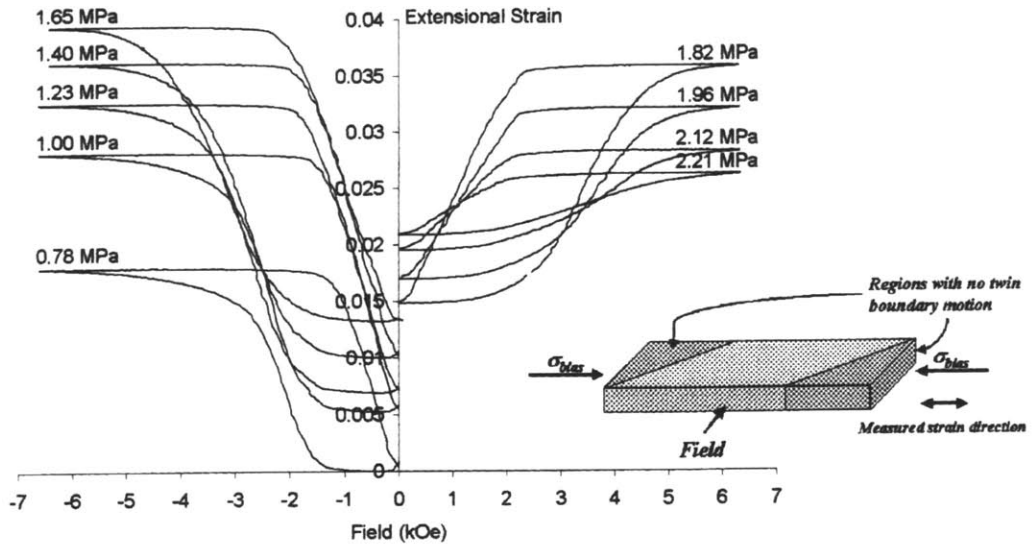

Figure 1-11: Field versus strain for a variety of prestress loads. The indicated stresses are the average stress from a spring load with a stiffness of 12 kN/m. The inset shows the constrained portions of the actuating FSMA crystal. From [3].

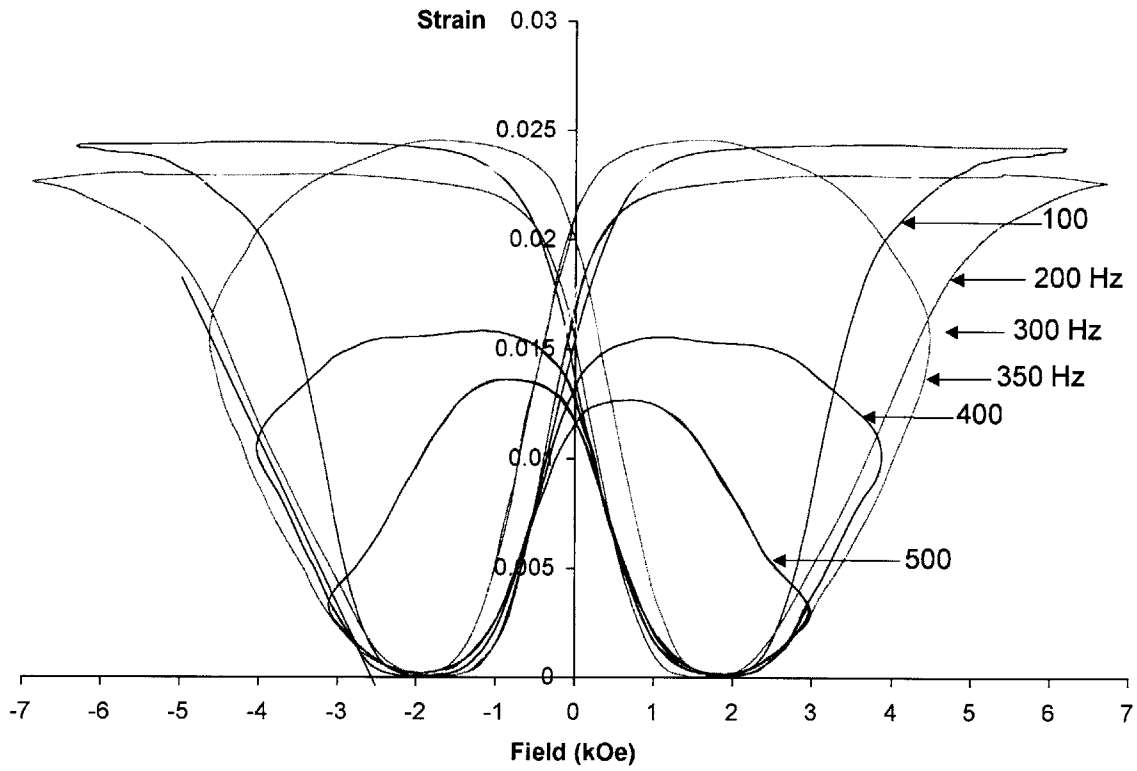

Figure 1-12: High frequency strain versus field response for Henry's actuator system. A prestress of 1.7 MPa was used for these curves. From [11].

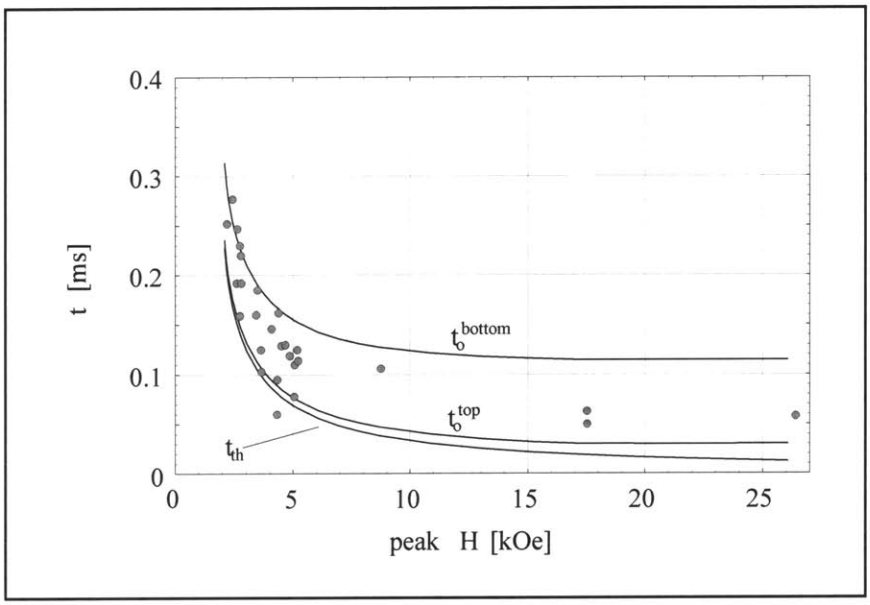

Figure 1-13: Onset time versus peak magnetic field. t_0^{bottom} and t_0^{top} represent the onset time predicted by the two extreme cases of Figure 1-14. t_{th} is the time it takes the magnetic field to reach the threshold for actuation. From [10].

core Helmholtz coil and a bank of high voltage capacitors to generate magnetic field pulses on the order of 1 T lasting less than a millisecond. He found that the onset time of actuation during these pulses varied within a well defined region (Figure 1-13). The onset time is the time between the magnetic field reaching H_0, and the most mobile twin boundary moving far enough to cause measurable actuation. Marioni found that mass inertia of the crystal was the limiting factor in onset time, and his data was bracketed by models of two situations shown in Figure 1-14. This work indicates that the limiting factor in an FSMA actuator's speed is simply the amount of energy available to move the actuated load. Equation (1.5) gives the expression for the energy available for magnetic actuation. The anisotropy energy of the crystal is the maximum energy available for actuation, which results in an actuator energy density of 1.9×10^5 Jm^{-3} and a blocking stress of approximately 3.0 MPa.

Using smaller magnetic field pulses, Marioni also studied the energy distribution of pinning sites in the crystals. These pinning sites present obstacles to twin boundary motion that can only be overcome by larger driving forces. The specific crystal tested showed a distribution of pinning sites with energies between $0.55\,\text{K}_\text{u}$ and $0.70\,\text{K}_\text{u}$. Stresses between 1.7 MPa and 2.2 MPa would be required to move the twin boundary past these obstacles.

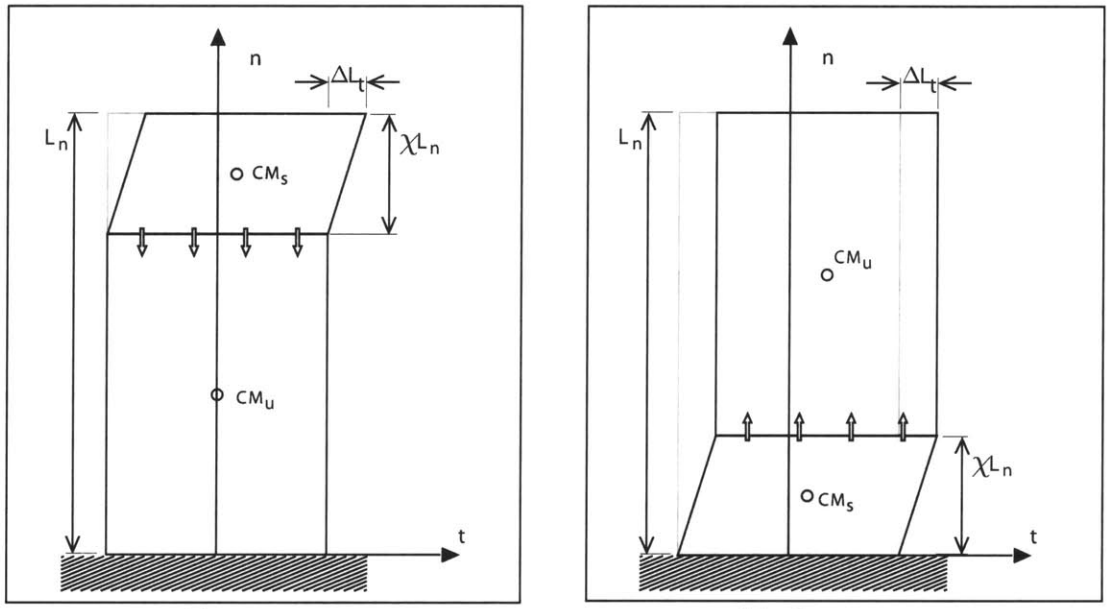

Figure 1-14: Two theoretical situations in which a single twin boundary is responsible for the onset of actuation. In situation (a) the twin boundary moves downward from the free end of the crystal, and only the the mass already swept by the twin is accelerated. In (b), a twin proceeds from the fixed end of the crystal upward, and the mass of both the swept region and untransformed region must be accelerated. From [10].

Pinning sites are responsible for the non-zero twinning stiffness, C_{tb}. In a theoretically perfect crystal, overcoming the twinning threshold stress would cause they entire crystal to transform.

1.3 Motivation for This Work

FSMAs have a lower energy density than thermally actuated SMAs, but much higher bandwidth. They have a raw output energy density that is comparable to mature active material technologies like PZT and Terfenol-D. FSMAs produce much higher output strains than PZT or Terfenol-D (6% as opposed to 0.1%), at much lower stress levels. Experiments have shown that the strain and energy density of FSMAs combine to limit FSMA actuation bandwidth to approximately 2 kHz [2]. FSMAs appear to fit into an empty niche in the spectrum of active materials, until the requirement of the magnetic field is considered.

The large magnetic field required, up to 0.8 T to reach saturation magnetization, is not trivial to produce. Electromagnets designed to provide the required field continuously or with duty cycles greater than a few percent must be substantially larger than the volume of the FSMA crystal. Appendix A examines the design of such magnets, and Table 1.2 summarizes the results of the design exercise, along with a comparison to commercially developed Ni–Mn–Ga actuators. Even magnet designs that are only utilized for short pulses of large currents must be large enough to fully envelope the FSMA crystal in the generated magnet field.

In conventional SMAs, heat can be generated by simple resistive heating of the SMA itself, or provided by radiation, conduction, or convection from some source that can be easily distanced from the actuator. Increasing the distance between the FSMA and the magnetic poles results in an increase in the energy and volume requirements for the magnet, both of which scale with the cube of the magnet's gap length. The combined properties of an electromagnet/FSMA actuator, with an effective energy density that is a small fraction of raw material energy density, could make it difficult to find a problem for which FSMAs are a good solution.

In an attempt to reduce the magnetic requirements for actuation, acoustic vibrations were induced in the Ni–Mn–Ga crystal while it was magnetically actuated [15]. This acoustically assisted actuation reduces the threshold field for actuation and increases the strain

Table 1.2: Collected data for commercial actuators available from AdaptaMat compared with optimized electromagnetic designs for identical crystal sizes. Electromagnet design is discussed in Appendix A. Actuator images and data from [14].

Commercial Actuator	FSMA Crystal Dimensions (mm)	% Volume Active Material	Optimized Theoretical Design	Estimated % Volume Active Material
A5-2 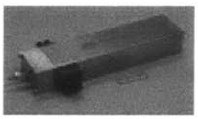	$0.52 \times 2.4 \times 84$	0.14%	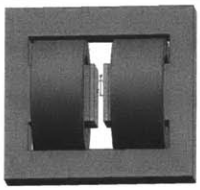	0.30%
A06-3 	$0.55 \times 2.2 \times 15$	0.12%	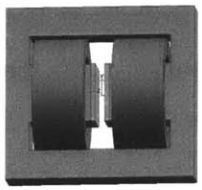	0.16%
A1-2000 	$15 \times 40 \times 25$	0.33%		0.63%

response at a given field. The limits and details of this effect are still being investigated; however, even with a very dramatic reduction in the magnetic requirements, a magnet of some sort will still be required.

The motivation for the work presented in this thesis came from the hypothesis that twin boundary motion could be induced using only acoustic forces. Two possible mechanisms for inducing twin boundary motion using acoustic stress were proposed. The first was to use resonant waves with stress intensities high enough to induce twin boundary motion. When the drive frequency of the waves was varied slightly off resonance, the crystal would change shape so that its new resonance would match the driving frequency. The second was to use asymmetrical acoustic pulses to extend or contract the crystal one pulse at a time.

The first proposed method of acoustic actuation was tested briefly in the apparatus used for acoustically assisted magnet actuation. A piezoelectric stack was used to vibration a small crystal at its fundamental longitudinal resonance with as much power as was available. This resulted in rapid heating of the piezoelectric stack and subsequent heating and transformation of the Ni–Mn–Ga crystal to austenite. Whether heating of the crystal was due to conduction from the piezoelectric stack, or whether plastic deformation was partially to blame is unknown [16]. However, this result led to the conclusion that a resonant standing waves ($\sim$100 kHz) with stress levels near the threshold stress of Ni–Mn–Ga (1 MPa) might be impossible to realize in the martensitic phase.

The second method proved to be the most plausible route to acoustic shape memory alloy actuation. Generation of suitable compressive or tensile longitudinal acoustic pulses with stresses on the order of 1 MPa proved to be difficult but not impossible. After several design iterations, an experimental device was created that was capable of generating twin boundary motion using acoustic pulses.

The main goal of this work was to understand and characterize acoustic pulse SMA actuation. Experimental results from four different actuators were gathered, under a variety of actuating conditions. The actuators, and the design process that led up to them, are discussed in Chaper 2. Measurements of the electrical input pulses, generated acoustic pulses, and the output stress and strain of the actuator were collected and are presented in Chapter 3. Chapter 4 provides analysis of selected measurements and discusses the affects of various actuation parameters. Finally, Chapter 5 discusses the potential for applications and future work with acoustic pulse SMA actuators.

Chapter 2

Experimental Apparatus

In this chapter, the experimental apparatus used to demonstrate acoustic actuation of FSMA crystals is described. Several design iterations were required to go from working theory to working actuator. Since the design requirements for a working acoustic pulse FSMA actuator were initially unknown, approximate requirements were determined for each iteration, and actuator prototypes were assembled to test the functionality of each design. The functional requirements were updated using the data collected at each iteration, and a new design was developed.

Section 2.1 describes the functional requirements for an acoustic pulse FSMA actuator. Section 2.2 describes the first design prototype, its inadequate performance, and the new design requirements that were developed from the experience gained. The remainder of the chapter describes the four actuators used in collecting the data presented in Chapter 3. The first two of these actuators, C0 and C1, were the first two functional designs. Actuator C2 included additional design improvements, as well as new components for actuating against an elastic load. The fourth actuator, C3, incorporated a stress sensor to aid in studying the behavior of the acoustic pulse.

2.1 Functional Requirements

In this section, the functional requirements for each of the components of the acoustic pulse actuator are described. Each of the subsections describes one of the components and the corresponding requirements, except for Section 2.1.2, which is devoted to the finite element simulations that were used to aid in the design of two of the actuator components, as well

as the design of the overall actuator.

2.1.1 Acoustic Pulse Generator

The initial requirements for a functional acoustic pulse actuator were developed using the material properties of Ni–Mn–Ga, from the literature on magnetic actuation (see Chapter 1), and linear models of acoustic waves in the actuator system. Many of the functional requirements were revised as experience was gained through experimentation.

The most fundamental requirement on the acoustic pulse FSMA actuator is that the acoustic pulse generator be able to generate shaped transient stress waves, with stresses larger than the twinning stress, σ_0, in the FSMA. In Ni–Mn–Ga, the generally accepted value of σ_0 is about 1 MPa. Generating a stress of this magnitude statically using magnetic fields is not difficult. However, it is more difficult to generate these stress levels in a transient acoustic wave.

The second requirement is that the magnitude of the actuating stress wave is asymmetric, so that when the actuator is being compressed the compressive stress is greater than σ_0, and the tensile stress is much less than σ_0. When the actuator is being extended the tensile stress is greater than σ_0, and the compressive stress is much less than σ_0. This requirement includes stress waves generated directly by the pulse generator, as well as any reflections that develop in the actuator.

The third requirement is not so much a requirement as a goal, namely, that the acoustic pulse actuator is as small as possible. Acoustic pulse actuation was originally conceived to eliminate the need for a bulky electromagnet from magnetic FSMA actuators. Replacing the electromagnet with a bulky pulse generator would not accomplish the original intent.

Due to the high energy densities and blocking stresses available in active material, it was decided that an active material would be used as the pulse generator. Several material technologies are capable of generating a force that can be converted into a 1 MPa stress on the FSMA. In order to maximize energy density, only actuators capable of generating the stress directly (i.e. without mechanical amplification) were considered. Piezoelectric and magnetostrictive materials are the only mature technologies capable of generating stresses higher than 1 MPa [17]. However, magnetostrictive devices are limited to significantly lower operating frequencies than piezoelectric devices, due to the inductive load of the electromagnets they require, and the formation of eddy currents in the magnetostrictive

material. Since piezoelectric devices can be operated at higher frequencies, they can generate actuation level stresses using smaller displacements, and therefore a shorter active material length than a magnetostrictive actuator. In order to determine more specifically what type of piezoelectric device would be required to implement the pulse generator, the results of a simple 1-D finite element simulation were used, as discussed below.

2.1.2 1-D Finite Element Simulation

A one-dimensional lumped mass finite element model was developed to help determine the displacements and pulse durations that might be required to generate actuation stresses in the FSMA crystal. The details of this model are discussed in Appendix B.

In the simulations, it was assumed that a piezoelectric device would be used as the pulse generator. The one-dimensional constitutive law for a longitudinally polarized piezoelectric device is

$$\epsilon_{33} = s_{33}^{E}\,\sigma_3 + d_{33}\,E_3 \tag{2.1}$$

$$D_3 = d_{33}\,\sigma_3 + \kappa_3^{\sigma}\,\kappa_0\,E_3 \ , \tag{2.2}$$

where ϵ_{33} is the longitudinal strain of the device, s_{33}^{E} is the material compliance at constant field, σ_3 is the stress, d_{33} the piezoelectric strain coefficient, E_3 is the electric field, D_3 is the charge density, κ_3^{σ} is the relative dielectric constant measured at constant stress, and κ_0 is the permittivity constant of free space [18]. This law provides an easy way to estimate the quasi-static response of a piezoelectric actuator. However, the dynamic response is more difficult to compute, which is why a finite element model was employed. For use in the finite element model, Equation 2.1 is multiplied by the the thickness of the piezoelectric and rewritten as

$$-s_{33}^{E}\,\sigma_3\,t_3 = -u_3 + d_{33}\,V \ , \tag{2.3}$$

where u_3 is the displacement of the piezoelectric device, t_3 is the thickness, and V is the voltage across the device. In this form, the equation shows that a positive applied voltage results in a compressive stress on the piezoelectric device, assuming the boundaries do not allow the device to expand. In the finite element model, the boundaries are elastic and the compressive stress propagates into the rest of the system as the piezoelectric device expands.

Table 2.1: Properties of piezoelectric materials used in acoustic pulse actuation experiments. d_{33} is the piezoelectric strain coefficient, g_{33} is the voltage coefficient, κ_3^T is relative dielectric constant. The quantities listed for the stack are for the entire assembly, not the bulk material of the individual layers. The device were purchased from Piezo System, Inc. [19]

Part Number	T140-A4E	T110-H4E	TS18-H5-104
Type	Single Layer	Single Layer	Stack
Thickness	1.02 mm	0.267 mm	18.0 mm
Stiffness	52 GPa	50 GPa	43 GPa
d_{33}	0.390 nm/V	0.650 nm/V	140 nm/V
g_{33}	24.0 mV·m/N	19.0 mV·m/N	0.16 mV·m/N
κ_3^T	1800	3800	N/A
Capacitance (5 mm×5 mm)	390 pF	1500 pF	1600 nF

A typical simulation result is shown in Figure 2-1. The left hand side of the piezoelectric was treated as though it were attached to a semi-infinite rod, so that no reflections occur at that boundary. The right end of the FSMA crystal is free. Simulations using the model shown in Figure 2-1(a) were run with a variety piezoelectric thicknesses and pulse durations to determine the magnitude of stresses that could be generated with a single layer piezoelectric device. The results are shown in Figure 2-2.

The peak input voltage for all of the results shown in Figure 2-2 was 120 V, which corresponds to a quasi-static displacement of 40 nm. The shape of the simulated input voltage wave was a highly asymmetric sine wave. The high frequency, f_{H}, portion of the sine wave looks like a raised cosine going from 120 V at $t = 0$ to 0 V at $t = 2/f_{\mathrm{H}}$. This voltage change quickly contracts the piezoelectric device and generates a tensile stress pulse. The low frequency, f_{L}, portion of the input pulse returns the piezoelectric actuator to 120 V, in order to prepare for the next pulse. The waves used in these simulations had an asymmetry of 40:1. The rise time, t_{r}, of the input wave, defined as the time from 10% to 90% of the maximum, can be calculated using the definition of the raised cosine function. It is approximately equal to

$$t_{\mathrm{r}} = 0.255\, f_{\mathrm{H}} \ . \tag{2.4}$$

The asymmetric waves will be referred to by the frequency of the raised cosine, the frequency

of the slow portion of the pulse, f_L, can be found using

$$f_L = 0.025\, f_H \ . \tag{2.5}$$

The time constant of this portion of the wave, t_f, can be calculated identically to t_r.

The current required to generate the compressive stresses shown in Figure 2-2(a) can be estimated using Equation (2.2) and the dimensions of the piezoelectric actuator. The charge on the piezoelectric is

$$q_3 \ = \ d_{33}\, F_3 + C_{33}\, V \ , \tag{2.6}$$

and maximum current is

$$I_{\max} = max\left(\frac{dq_3}{dt}\right) \ , \tag{2.7}$$

where C_{33} is the capacitance of the piezoelectric actuator, q_3 is the charge, and F_3 is the force. Figure 2-2(b) shows the estimated currents required to generate the stresses shown in Figure 2-2(a). The dotted line in Figure 2-2(b) represents the maximum current output of an M. S. Kennedy 610 amplifier. The MSK610 was the amplifier used during testing of the single layer piezoelectric actuator design, discussed in Section 2.2. The simulation results shown in Figure 2-2 indicate that acoustic pulse actuation using a single layer piezoelectric and the MSK610 might not be possible, since none of the simulations that result in 1 MPa or higher stress fall under the current limit of the MSK610. Testing confirmed this, and showed that the actual stresses induced by the single layer piezoelectric were much lower than the simulated results.

2.1.3 Reflector

One of the functional requirements for the acoustic pulse actuator came from simulation results like those shown in Figure 2-1. The reflection of the stress pulse off the free end of the FSMA results in an inverted stress wave, which could undo the work done by the original actuating stress wave. The brass reflector, in Figure 2-8(a), is in place to prevent this inverse reflected pulse.

Classical wave theory can be used to explain the inversion of the stress pulse reflecting off a free boundary. Wave theory also shows why the addition of a reflector prevents the

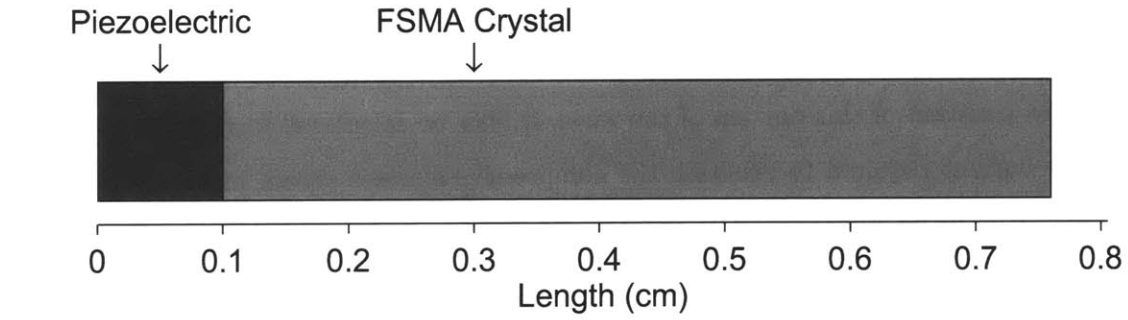

(a)

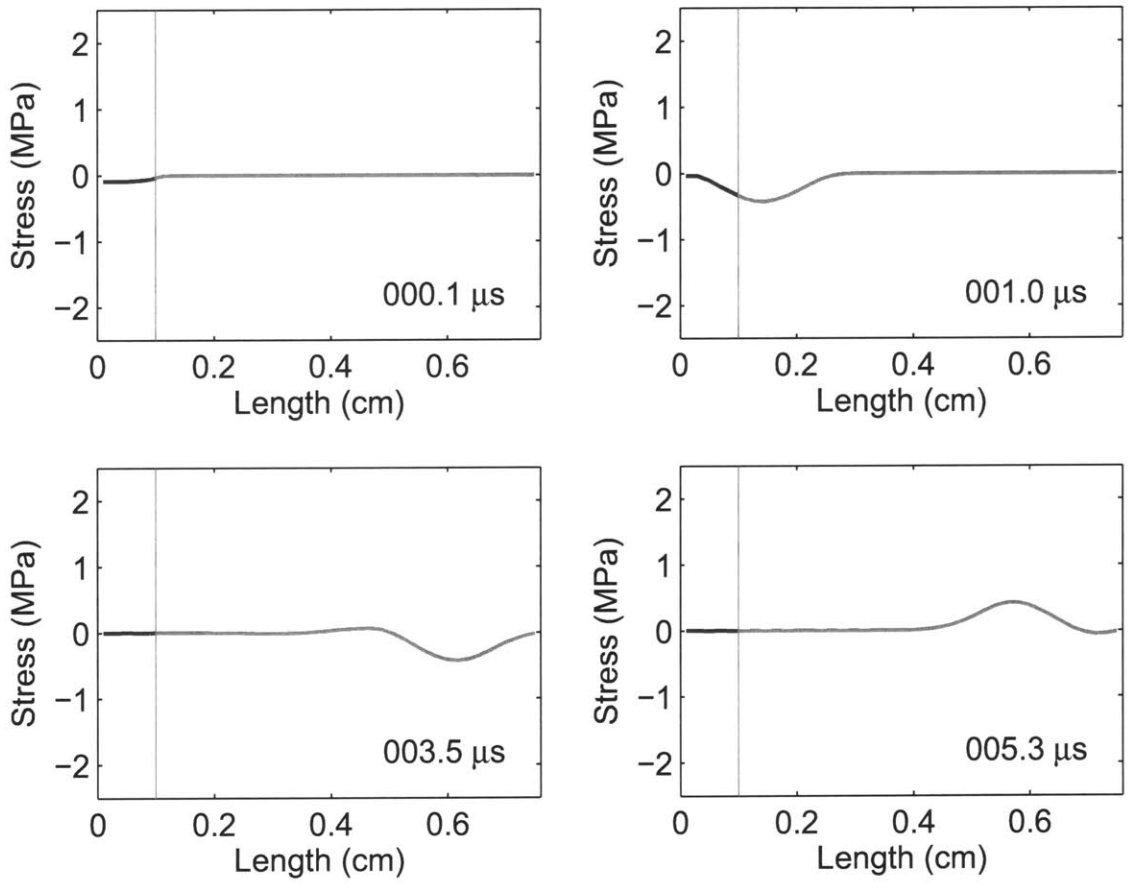

(b)

Figure 2-1: Simulation of an acoustic pulse FSMA actuator. (a) The model being simulated. The boundary conditions are that the right face of the FSMA is free and the left face of the piezoelectric pulse generator is nonreflecting. (b) Results of the 1-D linear elastic finite element simulation used to estimate the magnitude of stresses that can be generated in the FSMA crystal.

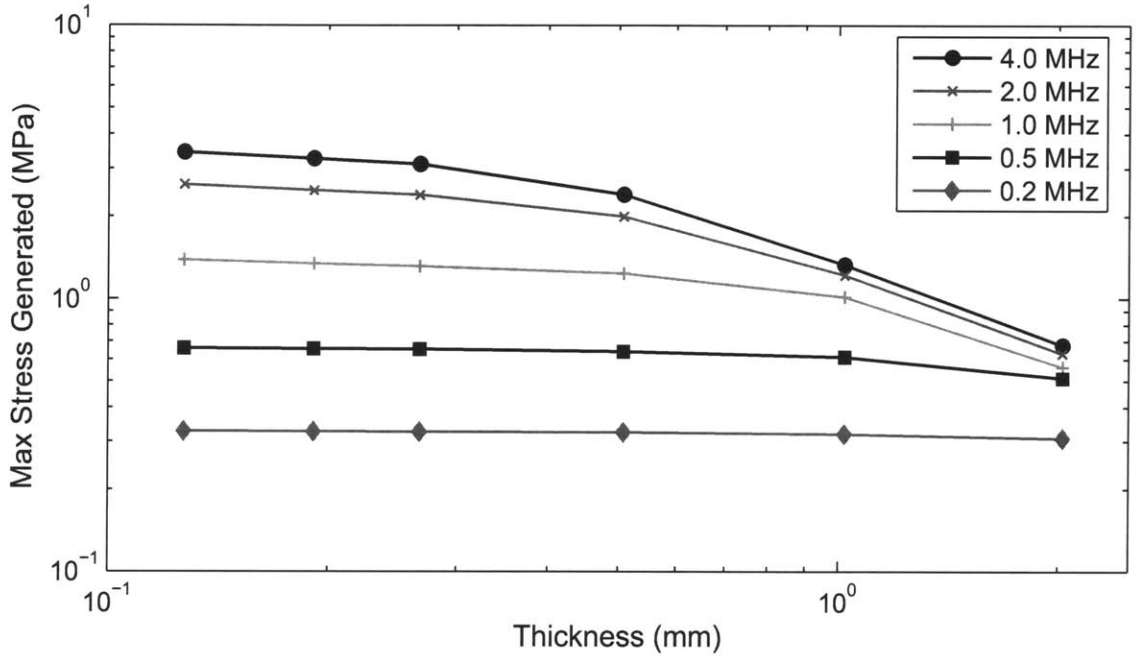

(a)

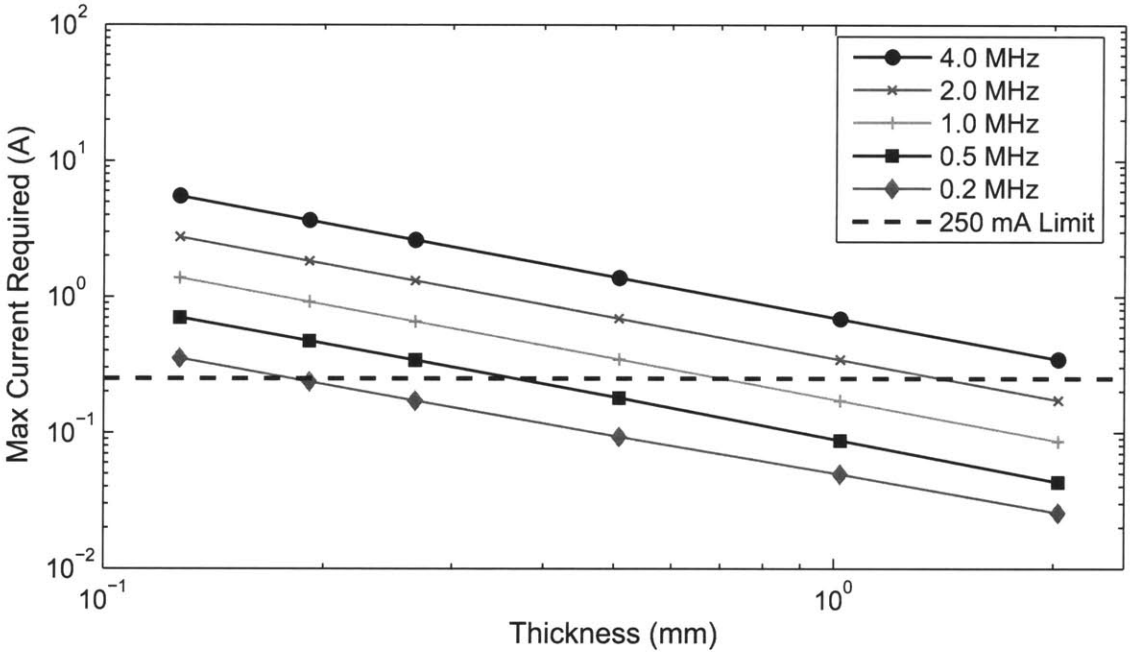

(b)

Figure 2-2: A collection of maxima from a series of simulations. (a) The maximum generated compressive stress taken from the midpoint of the crystal, plotted for several frequencies, f_{H}. (b) The peak current required to generate the stresses shown in (a).

Table 2.2: Acoustic impedance for selected material.

Material	Specific Acoustic Impedance
Brass	29 MPa·s/m
Ni–Mn–Ga	15 MPa·s/m
Steel	40 MPa·s/m
PZT 5A	20 MPa·s/m
Aluminum	14 MPa·s/m
Titanium	22 MPa·s/m
Glass	12 MPa·s/m
Epoxy	2.1 MPa·s/m

inverted pulse. In setting up the wave equation to study reflection off the boundary between two materials, we will assume our system consists of two infinitely long rods of identical cross-section, meeting at $x = 0$. A longitudinal wave propagates through the left hand rod from $-\infty$ and into the right hand rod. Assuming that stress and displacement are continuous across the boundary at $x = 0$, the solution to the wave equation is

$$u = \begin{cases} A(e^{ik_1x-i\omega t} + Re^{-ik_1x-i\omega t}) & \text{for} \quad x < 0 \\ TAe^{ik_2x-i\omega t} & \text{for} \quad x > 0 \end{cases} , \tag{2.8}$$

where

$$R = \frac{\sqrt{\frac{Y_1\rho_1}{Y_2\rho_2}} - 1}{\sqrt{\frac{Y_1\rho_1}{Y_2\rho_2}} + 1} , \tag{2.9}$$

$$T = 1 + R , \tag{2.10}$$

$$k_1 = \omega\sqrt{\frac{\rho_1}{Y_1}} , \tag{2.11}$$

$$k_2 = \omega\sqrt{\frac{\rho_2}{Y_2}} . \tag{2.12}$$

The quantity $\sqrt{Y\rho}$, referred to as acoustic impedance, is the material property that defines the behavior of the wave at the material boundary. See Table 2.2 for acoustic impedance values of selected materials. We will examine three combinations of materials, which result in three different wave behaviors at the boundary.

In the first combination, the material in the left hand rod has high acoustic impedance

and the material in the right hand rod has low impedance. In this case, the displacement wave reflected from the boundary has the same sign as the incoming wave. However, because it is traveling in the opposite direction, the stress caused by the wave has the opposite sign. The equation for the stress wave can be obtained by taking the first derivative of Equation (2.8) with respect to x, which results in

$$u' = \begin{cases} ik_1 A(e^{ik_1 x - i\omega t} - Re^{-ik_1 x - i\omega t}) & \text{for} \quad x < 0 \\ ik_2 TAe^{ik_2 x - i\omega t} & \text{for} \quad x > 0 \end{cases} . \tag{2.13}$$

In this first combination, the displacement amplitude of the transmitted wave is larger than both the incoming and reflected waves. Because the right hand rod has low acoustic impedance, the power of the transmitted wave is still smaller than the power of the incoming wave. As the impedance of the right hand rod approaches zero, the displacement amplitude of the transmitted wave approaches twice that of the incoming wave, but the energy of the transmitted wave approaches zero. The amplitude of the reflected wave approaches that of the incoming wave. However, the reflected and incoming stress waves have opposite signs. The inverted reflection is caused by the zero stress condition at the material boundary, which is essentially free when the impedance of the right hand rod is zero. The finite element simulation, in Figure 2-1, shows this behavior for a wave of very short duration.

In the second combination, the two materials have the same acoustic impedance. In this situation the reflected wave vanishes and the magnitude of the transmitted wave is identical to the incoming wave.

In the third combination, the left hand rod has a lower impedance than the right hand rod. In this case there again a reflected wave; however the reflected stress wave now has the same sign as the incoming stress wave. The brass reflector in Figure 2-8(a) sets up the third combination at the right hand end of the FSMA crystal. The reflected stress pulse will thus have the same sign as the actuating stress pulse and will not interfere with the work that is done by the actuating pulse. The large size of the reflector is meant to allow the wave to disperse before it reflects off the free end of the brass and returns to the FSMA. Attempts to optimize the shape of the reflector will be discussed in the next section.

2.1.4 Acoustic Horn Dissipator

While the brass block reflector used in the single layer actuator experiments prevents an inverted reflection from the end of the FSMA, there is still an inverted reflection from the end of the brass block. In order to minimize this reflection, an attempt was made to design a reflector shape that would disperse the reflection before it returned to the FSMA crystal. The design was carried out using a one-dimensional finite element model similar to the one mentioned in Section 2.1.2. However, the model was rewritten using conservative elements. The conservative element model was an improvement over the lumped mass model, and was found to closely match 1-D analytical solutions to the wave equations for simple shapes such as a straight rod and an exponentially thinning rod. See Appendix B for the comparison and derivation of these models.

Starting from an exponentially thinning horn, shown in Figure 2-3(a), MATLAB's `fminimax` routine was used to change the shape of the horn in an attempt to find a more dispersive shape. When MATLAB was allowed to vary size of the individual elements, an immediate problem became apparent. As Figures 2-3(b) and 2-3(c) show, the optimization favored the formation of reflectors using sharp changes in the horn's cross-sectional area. The resulting reflectors would exhibit different behavior in 3-D space than they do in the 1-D model. This optimization problem can be avoided somewhat by constraining the optimization, or by varying a parameterized function that describes the shape of the horn, rather than varying the size of the individual elements. After a wide variety of constraints and parameterizations were tried, a few possible horn candidates emerged. However, their performance (Figure 2-3(d)) was only marginally better than that of a block (Figure 2-3(e)) similar to the reflector already used. Because 3-D effects made the potential performance of the optimized horns questionable, the simple block reflector was used in all the apparatus in this thesis.

2.1.5 Bond Lines

One of the implicit requirements of the acoustic pulse actuator design is that the connections between the various pieces of the actuator must not separate during normal actuation. Also, in order to satisfy the first functional requirement of the acoustic pulse actuator, the connections must transmit the actuating pulse from the pulse generator to the FSMA and

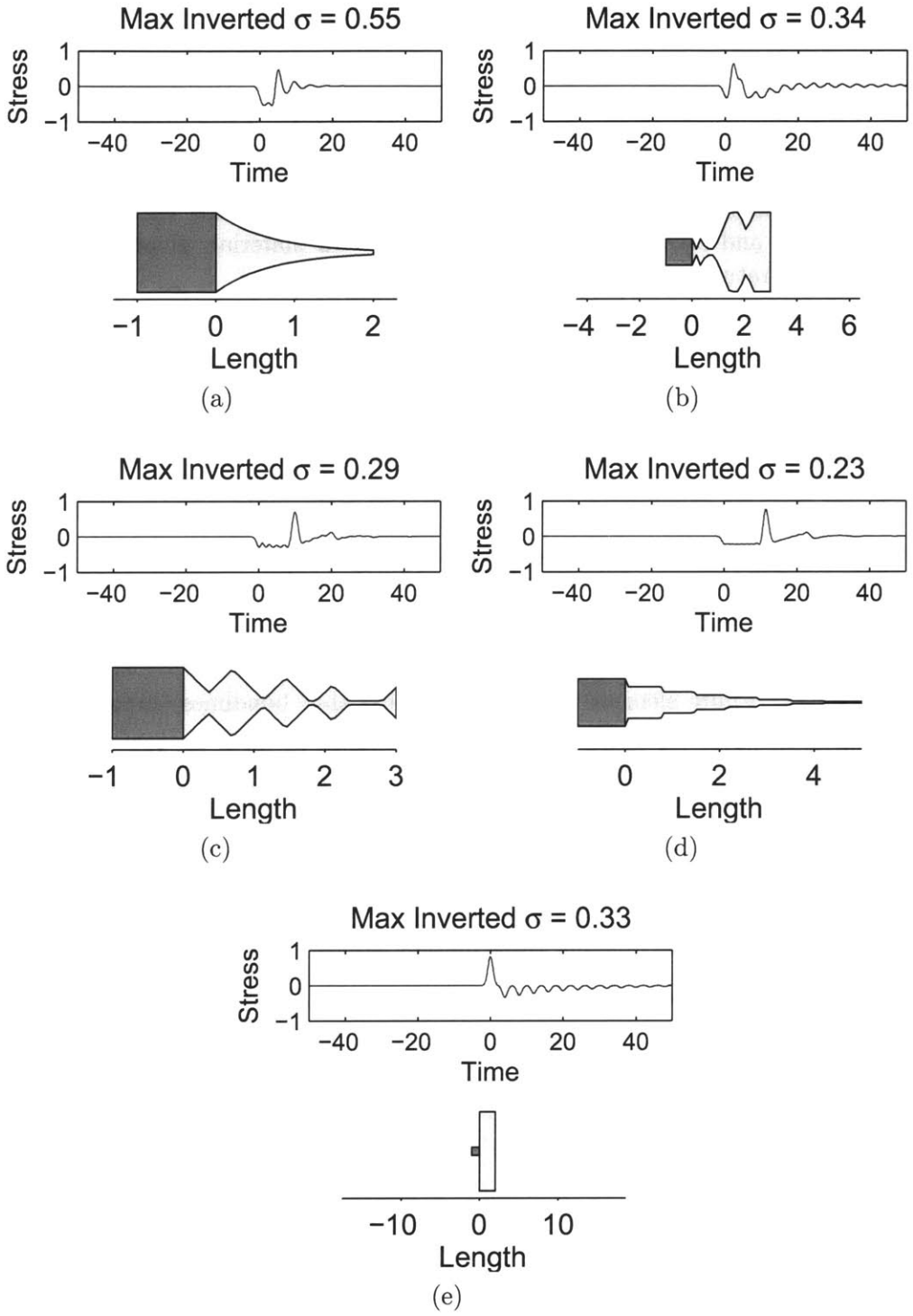

Figure 2-3: Potential dispersive horn designs. The stress plots in these figure show the reflection of a gaussian stress pulse with a magnitude of +1. The horn models are shown in profile, and have a thickness of 1. All dimensions are normalized about the unit pulse, and unit cube (darker square).

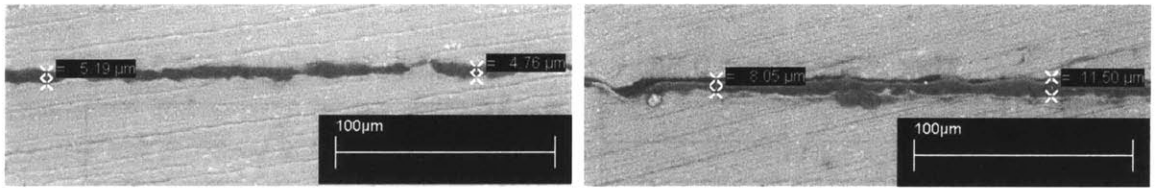

Figure 2-4: SEM images of epoxy bonds on aluminum. The bonds were prepared using the same cleaning and clamping techniques as used with materials glued together in the experimental apparatus.

into the reflector. Because of the sensitivity of Ni–Mn–Ga's actuation properties to changes in composition and heat treatment, metal-metal bonding was ruled out. Polymer adhesives, other than the heat curing variety, do not have any adverse affects on the FSMA. However, the maximum strength of adhesive bonds is only ~30 MPa, under ideal conditions.

The bond thickness of any polymer bonds in the actuator is important because of the effect thickness has on transmitting acoustic pulses between the other materials. A thinner bondline, while more susceptible to failure, also has a much smaller affect on transmission of acoustic waves. Finite element modeling indicated that bondlines thicker than 50 μm had a detrimental affect on wave propagation. In order to estimate the bond thickness of actual bondlines, dummy bonds were prepared using Loctite E-120HP epoxy and aluminum. E-120HP is one of the adhesives used in two of the acoustic pulse actuators. The same surface preparation and clamping techniques used when assembling the acoustic pulse actuators were used when assembling these dummy bonds. After the dummy bonds cured, they were examined in a scanning electron microscope, which showed that the bondlines were no thicker than 20 μm, as shown in Figure 2-4. By keeping surfaces flat, roughness low, and using consistent clamping forces, bonds with similar thickness were consistently achieved in the experimental actuators.

Conductivity is another important factor in adhesive bonds. In the single layer piezoelectric actuator apparatus, the piezoelectric was grounded through its bond to a steel backing. Although conductive adhesives were not used due to their low strength, conduction across a thin bondline was achieved, thanks to the surface roughness of the mating parts. DC measurements and impedance data over a wide range of frequencies (100 Hz to 40 MHz), indicated that the resistance of E-120HP bonds varied from assembly to assembly, but was never above 1 Ω. While good conductivity was necessary in the single layer piezoelectric

actuator, it caused measurement noise in other apparatus if insulators were not employed to electrically isolate sensors.

2.1.6 Drive Circuit Design

The electronics that drive the acoustic pulse generator are just as important as the active material used. Section 2.1.2 mentioned briefly the MSK-610 amplifier, which was used to drive the single layer piezoelectric actuator. The MSK-610 has a full power bandwidth of 9 MHz. However, its current limit of 200 mA hindered actuation of the single layer piezoelectric pulse generator at high bandwidth. Using multiple amplifiers in parallel could have improved the single layer actuator. However, a much more drastic improvement was necessary to get stress levels near σ_0.

A piezoelectric stack actuator, TS18-H5-104, replaced the single layer. The stack's capacitance is much higher than a single layer, so it draws much higher currents. In order to drive the stack from 0 V to 100 V with a rise time of 10 μs, a current of 16 A is required. A special circuit was designed to generate a sawtooth wave using two MOSFET switches to control the rise and fall of the waveform. Figure 2-5 shows the first design iteration of the circuit. Designated E0, this circuit was used in the first funtional acoustic actuation experiments, but did not perform as well as desired. Circuit E1 (Figure 2-6) is a redesign of the original circuit with a maximum burst current of approximatively 40 A, which results in a rise time of 4 μs for driving the piezoelectric stack to 100 V.

Circuits E0 and E1 function almost identically. To generate compressive pulses, a constant voltage at the gates of the low power p-type IRFU9310 MOSFETs allows any charge on the piezoelectric stack to slowly and continuously drain to ground. A square pulse on the gates of the higher power IRF820 MOSFETs force the piezoelectric stack to quickly charge up to 100 V, causing it to expand rapidly and generate a compressive stress pulse. As soon as the triggering pulse to the IRF820s subsides, the charge drains off the stack, and it returns to its original state. The relay in circuit E1 allows the circuit to be switched between compressive and tensile pulses. To generate tensile pulses, the stack is first charged to 100 V and then quickly discharged, contracting the stack and creating an tensile pulse.

Some control over the generated stress pulse is possible through the electronics. The voltage of the power supply, V_{in}, and the triggering pulse, V_{g}, affect the amplitude and leading edge slope of the sawtooth wave. The amplitude of the sawtooth wave is approximately

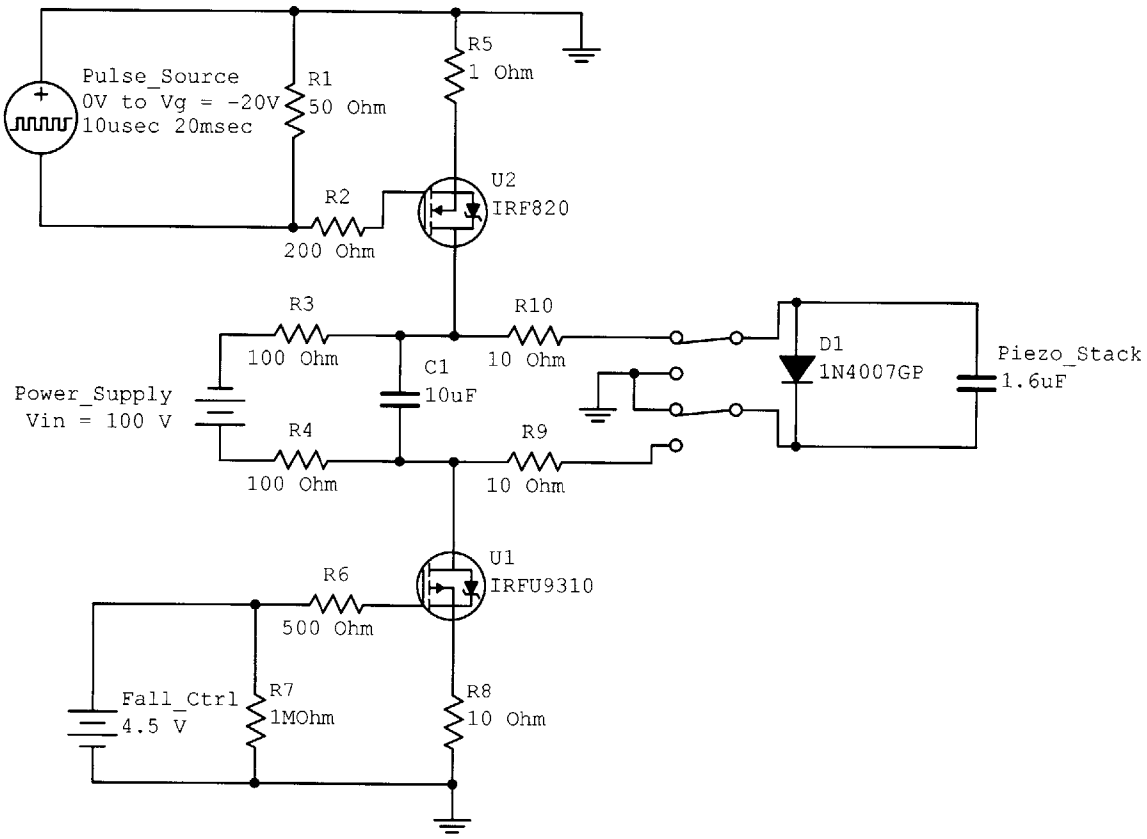

Figure 2-5: Circuit diagram for the first generation pulse circuit, designated E0.

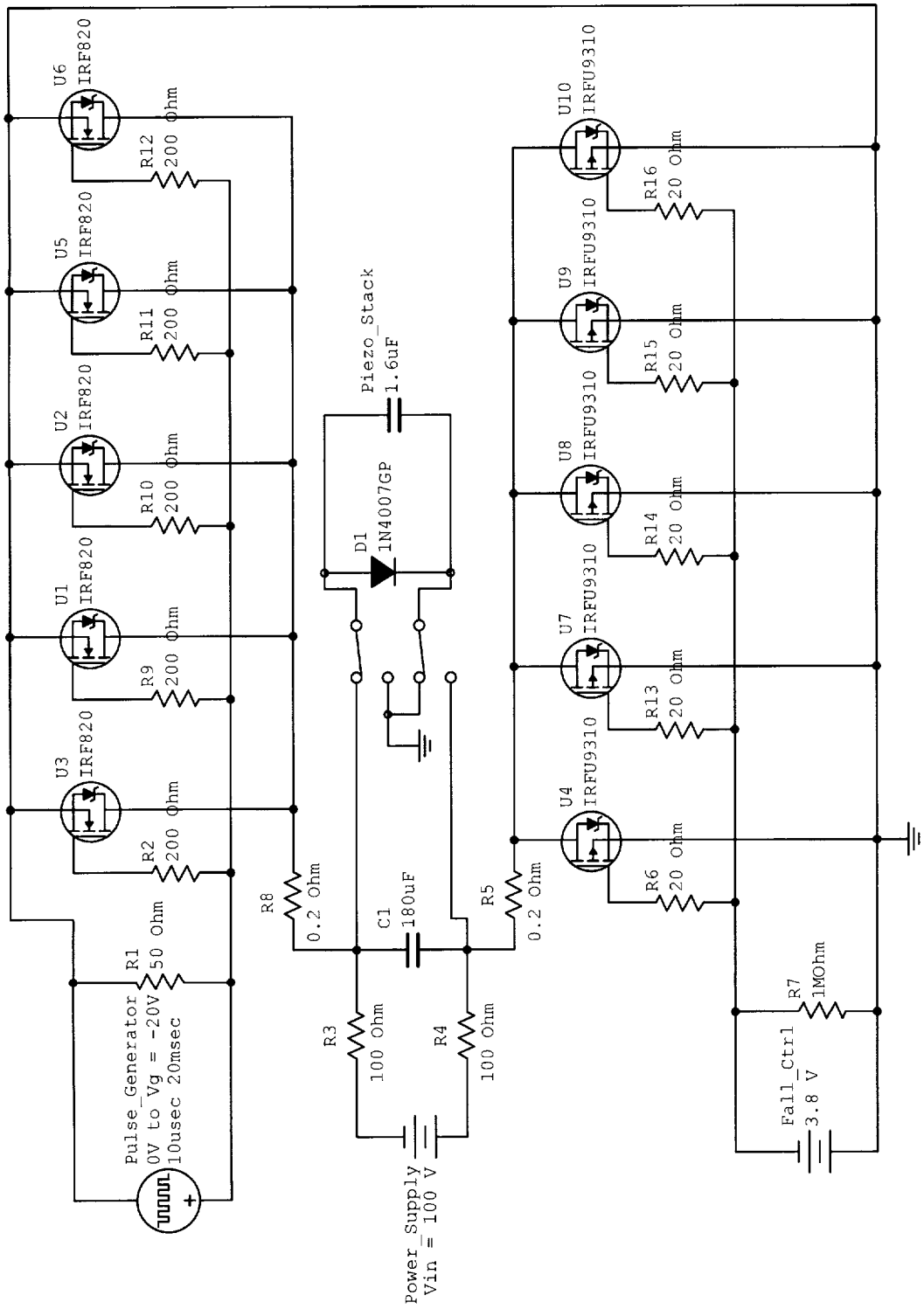

Figure 2-6: Second generation pulse circuit, designated E1.

equal to the power supply voltage, V_{in}. The triggering pulse is applied the gates of the high power MOSFET's, the amplitude of the pulse is referred to as the gate voltage, V_g. The gate voltage controls the drain-source current on the IRF820s, which in turn controls the rate at which the piezoelectric stack is charged. The gate threshold voltage for the pulse circuit is ~3 V and the saturation voltage is ~9 V. The effect V_g has on the leading edge of the input pulse is illustrated in Figure 2-7, and can be seen experimentally in Figure 3-7. The duration of the triggering pulse can also limit the peak voltage in the sawtooth wave, as shown in Figure 2-7(c). Pulses shaped by the duration of the gate pulse were not usually used during actuator testing, because the corner created at the falling edge of the triggering pulse causes larger contrary stresses than pulses which are allowed to reach V_{in}. The pulse repetition rate, f_r, is governed by the rate of the triggering pulses. However, if the drain-source current of the IRF-9310 is not sufficient to allow the piezoelectric stack return to its initial voltage between pulses, the amplitude of the sawtooth wave will decrease.

Two different characteristics of the MOSFET's limit the performance of the circuit E0. The burst current of the IRF820, 8 A, limits the minimum rise time of the stress generating pulse, and the continuous current limit of the IRFU9310, -1.1 A, limits the pulse repetition rate of the circuit. By using five transistors in parallel, E1 is able operate with faster rise times at higher repetition rates.

2.2 Single Layer Acoustic Pulse Generator

A single layer piezoelectric device has several advantages over a stack. It is smaller, simpler, stiffer, less expensive, and a smaller capacitive load. However, all of these advantages are negated by its low output displacement, which makes it incapable of generating a 1 MPa stress pulse. Testing with a single layer actuator did not result in acoustically induced twin boundary movement, but it provide some interesting results.

The simulations from Figure 2-2 were used to chose the thickness of the single layer piezoelectric pulse generator. A 1.02 mm thick piezoelectric sheet, T140-A4E, was chosen as a compromise between current draw and actuation stress output. The piezoelectric material is industry type 5A PZT, which has properties summarized in Table 2.1. The bulk sheet of material was cut into 5 mm by 7 mm pieces, which were used for pulse generators and stress sensors. The electrodes on either face of the piezoelectric material are

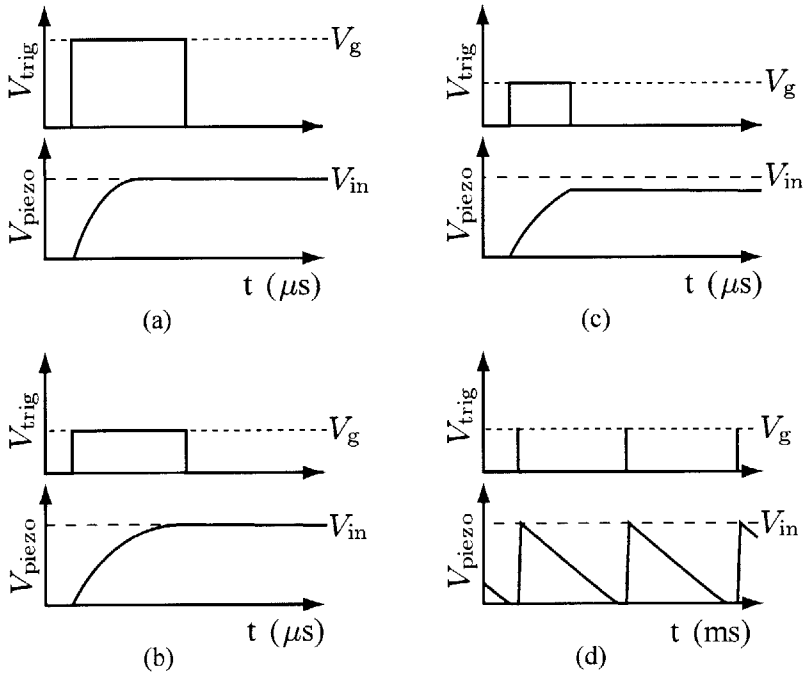

Figure 2-7: Shape of the input pulse generated by E0 or E1. V_{piezo} is the voltage measured at the piezoelectic stack, and V_{trig} voltage of the triggering pulse, applied to the gates of the IRF820s. Real input pulses show oscillations due to the reaction of the piezoelectric stack. (a) A typical input pulse. (b) A typical input pulse, lower gate voltage than (a) results in the lower slope of this curve. (c) An input pulse that is cutoff by the duration of the gate pulse. Note the sharp corner formed by the end of the gate pulse. (d) A series of pulses over a time scale on the order of milliseconds. The pulses in (d) are typical of those used in actuation, they reach both V_{in} and 0 V.

sputtered nickel, which provide a soldering surface and have a peel strength much higher than the adhesive bonds used to assemble the single layer acoustic pulse actuator. Single layer actuator testing was conducted with the three different device configurations shown in Figure 2-8.

All of the configurations shown in Figure 2-8 use three of the same components. The same FSMA crystal, designated X0, the steel support or backing, and the single layer piezoelectric pulse generator. The FSMA, X0, has the dimensions shown in Figure 2-9(a). The crystal had no major flaws. However, during the heat treatment and training process the twinning stiffness in one half of the crystal was observed to be noticeably higher than the other half. The support or backing material for the actuator consisted of a 3 in$\times$3 in$\times$3 in block of stainless steel. The large steel mass was provided as a volume in which the acoustic pulse could dissipate. The piezoelectric pulse generator measured 5 mm$\times$7 mm$\times$1.02 mm, which provided ample surface area for mounting the FSMA and making an electrical connections.

The bonds joining the various components of single layer acoustic pulse actuators were made using a two part Loctite epoxy, E-120HP. This adhesive is a slow curing epoxy with a tensile strength of 17-25 MPa on steel. The bond tensile strength proved to be greatly reduced on Ni–Mn–Ga and the nickel electrodes of the piezoelectric. However, the bond strength was sufficient for the experiments completed with the single layer actuator.

The first configuration shown in Figure 2-8(a) was the final attempt to achieve actuation using a single layer acoustic pulse generator. Asymmetric sine waves were generated using a Wavetek Model 29 waveform generator, and amplified using an MSK-610 high voltage amplifier. The Wavetek Model 29 is a digital waveform synthesizer and thus the output wave is discretized to a certain extent. The 10-bit A/D is more than sufficient for generating the waveforms used here. However, the cycle memory of 1024 samples per cycle results in a noticeable discretization of the fast portion of the asymmetric sine wave, which is the reason a maximum asymmetry of 40:1 was used during testing. At this level of asymmetry the discreetness is minimal.

The capacitive position sensor used in both the single layer pulse generator and stack pulse generator experiments is an ADE 3800. The output voltage of the ADE 3800 is captured by a HP54601B oscilloscope. The ADE 3800's sensitivity can be adjusted over a variety of ranges. Within each range, it produces a linear output voltage between $\pm$10 volts,

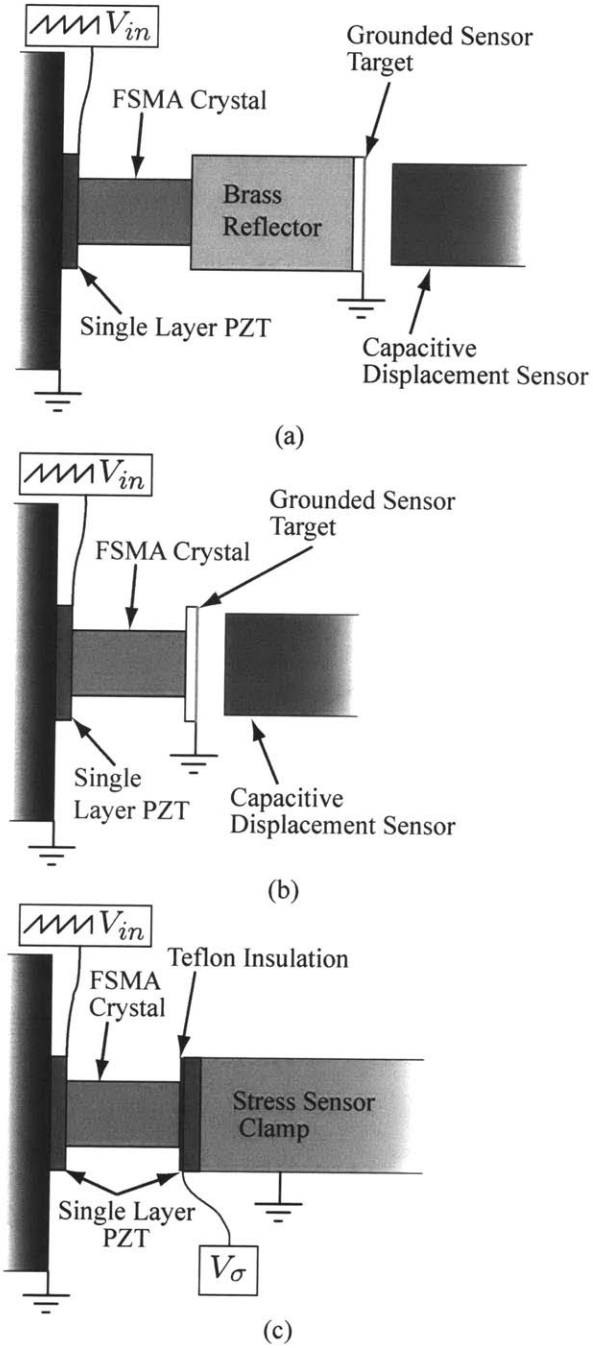

Figure 2-8: Apparatus configurations for experiments carried out using a single layer piezoelectric actuator. (a) Final assembly for attempting actuation. (b) Assembly used in impedance measurements and magnetic assistance experiments. (c) Stress wave measurement apparatus.

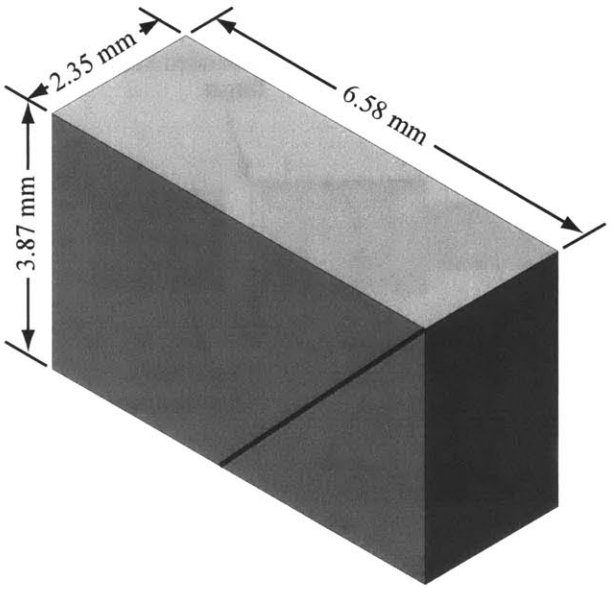

(a) Crystal X0

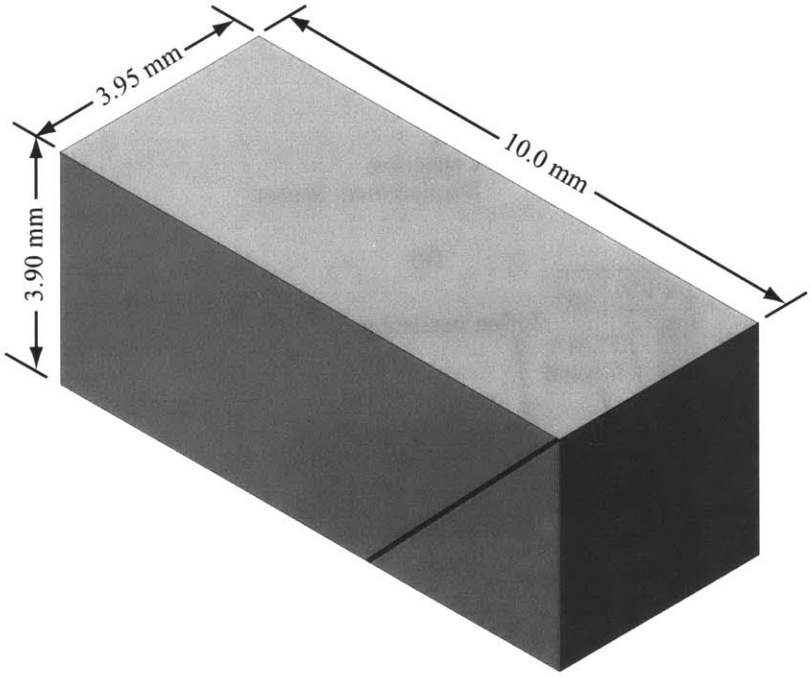

(b) Crystal X1

Figure 2-9: Ni–Mn–Ga crystals used throughout all experiments. Crystal X0 was used in the single layer actuator experiments and initial stack driven actuator experiments. Crystal X1 was used in the spring load apparatus. Dimensions are for the fully shortened state of the crystal. The fully extended lengths are 6.96 mm (a) and 10.6 mm (b). The diagonal line indicates the orientation of the twin planes.

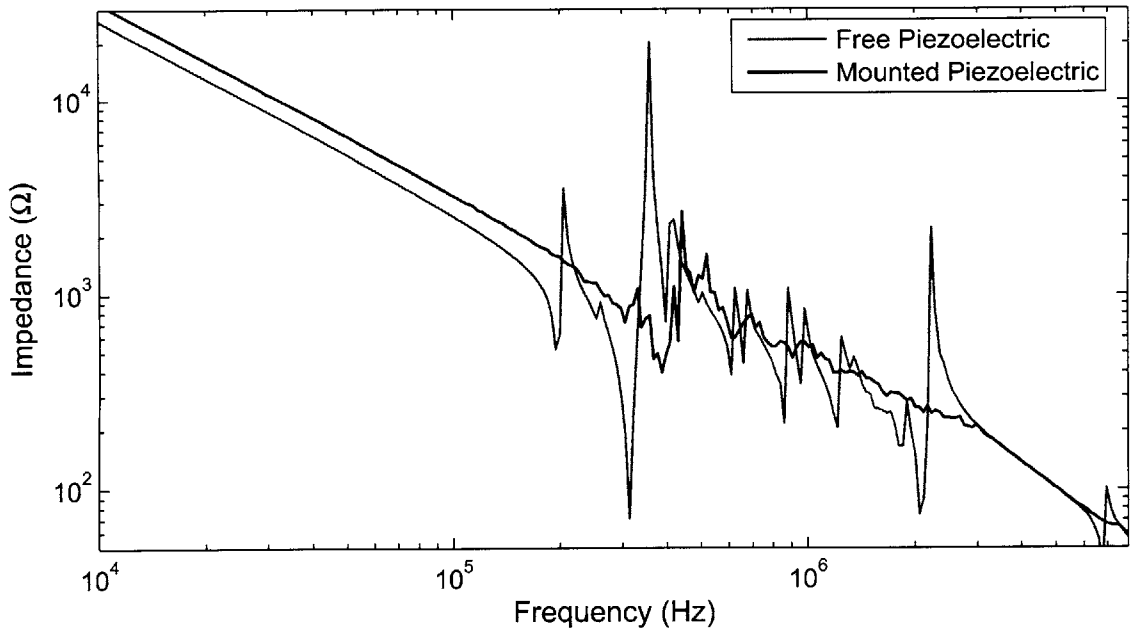

Figure 2-10: Impedance of the piezoelectric actuator, when it is free-standing or mounted on the steel block.

related to the position of any metallic object within a small range near the sensors face. The exact sensitivity and zero position depend on the size and type of the target metal being sensed. For this reason a calibration was made using a digital micrometer, with resolution 1 μm, for every sensor target that was used.

No data was collected using the single layer pulse actuator shown in Figure 2-8(a). Experiments with this configuration attempted to induce actuation acoustically, with no measurable results. The second single layer actuator, Figure 2-8(b), was used in two different sets of experiments: acoustic impedance measurements and assisted magnetic actuation. The following section describes these two experiments.

2.2.1 Impedance Measurements

An HP4194A Impedance Analyzer was used to measure the electrical impedance of the piezoelectric actuator over a wide range of frequencies and in a variety of states, from entirely free, to sandwiched between the FSMA crystal and the steel backing. These experiments effectively measured the frequency response of the actuator system, via the electromechanical coupling of the piezoelectric actuator. Figures 2-10 and 2-11 show the changes in response of the single layer piezoelectric as the system is assembled.

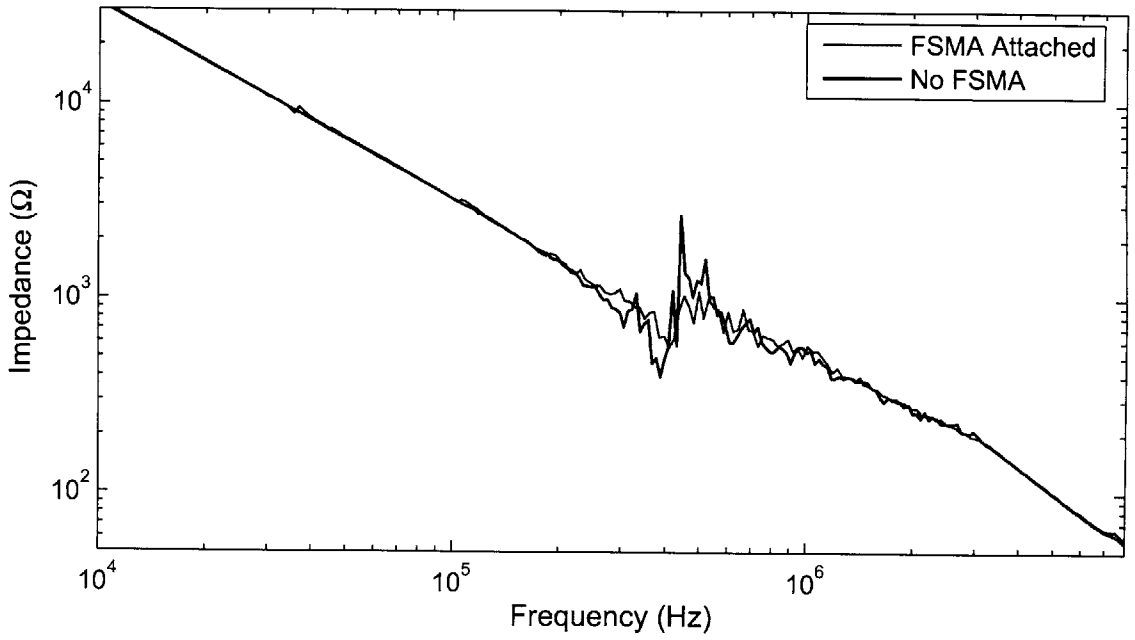

Figure 2-11: Impedance of the piezoelectric actuator when mounted without the FSMA attached and with the FSMA attached.

In order to show acoustic coupling between the piezoelectric pulse generator and FSMA crystal through the epoxy bond, impedance measurements where taken with and without the FSMA. Also, the FSMA was mounted on the pulse generator, impedance measurements were made with the FSMA in various partially compressed and extended states. The change in the dimensions and the elastic anisotropy of the FSMA crystal caused the measured resonant frequency associated with the FSMA to shift, as shown in Figure 2-12. The resonance shown indicates that acoustic coupling did in fact occur.

If the resonance associated with the FSMA is its fundamental longitudinal mode, then the estimated speed of sound in the compressed crystal is about 900 m/s, which is approximately half the speed of sound calculated using material properties found in literature [20]. There are two possible reasons for the error in this speed of sound estimate. The first, and most likely possibility is that resonance is not the fundamental longitudinal mode alone, and includes not only the FSMA, but also other parts of the system. The second is that this specific Ni–Mn–Ga crystal has a lower effective stiffness at the temperature this experiment was conducted at. The variation of stiffness with temperature is reported by Dai et al. [21]. They report a significant change in stiffness as the crystal's temperature approaches the austenite start temperature.

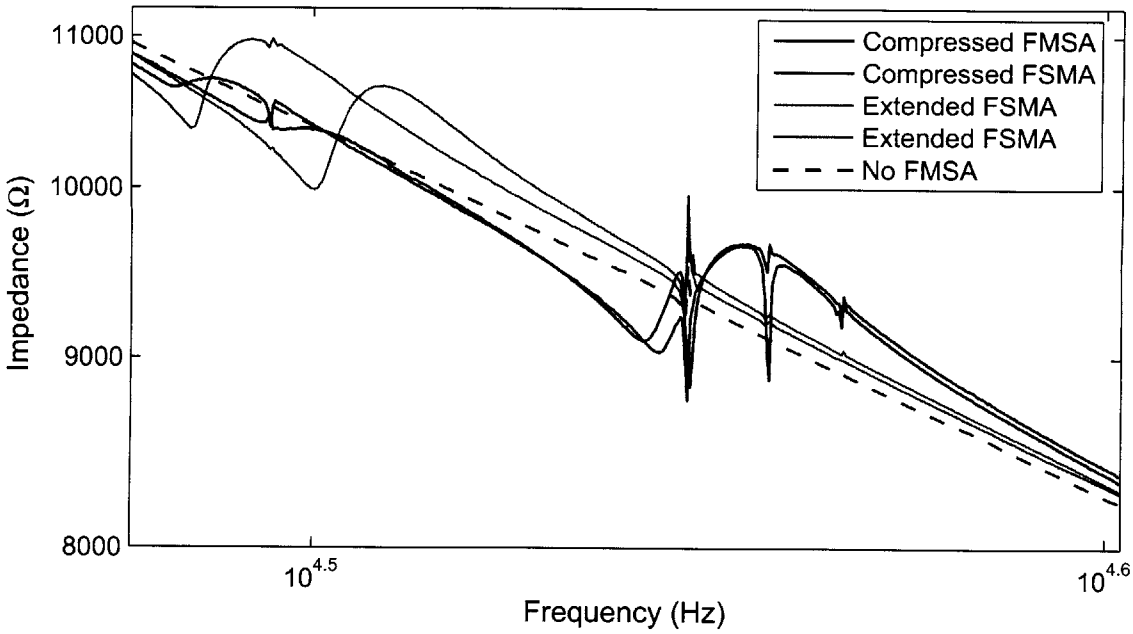

Figure 2-12: Impedance over a small frequency range of interest due to the small resonance/anti-resonance associated with attachment of the FSMA. The data compare compressed FSMA, extended FSMA, and no FSMA impedance measurements. The estimated speed of sound in the FSMA using this data is ~900 m/s.

The change in resonant frequency with deformation of the FSMA is also not easily explained. If it were dependent only on the length of the FSMA, the actual measured frequency shift would require a length change of 15%. The likely reasons for the excessive frequency shift are the changes in the width and anisotropic stiffness that accompany the change in length.

2.2.2 Assisted Magnetic Actuation

A second set of experiments using Figure 2-8(b) also showed good acoustic coupling between the FSMA and piezoelectric. In these experiments, the piezoelectric actuator was driven sinusoidally using the MSK-610, and while the piezoelectric was vibrating, a magnetic field perpendicular to the length of the crystal was slowly increased. At some threshold field, the crystal elongated enough to be measured by the capacitive position sensor. The threshold field was measured with and without the piezoelectric vibrations, and at various frequencies around the major resonance of the single layer piezoelectric. In between each measurement, the crystal was mechanically compressed so that the magnetic field could elongate it again.

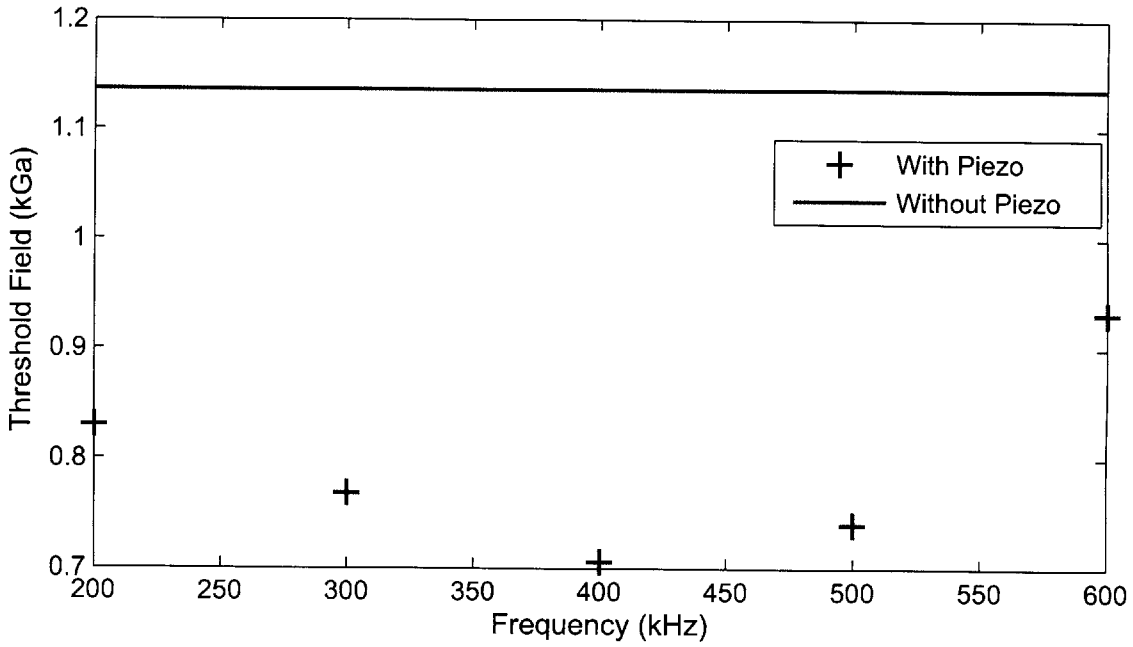

Figure 2-13: The effect of high frequency sinusoidal vibrations on the threshold field required for magnetic actuation. The piezoelectric drive voltage a constant 120 V peak-to-peak.

Figure 2-13 summarizes the data collected from this experiment. The reduction in threshold field is similar to that shown by Peterson [15].

2.2.3 Stress Pulse Measurements

The impedance measurements and assisted magnetic actuation experiments verified that sinusoidal vibrations were being transmitted into the FSMA. The stress pulse experiments described in this subsection show that individual acoustic pulses are able to travel through the FSMA.

Using the apparatus diagramed in Figure 2-8(c), the stress waves that traveled through the FSMA crystal were measured as they induced a voltage on the second single layer piezoelectric device. This piezoelectric sensor was isolated electrically from the actuator by a layer of teflon tape. The teflon tape precluded bonding the sensor in place, so a small jig was set up to hold the sensor in place with a minimal clamping force. The signal from the piezoelectric sensor was fed into a 10x probe, and then directly into the HP54601B scope. The sensor saw an input impedance of 100 MΩ in this configuration. The piezoelectric sensor has a capacitance of 550 pF which results in a time constant of 55 ms for the decay

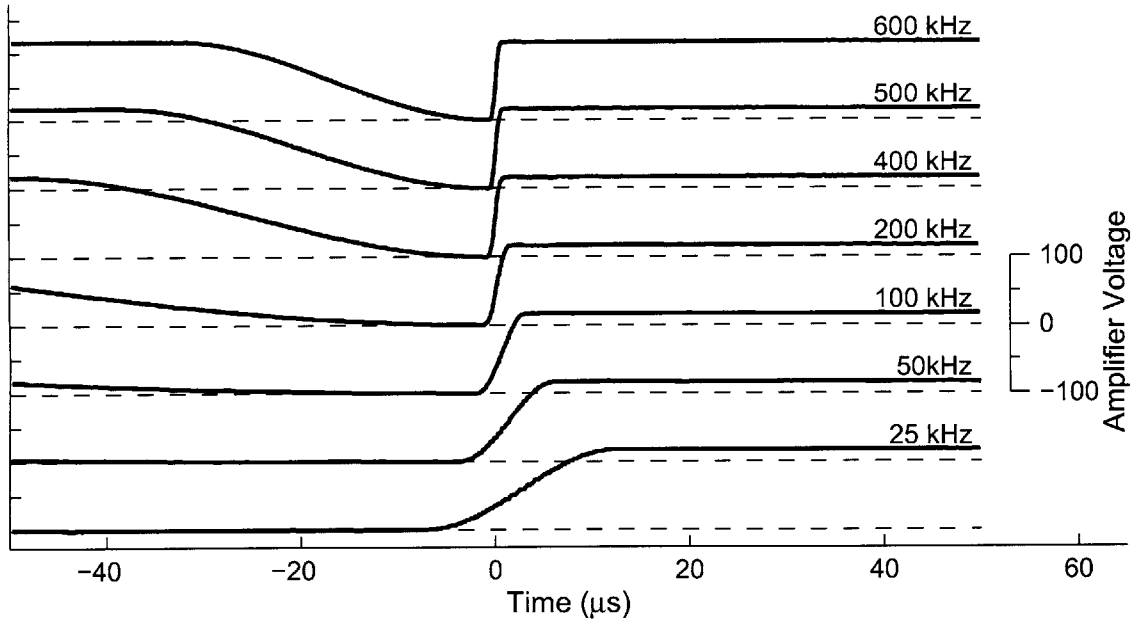

Figure 2-14: Input voltage to the single layer piezoelectric versus time, for several pulse frequencies. Traces are labeled with f_H.

of the sensor reading. Fortunately, this decay time is orders of magnitude longer than needed for measuring even the slowest input pulse, f_H =25 kHz.

Figures 2-14 through 2-16 show the data gathered using this apparatus. During this experiment, the voltage and current of the input wave, and the voltage of the output stress sensor were measured over a range of input wave frequencies. The FSMA was fully compressed the entire time, i.e., no actuation was achieved. The piezoelectric stress sensor was not calibrated, but using its material properties, a rough estimate of the stress can be made (Equation (2.15)).

The measured stresses indicate an order of magnitude discrepancy between the simulation results and the actual stresses generated. Figure 2-17(a) shows the difference between the maximum stresses measured and modeled. The discrepancy is at least partially due to the current limit of the MSK610 amplifier, which can be seen in Figure 2-17(b). However, it is apparent that this affect is not solely responsible for the difference. Given the limitations of the 1-D simulation, and the complexity of the experimental system (3-D geometry, bondlines, anisotropic FSMA properties), this discrepancy is not too surprising.

A comparison of tensile and compressive stress pulses showed no significant differences in pulse behavior in the single layer actuator. The low stress amplitude of the pulses induced

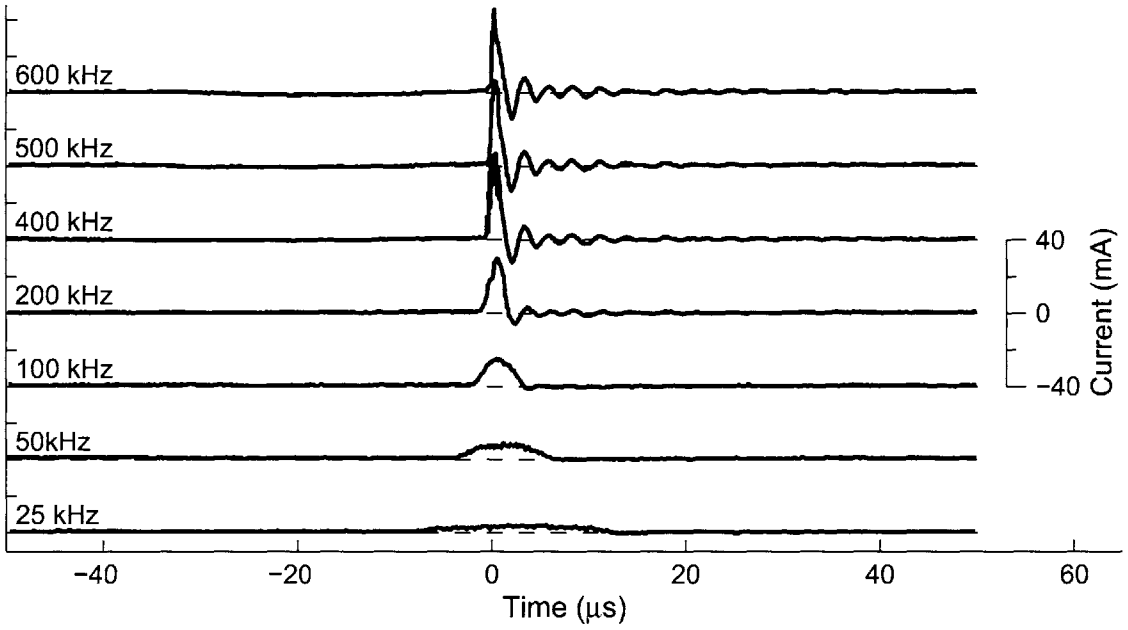

Figure 2-15: Measured input current to the single layer piezoelectric versus time, for several pulse frequencies. Traces are labeled with f_H.

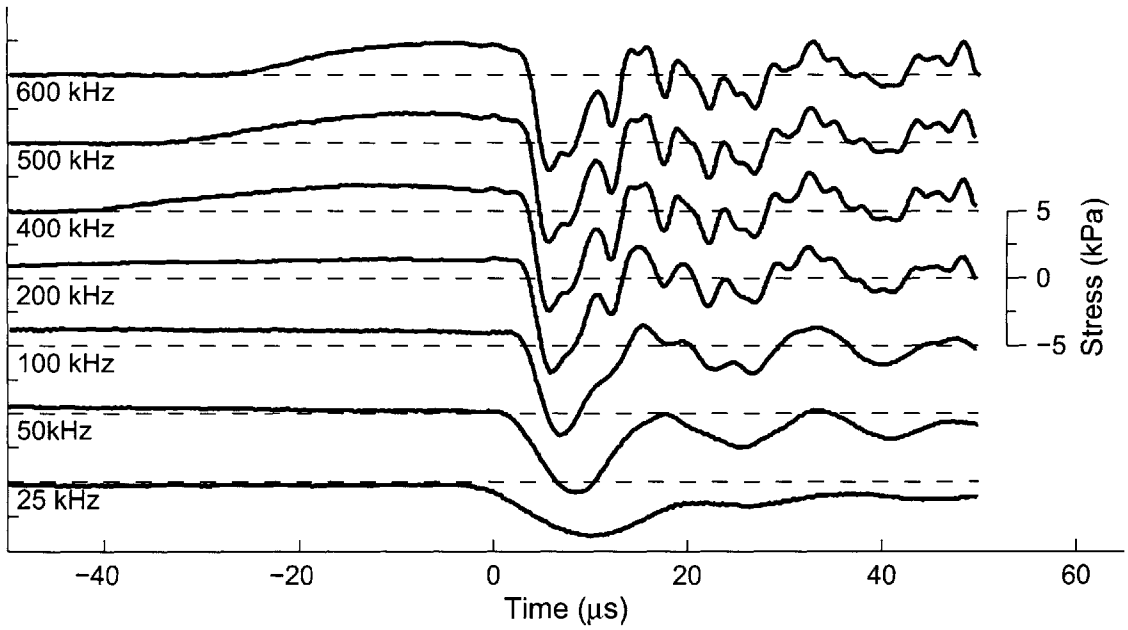

Figure 2-16: Measured stress for the single layer piezoelectric versus time, for several pulse frequencies. Traces are labeled with f_H. Time of flight estimates, from onset of the input pulse to the onset of the measured stress, indicate the speed of sound in the FSMA is 2000 m/s.

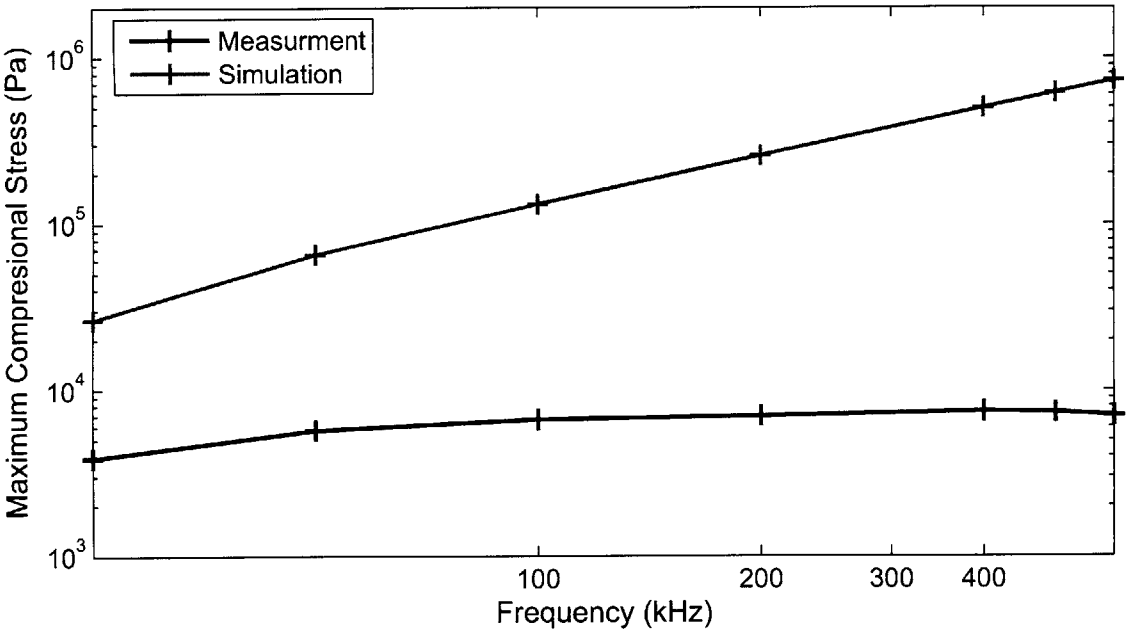

(a)

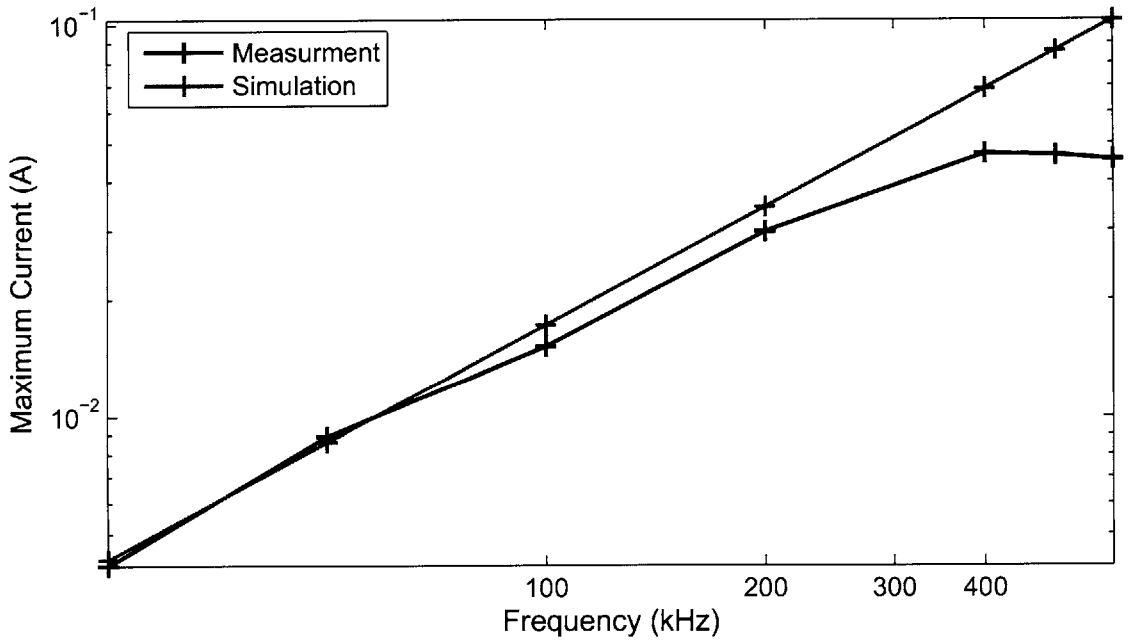

(b)

Figure 2-17: Comparison of maximum stress and maximum currents measured, and the simulated stresses and current.

with the single layer piezoelectric show no asymmetric effects from piezoelectric actuation, epoxy bonds, or twin boundaries.

2.3 Stack Driven Actuator

The acoustic pulse experiments with a single layer piezoelectric pulse generator failed to induce twin boundary motion. However, they did show that an asymmetric stress pulse could be induced in the FSMA. The measured stress generated by the single layer piezoelectric was on the order of one-hundredth the 1 MPa stress required to induce twin boundary motion. In order to increase the stress amplitude one hundred times, it was necessary to switch to a piezoelectric stack actuator. A stack allows operation at relatively low voltages with large displacements, but high currents are required, due to the stack's large capacitance compared with a single layer actuator (see Table 2.1). The stack used here, Piezosystems T18-H5-104, contains 140 layers of piezoelectric material, each approximatively 130 μm thick. The layer thickness limits the stack actuation voltage to approximately +100 V, above which arcing can occur between the stack layers. The nickel electrodes for each layer are co-fired with the PZT ceramic, which makes up the bulk of the layers, resulting in a solid sintered stack with physical characteristics very similar to the bulk ceramic.

The four actuators designed around this stack are briefly summarized in Table 2.3, which introduces some of the designations used when referring to the actuators. The remainder of this section describes the actuators and their components in detail.

2.3.1 Moonie Clamp Design

The large internal stresses that a stack can generate makes it necessary to prestress a stack actuator. Without a prestress, a transient stress pulse that puts the stack in tension could cause brittle failure. A prestress also improves piezoelectric performance by shifting the equilibrium polarization of the the piezoelectric material. Since a negative voltage applied to the stack could result in depolarization, only positive voltages are applied during actuation. A compressive mechanical prestress acts like a negative voltage bias, shifting the operating range of the piezoelectric, a making the applied positive voltage more effective. Previous work with PZT has found that a prestress of ~6.5 KSI (45 MPa) is optimal [22]. Ideally, the clamp providing the prestress would have zero stiffness. However, since zero stiffness

Table 2.3: The actuators used to study acoustic pulse actuation of Ni–Mn–Ga single crystals. The actuators and the components represented by these designations are described in detail in Section 2.3

Actuator Designation	Actuator Diagram	Crystal	Moonie Clamp	Electronics	Loading	Stress Sensor(s)
C0		X0	M0	E0	Free	S0
C1		X0	M1	E1	Free	S0
C2		X1	M2	E1	Spring	N/A
C3		X1	M2	E1	Spring	S1 and S2

Table 2.4: Properties of the three moonie clamps used during the acoustic pulse actuation experiments. All stress and stiffness values are calculated from material properties and beam theory. Stiffness is the stress per unit strain seen by the piezoelectric stack in the clamp. Max Stress is the maximum stress estimated in the clamps' beams.

Clamp Designation	Clamp Shape	Material	Prestress	Stiffness	Max Stress
M0		Brass	25 MPa	4.3 MPa	1200 MPa
M1		7075 Aluminum	25 MPa	5.2 MPa	400 MPa
M2		6-4 Titanium	45 MPa	3.5 MPa	450 MPa

is not possible, the clamp is designed to have a fraction of the stiffness of the piezoelectric stack.

The clamp design that was chosen for the acoustic pulse actuator, shown in Table 2.4, bears some resemblance to flexstensional sonar transducers referred to as moonie transducers [23]. However, unlike a moonie transducer, the transverse motion of the clamp's sides is not of interest for actuation purposes. The shape of the clamp allows a transverse stress to open it longitudinally, and after the stack is inserted, to close again with a prestress determined by the original shape of the clamp. Use of a clamp such as this also eliminates the need to bond directly to the piezoelectric stack.

All of the prestress clamps were cut from one solid piece using a Charmilles 480cc wire EDM, which has a positioning resolution of 0.01 mm. The cutting accuracy of the EDM is affected by the material being cut, the speed of the cut, and the wire being used to make the cut. Measurements of the finished clamps indicated that an accuracy of at least 0.001 in (0.025 mm) was achieved.

The first clamp, M0, was designed using simple, circular, constant thickness beams. In order to achieve a low stiffness and a good acoustic match to the piezoelectric material, the clamp was designed for and cut from brass. Although the clamp functioned well enough to hold the stack in place, yielding at the stress concentration points was apparent. Yielding of the clamp resulted in a reduced prestress on the stack. Although the first successful acoustic pulse actuation tests were made using this clamp, it was quickly replaced.

Clamp M1 was a design that eliminated the stress concentration problem by moving the stresses onto longitudinal beams. The curved beams in this design act only as a tool to open the clamp. The stiffness and prestress of the clamp are determined almost entirely by the slender longitudinal beams. M1 was machined from 7075 T6 aluminum because of its low stiffness and high yield strength. Using low stiffness aluminum allowed the longitudinal beams to be wide enough to be machinable. However, small errors in the machined thickness greatly affect the characteristics of the clamp.

The final clamp design M2 was machined from 6-4 titanium, because of it high yield strength, lack of ferromagnetism, and good acoustic match to the piezoelectric. The design of the curved beams in M2 is more complex than the previous two clamps. It incorporates elliptical beams and variable beam thickness to control the internal beam stresses and the stiffness. The ellipticity of the beams can be increased to help reduce stress concentration. The thickness of the beam is varied along its length in order to further reduce stress concentration and reduce the overall beam stiffness. MATLAB optimization routines were used to optimize the design and develop a clamp with the stress distribution shown in Figure 2-18. Because this clamp has a relatively low stiffness and no crucial sub-millimeter dimensions, small machining errors have only a small effect on its final performance. The bulk of the acoustic pulse actuation testing was conducted using this clamp.

2.3.2 Functional Acoustic Pulse Actuators

Figure 2-19(a) shows the configuration, designated C0, of the first apparatus to exhibit acoustic pulse induced twin boundary motion. Many of the components are identical to those used in the single layer actuator experiments, the same FSMA crystal, X0, was used, as was the ADE 3800 position sensor, E-120HP epoxy and the brass reflector. The acoustic pulse generator was a piezoelectric stack, held by moonie clamp M0, and driven by circuit E0. A single layer piezoelectric sensor was used to measure stress in nearly same manner

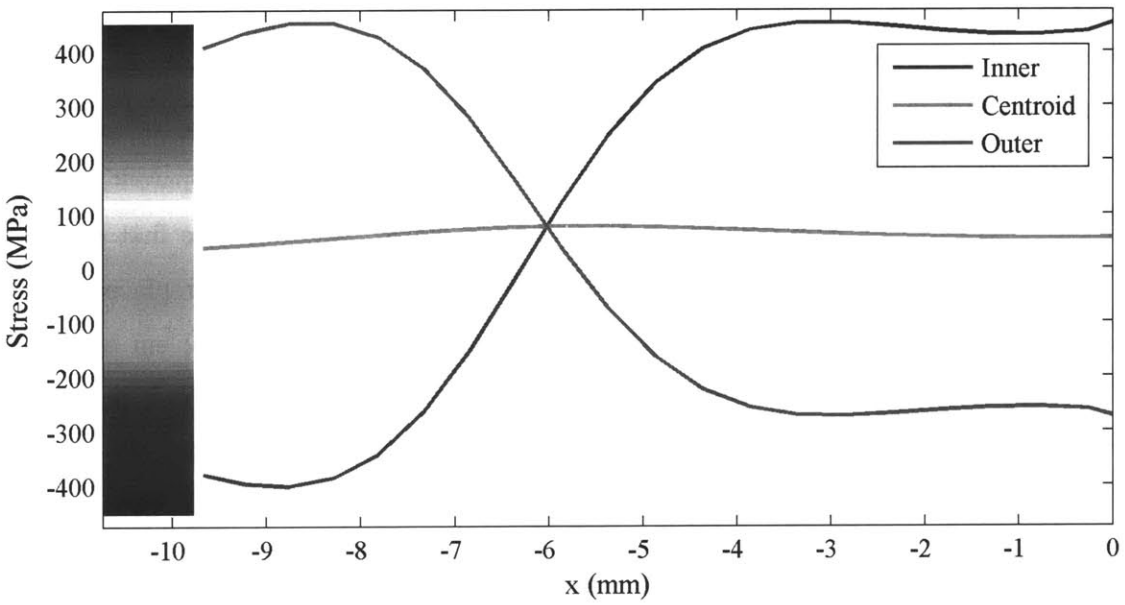

(a)

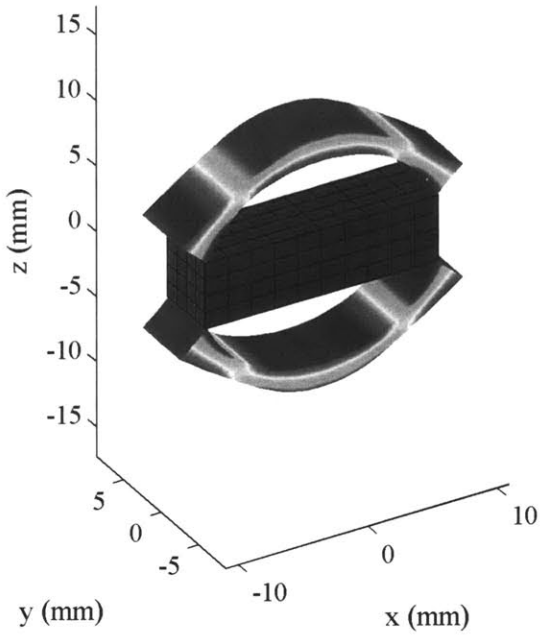

(b)

Figure 2-18: Stress distribution calculated for the design of clamp M2. The elements of the beam were treated individually as elliptical beams with linear thickness variation from one end to the other. The lines in (a) represent the stress in the beam along the edge indicated in the legend. (b) Shows a 3-D model of the moonie clamp's beams and the piezoelectric stack. The beams are shaded according the the longitudinal stress in each element, the shading legend is shown in (a).

as Section 2.2.3. However, the FSMA is now grounded through the moonie clamp, so the piezoelectric sensor can be bonded to the FSMA and also grounded through the clamp. The voltage reading from the stress sensor is taken from the electrically and physically isolated brass reflector. There is a small amount of interference between the capacitance gauge and stress sensor. However, the capacitance gauge uses a measurement signal with a much lower frequency (10 kHz) than the stress wave measurements, so the interference is filtered out by the ADE 3800 electronics.

The only changes from configuration C0 to C1 (Figure 2-19(b)) are the upgrade of the moonie clamp to M1 and electrical drive circuit to E1. These two changes significantly improved actuation and made extensional actuation possible for the first time.

2.3.3 The Spring Load Testing Apparatus

After data had been collected for acoustic pulse actuation with a free floating load, a spring load testing device was developed. The device is diagramed in Figure 2-20, and photographs of the device are shown in Figure 2-21. The device was designed to apply a longitudinal stress to the FSMA crystal while minimizing transverse stresses and moments on the crystal. The spring flexures being actuated against provide both a load, and a means of accurately measuring the force on the actuator. The length of the spring flexures ensures that they behave linearly over the entire displacement range of the acoustic pulse actuator. The pushrod, which transmits the spring load to the FSMA, contains two small flexures that allow the rod to bend while still transmitting a longitudinal load. The flexibility of the pushrod allows the brass reflector at the end of the FSMA to travel along a diagonal path without experiencing significant transverse forces. In this apparatus, the moonie clamp mounts to a pair of micrometer stages, which allows the clamp to be positioned so that pushrod is as straight as possible before actuation begins. A third micrometer stage is used to move the mount for the spring flexure along the direction of actuation. This micrometer stage allows a controlled actuator prestress (σ_{pre}) to be set prior to actuation. This prestress is applied to the entire actuator and is much smaller than the piezoelectric prestress imparted on the piezoelectric stack by the moonie clamp.

The force pushing against the acoustic pulse actuator is measured using a pair of strain gauges mounted on the sides of the spring load flexure. The stiffness and force of each flexure was calibrated using a set of precision gram weights and the ADE 3800 position

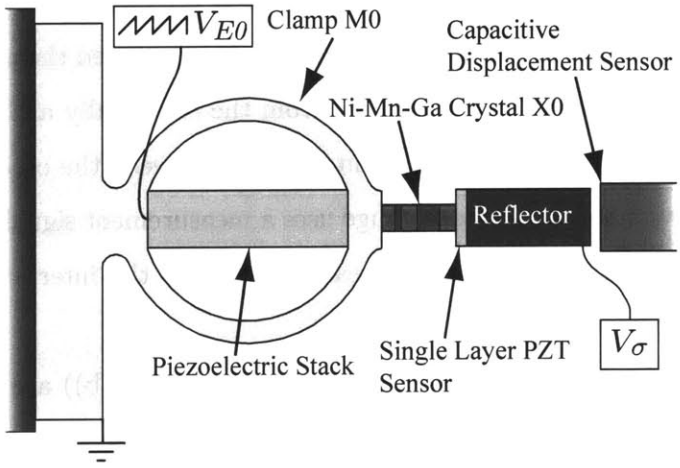

(a) Configuration C0

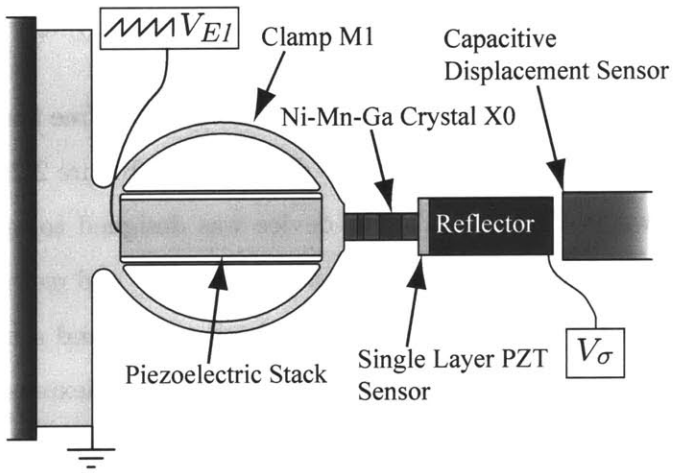

(b) Configuration C1

Figure 2-19: Apparatus configurations for the first acoustic pulse actuators. The configuration designations will be used to distinguish data in the next chapter.

Table 2.5: Calibration data for the flexures used in the spring load testing apparatus. The flexure modulus is calculated using Equation 2.14, which relates the stress on the actuating crystal to strain of the actuating crystal.

Designation	Force Calibration	Position Calibration	Spring Stiffness	Flexure Modulus
B0	2.20 N/V	0.123 mm/V	17.9 N/mm	11.5 MPa
B1	1.97 N/V	0.131 mm/V	15.0 N/mm	9.62 MPa
B2	1.23 N/V	0.165 mm/V	7.46 N/mm	4.78 MPa
B3	0.770 N/V	0.203 mm/V	3.80 N/mm	2.43 MPa
B4	0.477 N/V	0.254 mm/V	1.88 N/mm	1.21 MPa

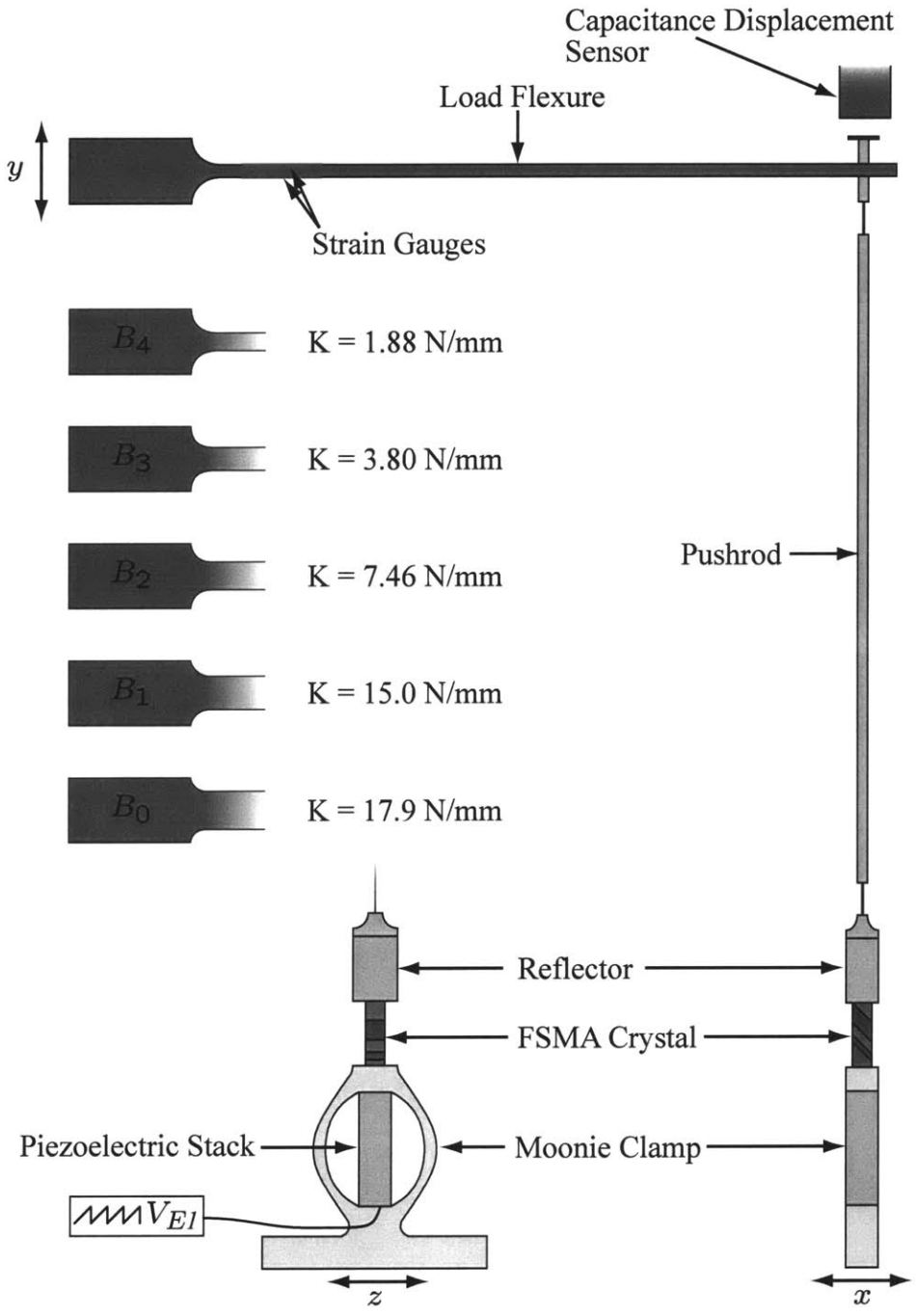

Figure 2-20: Diagram of the apparatus used to test the response of acoustic pulse actuation to a variety of loads.

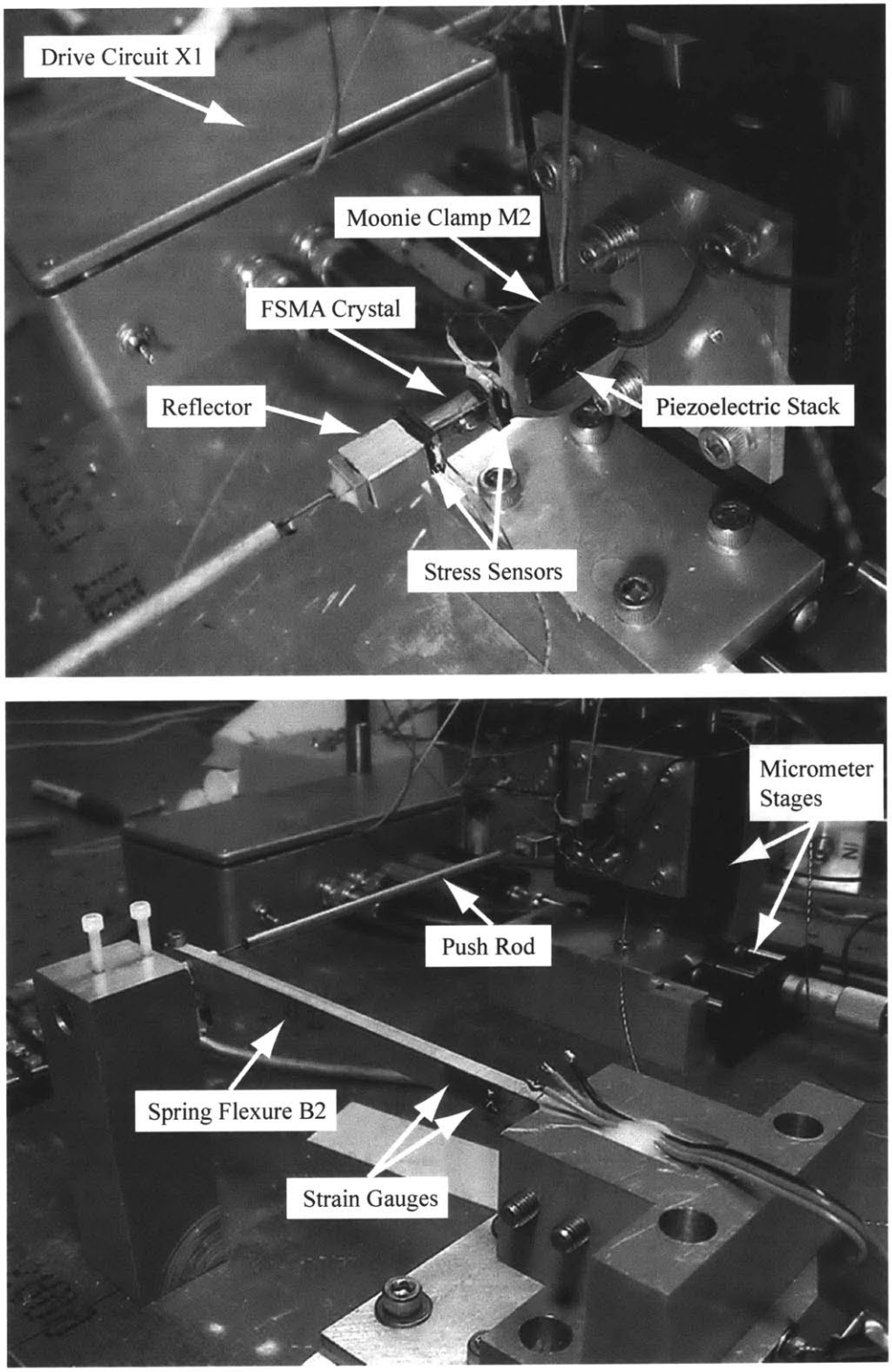

Figure 2-21: Images of the spring load testing apparatus. The particular configuration, C3, includes piezoelectric stress sensors. These were not included in the load characterization tests (configuration C2) because they reduce the effectiveness of the input acoustic pulses.

sensor. The calibration data is shown in Table 2.5. The strain gauges used were Vishay type EA-13-250BF-350, which were configured in a half-bridge and connected to a Vishay 2120A strain gauge conditioner. The stability of the strain gauge measurement is slightly higher than the stability of the capacitive position measurement made using the ADE 3800. The sensitivity of the strain gauge is higher than that of the ADE 3800, over the displacement range achieved by the acoustic pulse actuation. In the spring load apparatus the ADE measures the position of the end of the pushrod. The target on the end of the pushrod rotates significantly as the spring flexures bend during actuation. This rotation causes errors in the position measurement from the ADE. Therefore, data from the ADE will only be used as a secondary reference in this apparatus.

The force on the actuating crystal can be related directly to displacement of the crystal, through the stiffness of the flexure being actuated against. However, it is sometimes more useful to relate strain of the actuating crystal to the change in stress on the crystal, by using an effective flexure modulus, defined as

$$C_{\mathrm{B}i} = \frac{K_{\mathrm{B}i}\, l_{\mathrm{FSMA}}}{A_{\mathrm{FSMA}}} \ , \tag{2.14}$$

where l_{FSMA} is the length of the crystal, A_{FSMA} is the cross-sectional area of the crystal, and $K_{\mathrm{B}i}$ is the spring stiffness of flexure Bi.

A new FSMA crystal was selected for testing in the spring load testing apparatus. It was crystal X1, shown in Figure 2-9(b). Except for its dimensions, this crystal has nearly the same properties as X0. Again, one of the crystal's ends actuated more readily than the other immediately after heat treatment. Spring load testing was done with the easy end nearer the piezoelectric stack.

A bond between the FSMA and the titanium moonie clamp using E-120HP was not suitable for tests in this apparatus. The combination of a tensile actuator prestress and the vibration of acoustic pulses was enough to consistently cause bondline failure. After testing several manufacturer recommended metal-bonding adhesives, a 3M adhesive, DP-810, was found to provide an excellent bond. Although it never failed during extensive testing, it was only used on the most critical or permanent bonds, because it is quite difficult to clean up or remove the cured acrylic. DP-810 was used in the bond between the FSMA and titanium clamp, and the bonds that hold together the piezoelectric sensors discussed in

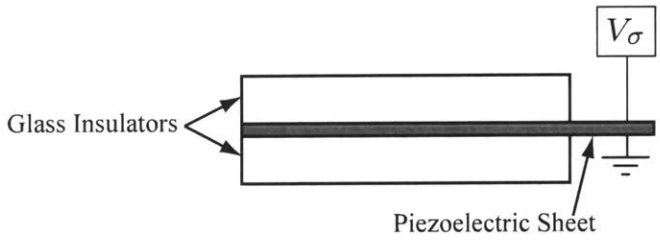

Figure 2-22: Diagram of the buildup of the piezoelectric sensors used for measuring stress waves at both ends of the FSMA crystal.

Section 2.3.4. All of the other bonds in this apparatus were made using Loctite 480, a cyanoacrylate with bond strength similar the E-120HP epoxy. Loctite 480 also dissolves readily in acetone, facilitating clean up and disassembly of the experimental apparatus when necessary. Loctite 480 would not be a good choice for actual actuator applications, because it ages quickly and becomes brittle.

2.3.4 Piezoelectric Stress Sensors

In order to better understand acoustic pulse actuation, the actuating stress wave was measured at both ends of the FSMA during actuation in the spring load apparatus, using apparatus C3. The sensors were built of a 0.27 mm thick piece of single layer piezoelectric material, T110-H4E, sandwiched between two pieces of flat roughened glass, as shown in Figure 2-22. The glass was necessarily thicker than the piezoelectric material, because its surface had to be roughened to achieve a strong bond. Thinner glass became impractically brittle when roughened. The installed sensors are visible at either end of the FSMA crystal in the photos of Figure 2-21. The sensor a the tip of the moonie clamp will be referred to as sensor S1 and the sensor at the reflector end of the FSMA will be referred to as S2.

The voltage from these stress sensors was again measured using a 10× probe and HP54601B oscilloscope. The time constant for voltage decay of the sensor reading was typically 0.5-0.9 s. The area of the piezoelectric sensor varied from sensor to sensor, which changed the capacitance and the voltage read. The stress at the ends of the FSMA can be estimated from the sensor voltage by using

$$\sigma = \frac{V_\sigma A_{\text{piezo}}}{g_{33} t_{\text{piezo}} A_{\text{FSMA}}} \ , \tag{2.15}$$

where

$$g_{33} = \frac{d_{33}}{\kappa_3^{\sigma}\,\kappa_0} \ , \tag{2.16}$$

which can be found in Table 2.1, A_{piezo} and t_{piezo} represent the area and thickness of the piezoelectric sensor respectively, and A_{FSMA} is the area of the face of the FSMA crystal attached to the sensor.

Chapter 3

Experimental Results

This chapter examines the data collected with the four successful acoustic pulse actuator configurations described in the previous chapter. The first actuator, C0, demonstrated that acoustic pulse actuation was possible. Although it was incapable of significant extensional actuation, the compressional actuation that was accomplished was proof of the acoustic actuation concept. The second actuator, C1, was capable of bidirectional actuation, although extensional actuation was still less effective than compressive. Both C0 and C1 actuated without a load, simply moving the free floating reflector. In apparatus C2, an acoustic pulse actuator worked against a spring load, and in C3 an actuator with a pair of stress wave sensors again actuated against a spring load. The data collected show the capabilities and limitations of several specific acoustic pulse actuators. Analysis of these results will be left to Chapter 4.

3.1 The First Functional Acoustic Pulse Actuator

Figure 3-1 shows compressional actuation results collected using apparatus C0. The actuator began with the crystal fully extended, and was compressed by a series of acoustic pulses. The initial extension was accomplished by placing a transverse magnetic field of 4 kG across the crystal, then removing it before actuation. Actuation began with several individual compressive acoustic pulses that were applied via manual operation of the pulse generator. The individual pulses reveal the inch-worm type actuation sequence. The piezoelectric stack expands quickly, in 60 μs, and contracts more slowly, over 100 ms. After the stack has completely contracted, the twin boundary motion induced by the pulse is

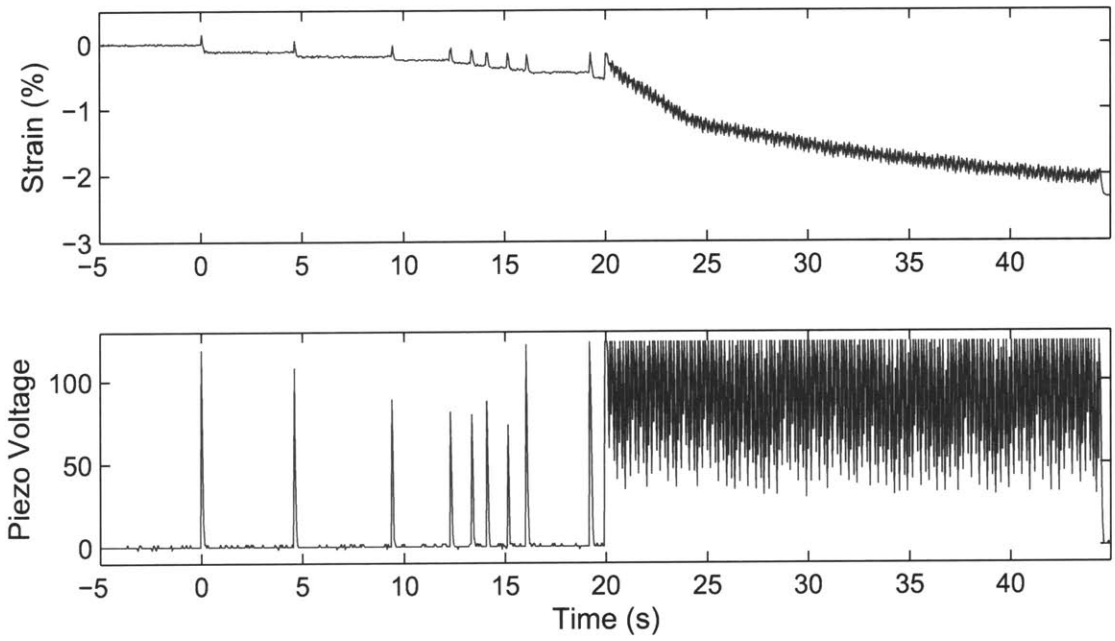

Figure 3-1: Strain calculated from measured displacement of the first successfully actuating apparatus, C0, versus time. The crystal began in an extended state and was compressed using acoustic pulses, first manually triggered, and then at a repetition rate of 7.5 Hz. The peak voltage on the piezoelectric is inaccurate due to measurement aliasing.

apparent as the new steady state position of the free end of the FSMA is different from that before the pulse. After several manually applied pulses, the pulse generator was run at 7.5 Hz for several seconds and significant actuation continued, but at a decreasing rate. The input pulse and propagated stress wave that accomplished this actuation are shown in Figure 3-2. The slow side of the input pulse lasts approximately 100 ms and extends well beyond the time range displayed in the figure. It is apparent that the stress wave is not ideal, reaching nearly the same tensile stress as compressive stress. The oscillations along the peak of the stress wave are due to the long input pulse relative to the period of the resonance of the piezoelectric stack. In 50 μs, a sound wave can travel from one end of the stack to the other approximately 7 times, based on speed of sound calculated from stack properties, resulting in the 7 small peaks along the major peak. The peak of the input pulse in these experiments was determined by the duration of the triggering pulse, as described in Section 2.1.6. This type of input results in a sharp peak where the input pulse stops rising and could be responsible for the large tensile stresses that follow the compressive pulse as in Figure 3-2.

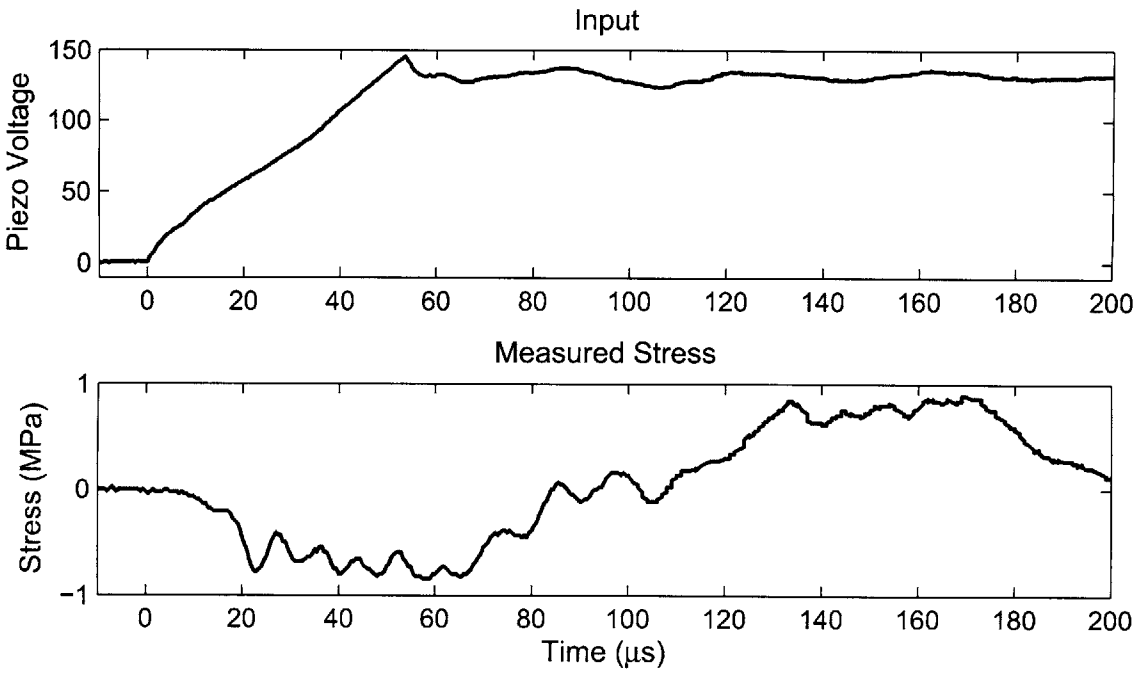

Figure 3-2: One of the pulses used in the actuation shown in Fig. 3-1. Stress is measured at the opposite end of the FSMA from actuating stack. Voltage on the piezoelectric stack falls back to 0 V over 100 ms.

Extensional actuation, starting from a fully compressed crystal, proved very ineffective with this apparatus, as shown in Figure 3-3. The induced strain was only slightly greater than that produced by the piezoelectric stack. The observed strain is small enough that it could almost be accounted for with thermal expansion. However, the repetition rate of the pulses was kept low, 5 Hz, so that the temperature increase of the stack during actuation was very low.

A comparison of the measured tensile and compressive stress pulse is shown in Figure 3-4. The figure shows that an input pulse with a δV of nearly 150 volts is required to obtain the same tensile stress that was generated with 100 V in compression. This poor performance indicates the piezoelectric stack/moonie clamp system is not contracting as quickly as it should, which could be caused by the prestress from the moonie clamp being too low. Deformation at high stress points in the clamp also indicated that it had yielded, which would cause it to no longer provide its designed prestress.

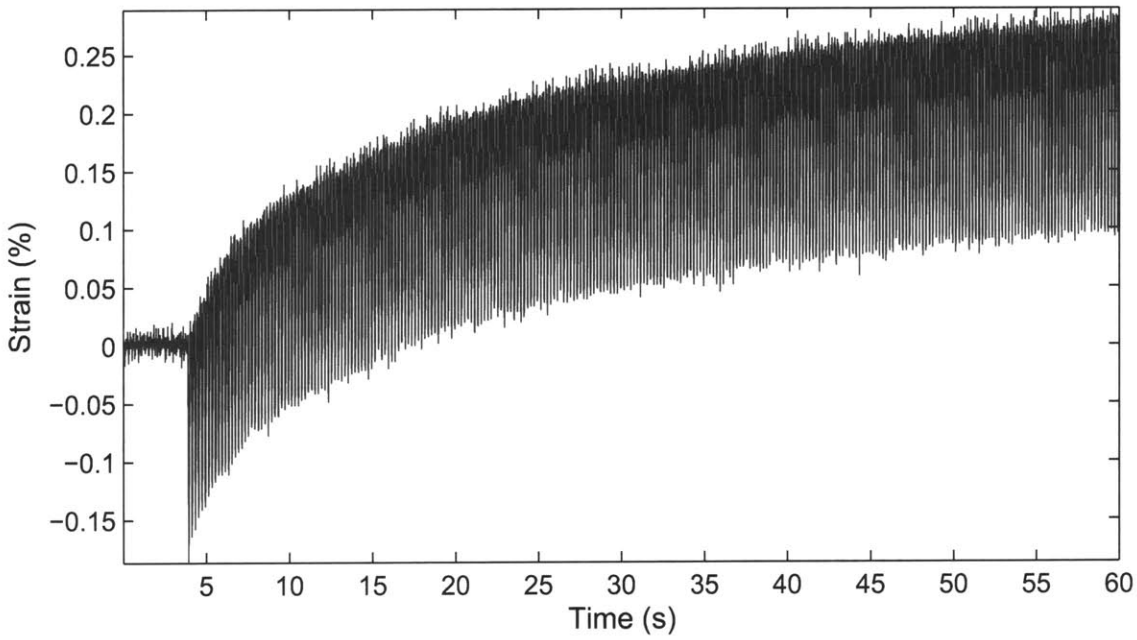

Figure 3-3: Calculated FSMA strain from an attempt to extended a the fully compressed crystal using apparatus C0. The strain obtained is barely larger than the strain of the piezoelectric stack. Input voltage was 180 V, nearly twice the rated voltage of the stack.

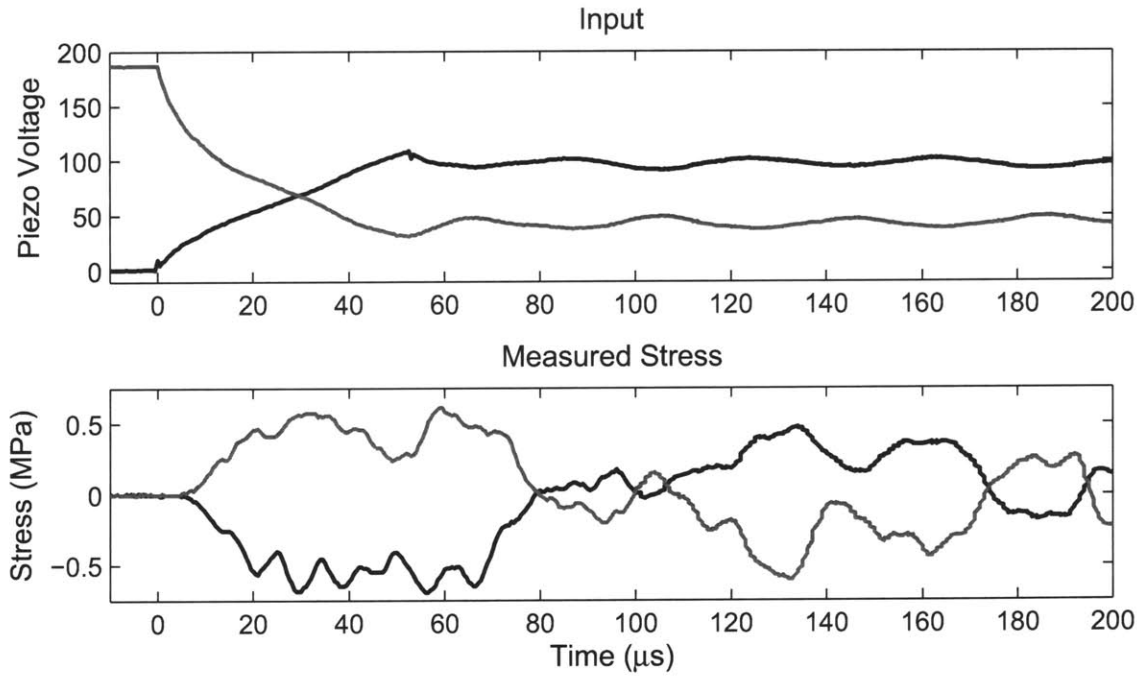

Figure 3-4: Comparison of the measured compressive (dark) and tensile (light) stress pulses used for actuation in apparatus C0. The pulses were propagated through a fully compressed crystal.

3.2 Bidirectional Actuation

Significant extensional actuation was first achieved using apparatus C1. Bidirectional actuation using this apparatus is shown in Figure 3-5. The extensional actuation shown is still less effective than compressional actuation, and the reasons for this are not apparent. One possibility is that even the redesigned moonie clamp behaved differently in compression and extension. With insufficient prestress in the moonie clamp, an asymmetric response can occur when the acceleration of the face of the piezoelectric stack is greater than the acceleration the prestress force can impart on the clamp. A rough estimate of these accelerations is

$$a_{\text{piezo}} = d_{\text{piezo}}/\tau_{\text{pulse}}^2 \ , \tag{3.1}$$

$$a_{\text{clamp}} = \frac{\sigma_{\text{pre}} A_{\text{piezo}}}{m_{\text{clamp}}} \ , \tag{3.2}$$

where d_{piezo} is the displacement of the piezoelectric stack's face, τ_{pulse} is the time constant of the input pulse, σ_{pre} is the moonie clamp prestress, and m_{clamp} is the mass of portion of the clamp that must be moved to maintain contact with the stack. Estimation of m_{clamp} without a complex model is difficult, but an order of magnitude estimate is that the mass of the tip of the clamp is about 1 g. The calculations using that estimate show that the maximum clamp acceleration may not be significantly larger than the stack acceleration for a prestress of 25 MPa, which is the designed prestress for clamp M1.

It should be noted that in the displacement data presented in this section, the transient displacement of the piezoelectric stack has been largely filtered out by the ADE 3800 position sensor. This results in a time average displacement that includes an offset due to the displacement of the piezoelectric stack. During extensional actuation, the contribution of the stack displacement to the time average displacement measurement is much larger than during compressional actuation. The values of these average displacement offsets were measured and compensated for in the presented data.

A set of experiments were run to observe the effect of pulse amplitude and pulse shape on actuation strain rate. Each experiment began with a fully compressed crystal, tensile pulses elongated the crystal for 1 s, then compressive pulses for 1 s, followed by 2 s of extension and 2 s of compression. Only strain was measured during the actuation cycles, the voltage pulse on the piezoelectric stack and stress pulses were measured under special conditions

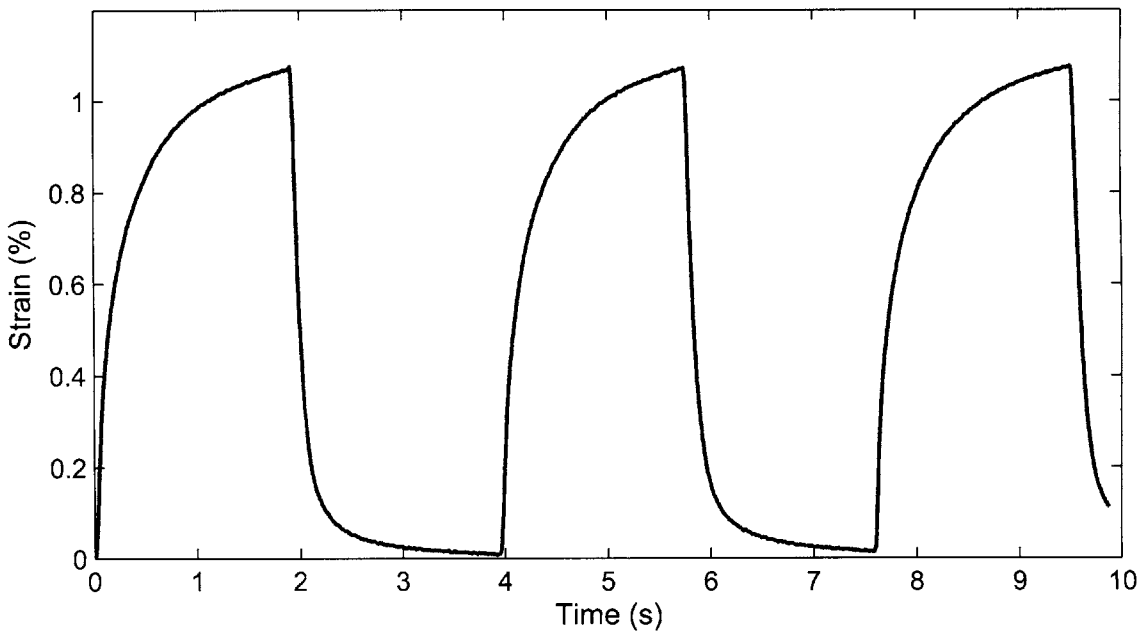

Figure 3-5: Bidirectional actuation using apparatus C1. V_{in}= 100 V, V_g= 12 V (saturated), f_r= 100 Hz.

prior to actuation. Each compressive stress pulse was measured through a single variant compressed crystal, while tensile stress pulse measurements were through a multi-variant extended crystal. A constant pulse repetition rate, f_r, of 100 Hz was used during actuation. The effect of input voltage, V_{in}, on the input pulse and the resulting stress pulses can be seen in Figure 3-6 and 3-7 respectively. The changes in rise time caused by varying V_g are visible in Figure 3-8, and the consequent effect on pulse shape is shown in Figure 3-8. A sample set of the strain curves resulting from actuation using these pulses is shown in Figure 3-10. Figure 3-11 shows tensile counterparts to the compressive stress pulses shown in Figure 3-7. Note the dispersion of the tensile pulses compared to the compressive, this is probably results from the conditions under which the stress pulses were measured. Dispersion of this nature is shown again in Section 3.5, and is discussed in depth in Section 4.2. The complete set of figures for this experiment, compressive and tensile pulses as well as strain curves, can be found in Appendix C. Analysis of the affects of pulse magnitude and shape on actuation, using these results, is carried out in Section 4.1.

The effect of pulse repetition-rate on actuation rate can be seen in Figure 3-12. The initial slope of the strain curves varies linearly with repetition-rate, which is expected. The

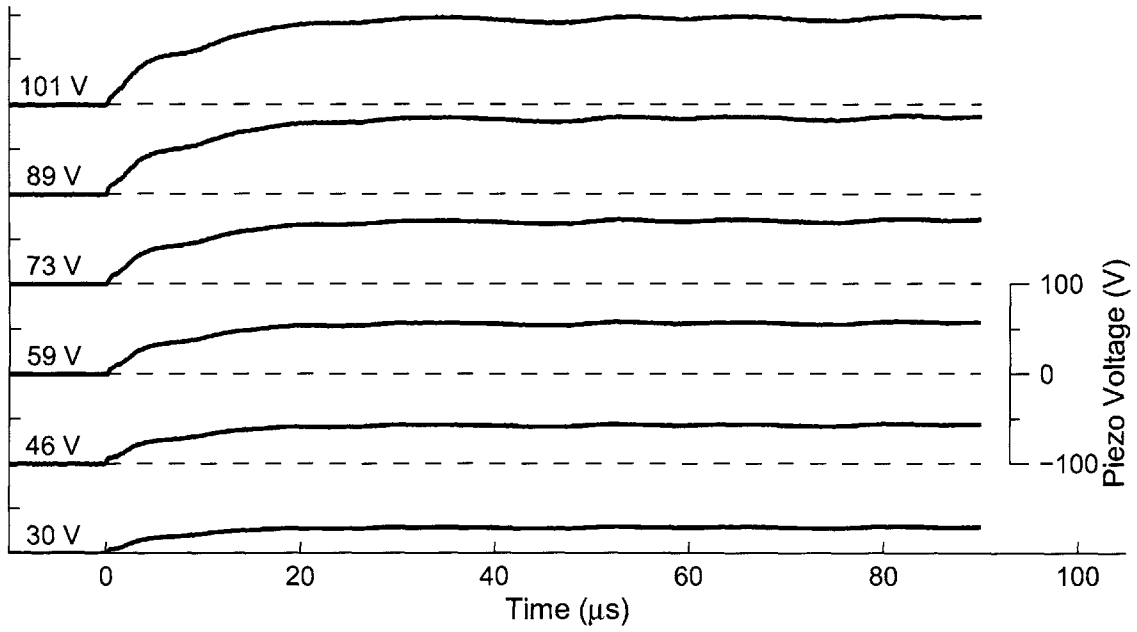

Figure 3-6: Piezoelectric stack voltage for compressive pulses in apparatus C1, with varying input voltages (left). V_g= 12 V (saturated), f_r= 100 Hz.

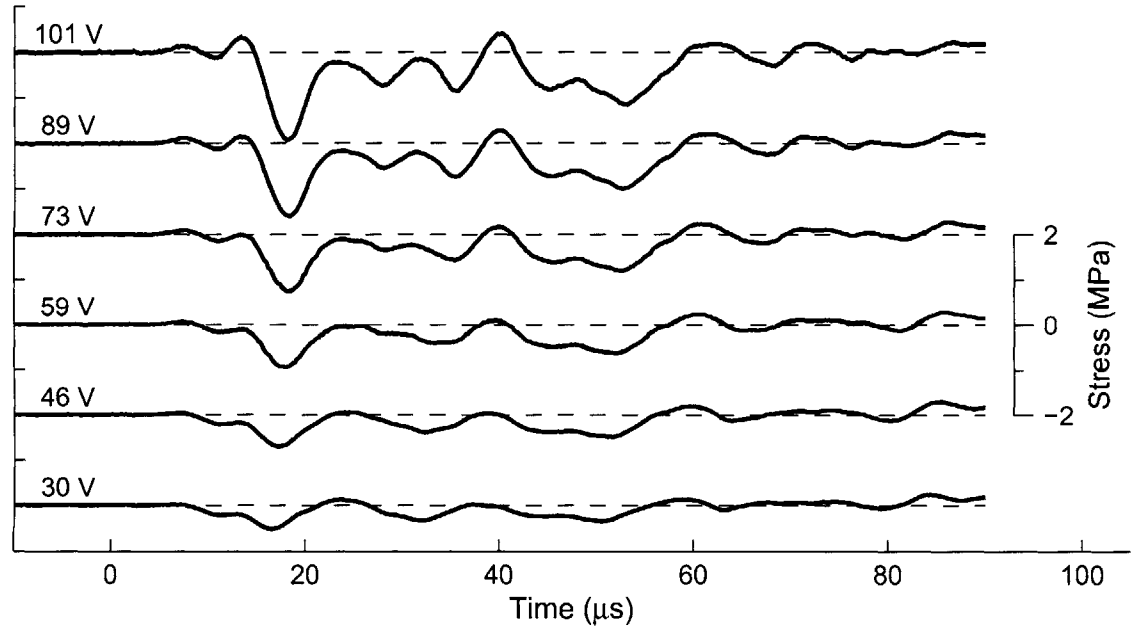

Figure 3-7: Stress sensor measurements for compressive pulses in apparatus C1, with varying input voltages (left). V_g= 12 V (saturated), f_r= 100 Hz. Stress measured when the FSMA crystal was fully compressed. Stress calculated from piezoelectric sensor voltage.

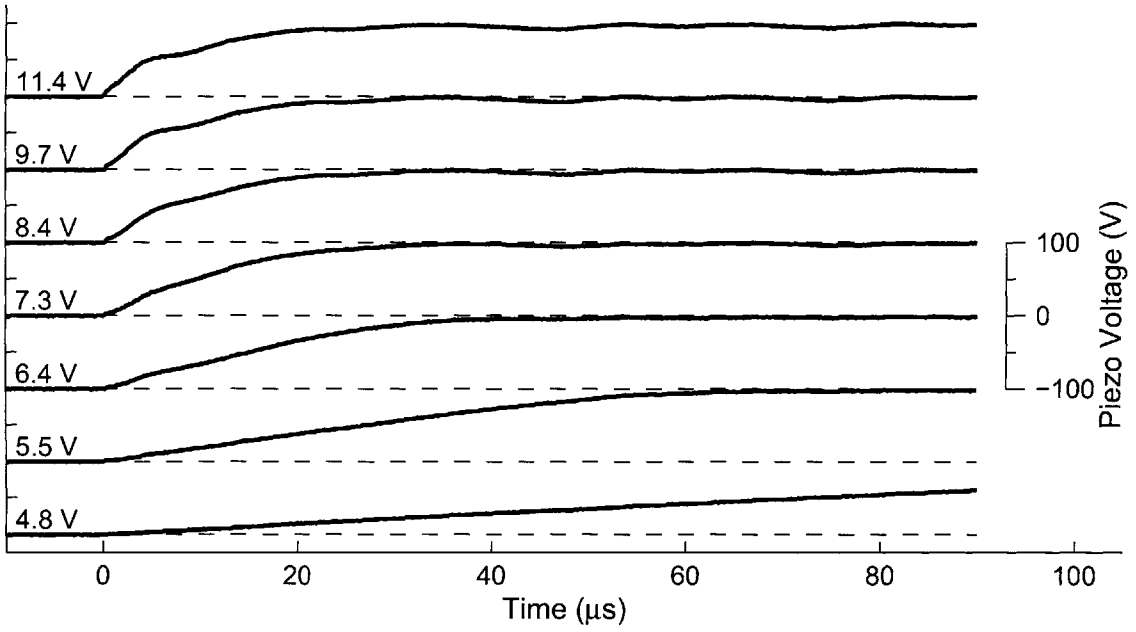

Figure 3-8: Piezoelectric stack voltage for compressive pulses in apparatus C1, varying gate voltages (left). V_{in}= 100 V, f_{r}= 100 Hz.

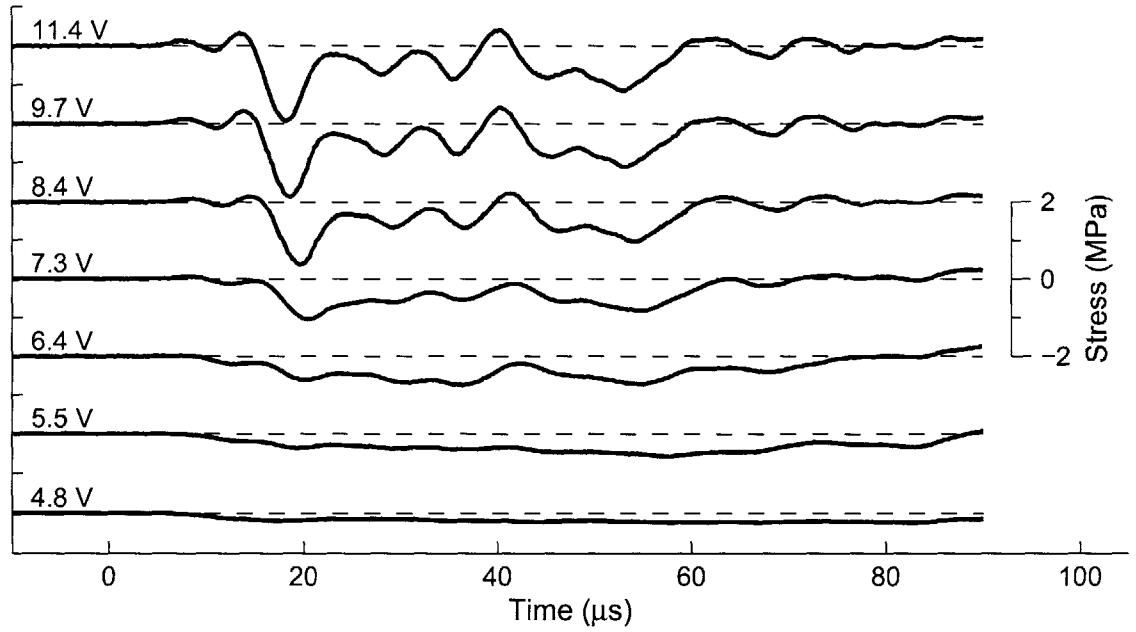

Figure 3-9: Stress sensor measurements for compressive pulses in apparatus C1, with varying gate voltages (left). V_{in}= 100 V, f_{r}= 100 Hz. Stress measured when the FSMA crystal was fully compressed. Stress calculated from piezoelectric sensor voltage.

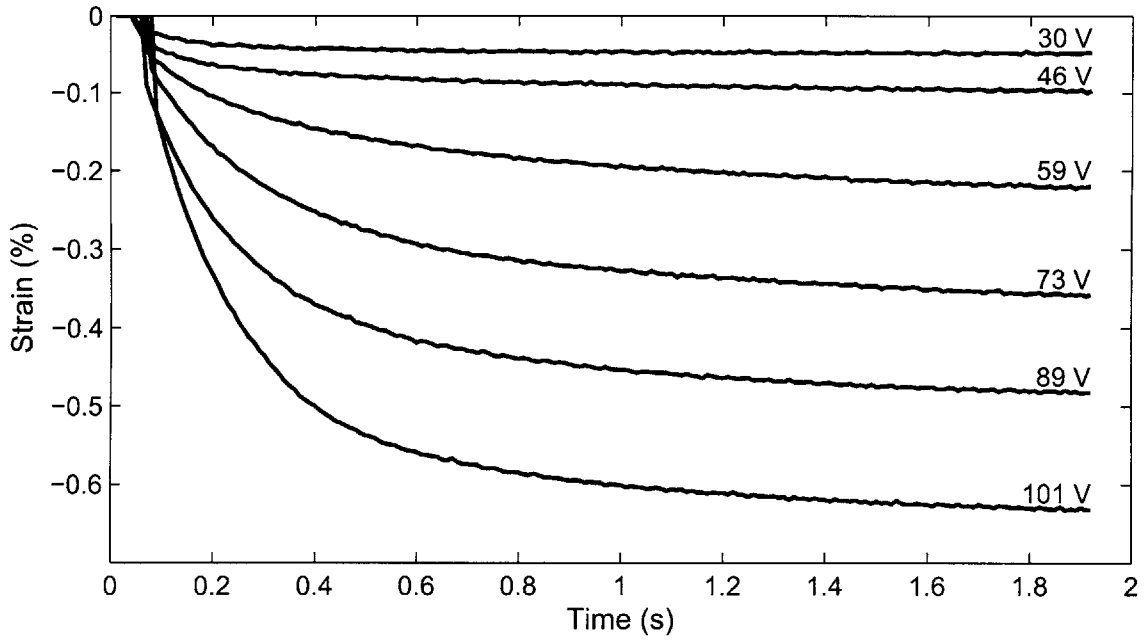

Figure 3-10: Compressional actuation strain for apparatus C1, with varying input voltage (right). V_g= 12 V (saturated), f_r= 100 Hz.

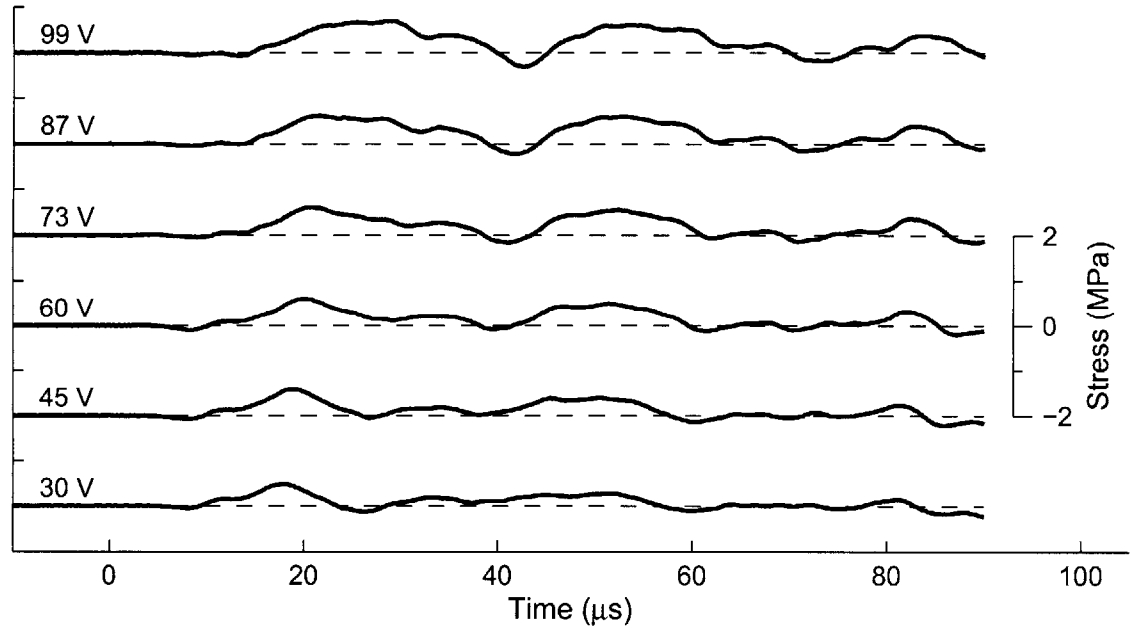

Figure 3-11: Stress sensor measurements for tensile stress pulses in apparatus C1, with varying input voltages (left). V_g= 12 V (saturated), and f_r= 100 Hz. Stress measured when the FSMA crystal was extended. Stress calculated from piezoelectric sensor voltage.

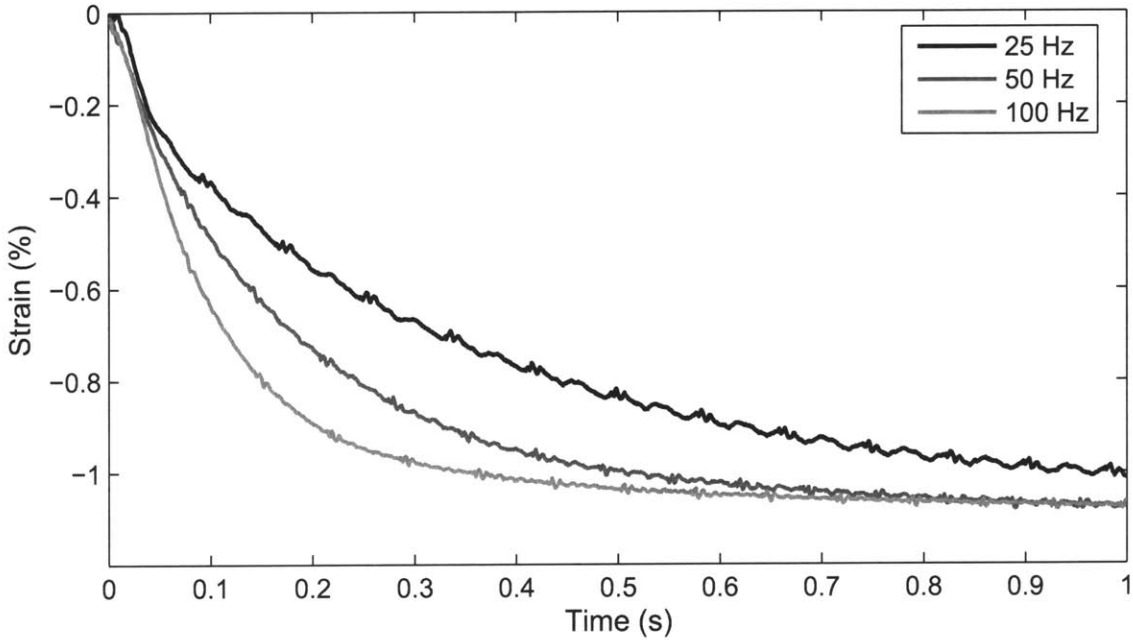

Figure 3-12: Compressional actuation strain for apparatus C1, with varying pulse repetition rate. V_g= 12 V (saturated), V_{in}= 100 V.

effect of repetition-rate diminishes as actuation continues and the effectiveness of each stress pulse decreases. The effect of repetition-rate should change once the reflected remanence of previous pulses begins interfering with new pulses. Stress wave measurements did not show any signs of such interference up to 100 Hz, in this apparatus.

3.3 Magneto-Acoustic Actuation

An electromagnet capable of generating a 4 kG field was placed around apparatus C1 (see Figure 3-13) in order to study the effect of a magnetic field on acoustic actuation and vice versa. Experiments were run in which a magnetic field, transverse to the length of the FSMA, was ramped linearly up and down using a triangle wave, while compressive acoustic pulses were continuously applied to the FSMA. A range of experiments were run using a variety of field levels, field ramp rates, and pulse amplitudes. The electronics were set up with V_g saturated at 12 V, and f_r = 100 Hz. The measured magnetic field was converted to an equivalent magnet stress using Equation (1.7).

Figure 3-14 through 3-17 show the data collected using a ramped magnetic field. Before every magnetic actuation measurement was made, the crystal was manually compressed, so

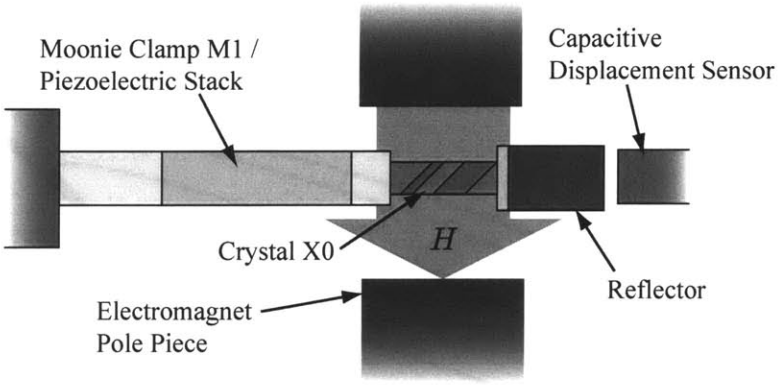

Figure 3-13: Schematic of the magneto-acoustic actuation setup. As the magnetic field shown increases the crystal elongates, and compressive pulses from the piezoelectric stack recompress the crystal as the magnetic field decreases.

that the crystal began as a single variant. The effects of acoustic actuation are two-fold in these experiments. The first obvious effect is that the compressive acoustic pulses act as a restoring force as the magnetic field is decreased. The second effect is that the acoustic pulses allow the magnetic field to accomplish more twin boundary motion at lower fields.

The displacement data for this set of experiments was median filtered to reduce the noise caused by the displacement of the piezoelectric stack. The time averaged displacement of the piezoelectric stack is constant in these experiments, since the acoustic pulse amplitude and direction where constant during each run. Therefore, no compensation was needed, to remove the displacement of the piezoelectric stack from this data.

3.4 The Spring Load Testing Apparatus

In order to ascertain the actuating capabilities of an acoustic pulse actuated Ni–Mn–Ga crystal, a spring load testing apparatus, C2, was used. This apparatus was used to measure acoustic actuation under a variety of spring loads and actuator prestresses, σ_{pre}. All of the testing was done using gate voltage of 12 V, and a pulse repetition rate of 50 Hz. A set of tests were run to determine the steady state response of the actuator to various input voltages and stresses (see Section 3.4.1). Section 3.4.2 presents the results of a large set of experiments which measure the time dependent response of the actuator to various actuator prestresses and load stiffnesses.

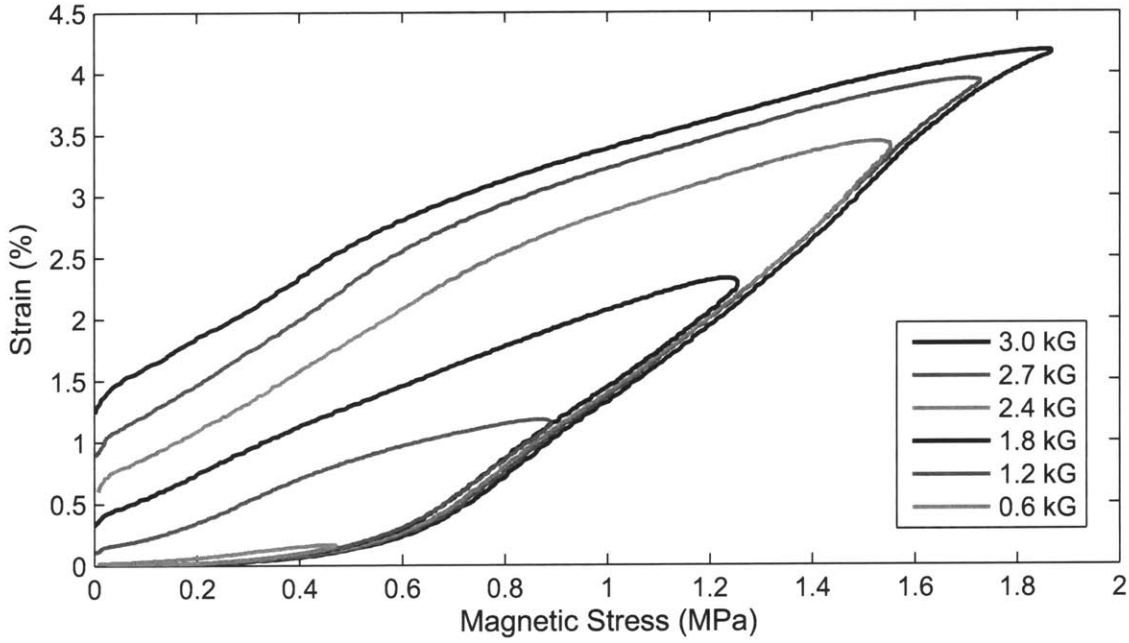

Figure 3-14: Compressional actuation versus varying magnet field cycles. Compressive pulses were applied while the magnetic field was ramped to varying levels and back to zero, with V_{in}= 100 V, V_{g}= 12 V, f_{r}= 100 Hz. The period of the magnetic field triangle wave was 10 s.

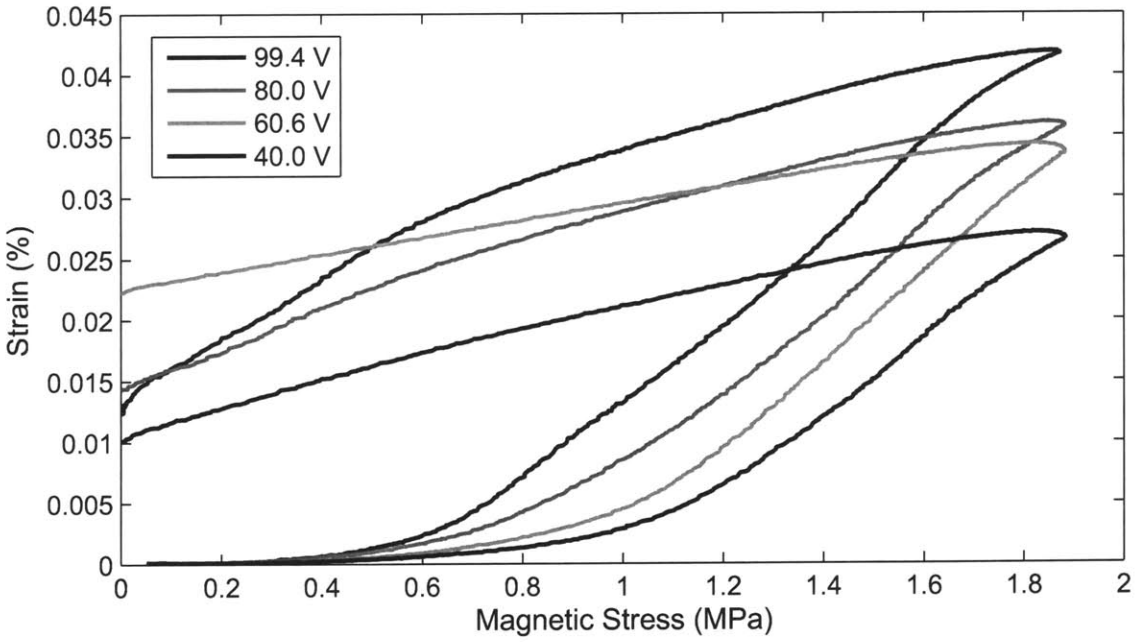

Figure 3-15: Various levels of compressional actuation versus a cyclic magnetic field. Compressive pulses with varying input voltage were applied while the magnetic field was ramped to 3 kG, V_{g}= 12 V, f_{r}= 100 Hz. The period of the magnetic field triangle wave was 10 s.

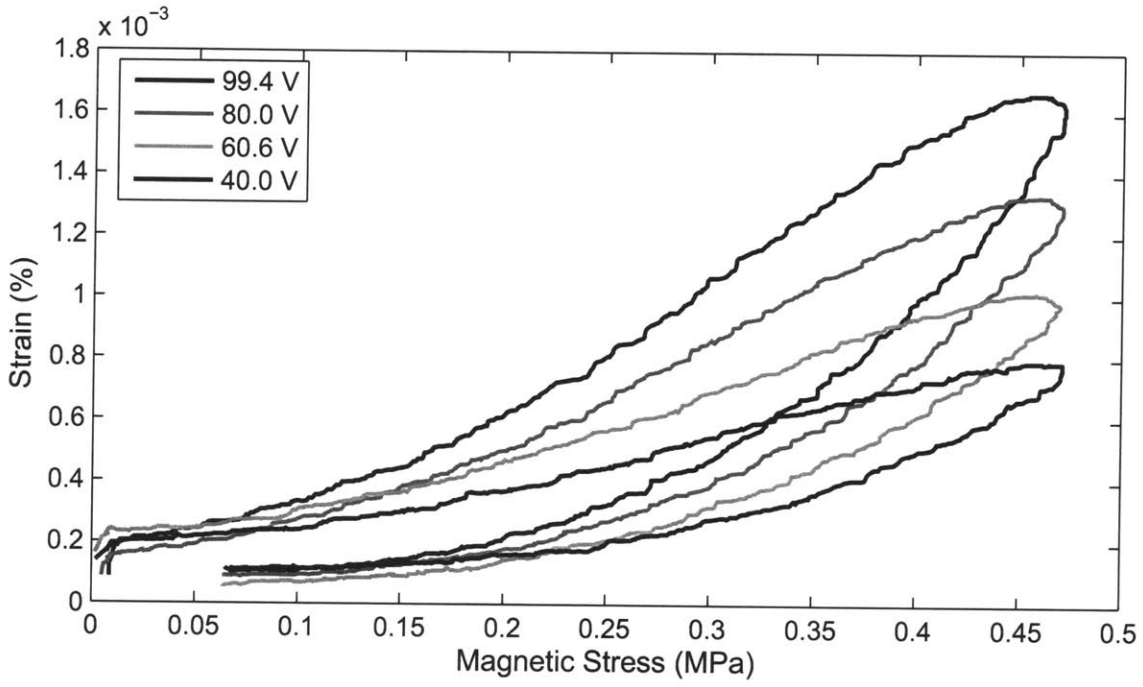

Figure 3-16: Various levels of compressional actuation versus a cyclic magnetic field. Compressive pulses with varying input voltage were applied while the magnetic field was ramped to 0.6 kG, V_g= 12 V, f_r= 100 Hz. The period of the magnetic field triangle wave was 10 s.

3.4.1 Steady State Strain Versus Input Pulse Amplitude

Figures 3-18 and 3-19 show the response of the loaded actuator versus input voltages at a variety of actuator prestresses. Actuation began at the prestress level indicated in the label on the left hand side of the graph, tensile pulses elongated the sample and reduced the tensile stress or increased the compressive stress. At each level of input voltage actuation was allowed to continue until steady state was reached. The time it took the system to reach steady state varied from 10 s to 60 s. Once steady state was reached, a reading was taken and the input voltage was increased. After the peak tensile voltage of 100 V was reached, the voltage was reduced and pulses were switched from tensile to compressive. The amplitude of the compressive pulses was increased in the same manner as the tensile, up to 100 V, where the actuation cycle was complete.

Figure 3-18 has many notable features. One of which is the performance of the actuator in compression versus tension. Even with an increased piezoelectric stack prestress (45 MPa) from the moonie clamp, M2, on the piezoelectric stack, the performance of compressional actuation is still superior to extensional actuation. Another feature is the lack of complete

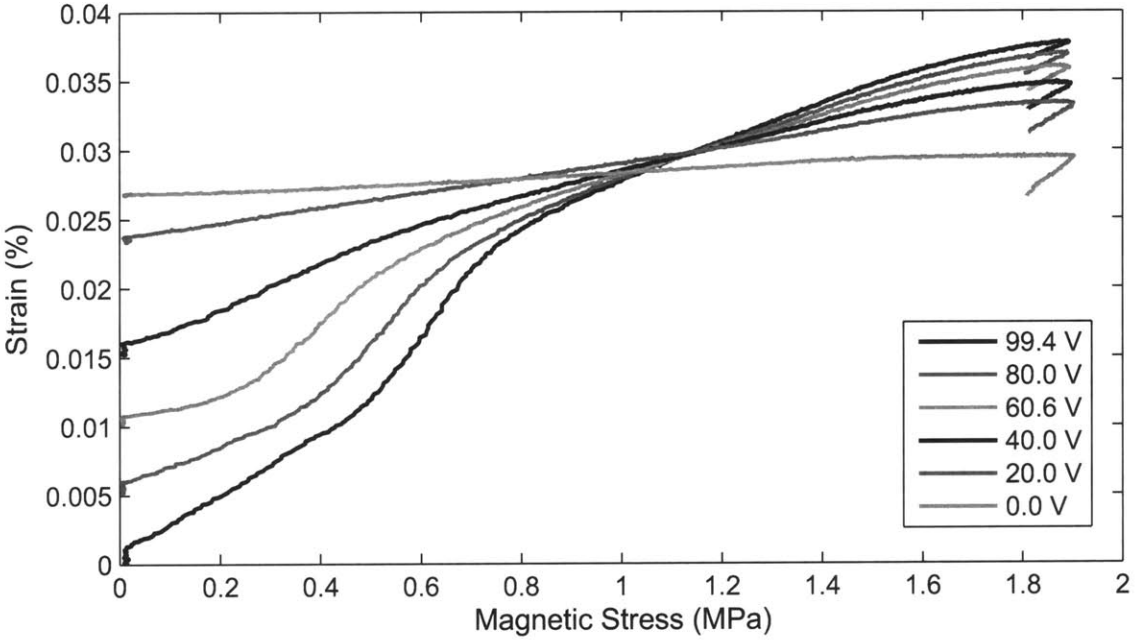

Figure 3-17: Various levels of compressional actuation versus a slowly cycling magnetic field. Compressive pulses with varying input voltages were applied while the magnetic field was ramped from 3 kG to 0 kG, V_g= 12 V, f_r= 100 Hz. The period of the field triangle wave was 60 s. The data begins 10 s before 3 kG is reached. The displacement measured is not quite equilibrium. Notice the continued actuation at zero field.

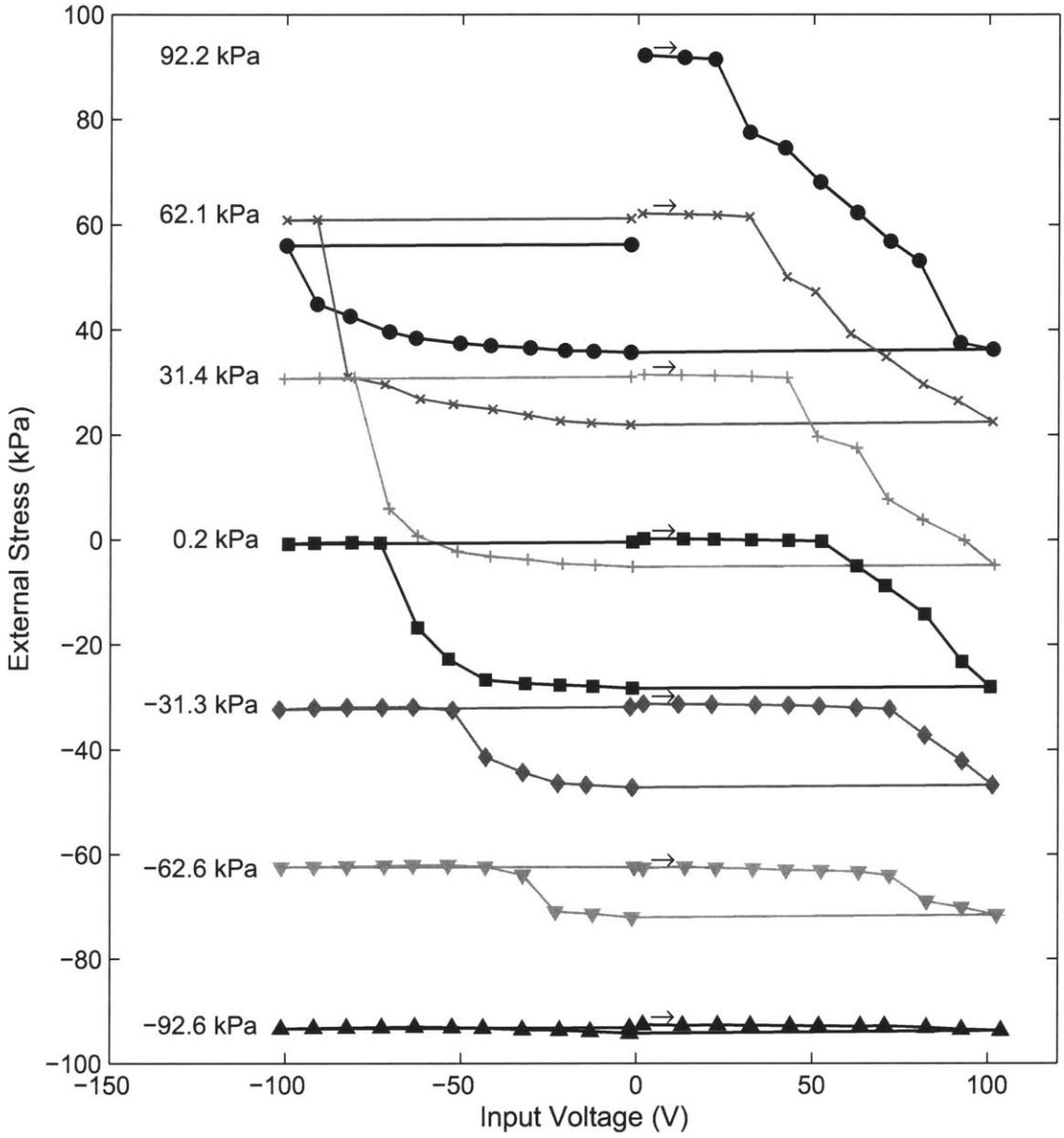

Figure 3-18: Stress on the actuator versus input voltage for several actuator prestresses using flexure B4. Negative values are assigned to the input voltage for compressive pulses. The label on each curve indicates the actuator prestress, measured before actuation begins. Each point represents the steady state position of the actuator at the specified voltage. The actuator began fully compressed was first extended and then compressed. V_g= 12 V and f_r= 50 Hz.

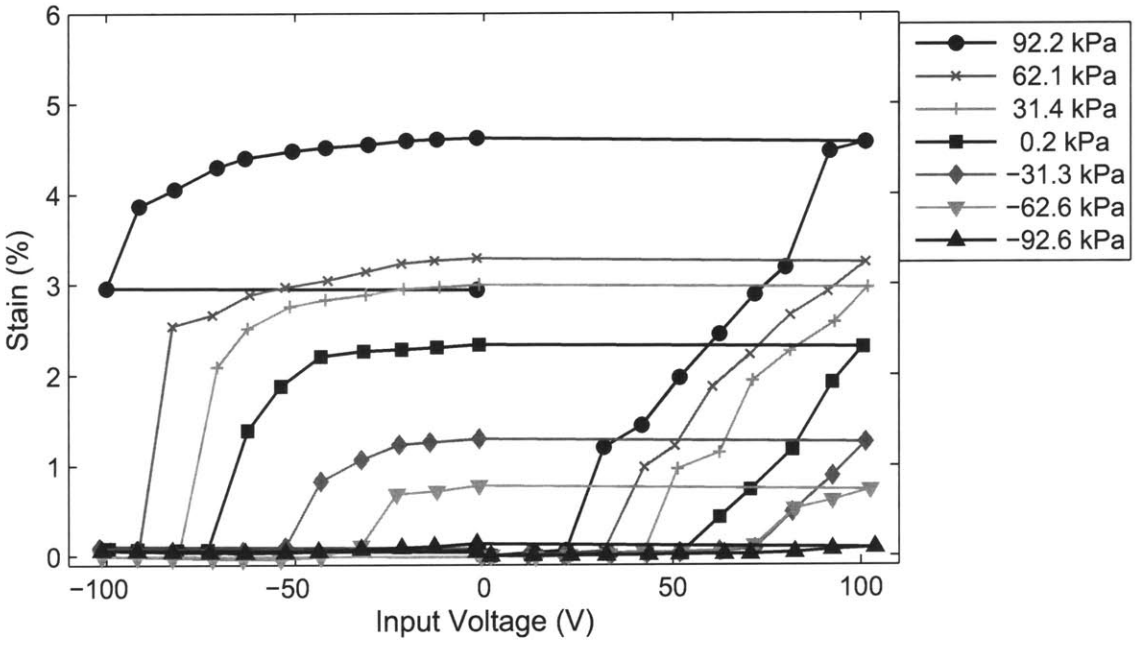

Figure 3-19: Actuation strain versus input voltage for several actuator prestresses using flexure B4. Negative values are assigned to the input voltage for compressive pulses. The legend indicates the actuator prestress values, measured before actuation begins. The data is identical to that in Figure 3-18 except that it has been scaled to strain units, and offset to the common, fully compressed, starting point.

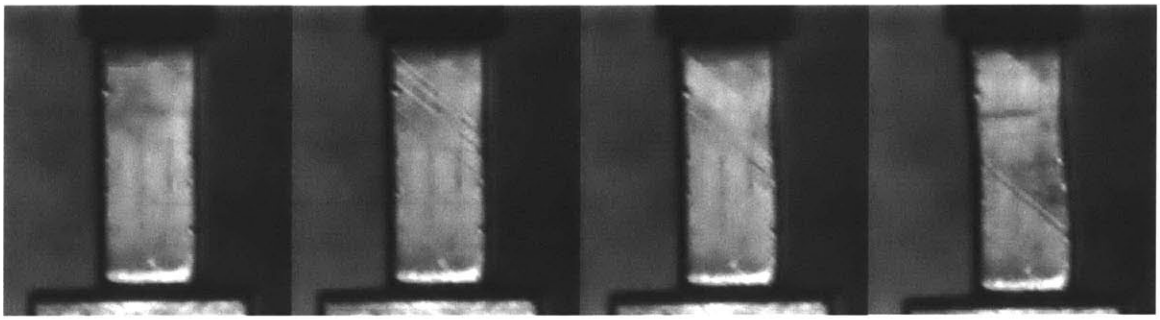

Figure 3-20: Photographs showing the progression of twin boundary movement during extensional acoustic actuation. The final images show partial separation of the FSMA crystal from the moonie clamp, represented by the movement of a twin boundary across the end face of the crystal.

compressional actuation under the largest tensile actuator prestress. This was due in part to the prestress, as partial separation of the bond between the FSMA and the moonie clamp occurred. The separation did not result in total bond failure, but the acoustic transmission of the bond was greatly reduced. Partial separation is easy to detect through visual observation of the twin boundary movement. Twins forming in the areas that should be constrained by adhesive, indicate that the bond has partially failed. Figure 3-20 show a sequence of images taken during acoustic pulse extension of the crystal, the final image shows a partially separated bond.

Loctite 420 was used in the bond between the FSMA and moonie clamp in this experiment, which was an improvement over previous adhesives, but still not strong enough for the stresses at this critical bond. During the rest of the experiments presented in this section, a 3M 810dp acrylic was used. It showed no signs of failure through extensive testing.

3.4.2 Time Dependent Actuation With Various Loads

Figures 3-21 through 3-25 show actuation over time for the full set of spring flexures used in apparatus C2. The compressive actuator prestress limit for this data was determined by the point at which visible actuation no longer occurred. The tensile actuator prestress limit was determined by prior experience with failed adhesive bonds. A time limit of 60 s was chosen, because most actuation occurred within this time, though at least one exception can be seen in Figures 3-24 and 3-25.

Figure 3-25 shows erratic, though still monotonic, behavior as the FSMA actuates over

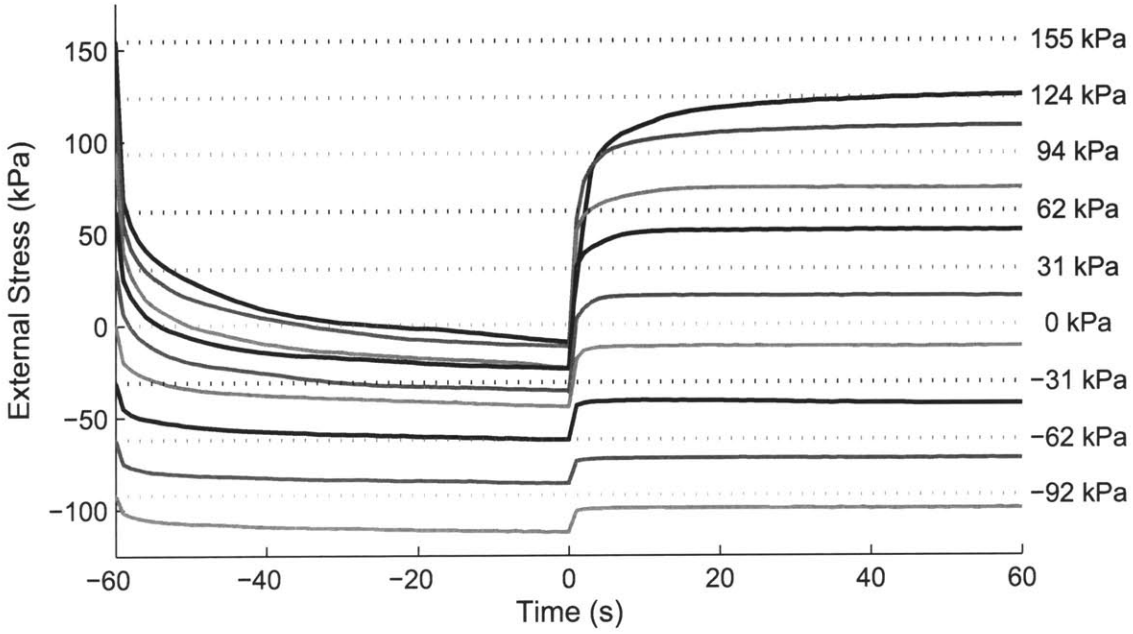

Figure 3-21: Actuator stress versus time for a variety of actuator prestresses using flexure B0, stiffness = 11.5 MPa. The right-hand labels indicate the actuator prestress on the actuator, measured before actuation begins. Each actuation test began with a fully compressed crystal. V_{in}= 100 V, V_{g}= 12 V, f_{r}= 50 Hz.

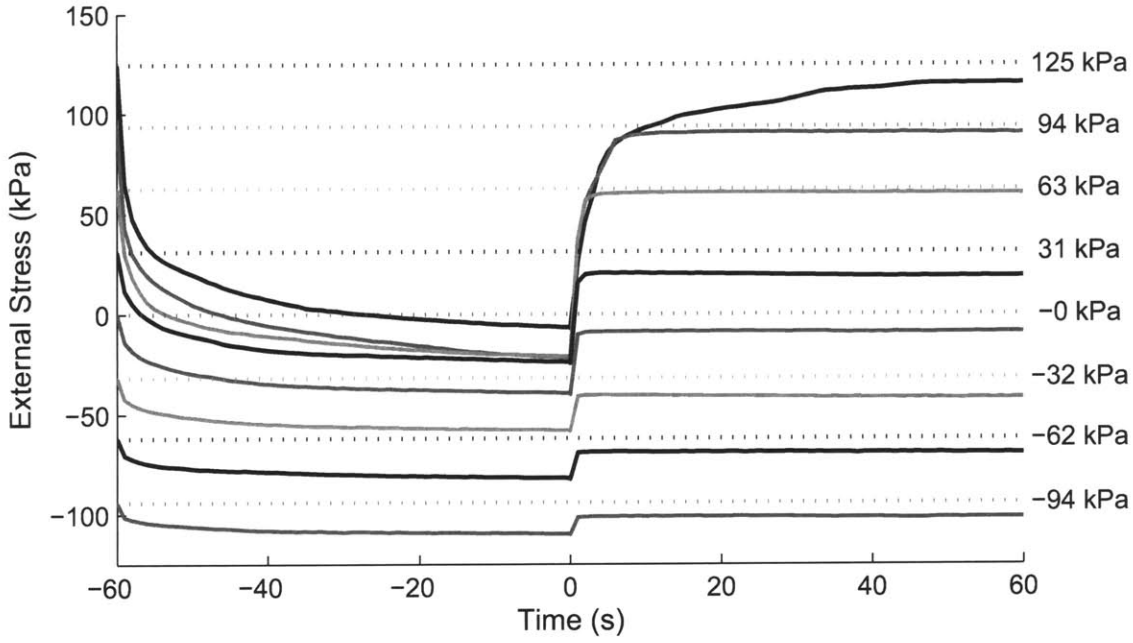

Figure 3-22: Actuator stress versus time for a variety of actuator prestresses using flexure B1, stiffness = 9.62 MPa. The right-hand labels indicate the actuator prestress on the actuator, measured before actuation begins. Each actuation cycle began with a fully compressed crystal. V_{in}= 100 V, V_{g}= 12 V, f_{r}= 50 Hz.

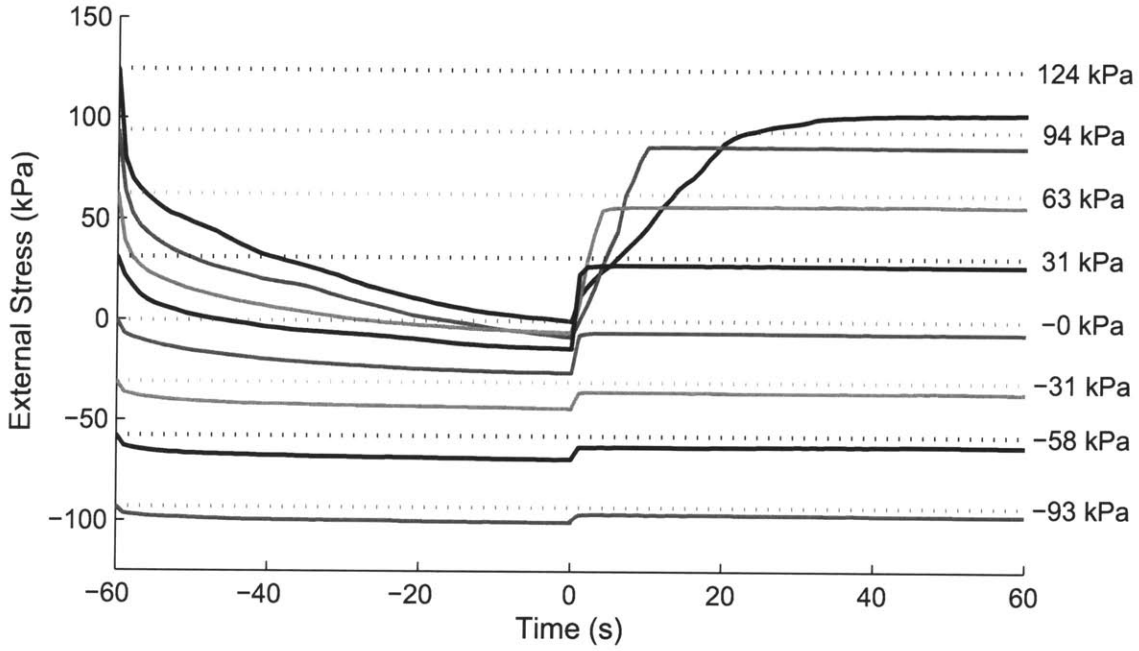

Figure 3-23: Actuator stress versus time for a variety of actuator prestresses using flexure B2, stiffness = 4.78 MPa. The right-hand labels indicate the actuator prestress on the actuator, measured before actuation begins. Each actuation cycle began with a fully compressed crystal. V_{in}= 100 V, V_{g}= 12 V, f_{r}= 50 Hz.

large strains. Behavior of this sort results from the non-uniform distribution of pinning sites throughout an FSMA crystal [13]. It is most apparent in Figure 3-25 for two reasons. One, the maximum strain of that cycle is nearly 5%, which means a large volume fraction of crystal has transformed; and two, twinning has occurred in one of the supposedly fixed regions of the FSMA. When X1 is fully bonded, it is capable of ~3.5% strain. Partial separation of the bond between the crystal and the reflector resulted in the higher strain. The stresses that were overcome to break down the bond represent a type of macroscopic pinning stress. The large volume fraction of the crystal that was transformed increases the chances of encountering other high stress pinning sites. The behavior resulting from the non-uniform pinning obstacles is discussed in section 4.3.

Figure 3-26 shows the effect of repetition rate on peak-to-peak output stress of a full actuation cycle. Two cycles lasting 30 s each were completed and the peak-to-peak stress for the second cycle was recorded. The input voltage was maintained at 100 V, and V_{g} = 12 V throughout the test. Three identical series of data were collected at 27 points between 10 Hz and 100 Hz, the average and standard deviation of these three runs is shown in

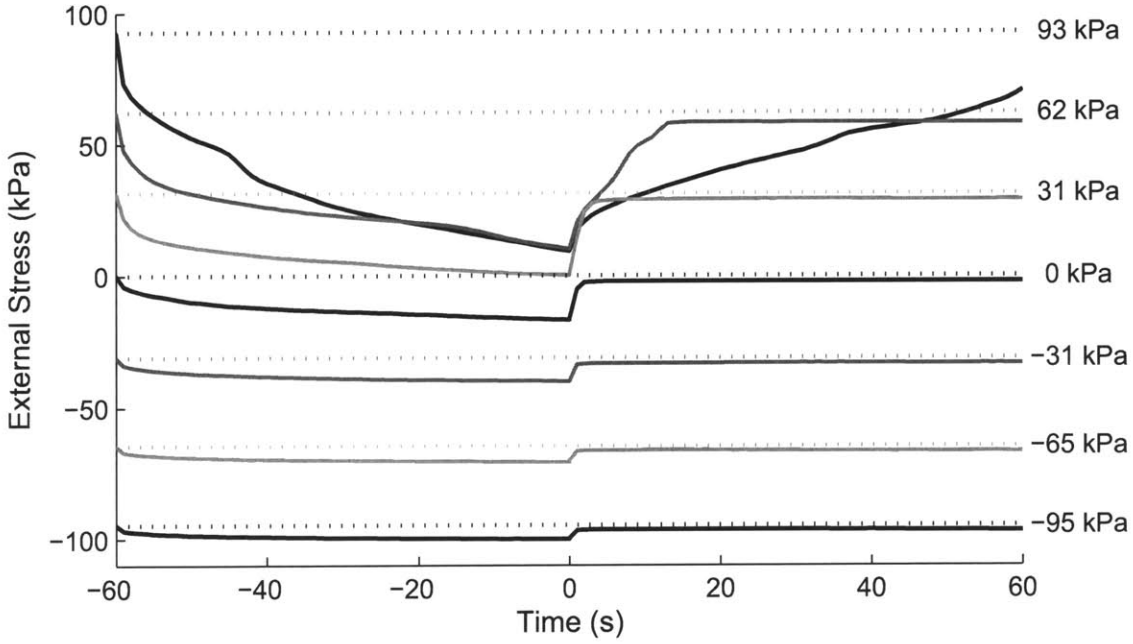

Figure 3-24: Actuator stress versus time for a variety of actuator prestresses using flexure B3, stiffness = 2.43 MPa. The right-hand labels indicate the actuator prestress on the actuator, measured before actuation begins. Each actuation cycle began with a fully compressed crystal. V_{in}= 100 V, V_{g}= 12 V, f_{r}= 50 Hz.

Figure 3-26. The data shows a peak at 70 Hz, along with several other peaks and valleys. These features must somehow be associated with the positive and negative interference of the sequential pulses through the spring load system. However, the specific resonant modes they represent are unknown.

3.5 Piezoelectric Stress Sensors

The acoustic pulse actuator was modified to include piezoelectric stress sensors, described in Section 2.3.4, at both ends of the FSMA crystal. An experiment was conducted in which the crystal was actuated at 50 pulses per second for 1 s intervals, and the final stress wave of every interval was recorded. The crystal began each run fully compressed, was extensionally actuated for 10×1 s bursts, then compressed for 10×1 s bursts. This was done at 5 different input voltages. Figure 3-27 shows the strain accomplished during this actuation. The flexure that was actuated against was B4, and the initial actuator prestress was set near zero.

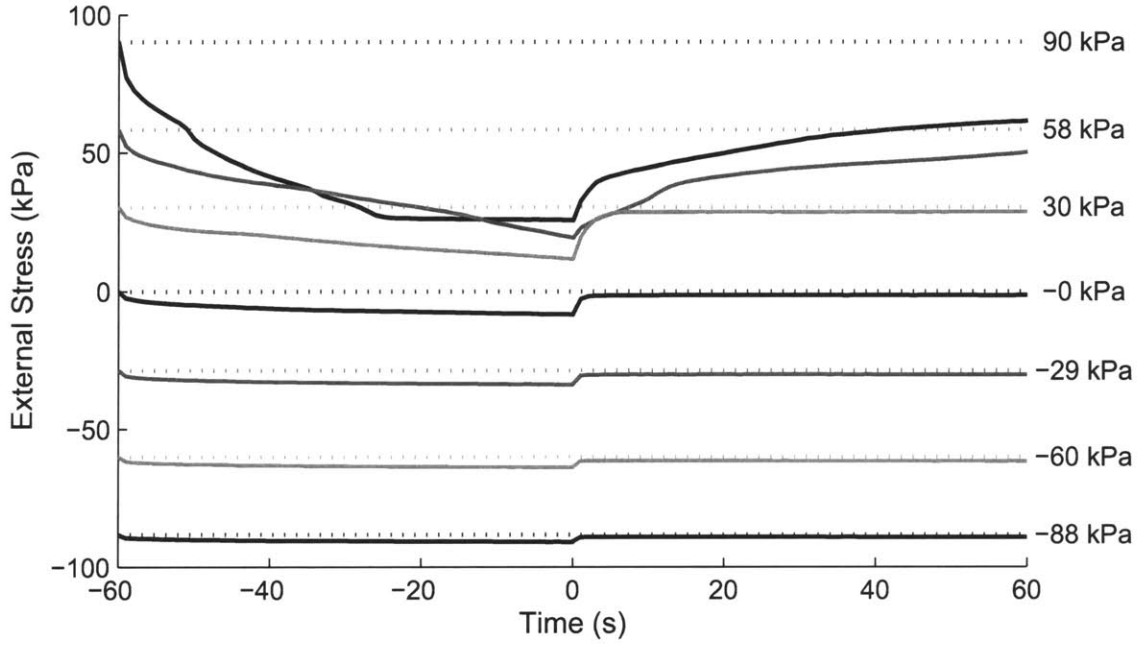

Figure 3-25: Actuator stress versus time for a variety of actuator prestresses using flexure B4, stiffness = 1.21 MPa. The right-hand labels indicate the actuator prestress on the actuator, measured before actuation begins. Each actuation cycle began with a fully compressed crystal. During final, high tensile actuator prestress cycle, separation of the bond between the FSMA crystal and the reflector was visible. V_{in}= 100 V, V_{g}= 12 V, f_{r}= 50 Hz.

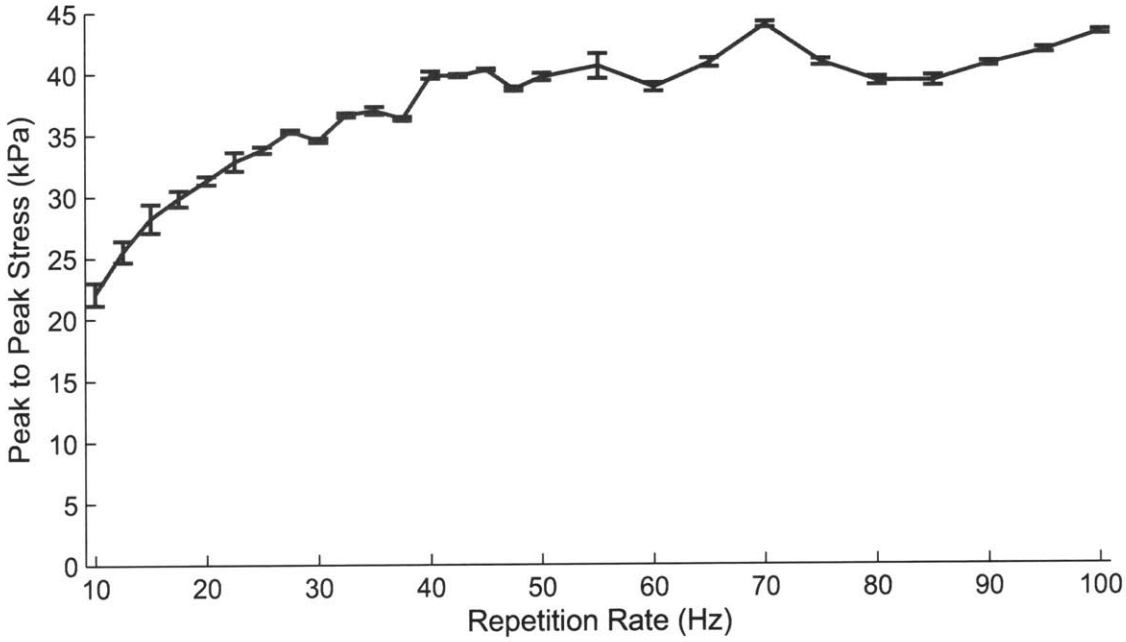

Figure 3-26: Peak-to-peak bidirectional actuation stress versus pulse repetition rate. Three consecutive experiments were run, the average result with standard deviation error bars is shown. V_{in}= 100 V, V_{g}= 12 V, σ_{pre}= 64 kPa and the flexure is B2.

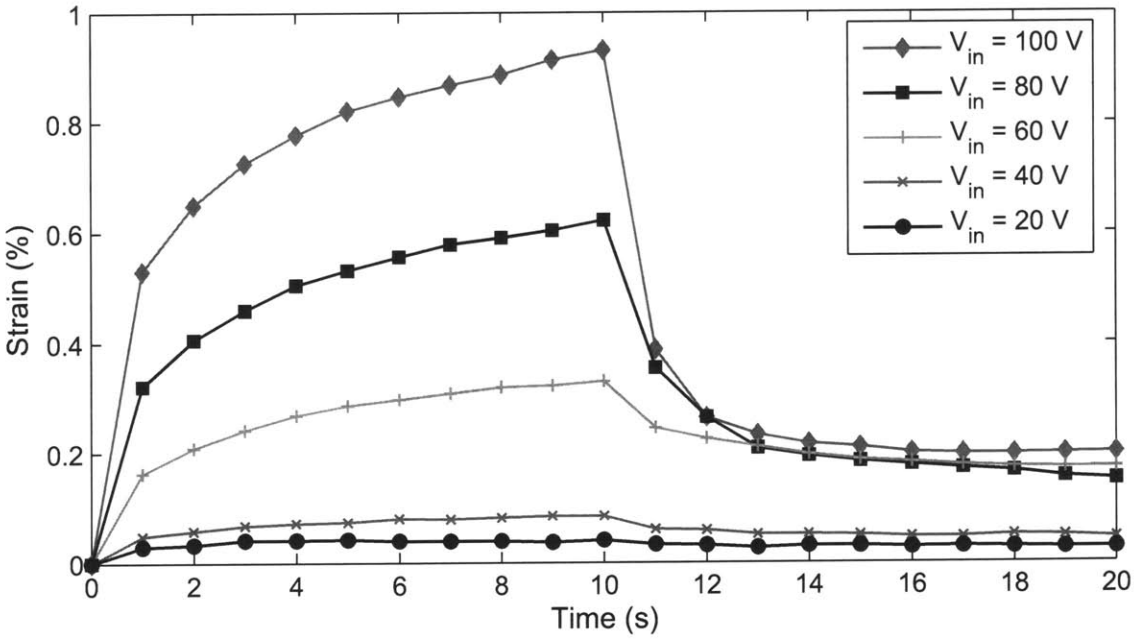

Figure 3-27: Strain cycles with varying input voltage during which the stress data shown in Figures 3-28 through 4-16 was collected. Before every strain data point was recorded the final stress pulse leading up to that data point was recorded. V_{g}= 12 V, f_{r}= 50 Hz.

Measuring the stress wave at either end of the actuating crystal gives a partial picture of processes that occur during acoustically induced twin boundary motion. Figure 3-28 shows the final compressive and tensile stress pulse measured during the strain cycles in Figure 3-27. An interesting phenomena can be seen in the data for S2 in Figure 3-28. The measurements show that the magnitude of the first peak that reaches S2 is nearly unchanged by the magnitude of the initial pulse at S1. This phenomenon indicates stresses larger than the threshold stress are being scattered or dispersed as they move twin boundaries and do not reach S2 at the expected time. This same phenomenon can be observed in the differences between Figure 3-7 and Figure 3-11. However, this data also shows much larger stress peaks following the initial stress peak that reach S2. Further discussion and possible explanations for this behavior will be explored in Section 4.2.

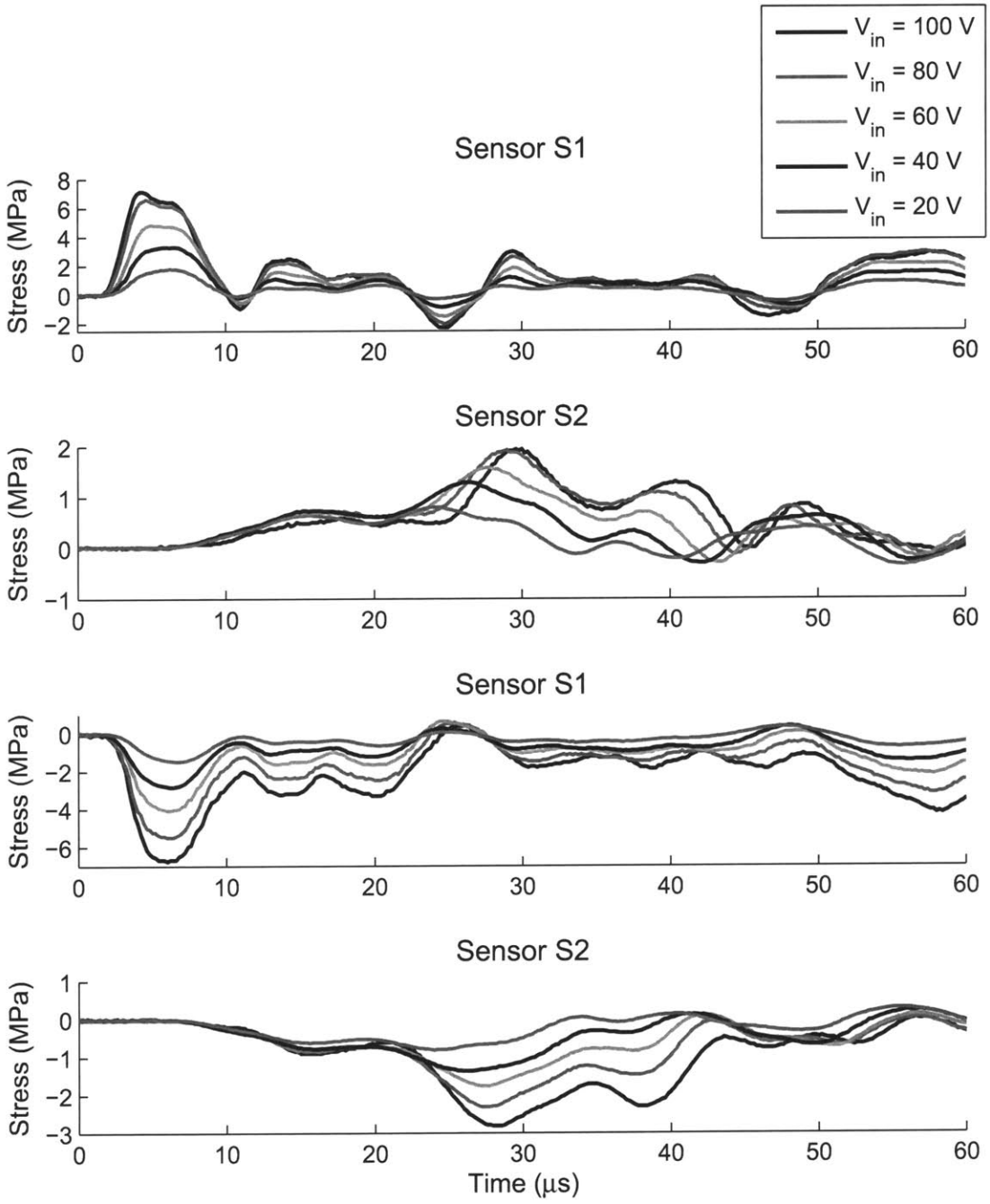

Figure 3-28: The final tensile and compressive stress waves measured during the actuation shown in Figure 3-27 at varying input voltages. S1 is located between the FSMA and moonie clamp. S2 is located between the FSMA and reflector. V_g= 12 V, f_r= 50 Hz.

Chapter 4

Data Analysis

The results shown in Chapter 3 quantify the behavior of a few specific acoustic pulse actuator configurations. This chapter identifies trends in the results, and determines how these trends may be applicable to the general design of acoustic pulse actuators. The first section will look at the effect of changing various actuation parameters on the actuator output. The second section will examine the behavior of the Ni–Mn–Ga crystal and its interaction with acoustic pulses.

4.1 Actuation Parameters

Many parameters were varied while obtaining the results shown in Chapter 3. In this section, we will examine measured effects that five parameters had on acoustic actuation. These five parameters are: pulse input voltage (V_{in}), gate voltage (V_{g}), repetition rate (f_{r}), actuator prestress (σ_{pre}), and load stiffness (C_{L}).

4.1.1 Input Voltage, V_{in}

Changing the input voltage to the pulse generator circuit indirectly increases actuation strain and actuation rate by generating larger stresses with the piezoelectric stack. Figure 4-1 shows the relationship between input voltage and maximum stress generated. Results from the 1-D model, discussed in Section 2.1.2, indicated that the generated acoustic stresses should be proportional to the input voltage. Measured compressive stress pulses show a nearly linear relationship between V_{in} and generated stress, with some non-linearity

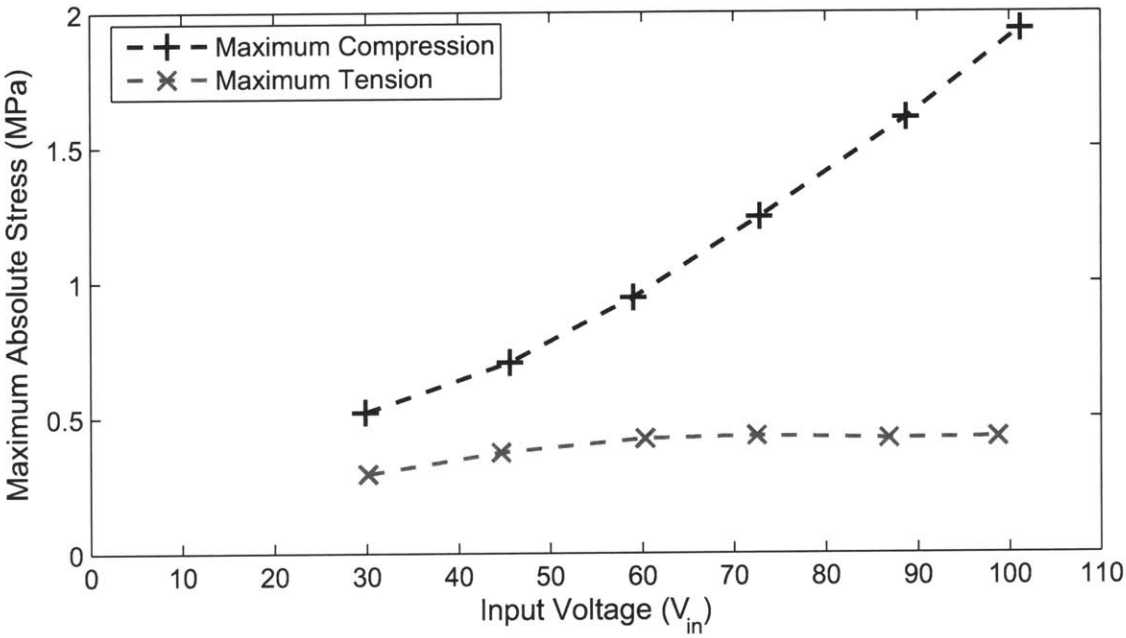

Figure 4-1: Maximum measured transient stress versus pulse amplitude (V_{in}) in apparatus C1. Input voltage was varied while $V_{\text{g}} = 12$ V. The data points were collected from the results in Figures 3-7 and 3-11.

which is likely caused by the nonlinear response of the piezoelectric stack to voltage. Measurement of tensile pulses however, shows a very different trend.

The theory used to explain the difference between the two stress measurements assumes that the difference was caused by the state of the crystal when the stress pulses were measured. The measured compressive pulses were applied to a compressed single variant crystal. The compressive stress pulses traveled through the crystal and reached the piezoelectric stress sensor without causing any twin boundary motion, because none of the crystal could be further compressed. In an attempt to achieve the same effect in tension, tensile pulses were applied to a fully extended crystal. However, a fully extended crystal is not a single variant. The constrained ends of the crystal cannot be transformed to the extended variant without detaching them from the rest of the apparatus. Figure 4-2(b) shows the extended crystal and the temporary twin movement that could be caused by a tensile pulse in the extended crystal. The twin movement is temporary, because the twin boundary that forms does not lie on a {202}-plane and requires a stress to maintain its position. When the tensile stress is removed the boundary falls back, closer to the {202}-plane. The current theory is that the tensile stress pulses cause twin boundary motion of this sort, and stresses

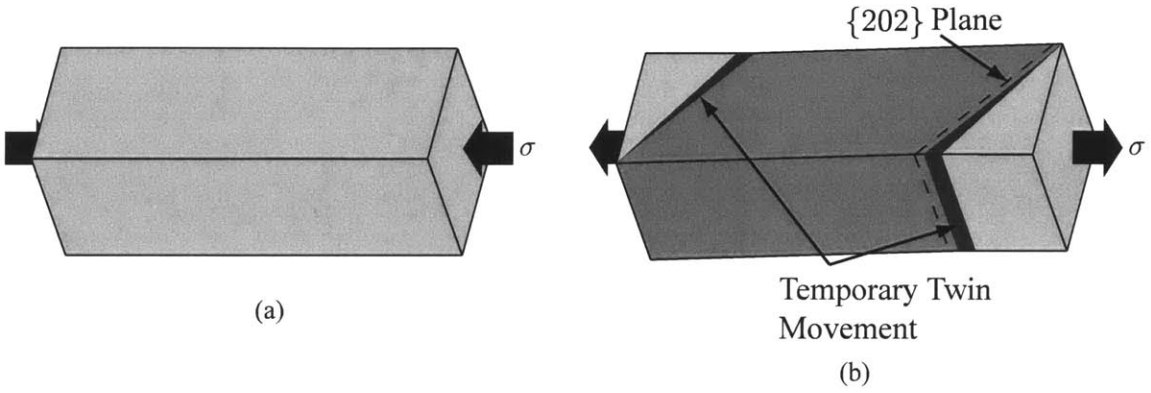

Figure 4-2: Illustration of the effect of (a) a compressive stress on a compressed, single variant crystal, and (b) a tensile stress on an extended crystal. (b) shows how the twin boundary can extend into the constrained portions of the crystal when a tensile stress is applied.

larger than σ_0 were scattered or dispersed as they caused this motion.

The theory that the tensile pulses were scattered or dispersed by twin boundary motion is corroborated by the actuation strain data collected. Figure 4-3 shows that the small measured tensile stress had little effect on the strain induced by the tensile pulses. The figure also shows the nearly linear relationship between induced strain and peak compressive stress (measured through a compressed crystal). Note that the threshold stress predicted by a regression of the compressional strain data corresponds well with the threshold stress theoretically measured by the tensile stress pulses. Although this threshold stress is low for Ni–Mn–Ga, it is not outside the expected range for the static twinning threshold stress.

Figure 4-4 shows the indirect relationship between V_{in} and actuation strain. Increasing V_{in} monotonically increases the strain achieved in 2 s by apparatus C1. A similar, though less linear, relationship is seen between V_{in} and steady state actuator stress when actuating against a spring load. Figure 4-5 shows a single cycle from the results shown in Figure 3-19. As V_{in} increases for the tensile pulses, actuation remains minimal until a threshold voltage is reached. After the threshold voltage is reached the change in actuator stress per change in V_{in} is nearly constant. Compressive pulses cause a similar behavior, though the threshold occurs more gradually and the maximum slope (stress per volt) is much higher.

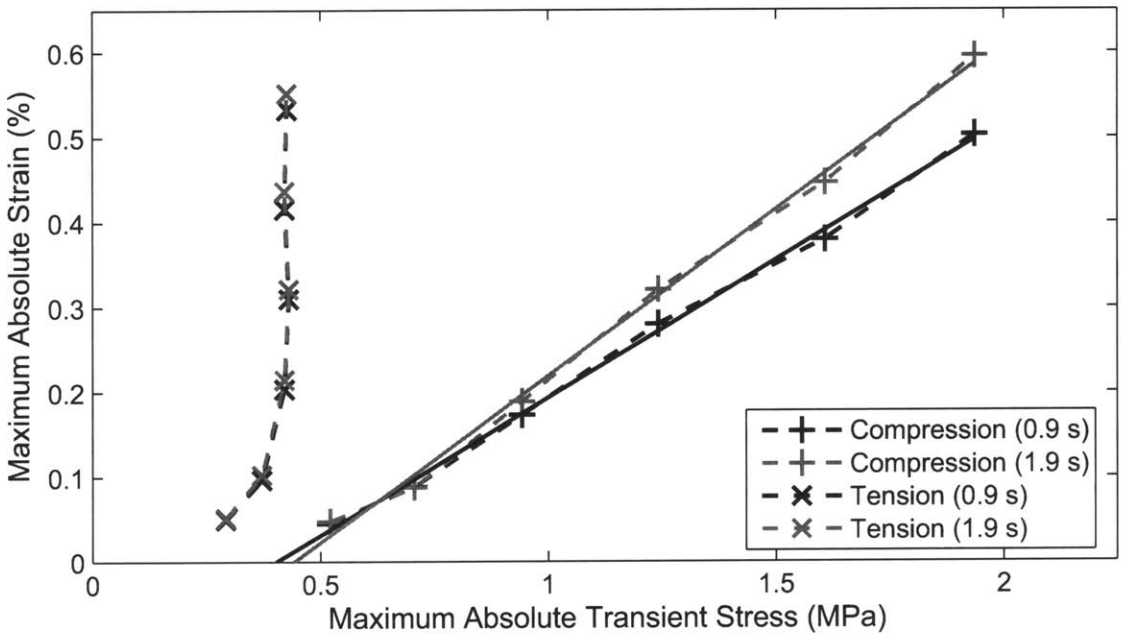

Figure 4-3: The effect of maximum pulse stress on actuation for changing V_{in} in apparatus C1. Maximum strain achieved after 0.9 s (90 pulses) and 1.9 s (190 pulses) of actuation versus the maximum measured stress in the actuating pulse. The absolute value of the stress and strain is shown for the sake of the comparison. The input voltage was varied linearly between 20 V and 100 V, V_{g}= 12 V (saturated), f_{r}= 100 Hz. Collected from results in Figures 3-7, 3-10, 3-11 and C-7.

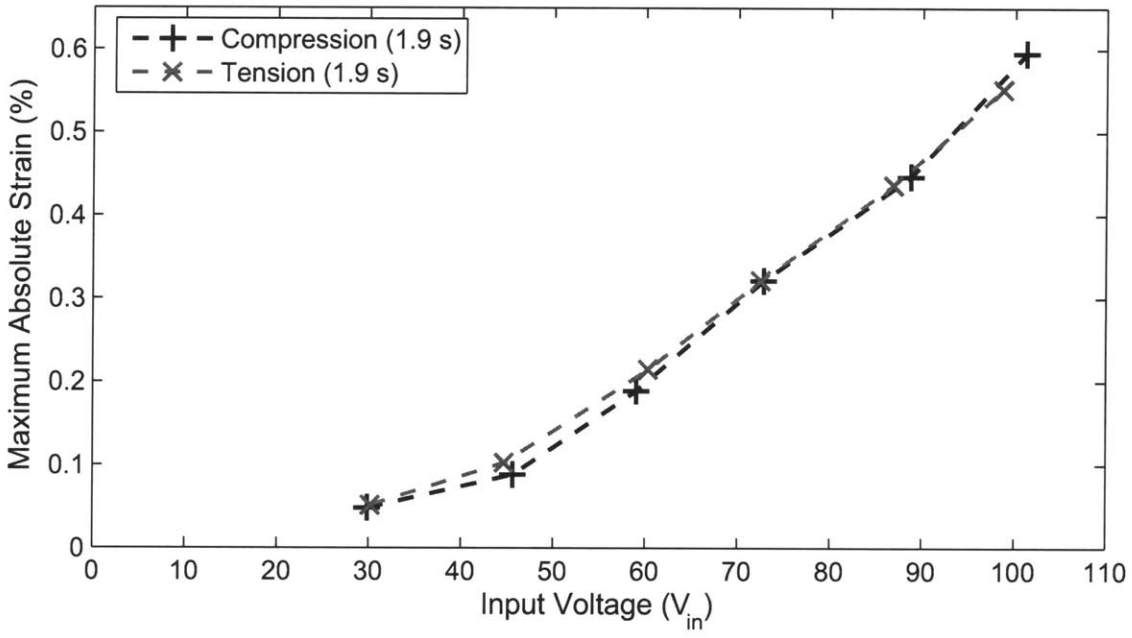

Figure 4-4: The effect of pulse amplitude (V_{in}) on actuation in apparatus C1. Maximum strain achieved after 1.9 s (190 pulses) of actuation versus V_{in}. The absolute value of strain is shown for the sake of the comparison. The input voltage was varied linearly between 20 V and 100 V, V_{g}= 12 V (saturated), f_{r}= 100 Hz. Collected from results in Figures 3-7, 3-10, 3-11 and C-7.

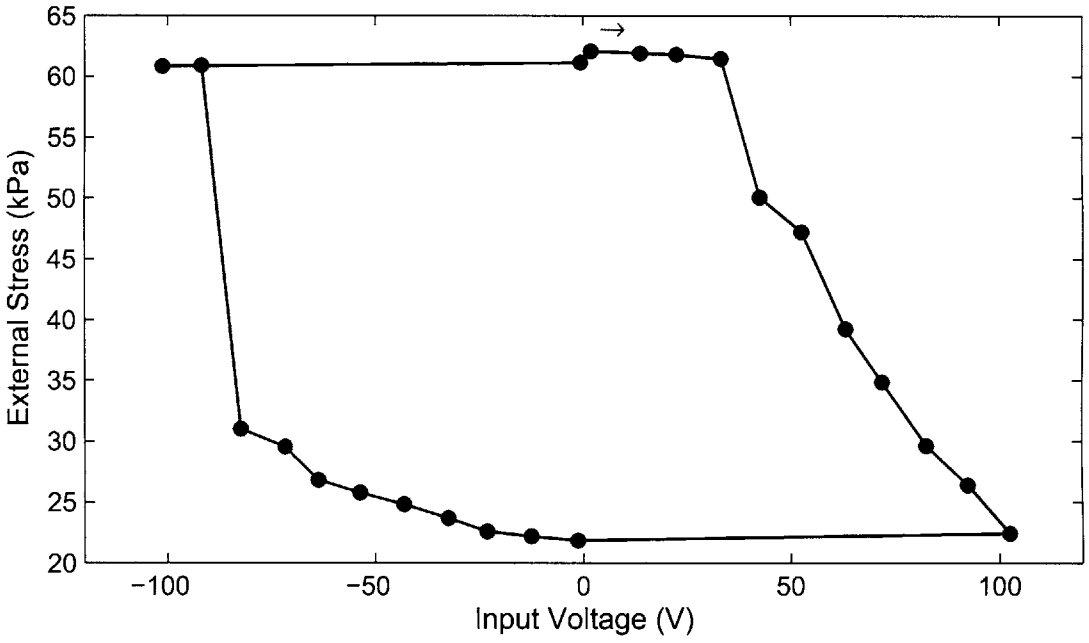

Figure 4-5: Stress on the actuator versus input voltage in apparatus C2. Negative values are assigned to the input voltage for compressive pulses. Each point represents the steady state position of the actuator at the specified voltage. The actuator began fully compressed, was first extended and then re-compressed. An actuator prestress of 62.1 kPa was applied prior to actuation. V_g= 12 V and f_r= 50 Hz. Selected from Figure 3-19.

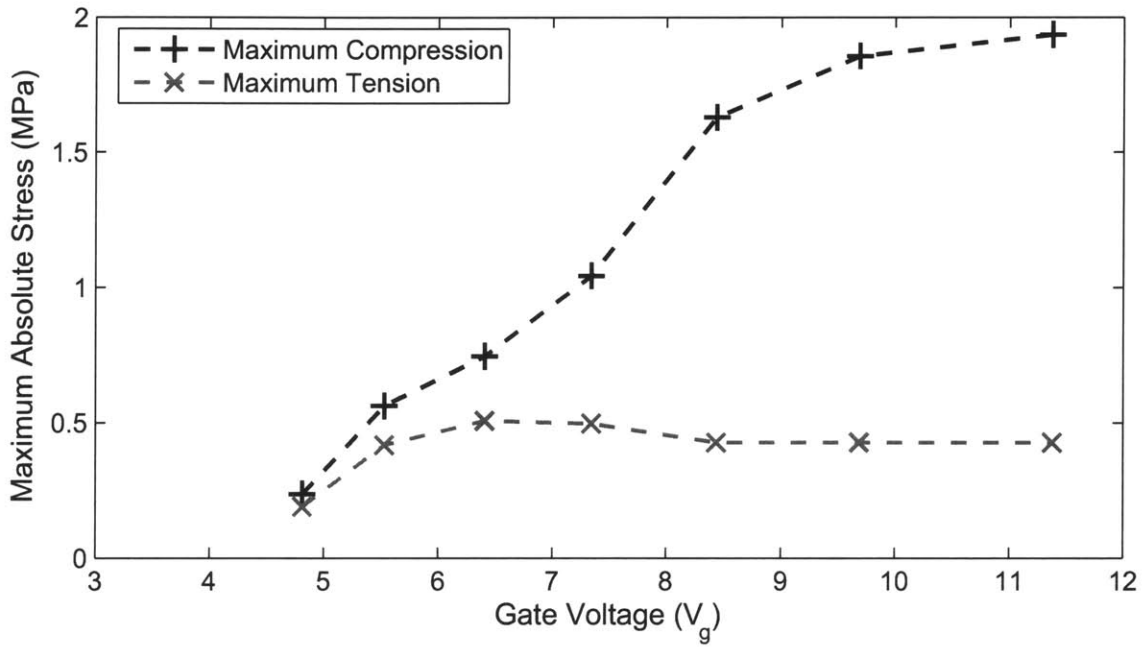

Figure 4-6: Maximum measured transient stress versus V_g in apparatus C1. Gate voltage was varied while $V_{in} = 100$ V. The data points were collected from the results in Figures 3-9 and C-12.

4.1.2 Gate Voltage, V_g

Adjusting the gate voltage effectively changes the stress pulse shape, by changing the rise time, t_r, of the voltage pulse that drives the piezoelectric stack. The change in rise time also changes the maximum generated stress, Figure 4-6 shows the relationship between maximum generated stress and V_g. Since the relationship between V_g and the maximum current output by the pulse generator circuit is non-linear, there is not a linear relationship between V_g and the t_r. However, the relationship between generated stress and V_g is nearly linear, if the last point, at 11.5 V, is excluded ($R^2 = 0.982$). Exclusion of the last point can be justified by the fact that the saturation voltage of gates of the pulse generator circuit transistors is about 9 V.

Although there is a near linear relationship between V_g and the maximum generated stress, the changes in pulse shape affect generated twin boundary motion, and the relationship between maximum stress and actuation strain is not linear (see Figure 4-7). The relationship between V_g and actuation strain is also nonlinear, though the relationship is still monotonic (see Figure 4-8). The reasons for the effect of pulse shape on induced actuation are not known.

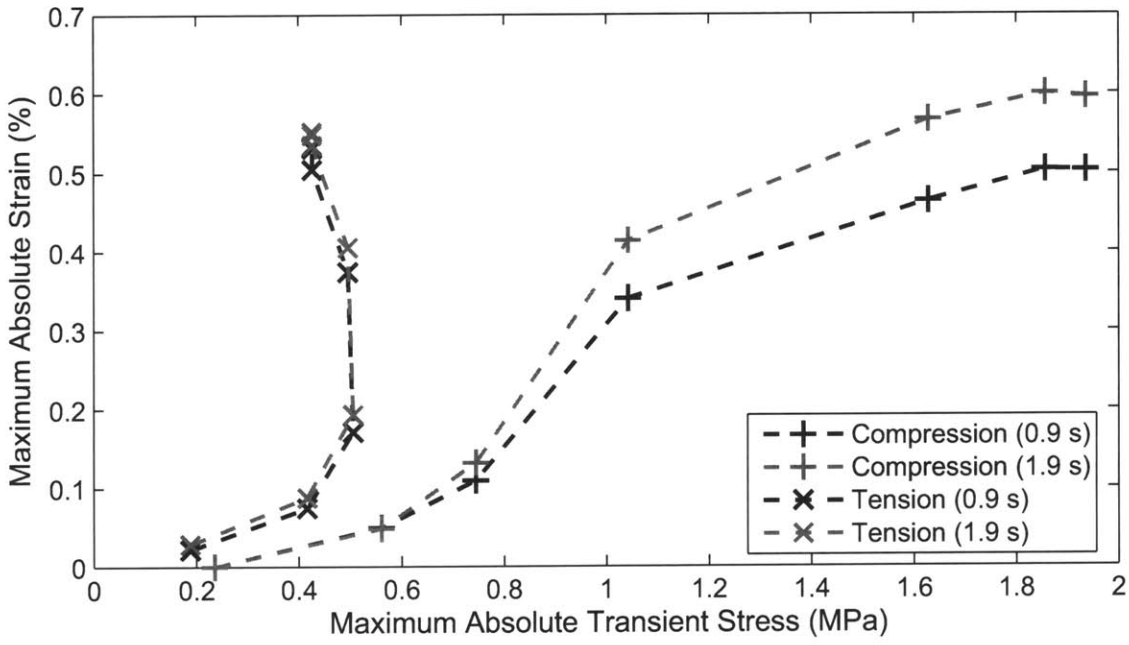

Figure 4-7: The effect of maximum pulse stress on actuation for changing V_g in apparatus C1. Maximum strain achieved after 0.9 s (90 pulses) and 1.9 s (190 pulses) of actuation versus the maximum measured stress in the pulses. The absolute value of the stress and strain are shown for the sake of the comparison. The gate voltage was varied as shown in Figure 3-8, V_{in}= 100 V, f_r= 100 Hz. Collected from results in Figures 3-9, C-10, C-12 and C-13.

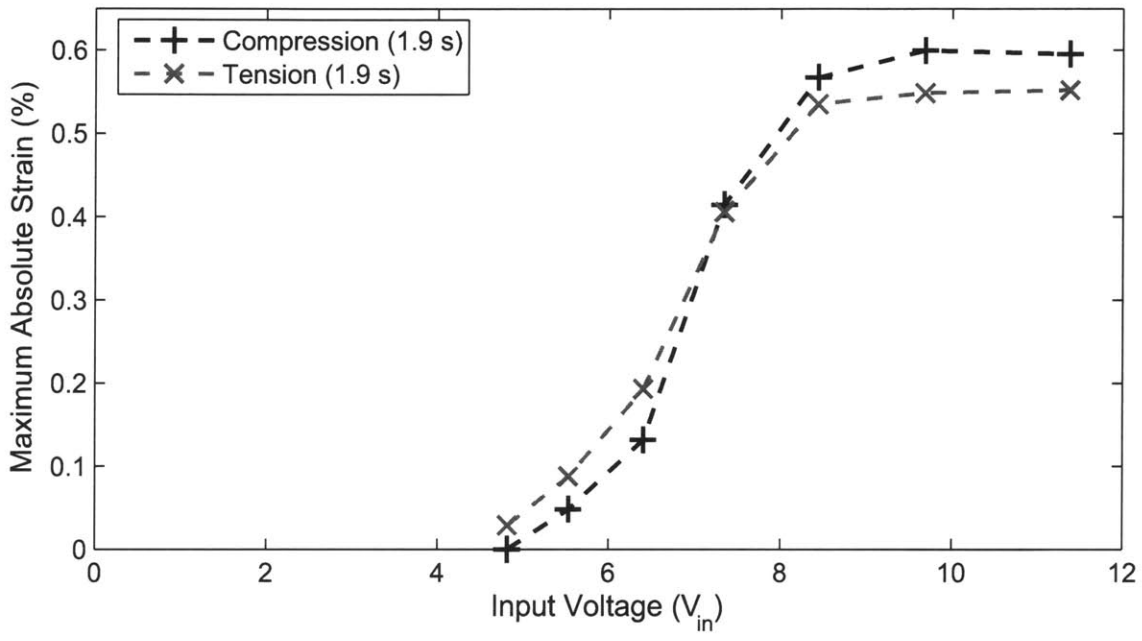

Figure 4-8: The effect of changing pulse shape (V_g) on actuation in apparatus C1. Maximum strain achieved after 1.9 s (190 pulses) of actuation versus V_g. The absolute value of strain is shown for the sake of the comparison. The gate voltage was varied as shown in Figure 3-8, V_{in}= 100 V, f_r= 100 Hz. Collected from results in Figures 3-9, C-10, C-12 and C-13.

4.1.3 Pulse Repetition Rate, f_r

Increasing pulse repetition rate, f_r, increases the number of actuating pulses per second, so increasing f_r should monotonically increase actuation rate, up to the frequency at which sequential stress pulses begin interfering with each other. The results shown in Figure 3-26 indicate that this interference occurs at relatively low frequencies (about 50 Hz), in apparatus C2. In order to take advantage of high repetition rates, an actuator would need to be carefully designed to eliminate stress pulse interference at the desired f_r. Determining the maximum effective repetition rate for any given actuator could possibly be done using a model, but getting an accurate result would be difficult. It would be more practical to use a prototype to determine the maximum f_r empirically.

4.1.4 Actuator Prestress, σ_{pre}

The effect of actuator prestress on actuation was studied using spring loads in apparatus C2. Figure 3-18 shows the effect that input voltage and prestress have on steady state actuator output stress for a single spring load. A tensile prestress increases the extensional

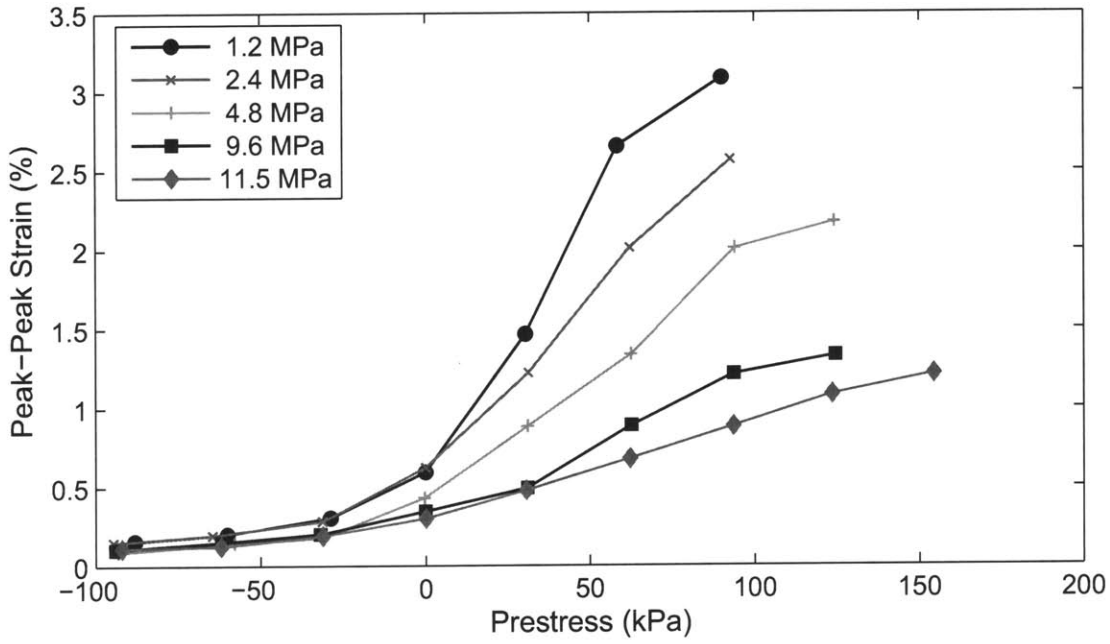

Figure 4-9: Total compressional strain versus actuator prestress for bidirectional actuation against flexures B0 through B4. The legend indicates the stiffness of the flexure that was actuated against. Results collected from Figures 3-21 through 3-25.

strain output and decreases the threshold voltage required to initiate extension. At the same time, an tensile prestress also decreases the effectiveness of compressional actuation. A compressive prestress causes the opposite to occur, favoring compressional actuation over extensional. The extent to which compressional actuation is more effective than extensional, is made apparent by the increased bidirectional actuation caused by a tensile prestress.

Figure 4-9 summarizes the effect of actuator prestress on peak-to-peak output strain for time dependent stress curves from Subsection 3.4.2, which used a constant input voltage of 100 V. The basic trend shown in this data is the increase of peak-to-peak output strain with an increase in tensile prestress. If the actuator could tolerate higher tensile prestresses, higher peak-to-peak strains could be realized for many of the flexures. However, at some point either strain saturation will occur, or compressional actuation will not be able to overcome the tensile prestress. Actuation against a 94 kPa tensile prestress with flexure B4 resulted in both strain saturation and the inability to fully compress (see Figure 3-25), so it is unlikely that higher strains could be achieved by using a larger prestress with flexure B4.

Figures 4-10 shows energy density of the actuator versus actuator prestress. The energy

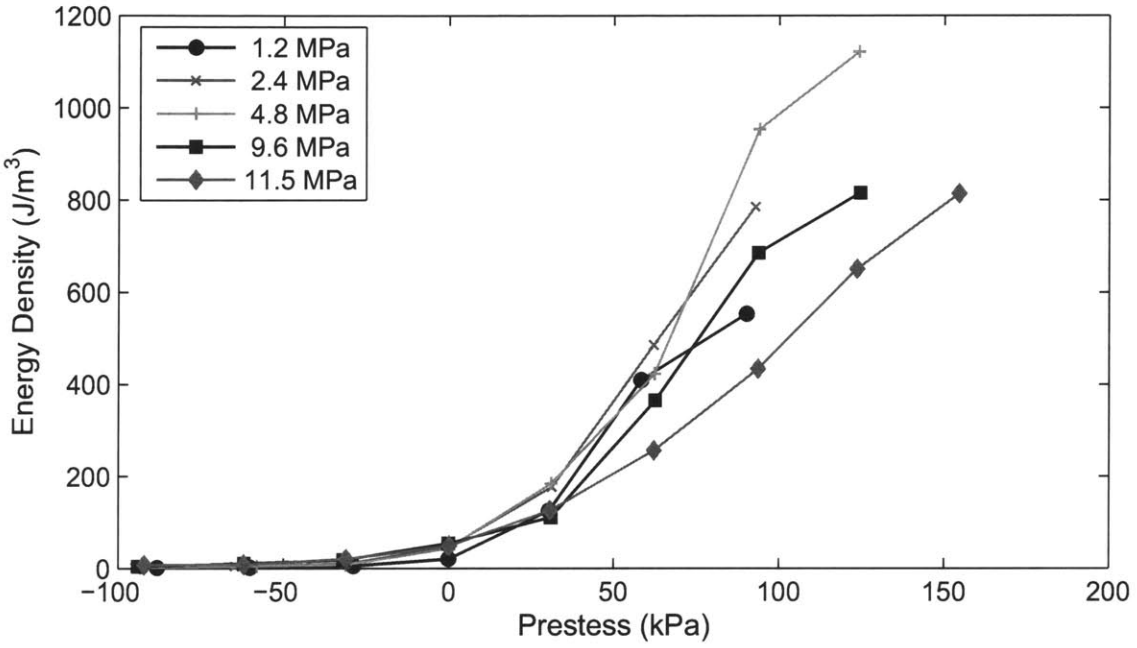

Figure 4-10: Total compressional energy output versus actuator prestress for bidirectional actuation against flexures B0 through B4. The legend indicates the stiffness of the flexure that was actuated against. Results collected from Figures 3-21 through 3-25.

density is calculated based on the work done by the actuation cycles shown in Figures 3-21 through 3-25 using

$$u = \frac{1}{2}\,\Delta\epsilon\,\Delta\sigma \ , \tag{4.1}$$

where $\Delta\epsilon$ is the difference between the peak extensional strain and final strain achieved by compressional actuation, and $\Delta\sigma$ is the difference between the peak stress and the final stress. A tensile prestress has the same effect on energy density that it did on peak-to-peak strain, causing it to increase monotonically within the range of the experiments conducted.

4.1.5 Load Stiffness, C_{L}

Figure 4-9 shows that peak-to-peak strain increases with decreasing load stiffness, which is expected for an actuator working against a spring load. Actuation against B4 nearly resulted in full range actuation, i.e., saturation strain in both directions. A flexure more compliant than B4 could allow the actuator to complete a full range cycle.

Figure 4-11 shows energy density versus stiffness for the same data as Figure 4-10. For high tensile prestress it is apparent that the output energy density of the acoustic pulse

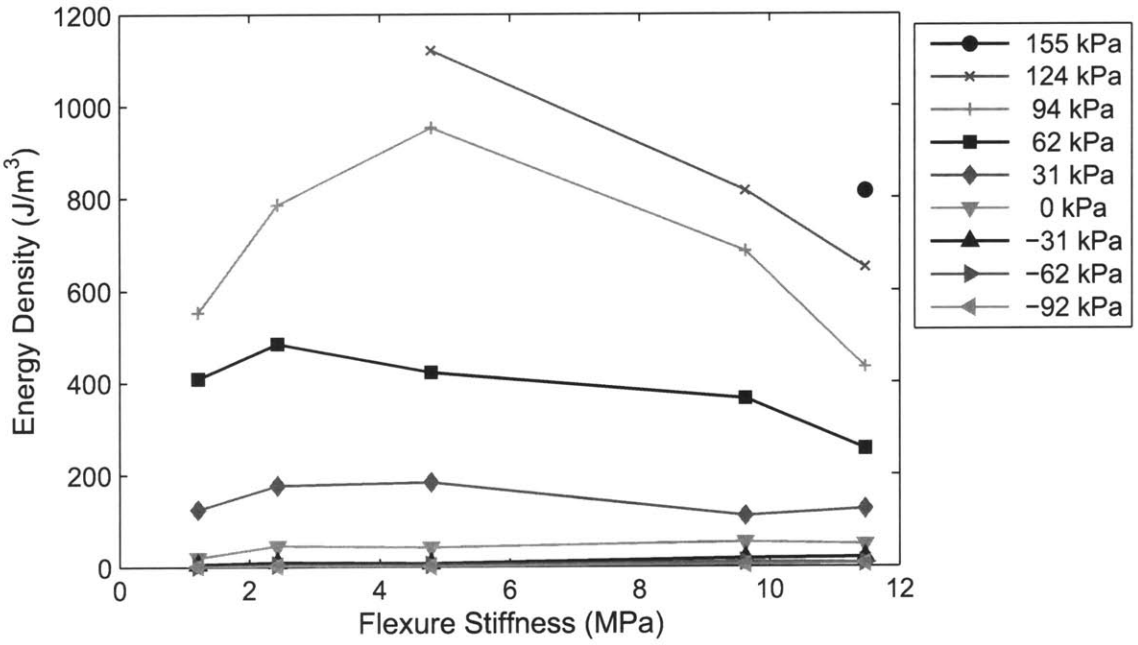

Figure 4-11: Total compressional energy output versus flexure stiffness for bidirectional actuation against flexures B0 through B4. The legend indicates the initial actuator prestress being actuated against. Results collected from Figures 3-21 through 3-25.

actuator was affected by the load stiffness. Whether this affect was caused by a system resonance which changes with flexure stiffness, or a by the response of the actuator to the load alone is unknown. In piezoelectric stacks a similar peak in energy density is observed with a load stiffness of about 14 GPa [22]. Since the acoustic pulse actuator has a lower energy density and higher strain output than a piezoelectric stack, we would expect the optimal load stiffness to be much lower than 14 GPa.

4.2 Acoustic Pulses and Twin Boundaries

The previous section showed that input pulse magnitude and pulse shape are critical to inducing twin boundary motion. A better understanding of the interaction between twin boundaries and acoustic pulses could lead to the design of a more effective pulse shape. This section examines pulse measurements made during actuation, from Section 3.5, and presents some theories that may prove helpful in understanding acoustic pulse induced twin boundary motion in FSMAs.

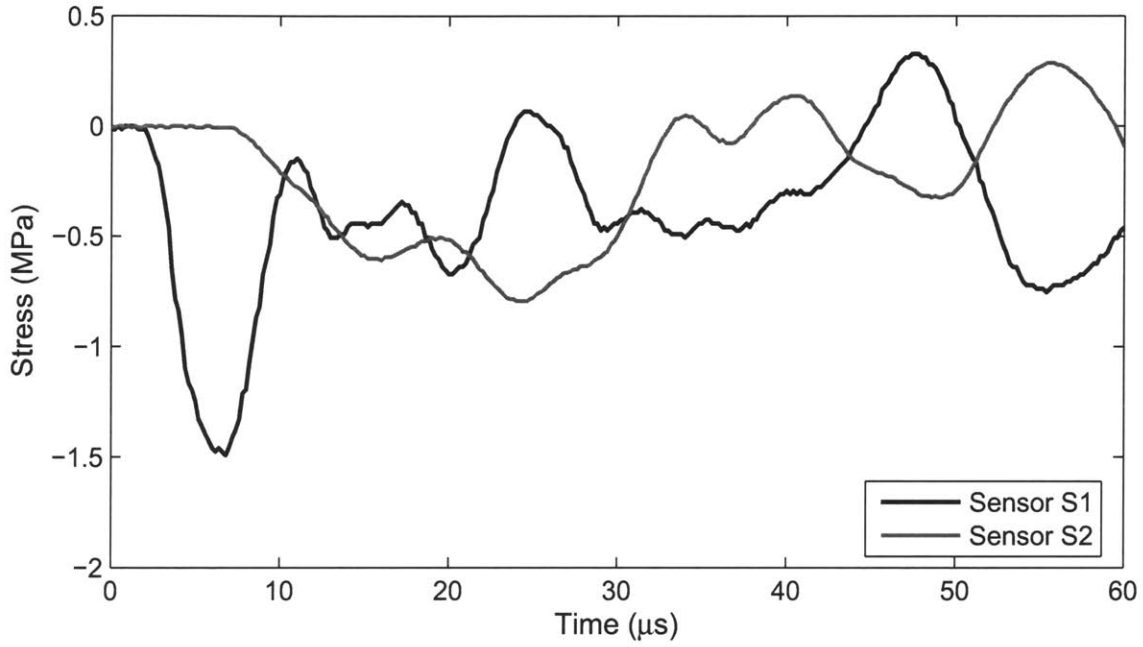

Figure 4-12: A compressive stress pulse measured in S1 and S2, at $t = 20$ s in the actuation cycle shown in Figure 3-27. S1 is located between the FSMA and moonie clamp. S2 is located between the FSMA and the reflector. The input parameters are V_{in}= 20 V, V_{g}= 12 V, f_{r}= 50 Hz.

4.2.1 Pulse Shape Observations

The stress pulse measurements shown in Section 3.5 reveal some interesting trends, but also have features that are difficult to explain. Because only two sensors are used to measure the stress pulse, only a partial description of the actuation stress pulse can be reconstructed.

Examination of the stress pulse will begin with an example pulse, see Figure 4-12, and a schematic showing the system that the pulse is traveling through, see Figure 4-13. The time $t_0 = 0$ s, marks the rise of the triggering pulse that initiates pulse generation. Approximately 2 μs after t_0 the piezoelectrically generated stress pulse reaches sensor S1. The stress peaks at approximately 6 μs, the stresses leading up to and including this peak will be refereed to as the initial stress pulse at S1. At this time it is unlikely that reflections are affecting the measurement at S1. However, approximately 2 μs after the peak, high stress tensile pulse curves show a small dip (see Figure 3-28), which is probably a reflection from one of the end of the piezoelectric stack, or from the bond lines around the sensors and FSMA.

At the same time the stress at S1 peaks, the first measurable portion of the stress pulse reaches S2. The measured pulse at S2 looks quite different from the pulse at S1. It takes

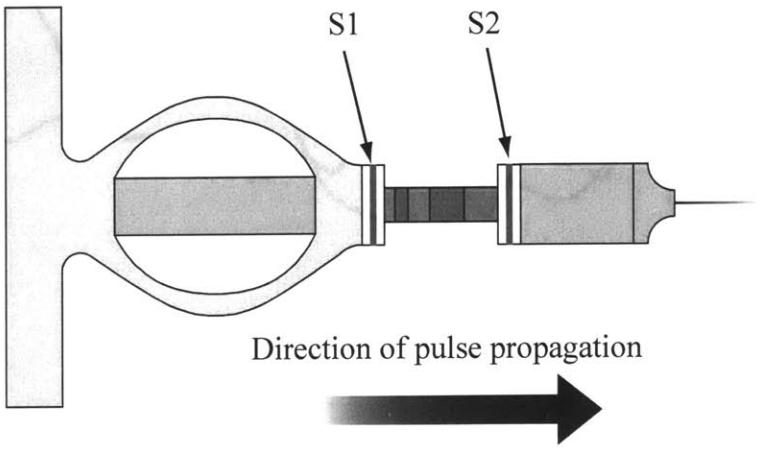

Figure 4-13: Schematic of the actuator and stress sensors in apparatus C3.

about 9 μs to go from stress onset to stress peak at S2, as opposed to 4 μs at S1. The stress magnitude has also changed from S1 to S2, more dramatically for large initial stresses at S1. The magnitude of the initial stress peak at S2 remains small, never exceeding 1 MPa, no matter what the magnitude of the initial stress peak at S1. Following the initial stress peak at S2, there is a second larger stress peak that occurs somewhere in a range of times between 23 μs and 30 μs, depending input pulse (see Figure 3-28). The magnitude of this secondary stress pulse at S2 is related to the magnitude of the input pulse, but is only a fraction of the magnitude of the initial stress pulse at S1.

The speed of the fastest portion of the pulse traveling through the crystal is approximately 2400 m/s, based on the onset time of the initial stress pulse at each sensor. If we measure the speed of the group velocity of the pulse, using the peaks of the initial stress pulse at each sensor, we find it is closer to 1300 m/s. These measurements change little with pulse amplitude or the strain of the FSMA crystal. Estimating material stiffness from these two numbers results in 45 GPa for the high speed, and 14 GPa for the low speed.

Figure 4-14 shows two stress measurements at S1 and S2 aligned by their initial stress peaks. This alignment also seems to align other pulse features further along in time. However, beyond the initial stress peaks at S1 and S2 reflections complicate the pulse measurements making analysis more difficult.

The secondary stress peak measured at S2 will be examined further, because it is possible

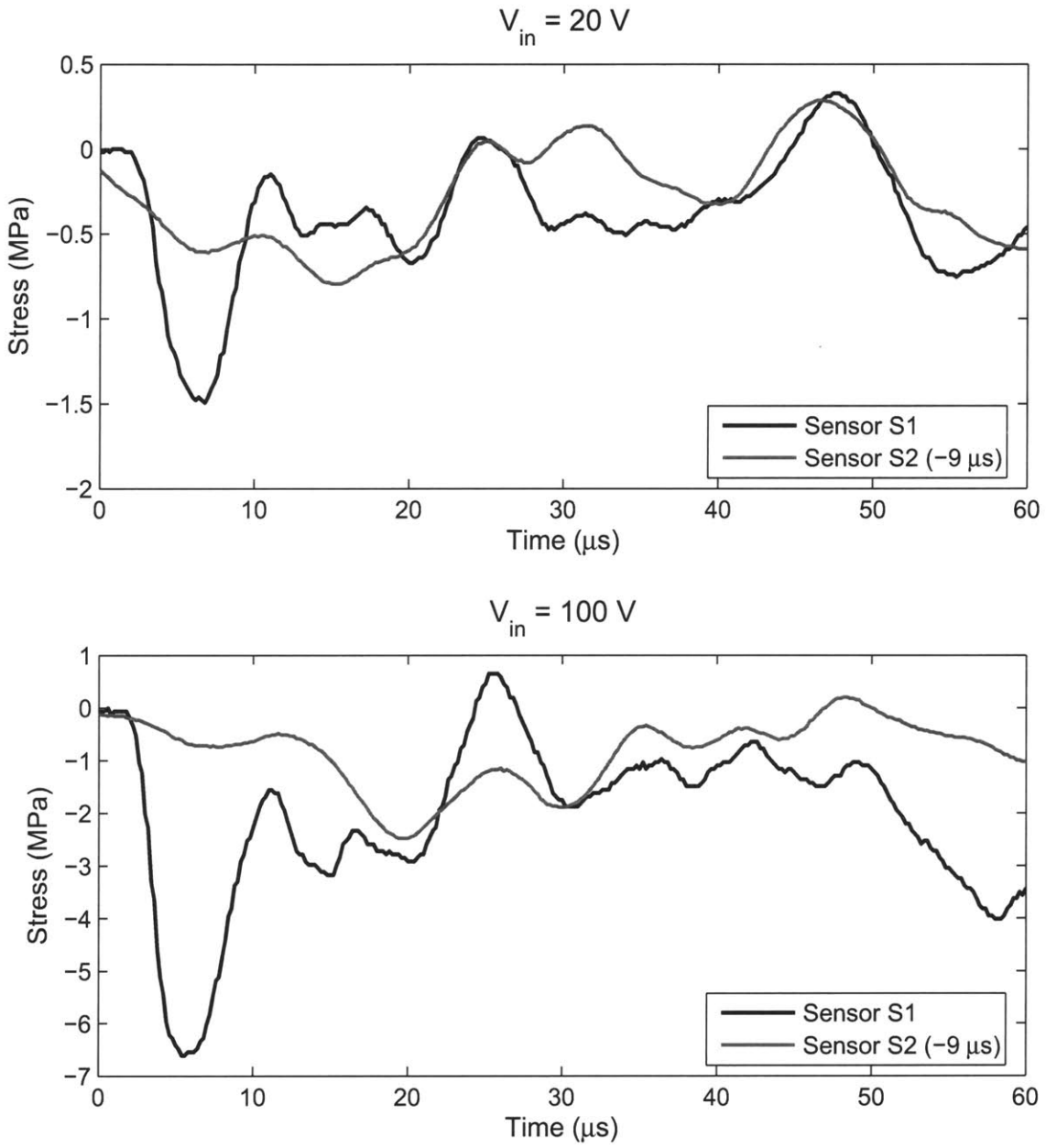

Figure 4-14: Compressive stress pulses measured in S1 and S2, at $t = 20$ s in the actuation cycle shown in Figure 3-27. Two different input voltages are shown (V_{in}= 20 V and 100 V). The measurement from S2 is offset horizontally by 9 μs to align initial peaks at each sensor. The wave group velocity measured here is 1300 m/s. S1 is located between the FSMA and moonie clamp. S2 is located between the FSMA and reflector. The other input parameters are V_{g}= 12 V, f_{r}= 50 Hz.

that it represents a portion of the initial stress peak at S1. The only stresses that could be affecting S2 at the time of the secondary peak are stresses being transmitted through the crystal, and reflections of stresses that have already passed through S2. The stress waves that have passed through S2 will only encounter boundaries result in an inverted reflection, i.e., any reflected stress waves would subtract from the secondary stress peak measurement, not add to it. As for waves propagating through the crystal, examining the low amplitude pulse in Figure 4-14 reveals that the only wave with enough time to reach the far end of the crystal and sufficient magnitude to generate the secondary peak at S2 is the initial stress peak at S1.

4.2.2 Plastic Waves

The behavior of the stress pulses examined appears similar to a plastic wave generated in a homogenous anisotropic material. Figure 4-15 shows an illustration of a plastic wave propagating in an ideal plastic material. Similar to what is shown in the pulse measurements, a portion of the wave, with stress lower than σ_0, travels quickly though the material. The high stress portion of the wave travels more slowly, specifically at the speed of the plastic wave given by

$$c_{\mathrm{P}} = \sqrt{\frac{S}{\rho}} \tag{4.2}$$

where S is the idealized plastic stiffness (see Figure 4-15(a)), and ρ is the density of the material. However, plastic deformation does not occurs uniformly in an FSMA crystal, as it does in a homogeneous material. The twin boundaries define the places in the crystal were plastic deformation can begin, and the direction in which the plastic wave can travel.

If the FSMA crystal behaved like a homogeneous plastic material, no stress larger than the threshold stress could travel through the crystal without causing some deformation at every point in the crystal. The spatially discretized plasticity of the FSMA crystal may allow large stresses to be transmitted without deformation throughout the crystal, which could account for the large magnitude of the secondary stress pulse at S2.

4.2.3 Stress Wave Dispersion

Whether the secondary stress pulse at S2 is part of the initial stress pulse at S1, or not, its magnitude should be related to the magnitude of the initial stress pulse at S1, because the

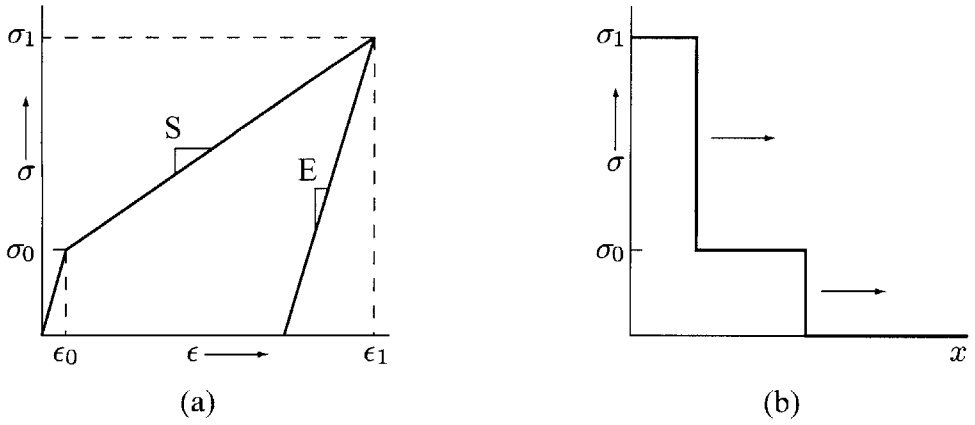

Figure 4-15: (a) Idealized stress strain relationship for a material. (b) Idealized elastic and plastic waves moving through a rod of the material from (a). Both waves were initiated at the same time. However, the plastic wave travels more slowly than the elastic wave. From [24]

initial pulse is representative of the total energy that is put into the system. Figure 4-16 shows the ratio of the the magnitude of the secondary stress pulse at S2 to the magnitude of the initial stress pulse at S1. The figure shows a disparity between stress transmitted through the crystal by tensile pulses and compressive pulses. Tensile stress pulses are absorbed more readily than compressive pulses. This result is probably caused by the number of twin boundaries that can move to compress the crystal versus the number that can move to extend the crystal. If actuation had started with a fully extended crystal compressive pulses would probably have been absorbed more readily than tensile pulses. However, no more than 1% strain was achieved during these tests, which corresponds to only 17% of the crystal transforming to the extended variant.

A decrease in the magnitude of the secondary stress pulse at S2 also occurs as the crystal extends. Since the second extended variant has a slightly different stiffness than compressed variant, it is possible that it causes scattering of the stress wave. Scattering would occur only at the boundaries between the two variants, so transmission would decrease until the number of twin boundaries stopped increasing, which occurs at some point before 50% transformation is achieved. Another possibility is that the stiffness of the twin boundary itself causes the increased scattering. This possibility seems unlikely due to the small thickness of the twin boundaries, but it must be remembered that twin boundaries are

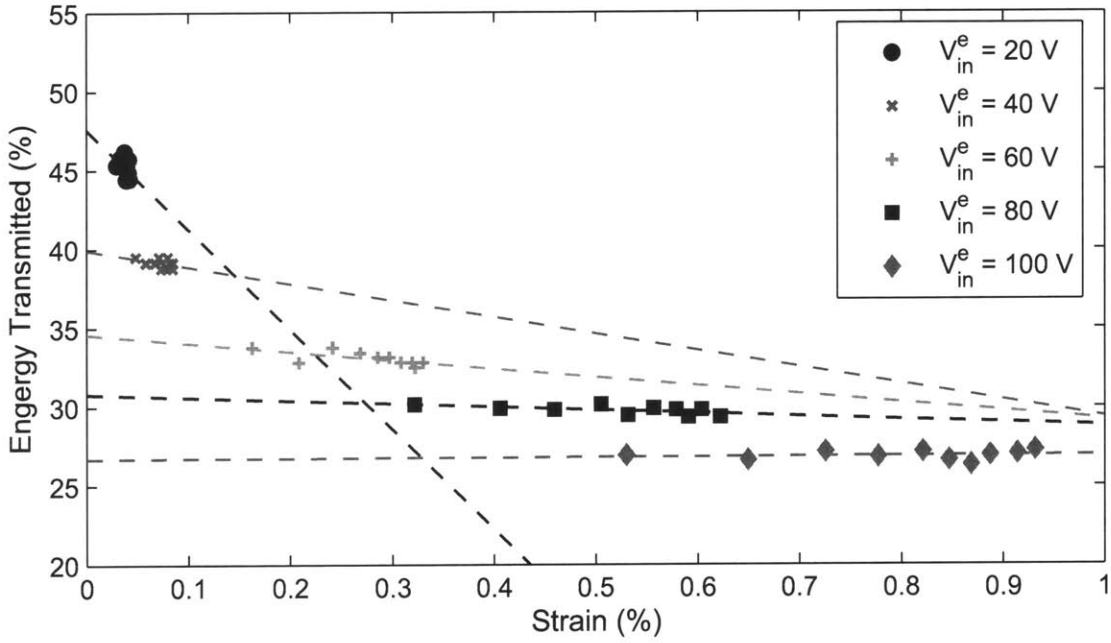

(a) Tensile Pulses

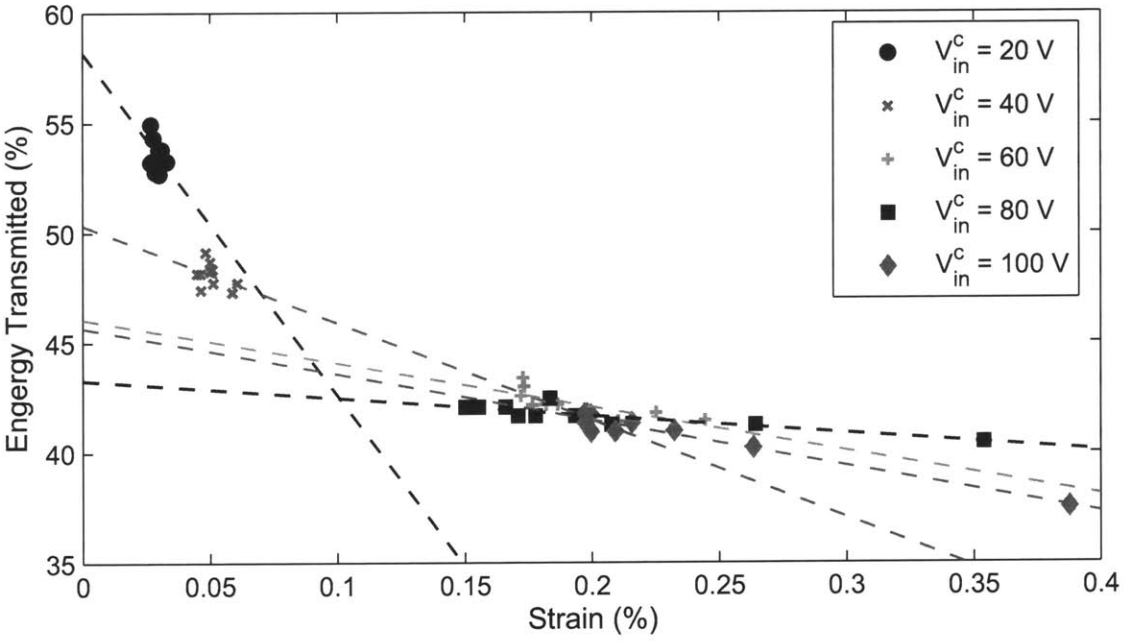

(b) Compressive Pulses

Figure 4-16: Ratio of the magnitude of the secondary stress pulse at S2 to the magnitude of the initial stress pulse at S1, versus the actuation strain measured immediately after the stress pulse measured. Stress pulses were recorded once per second. Each dotted line is a linear regression of the data at one input voltage. The legends indicate the input voltage (V_{in}), other input parameters are V_{g}= 12 V, f_{r}= 50 Hz.

mobile under the stresses of these pulses.

4.2.4 Twin Boundary Velocity

In previous work, the maximum velocity for the tip of a transforming crystal was theorized and measured to be about 6 m/s [2] for magnetic actuation. This limit is caused by the balance between the anisotropy energy of the FSMA crystal and the kinetic energy imparted on the crystal as it transforms. The maximum tip velocity induced by a stress could exceed the maximum magnetically induced velocity, since the energy from an external stress is not limited by the anisotropy energy. The twin boundary velocity can be estimated from tip velocity by

$$c_{\mathrm{tb}} = \frac{v_{\mathrm{tip}}}{n\,\epsilon_0} \ , \tag{4.3}$$

where v_{tip} velocity of the tip of the crystal, n is the number of mobile twin boundaries, and ϵ_0 is the twinning strain. Based on Marioni's work [2], an estimate of the twin boundary velocities during magnetic actuation is approximately 10 m/s.

The maximum stresses measured during acoustic pulse actuation are on the order of 8 MPa, which is roughly three times the maximum effective stress that can be generated by the anisotropy energy of the crystal during magnetic actuation. Without a model of the effect of stress on twin boundary velocity, we will assume that twin boundary velocity is roughly proportional to external stress, and get a very rough estimate of 30 m/s for twin boundary velocity during a large acoustic pulse. The assumption that twin boundary motion is proportional to stress is based on two assumptions with some basis in literature: first, that the maximum velocity of a twin boundary is governed by the velocity of the partial dislocations which move to sweep out each new twin plane [25], and second, that the velocity of dislocations is proportional to some power of the external stress, with an absolute limit of the speed of a transverse shear wave in the material [26].

Using these twin boundary velocity estimate as the plastic wave velocity at the twin boundaries requires that 5% of the FMSA crystal behave plastically to account for the 8 μs delay of the secondary stress pulse at S2. It seems unlikely that the twin boundaries would temporarily move over 5% of the crystal in the presence of a large stress, and only leave at most 1% of the crystal transformed after the stress subsides.

4.2.5 Extension Induced by Compressive Pulses

An interesting phenomenon that could help understand the pulse behavior, but was never captured quantitatively, is extensional actuation caused by the reflections of compressive pulses. This phenomenon occurs in a a fully compressed crystal without a tensile actuator prestress. The actual strain produced is very small and difficult to measure, but the change in the transmitted stress wave is dramatic. A mechanically compressed crystal will transmit a compressive pulse without the dissipation and scattering of the secondary stress peak at S2 discussed above. After only few compressive pulses the pulse measured at S2 quickly divides into an initial and secondary stress pulse. It seems that since the compressive pulse is not dispersed within the crystal, the inverted reflections that result from the larger stress wave reaching the end of the reflector are large enough to extend the crystal. Eventually, a steady-state position is reached where each compressive pulse does some work, is partially dispersed, and the tensile reflections undo the compressional work so that the crystal remains in a nearly compressed position.

4.3 Nonuniform Twin Movement

Twin boundary motion in an FSMA crystal can be impeded by a variety of obstacles or pinning sites [13], similar to pinning sites that prevent typical dislocation movement. The stress required to move the twin boundary past any one of the obstacles is the pinning stress. The spatial distribution of obstacles and their pinning stresses in a crystal governs the stiffness of an actuating crystal. Figure 4-17 shows crystal X1 under five different static tensile loads. The most mobile twin boundaries move with under 500 kPa of stress while the ones pinned by the highest stresses require 1 MPa. A non-random distribution of pinning sites, combined with limited number of mobile twin boundaries in the crystals studied, is the likely cause of the somewhat erratic actuation of the crystal. This erratic behavior can be seen when actuating against low stiffness loads in Section 3.4, i.e., when actuating over large strains.

The erratic behavior of twin boundary motion can also be seen in an acoustically assisted twin boundary motion experiment. Acoustic vibrations can be added to a static stress to increase the maximum stress seen by the twin boundaries, and in effect loosen them. This twin loosening behavior can be seen easily by applying a constant compressive stress to an

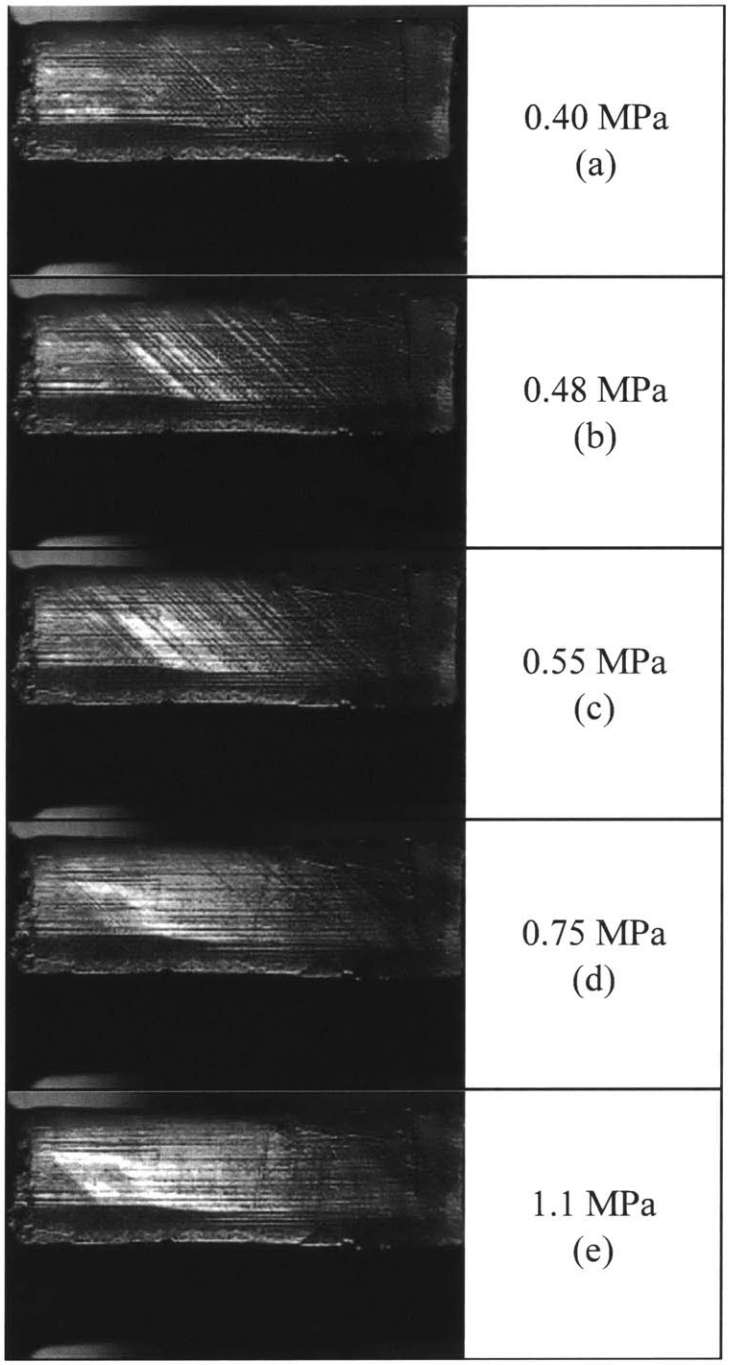

Figure 4-17: Photographs of twin variants in crystal X1. (a) The threshold stress has been reached and the twin boundaries have moved slightly. (b) and (c) Twin boundaries begin to sweep across larger portions of the crystal. The external stress is large enough to overcome most pinning obstacles. (d) High stress obstacles prevent twin boundaries from sweeping out small portions of the crystal. (e) The crystal is fully extended. Only the ends, which are held by adhesive to the rest of the apparatus, remain in the original variant.

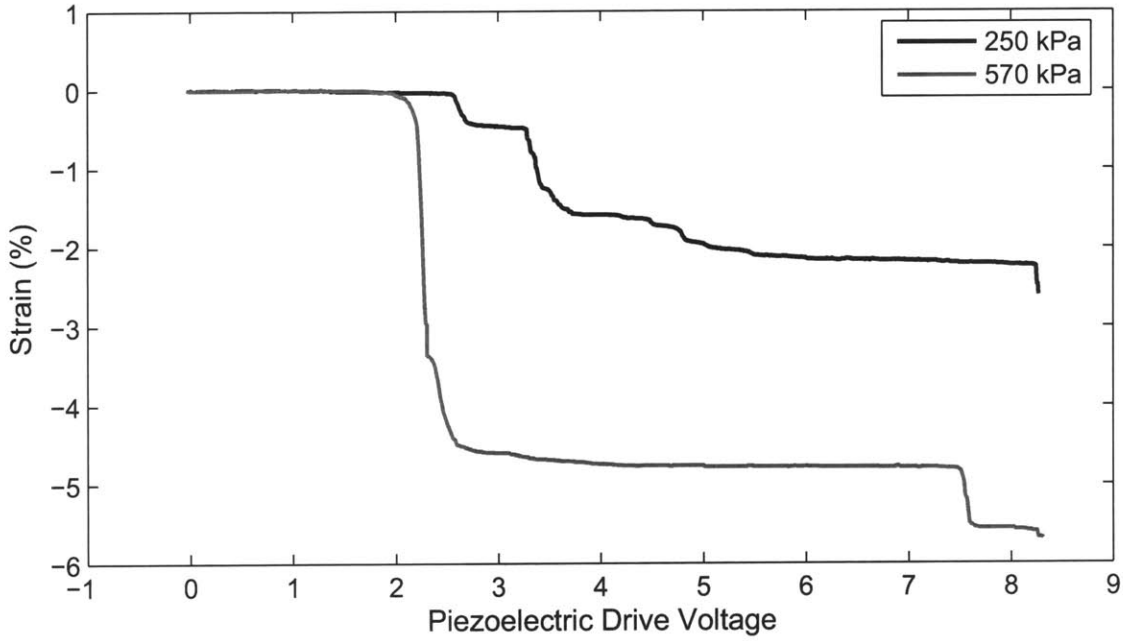

Figure 4-18: Example of nonuniform mechanical actuation. The extended crystal, X0, was put under a small stress, then 40 kHz sinusoidal vibrations from a piezoelectric stack were introduced and their amplitude was slowly increased. The vibrations helped the static stress overcome twinning obstacles. The legend indicate the initial mechanical stress applied.

extended FSMA crystal and adding oscillatory acoustic vibrations of increasing magnitude using a piezoelectric stack. The FSMA remains unchanged, until at a certain level of vibration the pinning site with the lowest stress is overcome, and a twin boundary moves until it reaches the next higher stress pinning site. Figure 4-18 shows the results from this experiment performed on crystal X0.

One effect that reduces the erratic behavior of the FSMA over time is an increase in the number of twin boundaries that form during actuation. Immediately after heat treatment crystals typically have on the order of 10 twin boundaries that account for almost all twin movement, as observed by Marioni [13]. Once the crystal has been acoustically actuated several times, new twins are visible during actuation. Eventually the number of twin boundaries appears to increase by a factor of 5 to 10, as can be seen in Figure 4-17. These additional twin boundaries also seem to reduce the threshold stress of the of the crystal. For instance, X1's initial threshold stress was measured at nearly 1 MPa, and after many acoustic actuation cycles the threshold was measured at 0.4 MPa.

Chapter 5

Conclusions

This chapter summarizes some of the major accomplishments and findings of this thesis. Discussion of the experimental actuator's capabilities is followed by a comparison with other active material technologies, and a discussion of the theoretical limitations of acoustic pulse actuation. Finally, promising directions for future work and possible applications are discussed.

5.1 Summary of Major Results

Free actuation. Actuation without a load was tested to determine the effect of the input parameters (V_{in}, V_{g}, and f_{r}) on total strain and strain rate. In apparatus C1, these parameters were set to their maximum in order to obtain bi-directional actuation curves with 1% strain, achieved in 1 s (see Figure 3-5). These actuation curves represent some of the most effective acoustic pulse actuation observed. Actuation past 1% strain continues to slow as the crystal begins to approach saturation. The saturation strain in actuator C1 is ~2.5%, due crystal X0's shape and the resulting short active length. To achieve strains near saturation, actuation durations of several seconds were required. The actual time taken to reach saturation varied randomly from run to run.

Actuation against a load. An actuator's ability to do work against a load is one is its critical characteristics, so the ability of an acoustic pulse actuator to work against a spring load was quantified. Actuation against a spring load was achieved more slowly than actuation with a free load. The slow actuation is partially due to the difference in size and twinning properties of the crystal used, and probably partially due to the more complex

apparatus, C2. The maximum output energy density of the actuator in C2 was 1100 J/m^3, which was achieved with a 150 kPa tensile prestress and flexure B2. This energy density represents approximately 1% of the theoretical energy density of a magnetically actuated FSMA crystal. The effective energy density of magnetic actuators is also limited to about 1% of the theoretical energy density of the crystal, due to magnet size constraints. The average power output during the 60 second compressional portion of the actuation cycle was 2 μW. However, higher power outputs could be achieved by reducing the cycle period and sacrificing some of the output strain.

Theoretical limitations. We have presented the current capabilities of experimental acoustic pulse actuation, but it is also important to understand the theoretical limits of acoustic pulse actuation. The real limits of acoustic pulse actuation are determined by the actuating material used and the acoustic pulses that can be generated. The most obvious limitations come from the actuating material. The maximum actuator strain and static holding force can be determined directly from twinning strain and twinning threshold stress of the actuating material. The maximum actuating stress should also be related to the twinning threshold stress. However, acoustic pulses act in two ways in the material, both to induce twining, and to allow twinning to occur more readily in the presence of an external stress, so the maximum actuating stress will likely be less than the threshold twinning stress. In theory, an ideal acoustic pulse with an amplitude of twice the threshold stress would be able to induce twin boundary motion in the presence of a static stress that has nearly the magnitude of the threshold stress. However, even with significant design effort, such a pulse would be nearly impossible to realize, although significant improvements over the current actuator should be possible.

Active material comparison. Given the maturity of acoustic pulse actuation, comparison with conventional active material actuator technologies is a bit premature. However, such comparisons are useful in determining what direction study of acoustic pulse FSMA actuation should take. Table 5.1 shows the actuation properties of several active material technologies. It is apparent that acoustic pulse FSMA actuation is not going to be a competitive active material actuator technology in the conventional sense. However, its unique ability to hold a position no power input, high output strain, and lack of moving parts, are properties that may make it a useful solution to specific engineering problems.

Table 5.1: Actuation characteristics of several active materials. The data represent material material capabilities not actuator capabilities, except in the case of voice coils and acoustically actuated FSMAs.

Actuator Type	Maximum Strain (%)	Maximum Pressure (MPa)	Elastic Energy Density (J/cm^3)	Maximum Efficiency (%)	Specific Density	Relative Speed (full cycle)
Electroactive Polymer Silicone (CF19-2186)[a]	63	3.0	0.75	90	1	Medium
Electrostatic Devices (Integrated Force Array)[a]	50	0.03	0.0015	>90	1	Fast
Electromagnetic (Voice Coil)[a]	50	0.10	0.003	>90	8	Fast
Piezoelectric Ceramic (PZT)[a]	0.2	110	0.10	>90	7.7	Fast
Shape Memory Alloy (TiNi)[a]	>5	>200	>100	<10	6.5	Slow
Electrochemo-mechanical Conducting Polymer (Polyaniline)[a]	10	450	23	<1	1	Slow
Magnetostrictive (Terfenol-D)[a]	0.2	70	0.0027	60	9	Fast
Natural Muscle (Human Skeletal)[a]	>40	0.35	0.07	>35	1	Medium
FSMA (magnetic)[b]	6	2	0.10	<10	7.8	Medium (1 kHz)
FSMA (acoustic pulse)	6	0.2	0.001	<1	7.8	Slow (1 Hz)

[a]Data from [17]
[b]Data from [27]

5.2 Future Work

Being a relatively new concept to study, there are many areas of acoustic pulse SMA actuation that could be explored in depth. This section discusses a few of the areas that might be important to developing useful acoustic pulse actuators.

Polymer bond-lines. The polymer bond-lines are literally the weak point of the actuators discussed in this work. Although bonds strong enough to withstand the rigors of continuous actuation were created using acrylics, the acoustic properties of the bonds are still in doubt. Developing a technique for joining an FSMA crystal to another metal using welding or diffusion bonding may be difficult, but would greatly improve bond strength and acoustic transmission. The difficulty in using metal-metal bonding techniques, would be in maintaining crystal composition and homogeneity. If an excessively long actuating crystal were used, only a small region would be rendered inactive by heating and diffusion, while the majority of the crystal remained unchanged.

Other SMA materials. Acoustic pulse actuators using other SMA materials might show great improvement over acoustic pulse actuators using Ni–Mn–Ga. Ni–Mn–Ga is quite brittle and has an extremely low twinning stress. The twinning stress of other SMAs is typically nearer 100 MPa, although alloys with a wide range of twinning stresses exist. For instance, even Ni–Mn–Ga has a 2 to 4 MPa twinning stress when it is in an orthorhombic phase, which occurs at compositions only a few percent from that of the crystals used for this work. An increased twinning stress, should allow greater output forces. However, generating and dissipating larger stress waves in order to utilize these materials may prove difficult or impossible.

Finite element modeling. Work is currently being conducted on finite element modeling of high intensity wave motion in FSMA crystals. This work should allow a better understanding of twin boundary motion in general and specifically that induced by acoustic waves. A model that accurately simulates acoustically induced twin boundary motion would allow the development of waves that more effectively produce twin boundary movement, as well as the development of entire actuators the efficiently handle pulse reflections and reverberations.

Transverse actuation. Using transverse shear waves to induce twin boundary motion should be at least as effective as acoustic actuation using a longitudinal waves, and perhaps

more effective. Using shear waves and a crystal cut at 45° to the crystals used in this work, one could create an actuator capable of transverse motion without any longitudinal motion, avoiding the problem of off-axis actuator movement seen in longitudinal actuators.

Hybrid magneto-acoustic actuation. The use of magnetic FSMA crystals, provides the possibility of a magneto-acoustic hybrid actuator concept. For instance, the tensile prestress that has proved advantageous in these experiments, could be provided by the field from a permanent magnet. This would provide a prestress with nearly zero stiffness, and could likely be made more compact than a mechanical prestressing device.

Applications. Acoustic pulse actuation of Ni–Mn–Ga represents a novel use of reversible plasticity to create an inch-worm type actuator. The current generation of actuator is capable of large strains (over 5%) against stresses reaching up to 100 kPa. If the challenges of erratic behavior and weak bonds can be overcome, acoustic pulse actuators may become useful as micropositioners, due to their high strains, lack of moving parts, and ability to hold a position while using no power. If the problems of low pulse efficiency, slow actuation rate and low output stress can be overcome through a better understanding of the wave mechanics during actuation, an energetically competitive active material actuator could be developed.

Appendix A

Electromagnet Design for FSMA Actuators

In order to understand the capabilities and limitations of magnetic FSMA actuation, this appendix investigates the design of electromagnets for continuous actuation of Ni–Mn–Ga single crystals. The design of the electromagnets used for FSMA actuation is important because the electromagnet represents a significant, if not dominant, volume of any FSMA actuator.

The most ubiquitous active materials today are piezoelectric ceramics. In many ways FSMAs are similar to piezoelectric material, in that they provide a strain when an actuating field is applied. Although their strain and stress outputs are quite different, their material energy densities are similar-about 100 kJ/m^3. In a piezoelectric actuator, mechanical amplification of the small displacements of the active material are usually required, which diminishes the effective energy density. FSMA actuators provide relatively large displacements directly. However, actuating with a magnetic field poses a much greater design challenge than actuating with an electric field.

Comparison of electrical and magnetic fields in general reveals some of the differences between the actuation of these two materials. Since there is such a large difference between the electrical conductivity of air and good conductors, an electric field can be generated far from its point of application, and carried via conductive wires. A magnetic field can be transported similarly through an iron or other soft magnetic core. However, this transfer is not as effective over long distances for several reasons. The difference in permeability

Table A.1: Dimensions of the example crystal used to provide numerical results in this design study.

Dimension	Inches
l (Actuation Direction)	0.625
w	0.3125
t	0.1

between iron and air is not great enough to prevent the flux lines from escaping over long distances, and there is a saturation magnetization in iron that limits the minimum cross-section of the core. In an efficient magnet, the field must be generated as close as possible to the point were it is expected to do useful work. Thus, wherever an FSMA actuator will be used, it must be accompanied by an electromagnet. This reduces the effective energy density of the material by a large factor.

In order to determine the potential energy density of an entire FSMA actuator, two prototypical electro-magnet designs are examined in this appendix. The size of the magnets is determined using the magnetic field required to actuate a Ni-Mn-Ga crystal. Example dimensions are given in Table A.1. These dimensions will be used to give the reader a feeling for the design when the symbolic equations become complex. The symbolic equations are simplified as far as possible to determine how changes in the magnets dimensions affected performance and overall size, although closed form solutions are seldom found.

The two magnet designs being studied are shown in Figure A-1. Each has a copper coil, partially surrounding a core built from transformer grade silicon steel. Two permanent magnets are attached to the poles of the steel core on either side of the gap in which the Ni–Mn–Ga crystal would normal reside during actuation. Figure A-1(a) shows an H-frame magnet. Its sharp corners cause some magnetic losses, but its straight line, symmetric geometry may allow it to be easily incorporated into an existing application. Figure A-1(b) shows a C-frame magnet. Its shape minimizes magnetic losses, but it may be awkward to install in existing machine designs.

The magnetic field required to actuate a Ni–Mn–Ga crystal to strain saturation can be as low as 3 kOe, without a load to actuate against. The maximum useful field for actuation is determined by the anisotropy energy of the crystal, and is typically near 7.5 kOe [10]. The required field strength of the electromagnets discussed in this appendix will be 7.0 kOe,

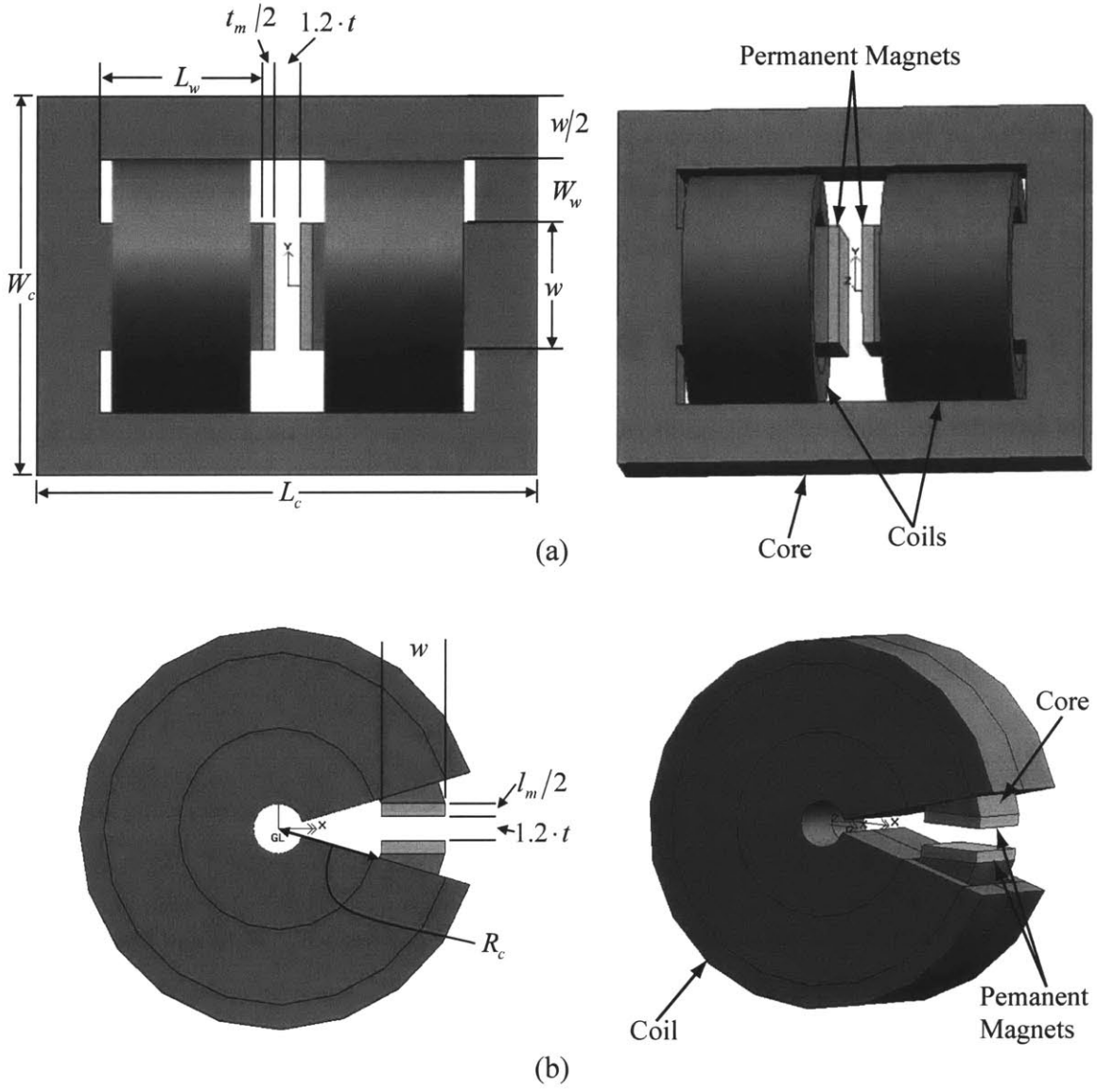

Figure A-1: Comparison of the geometry of the magnet designs examined in this appendix. Actuation directions is out of the page relative to the left-hand view. (a) H-Frame design. (b) C-Frame design.

unless otherwise stated.

The permanent magnets shown in Figure A-1 are used to supplement the field provided by an electromagnet, which reduces the required DC power input to the electromagnet. The two permanent magnets, with the same length and width as the crystal, are placed on either side of the crystal to limit fringing and leakage of the magnetic field. Accurate calculation of the required thickness of permanent magnet can be difficult, and may require simulation or prototype build-up and testing to ensure the desired field is realized. The choice of permanent magnet type is not difficult, as NdFeB magnets are readily available and are one of the strongest known types of permanent magnet.

A.1 Permanent Magnet Design

The formulas for calculating the required thickness of NdFeB or the resultant magnetic field strength can be extracted from existing literature and give

$$t_m = \frac{K_2 t_g}{H_c \mu_0 \left(\frac{1}{B_g} - \frac{K_1}{B_r}\right)} \text{ [28]}, \tag{A.1}$$

or

$$\mu_0 H_g = B_g = \frac{B_r}{\frac{K_2 t_g}{t_m} + K_1} \ , \tag{A.2}$$

where

$$t_g = 1.2t \ , \tag{A.3}$$

and t_m is the thickness of permanent magnet required to generate B_g, B_g is the flux density in the gap between the magnets which is directly related to H_g, the field strength in the gap, $K1$ and $K2$ are constants which will be discussed, H_c is the coercive field of the permanent magnets, B_r is the remnant magnetization of the permanent magnet, and μ_0 is the magnetic permeability of air. Equation (A.1) assumes that the permanent magnets are operating in a linear portion of their $B - H$ demagnetization curve. In the case of very hard magnetic materials, this portion of the curve can be approximated by a line from B_r at zero field to zero internal flux at $-H_c$. B_r and H_c are available from magnetic material data sheets; for NdFeB in general, they are around 12 kG and 12 kOe [29], respectively. Equation 2 uses the assumption that $H_c \mu_0 = B_r$ in order to show a simplified relationship between magnet

thickness, gap thickness and field in the gap. The assumption appears to be true for generic NdFeB magnets, since $\mu_0 = 1$ when working in Oe and G. Equation (A.3) indicates that the desired air gap is 20% thicker than the crystal. This gap insures that there is no physical interference between the crystal and the magnets surface. K_1 and K_2 are factors that depend on the permanent magnet and electromagnet core geometry. K_2 is usually between 1.05 and 1.45, and depends on losses in the steel core due to finite permeability and sharp corners [30]. K_1 is usually much larger than K_2, and can reach values as high as 20 in magnets with large gaps. The formulas used to estimate K_1 in the H-frame and C-frame are identical, because the permanent magnets are in similar positions. In reality, there is a small difference due to the asymmetry of the C-frame, but this was not accounted for in the literature and is ignored here. K_1 is given by

$$K_1 = 1 + \frac{t_g}{A_g}\left[0.78\,(l+w) + 0.077\,(4t_g + t_m)\right] \quad , \tag{A.4}$$

where A_g is the cross-sectional area of the gap, or simply the product of l and w. This equation accounts for fringing of the magnetic field as it passes through the gap and for flux leakage around the permanent magnets and throughout the core. The images in Figure A-2 illustrate leakage and fringing in the H-frame magnet. Figure A-2(a) shows fringing in the gap when an electromagnet field is reinforcing the field of the permanent magnets. A small amount of leakage can be seen on the edges of the magnets. This leakage is magnified in Figure A-2(b), by generating an electromagnet field in the opposite direction of the permanent magnets' field.

It should be noted that K_1 depends on the magnet thickness, so Equation (A.1) is not quite explicit. However, the effect of t_m on K_1 is relatively small, so it should not be difficult to get a good estimate of t_m with a rough initial guess and only a few iterations.

The equations for the required permanent magnet thickness are mostly dependent on the geometry of the actuating crystal. Without fringing and leakage effects the permanent magnet thickness would be linearly dependent on the crystal thickness. The extra dependence on gap thickness that comes from K_1 is harder to determine empirically. What we can say about K_1 is that it becomes much more important as B_g approaches B_r, and that it is minimized with respect to l and w when their dimensions are equal, or in other words, when the crystal has a square cross-section.

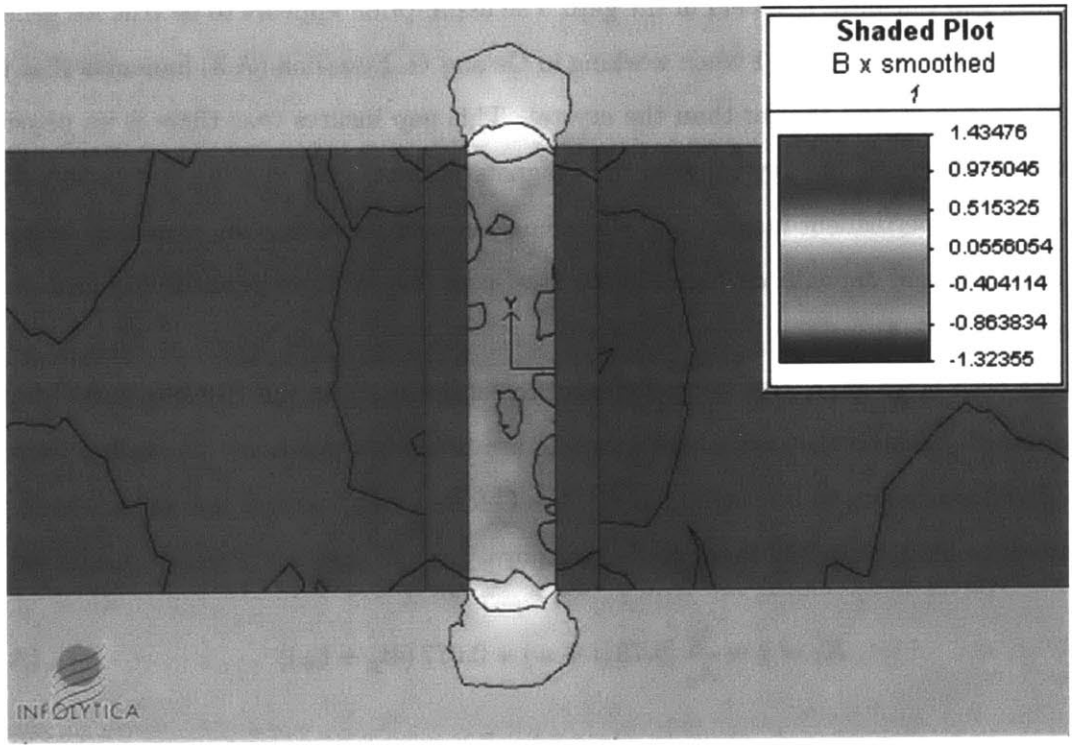

(a) $I = 10$ A

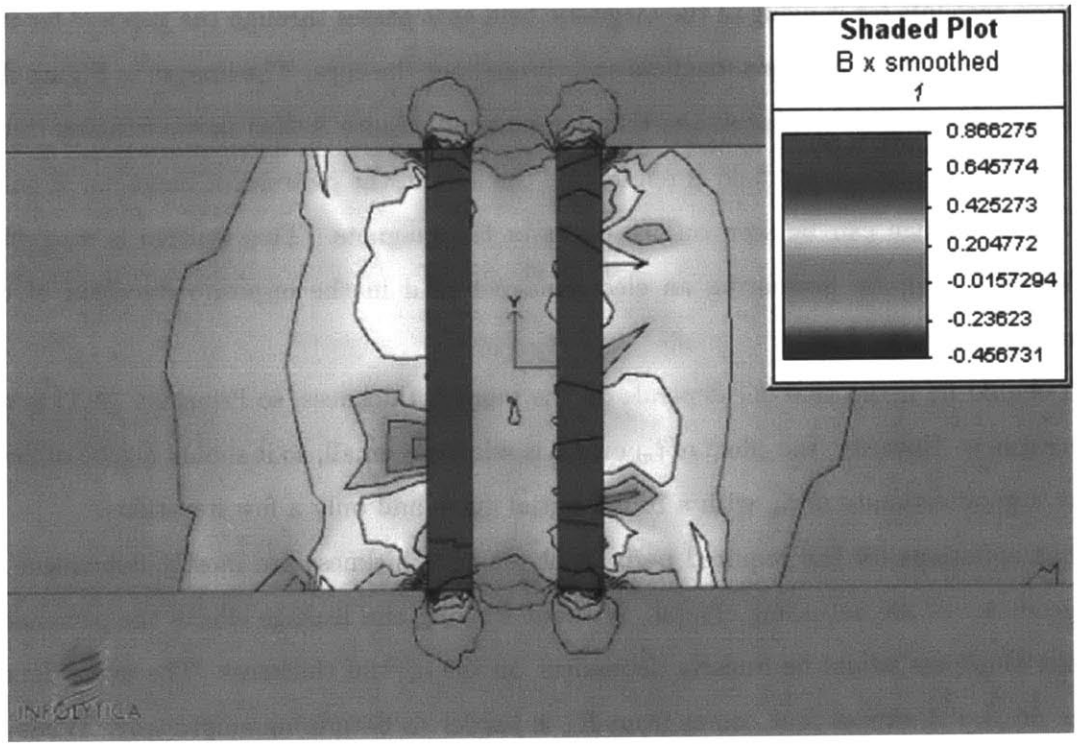

(b) $I = -10$ A

Figure A-2: Sample simulation results showing fringing and leakage field in the H-Frame electromagnet for two coil currents. Shading and contour lines indicate the magnitude of the x-component of the magnetic flux density, in Tesla.

For the example crystal, a t_m of 0.092 inches is estimated, along with a K_1 of approximately 1.50. Finite element simulation has been used to show that this will result in an average flux density in the gap of slightly more than the required 3.5 kOe. Of course the field is not uniform, and is below the required 3.5 kOe near the edges, but for the purposes of these design estimates, it is large enough. Non-uniformity and K_1 are closely related, so as long as we K_1 remains small the field uniformity should be suitable for actuation purposes. K_2 was set to 1 in the previous calculations.

A.2 Electromagnet Design

With the characteristics of the permanent magnet determined, we can move on to determining the size and shape of the electromagnet. The gap that the electromagnet sees is really

$$t_{ge} = t_g + t_m \ , \tag{A.5}$$

since the permanent magnets have permeability closer to air than iron for the field strengths we are working with. In order to estimate the size of the electromagnet, we are essentially interested in the amount of current we need to circulate to get the desired field. This current is usually referred to as the number of amp-turns (NI). However, we will assume only 1 turn of wire, except when it is truly necessary to deal with the number of wires in the coil. The maximum required current, switching to SI units, is given by

$$(NI)_{max} = \frac{K_{1e} K_{2e} B_{ge} t_{ge}}{\mu_0} \ , \tag{A.6}$$

where K_{1e} and K_{2e} are similar to K_1 and K_2, except applicable to the electromagnet, and B_{ge} is the electrically generated magnetic flux density in the electromagnet gap. There is no reason for K_{2e} to differ from K_2; however K_{1e} must be recalculated using a new equation and the new gap thickness, given by

$$K_{1e} = 1 + \frac{t_{ge}}{A_{coil}} \left(1.1 \left(P_{coil} \right) \frac{0.67a}{0.67a + t_{ge}} \right) \left(1 + \frac{t_{ge}}{a} \right) \ , \tag{A.7}$$

where

$$a = L_w \tag{A.8}$$

for the H-frame, and

$$\text{C-Frame: } a = \frac{\pi}{6}(2R_c + w - 2t_{ge}) \tag{A.9}$$

for the C-frame, L_w and R_c are magnet dimensions and can be found in Figure A-1. A_{coil} and P_{coil} are the area and perimeter of the electrical coil respectively, which are estimated for the two magnets in Sections A.2.1 and A.2.2. The equation for K_{1e} forces us to use successive iterations to zero in on desirable and accurate design parameters. However, these iterations are more involved than those for K_1, because they include electromagnet shape parameters, estimated in Sections A.2.1 and A.2.2.

With an estimate of $(NI)_{max}$ in hand, the required window area of the magnet can be estimated. This is the area required for enough copper wire to safely handle a continuous current $(NI)_{max}$. An estimate of the required cross-sectional area of wire per amp can be found in wire gage tables; it will be referred to here as A_I. This estimated area is essentially for pure copper, and does not account for things such as insulation thickness, and random packing of the wires. Estimating this packing factor for coil windings can be difficult, as it depends on winding method, wire shape, insulation thickness and wire gage. In medium gage wire (30-10 AWG) the effects of relative insulation thickness and packing tend to cancel each other out and result in a packing factors of 60-70%. The ideal packing factor for square wire is of course 100% and for circular wire it is 90.7%, without insulation. Carefully hand wound square wire can pack at up to 90%, while round wire usually doesn't pack over 80%. For this appendix, we will assume a packing factor of 70%, and the packing factor will be referred to as f_p. From these terms we can estimate the required window area as

$$A_w = (NI)_{max}\frac{A_I}{f_p} \ . \tag{A.10}$$

A.2.1 C-Frame Size Estimation

With an estimate of the area required by the electrical coil, we can come up with an estimate of the required dimensions of the C-Frame magnet. The gap in the core and coil is accounted for by removing a wedge from the window area of the coil, where the wedge is 20% larger than the gap itself. The total area taken up by the coil (A_w) and the wedge must be equal

to the area inside the core, so that

$$\pi R_c^2 - R_c \frac{1.2 t_{ge}}{2} - A_w = 0 \ , \tag{A.11}$$

which can be solved explicitly for R_c by using the positive result of the quadratic equation, giving

$$R_c = \frac{0.6 t_{ge} + \sqrt{0.36 t_{ge}^2 + 4\pi A_w}}{2\pi} \ . \tag{A.12}$$

Once R_c has been calculated, it can be plugged back into K_{1e} and be recalculated until the desired accuracy is obtained. Once this has been done, the total volume of the various parts of the magnet can be estimated, and in turn used to estimate the mass of the actuator. The volume of the core can be estimated using

$$V_c = 2\xi_c w l R_c + \pi w^2 l \ , \tag{A.13}$$

where

$$\xi_c = \pi - \frac{t_{ge}}{2R_c} \ . \tag{A.14}$$

The permanent magnet volume is easily calculated as

$$V_m = t_m \cdot w \cdot l \ . \tag{A.15}$$

The volume of the coil is a nontrivial calculation, and cannot be done with great accuracy. To allow easy calculation while still maintaining some accuracy, the coil cross section is broken up as shown in Figure A-3. The values of R_I and R_O from this cross section are calculated as

$$R_I = \frac{A_w}{\xi_E (2R_c + w)} \ , \tag{A.16}$$

and

$$R_O = \sqrt{\frac{A_w}{\xi_E} + (R_c + w)^2} - (R_c + w) \ , \tag{A.17}$$

where

$$\xi_E = \pi - \frac{1.2 t_{ge}}{2R_c} \ . \tag{A.18}$$

These values ensure that the coil window area at the top, bottom and outer edge of the

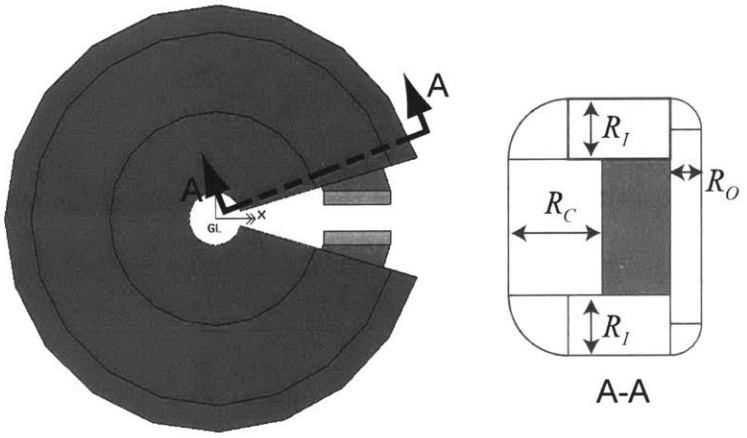

Figure A-3: The geometry used in estimating the volume and length of the C-Frame coil. The small shaded area represents the iron core and the coil fills the space bounded by the rounded rectangle with the indicated dimensions.

core is the same as the window area in the center. This approximation of the cross section should be larger than any manufactured coil shape, making this a somewhat conservative volume estimate. The total coil volume estimate is

$$\begin{aligned} V_E &= \xi_E \Big(R_c^2 l + \\ &+ \left((R_c + w)^2 - R_I^2 \right) R_I + \\ &+ \left((R_O + R_c + w)^2 - (R_c + w)^2 \right) (2R_I + w - 2R_O) + \\ &+ \xi_E \left(R_I^3 + (R_c + w) R_O^2 \right) \Big) \ . \end{aligned} \tag{A.19}$$

The coil perimeter and cross-sectional area are required to calculate K_{1e} and are estimated by

$$P_{coil} = \pi(R_i + R_o) + 2(l + w + R_c - R_o) \ , \tag{A.20}$$

and

$$A_{coil} = l(R_c + w) + R_o(2R_i - 2R_o + l) + \frac{\pi}{2}(R_c^2 + R_o^2) + 2R_i(R_o + R_c - w) \ . \tag{A.21}$$

A.2.2 H-Frame Size Estimation

The geometry and volume of the H-frame magnet can also be determined once A_w has been calculated. However, the designer has one dimension in this magnet that can be chosen independently. The basic dimensions of the H-frame, of which one can be chosen freely, are given by

$$L_w = \frac{L - l - t_g}{2} = \frac{\sqrt{A_w C_w}}{2} \ , \tag{A.22}$$

$$W_w = \frac{W - 2l}{2} = \sqrt{\frac{A_w}{2\,C_w}} \ , \tag{A.23}$$

$$C_R = \frac{L}{W} = \frac{2L_w + l + t_g}{2W_w + 2l} \ , \tag{A.24}$$

$$C_w = \frac{L_w}{W_w} = \frac{L - l - t_g}{W - 2l} \ , \tag{A.25}$$

where C_w and C_R are the aspect ratio of the coil window and the entire core, respectively. They are useful if there is no need to specifically set any L or W. Certain values of C_w can be found that minimize the coil volume or the core volume or both.

The core volume is given by

$$V_c = (4L_w + 2W_w + 2l) \cdot w \cdot l = 2 \cdot \left(\sqrt{A_w C_w} + \sqrt{\frac{A_w}{2\,C_w}} + l \right) \cdot w \cdot l \ , \tag{A.26}$$

which is minimized at C_w equal to $1/2$. However, it is fairly obvious that with the width twice as large as length the coil volume is not minimized.

The coil volume is calculated using the cross section in Figure A-4. This cross section should provide a reasonably conservative estimate of the coil volume, which is calculated using

$$V_E = 2L_w \left(2W_w \left(l + w \right) + \pi W_w^2 \right) = \sqrt{A_w C_w} \left(2\sqrt{\frac{A_w}{2\,C_W}} \left(l + w \right) + \pi \frac{A_w}{2\,C_w} \right) \tag{A.27}$$

By combining the coil volume and the core volume, the aspect ratio that minimizes the

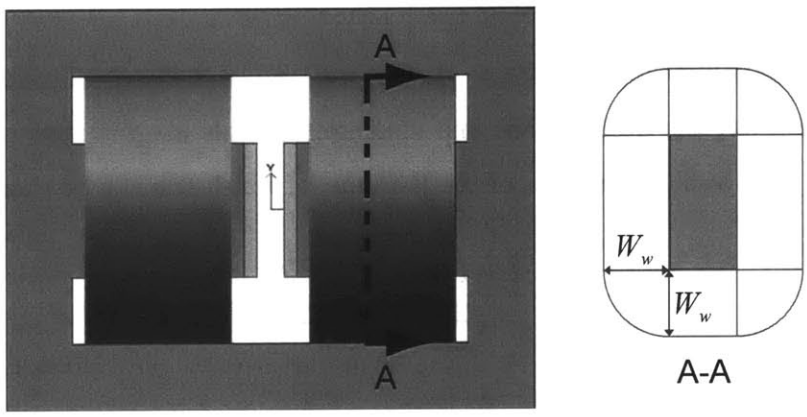

Figure A-4: The geometry used in estimating the volume and length of the H-Frame coils. The small shaded area represents the iron core and the coil fills the space bounded by the rounded rectangle with the indicated dimensions.

total volume can be found and is given by

$$C_w = \frac{2lw + \pi A_w}{4lw} \ . \tag{A.28}$$

This minimization is useful because only a rough estimate of A_w is necessary to get a good estimate of the coil window aspect ratio. The coil perimeter and cross-sectional area, which are required to calculate K_{1e}, are estimated by

$$P_{coil} = 2(\pi W_w + l + w) \ , \tag{A.29}$$

and

$$A_{coil} = \pi W_w^2 + 2W_w(l + w) \ . \tag{A.30}$$

A.3 Comparison of Example Designs

Now that the method for determining the design of the electromagnet has been laid out, we will return to the example crystal and present some numerical results. The electromagnet in this case is required to generate the same field as the permanent magnet, so that both 0.0 kOe and 7.0 kOe can be reached. The magnetization of the permanent magnet is unaffected by these field levels, so the magnetic fields sum linearly, and the required magnetic

Table A.2: Dimensions and electrical requirements for an electromagnet design to actuate the example crystal based on the equations presented.

	C-Frame	H-Frame	Units
l	0.625	0.625	Inches
w	0.3125	0.3125	Inches
t	0.1	0.1	Inches
V_s	0.0195	0.0195	Cubic Inches
V_m	0.0116	0.0116	Cubic Inches
K_{1e}	2.82	2.88	N/A
$(NI)_{max}$	3570	3660	Amp-Turns
A_w	10.5	10.8	Square Inches
R_c	1.85		Inches
C_w		43.8	N/A
L_w		15.4	Inches
W_w		0.351	Inches
V_c	2.42	12.2	Cubic Inches
V_e	39.2	34.2	Cubic Inches
ζ	0.057%	0.047%	Percent Volume

field from the electromagnet is 3.5 kOe. Table A.2 shows the dimensions of two possible electromagnets designed using the equations presented.

A quick comparison of the volume of the FSMA crystal, V_c, to the volume of the electromagnets, V_e, in Table A.2 shows how large the electromagnets are. The example FSMA crystal has a volume on the order of 0.1% of the volume of the electromagnet. That means the effective energy density, instead of 100 kJ/m^3, is closer to 100 J/m^3.

There is of course room for improvement in the design calculation used here. The large value of K_{1e} can be reduced by using a thinner crystal, and perhaps by reducing the excess gap space provided for the crystal's movement. Caution must be used in further reducing the crystal's thickness, since a thin crystal could buckle when actuated, rather than produce useful motion. The magnitudes of the required magnetic field could also be adjusted, as some FSMA samples are softer than others and actuate under very low field strength, down to 1 kG. Also, during actuation, the crystals typically have a relative permeability of around 2 or 3, and this fact could be used to reduce the gap reluctance and the K values, and allow a smaller magnet.

One of the problems with minimizations such as the one used to minimize the volume of the H-Frame geometry in Table A.2 is that they can result in unrealistic numbers for

some variables. In this case, it seems that increasing the length of the magnet to reduces the thickness of the electrical coils, and thus the total length of wire in the windings, helps minimize the overall magnet volume. However, it results in magnet dimensions that may be useless because of one excessively large dimension. This problem can be eliminated by setting a ceiling for the aspect ratio of the coil window, although this results in a design that is further from the minimum volume. Limiting the aspect ratio to 2 and recalculating the rest of the dimensions results in a volume fraction (ζ) of 0.029%, which is not an improvement in overall volume, but probably an improvement in the usability of the magnet.

A.4 2-D Finite Element Modeling

Since neither of the volume fractions calculated were very appealing, a 2-D magnetic finite element modeler (Maxwell SV) was used to determine if this magnet design is overly conservative.

Figure A-5 shows the zero and peak-to-peak magnetic fields across the simulated H-Frame magnet's gap. The simulated magnet has dimensions determined by the example FSMA crystal, setting C_w =2, and using the design equations from Section A.2.2. The maximum and minimum current used in the simulation are $(NI)_{max}$ and$-(NI)_{max}$, also from the design equations. The zero current field in the simulation appears to match the design target of 0.35 T (3.5 kOe). However, the high and low fields differ from the zero current field by a bit more the 0.35 T the electromagnet was designed for. This discrepancy is partially due to the fact that this simulation is only two dimensional.

Since the simulation is only two dimensional, there is some flux leakage and fringe field that is not modeled due to the assumption that the magnet is infinite in the z-direction. The design equations can be modified to behave the same way, so that the design equations and simulation match more closely. The parameter K_{1e} is all that needs modifying and is changed as follows:

$$K_1 = 1 + \frac{t_{ge}}{b}\left(2.2\frac{0.67a}{0.67a + t_{ge}}\right)\left(1 + \frac{t_{ge}}{a}\right) \quad , \tag{A.31}$$

where

$$b = W_w \tag{A.32}$$

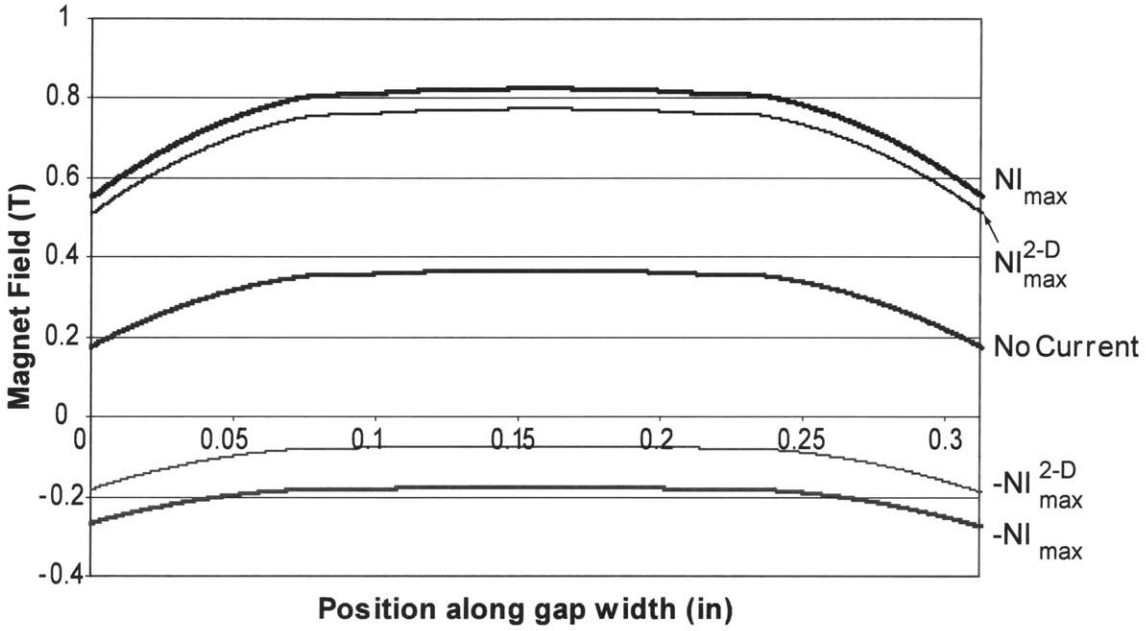

Figure A-5: Magnetic field along the width of the magnets gap. The zero current field is due entirely to the permanent magnets. $(NI)_{max}$ and $(NI)_{max}^{2-D}$ are calculated using the design equations.

for the H-frame, and

$$b = \frac{(R_i + R_o)}{2} \tag{A.33}$$

for the C-frame. The design equations where used to recalculate $(NI)_{max}$ using this 2-D K_{1e}. The lines marked $(NI)_{max}^{2-D}$ in Figure A-5 are the simulation results for the current requirement estimated by the 2-D K_{1e}. These results are useful only for comparing results with the 2-D simulation, the original K_{1e} should be used when designing a real magnet.

It can be seen in Figure A-5 that fringing at the edges of the magnet significantly decreases field strength near the edges. However, the fringing will be neglected, because as Figure A-6 shows, if the FSMA crystal's permeability is assumed to be 2.5, the magnet is more than strong enough to compensate for fringing. In fact, if low field levels at the edges of the crystal can be ignored, redesign of the magnet, with this permeability included, results in a volume fraction of up to 0.3%. However, this redesign compromises some of the robustness gained by designing with low permeability.

Two small insights were gained while working with the magnet design. The first was that there is a crystal thickness that optimizes the volume fraction. This result is not

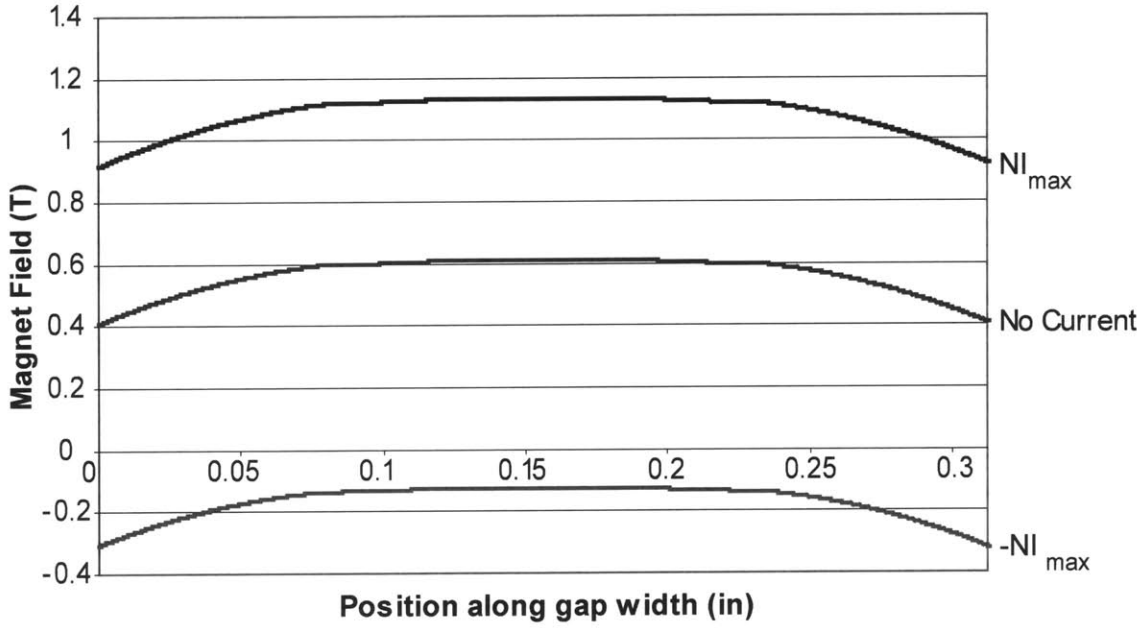

Figure A-6: Magnetic field along the width of the magnet gap, with an FSMA crystal, relative permeability, $\mu = 2.5$, added to the gap. The zero current field is due entirely to the permanent magnets. $(NI)_{max}$ was calculated using the design equations, with $\mu = 1.0$.

surprising. As the crystal gets thinner the magnet gets smaller, but at some point the crystal begins to get smaller faster than the magnet. While it may be difficult to find this minimum empirically, it is easy to identify using a numerical method. The second insight is that the magnet's overall size does affect the optimum volume fraction, which is contrary to some early "back of the envelope" calculations that were done for this magnet design. From those calculations it was concluded that the thermal and magnetic properties of a magnet scaled at the same rate, and therefore there was no benefit to making a larger or smaller magnet. The design equations, however, show that a larger crystal requires a relatively smaller magnet.

As a final check of the design equations, Table A.3 compares the size of the three currently available commercial actuators with the estimated required volume for their electromagnets based on the design equations developed in this appendix. Since the AdpataMat actuators consist of little more than an electromagnet and some protective casing, the size estimates do not differ greatly from the actual dimensions.

Table A.3: Comparison of actuator dimensions estimated with the design equations and existing commercially available actuators [14].

Actuator	Crystal Size (mm)	Actuator Volume	Estimated Volume (μ_r=1)	Estimated Volume (μ_r=2.5)
A5-2	$0.52 \times 2.4 \times 84$	73.8 cm^3	94.1 cm^3	35.4 cm^3
A06-3	$0.55 \times 2.2 \times 15$	15.2 cm^3	39.8 cm^3	11.1 cm^3
A1-2000	$15 \times 40 \times 25$	4520 cm^3	10,700 cm^3	2730 cm^3

A.5 Thermal Issues

Once the magnets size has been determined, the real number of wire turns must be determined. Keeping the number of turns to a minimum is important. This reduces coil resistance and coil impedance. However, power supplies can usually provide only a limited amount of current before they overload or overheat. The minimum number of turns with the maximum reasonable current should be used to limit both current required and heat produced.

The heat generated by an electromagnet can be significant, and we must keep in mind that FSMAs are still SMAs at heart. If the temperate of the crystal rises above the austenite start temperature ($\sim$34 $^\circ$ C) the crystal structure becomes cubic and actuation ceases. A temperature increase could not only be brought on by resistive heating of the coil, but also by internal heating of the FSMA. As with any plastic deformation, twin-boundary motion does not occur without energy loss, which results in heating of the crystal. This energy loss can be seen in the large hysteresis typical of the FSMA actuation loop. Also, a high frequency magnetic field may begin to produce eddy currents in the FSMA material. These induced currents cause resistive heating, and could significantly heat the FSMA. Developing FSMA laminations, to eliminate eddy currents, may be possible. However, a laminated actuator would probably suffer a significant performance loss.

Comparison of the conductive cooling equations and the power input to an FSMA actuator indicate that they both scale equally with changes in size. That is, any increase in the speed of cooling for a smaller actuator will be matched by an increased in the power input into the actuator. This power increase is required because the resistance of the electromagnetic coil increases as the size decreases.

A.6 Induction Issues

When designing an electromagnet for maximum speed, one of the major areas of concern is often the core material and construction. Up to this point we have simply assumed that the core is ferromagnetic and begins to saturate somewhere above 0.7 T. These properties can be found in almost any iron or steel core. In order to get any kind of AC performance from a core, it must be made of thin laminations, which prevents the generation of parasitic eddy currents. The thickness of the laminations can affect the permeability of the core, decreasing it as the thickness decreases. If the permeability of the core gets too low, the magnetic return path can no longer be treated as a ideal magnetic conductor, and the required magnetization force for the entire magnet will increase.

The alloy of the core also greatly affects its permeability, as well as the core's hysteresis. Most steels exhibit a hysteresis in their magnetization loop, which typically gets larger with larger permeability. Since this hysteresis can cause heating and limit the AC frequency of the magnet, faster magnets typically use lower hysteresis, lower permeability steels. In most cases a steel is chosen that is a compromise between permeability and hysteresis. There are other ferromagnetic materials that are used for high speed, high permeability applications that have much better characteristics than steels. However, the price and availability of laminations of these alloys can be prohibitive when compared to steel. For the purposes of this appendix, the affects of the magnetic hysteresis will be largely ignored, not because it is likely to be negligible, but because it is difficult to work with mathematically, and because the hysteresis in the FSMA crystal is more critical, since that material cannot be changed.

Ignoring the effects of the core's hysteresis, the time constant of the magnetic coil can be approximated from the coil dimensions as

$$\tau = \frac{\mathcal{L}}{\mathcal{R}} = \frac{\mu_0 f_p A_g A_w^2}{\rho t_{ge} V_e} \quad , \tag{A.34}$$

where $\mathcal{L}$ is the coil's inductance, $\mathcal{R}$ is the coil's resistance, ρ is resistance per unit length of the coil wire. Equation (A.34) shows that the coil time constant is independent of the wire size or number of turns in the coil, assuming that all wire sizes have the same packing factor. This result is due to the fact that every turn of the coil adds an equal amount of resistance and inductance to the circuit. In fact, the only adjustable parameter that the time constant depends on is the volume of the coil V_e. In the H-frame magnet, the coil

volume is inversely dependent on the window aspect ratio. So as the total volume of the magnet is minimized, the coil volume shrinks and the time constant is increased. Fast coils are short and fat, which provides more resistance for every turn, because the average turn is longer than in a long slim coil. Large laboratory electromagnets are most often short and fat, because the smaller time constant allows for better field control and the heat generated by the extra resistance can be easily removed with water-cooling in a lab.

Even though the time constant is not dependent on the number of turns in the coil, the real bandwidth of an electromagnet usually is, because in reality the bandwidth depends on the inductance,

$$\mathcal{L} = \frac{N^2 \mu_0 A_g}{t_{ge}} \ . \tag{A.35}$$

Since most amplifiers are limited to a certain voltage range, the magnet's inductance can sharply limit bandwidth, with the maximum bandwidth given by

$$\omega_{\max} = \sqrt{\frac{\mathcal{V}_{\max}^2}{\mathcal{L}^2 I_{\max}^2} - \frac{\mathcal{R}^2}{\mathcal{L}^2}} \ . \tag{A.36}$$

Assuming that the amplifier can provide the maximum current the magnet is design for, the voltage limit of the amplifier limits the bandwidth. If the amplifier were strictly limited by power output, the bandwidth would again only depend on the coil time constant. Since this is often not the case, the number of turns is chosen based on the available or desired voltage range and desired bandwidth. Of course, the maximum bandwidth can never be greater than the power-limited bandwidth,

$$\omega_{\max} = \frac{2}{\mathcal{L}} \sqrt{\frac{\mathcal{P}_{\max}^2}{I_{\max}^4} - \frac{\mathcal{R}^2}{\mathcal{L}^2}} \ . \tag{A.37}$$

Once the magnet's bandwidth has been maximized, the bandwidth of the actuator may still be limited by the FSMA itself. As discussed in Chapter 1, the magnetic actuation bandwidth is limited by the anisotropy energy of the FSMA. Every full cycle the crystal could put twice the energy from its anisotropy into its own motion and the system it is driving, assuming the crystal is being bidirectionally magnetically actuated. For a crystal that is 5 mm×5 mm×10 mm, all of the anisotropy energy is required simply to move the crystal at approximately 2000 Hz.

Table A.4: Comparison of actuation characteristics of several linear actuator technologies [17].

	Energy Density (J/cm^3)	Maximum Strain (%)	Maximum Stress (MPa)	Bandwidth (Hz)
PZT	0.12	0.2	110	1e6
Voice Coil	0.025	50	0.1	1e3
FSMA	0.001	5	2	1e3
Terfenol-D	0.025	0.2	70	1e3
SMA	> 25	> 5	> 200	1e0
Hydraulic	> 1000	> 50	> 2000	1e2
Muscle	0.07	40	0.35	1e1

A.7 Comparison of Actuator Technologies

In order to understand what all of this information is really saying about FSMA actuators, it is helpful to compare them with other linear actuators. Table A.4 lists some of the characteristics of some common linear actuators. Note that the listed energy density for the FSMA actuator assumes a 1% volume fraction, which is higher than estimated in this appendix. Because of the required electromagnet, the FSMA actuator's energy density is lower than even a voice coil actuator.

The voice coil data in Table A.4 is for a specific voice coil design. Most voice coil designs have similar energy densities, but the stress and strain relationship in coils can vary greatly. It may even be possible to design a voice coil with identical properties to the FSMA actuator. Most of the other actuators technologies are not comparable to FSMA actuators in one characteristic or another, which means that FSMA actuators would have a niche to fill, if electromagnetic solenoid actuators didn't already occupy it.

A.8 Conclusion

One application for which FSMAs are being considered is low frequency sonar transducers. Most sonar actuator designs focus on the amplification of the very small strains of piezoelectric transducers. Stroke amplification is not only unnecessary when using FSMAs, it may even hinder actuation due to low actuation stress available from an FSMA. One of the simplest sonar transducer designs that works well with high strain materials is a dou-

ble ended piston. Initial calculations using FSMA properties and a double-ended cylinder design indicate that approximately 6% of the piston surface would have to be covered by the active material. The surface area ratio for the face of the H-frame magnet examined in this appendix was only 1.5%. With some design improvements, these numbers indicate that before thermal considerations are taken into account, an FSMA sonar transducer may be possible. Thermal considerations and static forces in deep waters would seem to necessitate a fluid backed sonar transducer. However, this would greatly decrease the efficiency of a piston transducer. Design of a fluid backed FSMA sonar transducer has not yet been analyzed.

A recent advance in the development of FSMAs, that may help create viable actuators is the addition of a mechanical dither to the actuating crystal. Typically, dither is a small vibration used to compensate for backlash in mechanical systems [31]. In most systems, dither is added to the control input. In an FSMA actuator it is possible to add dither using a secondary actuator. A small piezoelectric actuator can be used to vibrate the entire FSMA crystal. The extra transient forces in the crystal help linearize the crystal's response to the magnetic field, reducing both the hysteresis width and the minimum actuation field. This technique is limited by the brittleness of the FSMA material, and the additional energy that is being dissipated as heat in the piezoelectric and the crystal.

Even with careful design and recent advances, it appears that Ni–Mn–Ga actuators are not energetically competitive with existing active material actuators, when the electromagnet is considered. Future FSMA materials may have higher permeability, or actuate parallel to the magnetic field instead of perpendicular, which would make more compact electromagnet designs possible.

Appendix B

1-D Elastic Models

This appendix describes the finite element modeling that was used as a design aid during the development of the actuators presented in this thesis. The first three sections describe the lumped mass model, the consistent mass finite element model, and a continuum model for the specific case of an exponential horn. The last section compares the three models for three different reflectors, including the exponential horn.

B.1 1-D Lumped Mass Model

The system modeled in this section, using the lumped mass model, consists of an acoustic horn and a damping term at $x = 0$, to simulate an infinitely long rod on the left hand side of the horn. The opposite end of the horn is free. The horn's shape is governed by

$$a = e^{-x/l_1} \quad , \tag{B.1}$$

where a is the area of the horn, and l_1 is the characteristic length of the horn. The total length of the horn is l_2, which is independent of l_1. The element length in this model is held constant for each element, and is given by $l_e = l_2/N$. The mass of each element is determined by l_e and the average cross-sectional area of the element. A representation of the areas used is shown in Figure B-1. The stiffness of the connection between two elements is determined by the elastic modulus E, the element length l_e, and the average cross-sectional area spanned by the connection. Figure B-2 shows an example element from the model. The area and mass of each element, and the stiffness of each element boundary are given

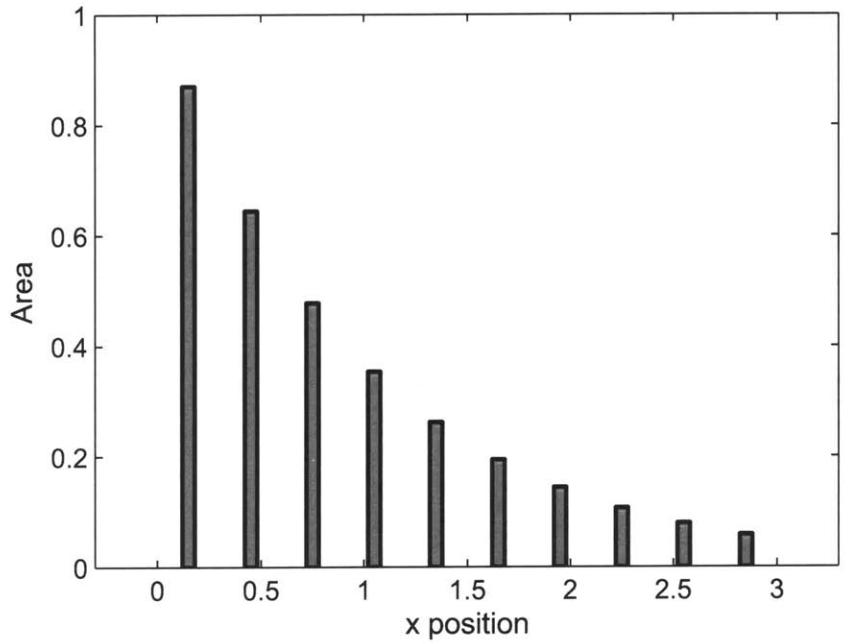

Figure B-1: Cross-sectional areas at the mass centers used in the lumped mass model, to compute the data shown in Figure B-8. The number of elements is $N = 10$.

by

$$a_i = e^{-l_e\, i/l_1} \ , \tag{B.2}$$

$$m_i = \frac{1}{2}\,\rho\,(a_i + a_{i+1})\,l_e \ , \tag{B.3}$$

$$k_i = E\,\frac{a_i}{l_e} \ . \tag{B.4}$$

The balance of forces on each lumped mass results in the differential equation

$$m_i \ddot{q}_i + k_i(q_i - q_{i-1}) + k_{i+1}(q_i - q_{i+1}) = F_{\text{ext}} \ , \tag{B.5}$$

where F_{ext} is the external force on the element. Gathering the terms for all of the elements, Equations (B.5) can be written in matrix form as

$$\mathbf{M}\,\ddot{q} + \mathbf{K}\,q = \mathbf{F}_{\text{ext}} \ , \tag{B.6}$$

or

$$\ddot{q} = \mathbf{M}^{-1}\mathbf{F}_{\text{ext}} - \mathbf{M}^{-1}\mathbf{K}\,q \ . \tag{B.7}$$

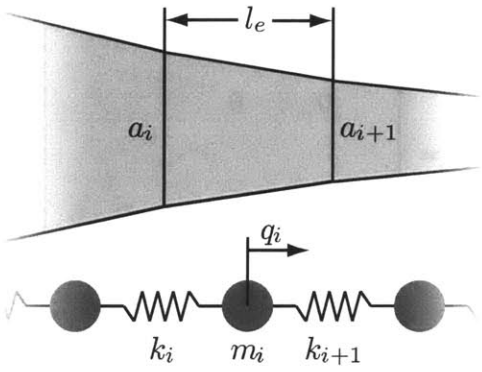

Figure B-2: An single element for the lumped mass model, labeled with the variables used in Equations (B.2) through B.4.

This equation can be incorporated into a state space model of the lumped mass system, in which the state is given by

$$x = \begin{bmatrix} \dot{q} \\ q \end{bmatrix} . \tag{B.8}$$

The state space equations are

$$\dot{x} = \mathbf{A}x + \mathbf{B}u , \tag{B.9}$$

$$y = \mathbf{C}x + \mathbf{D}u . \tag{B.10}$$

The $\mathbf{A}$ matrix is made up of four submatrices, so that

$$\mathbf{A} = \left[\begin{array}{c|c} \mathbf{A}_{11} & \mathbf{A}_{12} \\ \hline \mathbf{A}_{21} & \mathbf{A}_{22} \end{array}\right] . \tag{B.11}$$

$\mathbf{A}_{11}$ is zero, except for the ad-hoc damping term which simulates the semi-infinite rod on

the left hand side of the horn, so that

$$\mathbf{A}_{11} = \begin{bmatrix} -\sqrt{\frac{k_1}{2m_1}} & 0 & & \cdots & \\ 0 & 0 & & & \\ & & \ddots & & \\ & & & 0 & 0 \\ \vdots & & & 0 & 0 \end{bmatrix}, \tag{B.12}$$

$\mathbf{A}_{12}$ is equivalent to $-\mathbf{M}^{-1}\mathbf{K}$, which can be expanded as

$$\mathbf{A}_{12} = \begin{bmatrix} -\frac{k_2}{m_1} & \frac{k_2}{m_1} & 0 & & & & \\ \frac{k_2}{m_2} & -\frac{k_2+k_3}{m_2} & \frac{k_3}{m_2} & & \cdots & & \\ 0 & \frac{k_3}{m_3} & -\frac{k_3+k_4}{m_3} & & & & \\ & & & \ddots & & & \\ & & & -\frac{k_8+k_9}{m_8} & \frac{k_9}{m_8} & 0 \\ \vdots & & & \frac{k_9}{m_9} & -\frac{k_9+k_{10}}{m_9} & \frac{k_{10}}{m_9} \\ & & & 0 & \frac{k_{10}}{m_{10}} & -\frac{k_{10}}{m_{10}} \end{bmatrix}, \tag{B.13}$$

for a ten element model. $\mathbf{A}_{21}$ is the identity matrix and $\mathbf{A}_{22}$ is zero.

In the state space equations, $\mathbf{B}u$ replaces $\mathbf{M}^{-1}\mathbf{F}_{\text{ext}}$. The vector u has only one element, which is the input pulse. The matrix $\mathbf{B}$ is given by

$$\mathbf{B} = \begin{bmatrix} \frac{k_1}{m_1} \\ 0 \\ 0 \\ \vdots \\ 0 \\ 0 \\ 0 \end{bmatrix}. \tag{B.14}$$

which shows that the input propagates into the horn model through the spring of the first element. The vector y is the output of the state space model. The $\mathbf{C}$ matrix determines how the states affect the outputs. In order to recover the stress between the horn and left

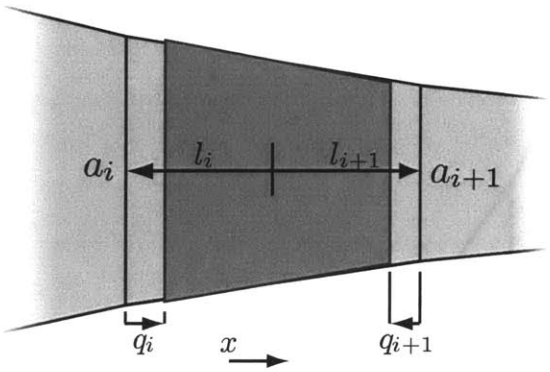

Figure B-3: An single element for the consistent mass model, labeled with the variables used in Equations (B.19) and B.20. The lighter colored element is unstressed, the darker is compressed.

hand rod, we use

$$\mathbf{C} = \left[\mathbf{C}_1 \middle| \mathbf{C}_2 \right] , \tag{B.15}$$

where

$$\mathbf{C}_1 = \left[0 \quad 0 \quad 0 \quad \cdots \quad 0 \quad 0 \quad 0 \right] , \tag{B.16}$$

$$\mathbf{C}_2 = \left[\sqrt{\frac{k_1}{2m_1}} \quad 0 \quad 0 \quad \cdots \quad 0 \quad 0 \quad 0 \right] , \tag{B.17}$$

and

$$\mathbf{D} = 0 , \tag{B.18}$$

since we do not need any information from the input in the state space outputs.

Once the state space model is complete, either MATLAB's `lsim` or `freqresp` function are used to simulate the system response for various input waves.

B.2 1-D Consistent Mass Finite Element Model

This simulation is similar to the lumped mass simulation, except the mass and stiffness are calculated using a consistent mass finite element method. Figure B-3 shows a single element used in the model. The equations that follow derive the stiffness and mass terms for the element, from the potential and kinetic energy equations for the element.

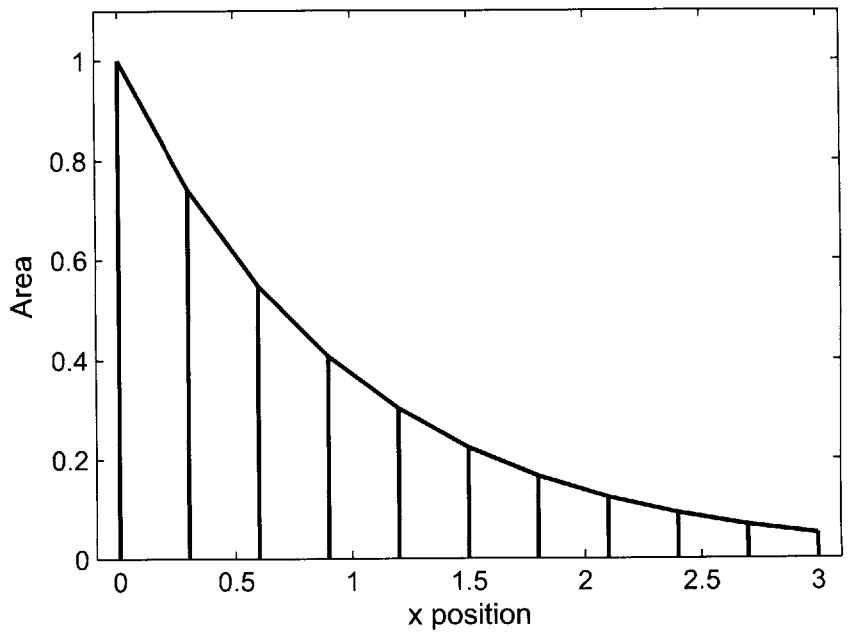

Figure B-4: Cross-sectional areas at element boundaries used in the consistent mass finite element model to compute the data shown in Figure B-8

The derivation of the spring and mass matrices used in constructing the **A** matrix is more involved here than in the lumped mass model. The derivation begins with linear interpolations for the area and displacement throughout each element, given by

$$a(x) = \frac{a_i(x - l_{i+1})}{l_i - l_{i+1}} + \frac{a_{i+1}(x - l_i)}{l_{i+1} - l_i} \quad , \tag{B.19}$$

and

$$w(x,t) = \frac{q_i(x - l_{i+1})}{l_i - l_{i+1}} + \frac{q_{i+1}(x - l_i)}{l_{i+1} - l_i} \quad , \tag{B.20}$$

respectively. The first derivative of the displacement with respect to x is

$$w'(x,t) = \frac{q_i - q_{i+1}}{l_i - l_{i+1}} \quad . \tag{B.21}$$

Since q_i and q_{i+1} are the only time dependent terms in $w(x,t)$, the first derivative with respect to time is

$$\dot{w}(x,t) = \frac{\dot{q}_i\ (x - l_{i+1})}{l_i - l_{i+1}} + \frac{\dot{q}_{i+1}\ (x - l_i)}{l_{i+1} - l_i} \quad . \tag{B.22}$$

The potential energy of each element is given by

$$\begin{aligned} U_p &= \int_{l_i}^{l_{i+1}} \frac{1}{2} E\, a(x)\, w'(x,t)^2\, dx \\ &= -1/4\, \frac{E\,(q_i - q_{i+1})^2\,(a_i + a_{i+1})}{l_i - l_{i+1}} \quad . \end{aligned} \tag{B.23}$$

The coefficients of the potential energy equation can be gathered into a stiffness matrix for the element,

$$\mathbf{k}_i = \begin{bmatrix} -1/4\,\frac{E(a_i+a_{i+1})}{l_i-l_{i+1}} & 1/4\,\frac{E(a_i+a_{i+1})}{l_i-l_{i+1}} \\ 1/4\,\frac{E(a_i+a_{i+1})}{l_i-l_{i+1}} & -1/4\,\frac{E(a_i+a_{i+1})}{l_i-l_{i+1}} \end{bmatrix} , \tag{B.24}$$

which can in turn be gathered into a stiffness matrix for the modeled reflector, so that

$$\mathbf{K} = \begin{bmatrix} \mathbf{k}_1 & 0 & 0 & \cdots \\ 0 & \mathbf{k}_2 & 0 & \\ 0 & 0 & \mathbf{k}_3 & \\ & \vdots & & \ddots \end{bmatrix} . \tag{B.25}$$

The kinetic energy of each element is

$$\begin{aligned} U_k &= \int_{l_i}^{l_{i+1}} \frac{1}{2} \rho\, a(x)\, \dot{w}(x,t)^2\, dx \\ &= -1/24\,\rho \left(2\,(a_i + a_{i+1})\,\dot{q}_i\,\dot{q}_{i+1} + (3\,a_{i+1} + a_i)\,(\dot{q}_{i+1})^2 + \right. \\ &\quad \left. +(3\,a_i + a_{i+1})\,(\dot{q}_i)^2 \right) (l_i - l_{i+1}) \quad . \end{aligned} \tag{B.26}$$

The coefficients of the kinetic energy equation can be gathered into into a mass matrix,

$$\mathbf{m}_i = -\frac{1}{24}\,\rho \begin{bmatrix} (3\,a_i + a_{i+1})\,(l_i - l_{i+1}) & (l_i - l_{i+1})\,(a_i + a_{i+1}) \\ (l_i - l_{i+1})\,(a_i + a_{i+1}) & (3\,a_{i+1} + a_i)\,(l_i - l_{i+1}) \end{bmatrix} , \tag{B.27}$$

which can in turn be gathered into a mass matrix for the reflector being modeled,

$$\mathbf{M} = \begin{bmatrix} \begin{bmatrix} & \mathbf{m}_1 & \\ 0 & & \\ 0 & & \end{bmatrix} & \begin{bmatrix} \\ \mathbf{m}_2 \\ \\ 0 \\ \vdots \end{bmatrix} & 0 & \begin{bmatrix} \\ \mathbf{m}_3 \\ \\ \end{bmatrix} & 0 & \cdots \\ & & & & 0 & \\ & & & & & \ddots \end{bmatrix} . \tag{B.28}$$

The state space equations are set up with the state

$$x = \begin{bmatrix} \dot{q} \\ q \end{bmatrix} , \tag{B.29}$$

and the matrix coefficients, $\mathbf{A}$, $\mathbf{B}$, $\mathbf{C}$ and $\mathbf{D}$, are nearly identical to the matrices used in the lumped mass model:

$$\mathbf{A} = \left[\begin{array}{c|c} \mathbf{A}_{11} & \mathbf{A}_{12} \\ \hline \mathbf{A}_{21} & \mathbf{A}_{22} \end{array}\right] , \tag{B.30}$$

where

$$\mathbf{A}_{11} = \begin{bmatrix} -\sqrt{\frac{k_{11}}{2m_{11}}} & 0 & \cdots \\ 0 & 0 & \\ & \ddots & \\ \vdots & & 0 \quad 0 \\ & & 0 \quad 0 \end{bmatrix} , \tag{B.31}$$

$$\mathbf{A}_{12} = \mathbf{M}^{-1}\mathbf{K} \tag{B.32}$$

$$\mathbf{A}_{21} = \mathbf{I} \tag{B.33}$$

$$\mathbf{A}_{22} = 0 \tag{B.34}$$

$$\mathbf{B} = \begin{bmatrix} \frac{k_{11}}{m_{11}} \\ 0 \\ 0 \\ \vdots \\ 0 \\ 0 \\ 0 \end{bmatrix} , \tag{B.35}$$

$$\mathbf{C} = \left[\mathbf{C}_1 \middle| \mathbf{C}_2 \right] , \tag{B.36}$$

where

$$\mathbf{C}_1 = \begin{bmatrix} 0 & 0 & 0 & \cdots & 0 & 0 & 0 \end{bmatrix} , \tag{B.37}$$

$$\mathbf{C}_2 = \begin{bmatrix} \sqrt{\frac{k_{11}}{2m_{11}}} & 0 & 0 & \cdots & 0 & 0 & 0 \end{bmatrix} , \tag{B.38}$$

and

$$\mathbf{D} = 0 . \tag{B.39}$$

The subscripts of k_{11} and m_{11} indicate that they are the first entry in the stiffness or mass matrix for the first element.

With a state space equations in hand, MATLAB's `lsim` and `freqresp` are again used to obtain the systems response to an input pulse.

B.3 1-D Horn Continuum Solution

Below, we derive the solution to the differential equations for a longitudinal wave in an exponential horn. The horn is treated as a rod with changing cross-sectional area. A second rod is attached to the left hand side of the horn at $x = 0$, and propagates the input pulse into the horn and the reflected pulse out.

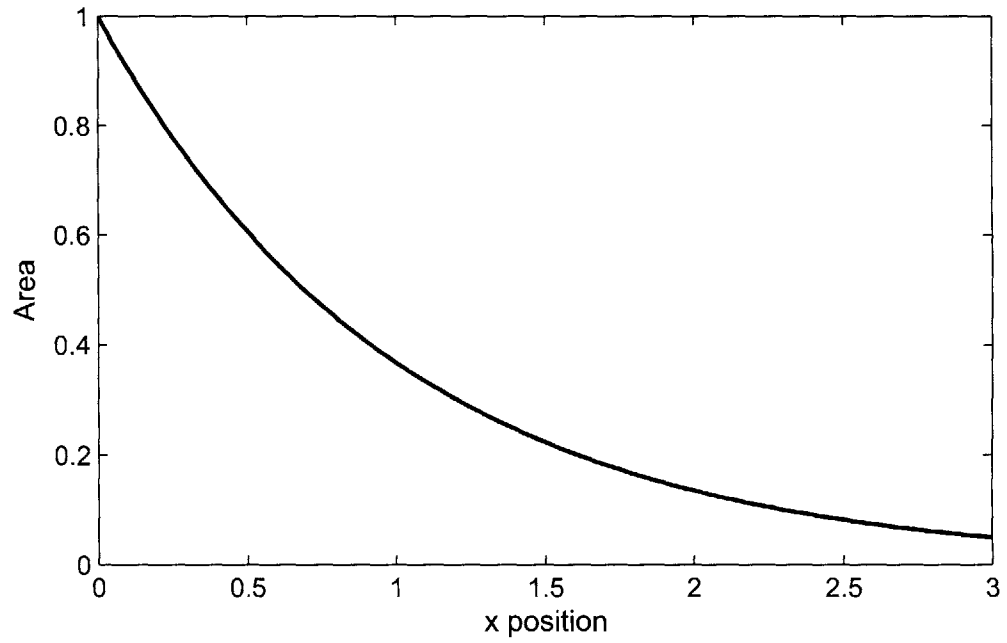

Figure B-5: Cross-sectional area of horn used in the differential equation solution for the data shown in Figure B-8

The differential equations governing the behavior of the wave in each rod are

$$\begin{aligned} \ddot{w}_1 &= w_1'' \ , \\ \ddot{w}_2 &= w_2'' - \tfrac{1}{l_1} w_2' \ , \end{aligned} \tag{B.40}$$

where w_1 and w_2 are displacement in the left hand rod and exponential horn respectively. If we assume solutions of the form

$$\begin{aligned} w_1 &= a\, e^{kx - i\omega t} \ , \\ w_2 &= a\, e^{kx - i\omega t} \ , \end{aligned} \tag{B.41}$$

and plug them into Equation (B.40), solving for zero results in

$$\begin{aligned} 0 &= -e^{kx - i\omega t} \left(\omega^2 + k^2\right) \ , \\ 0 &= -\frac{e^{kx - i\omega t} \left(\omega^2 l_1 + k^2 l_1 - k\right)}{l_1} \ . \end{aligned} \tag{B.42}$$

Four values of k of can can be obtained from the roots of Equation (B.42):

$$k_1 = i\omega \ , \tag{B.43}$$

$$k_2 = -i\omega \ , \tag{B.44}$$

$$k_3 = 1/2\,\frac{1+\sqrt{1-4\,{l_1}^2\omega^2}}{l_1} \ , \tag{B.45}$$

$$k_4 = 1/2\,\frac{1-\sqrt{1-4\,{l_1}^2\omega^2}}{l_1} \ . \tag{B.46}$$

The full solutions for w_1 and w_2, incorporating these k's, become

$$\begin{aligned} w_1 &= a_1\,e^{k_1\,x-i\omega t} + a_2\,e^{k_2\,x-i\omega t} \ , \\ w_2 &= a_3\,e^{k_3\,x-i\omega t} + a_4\,e^{k_4\,x-i\omega t} \ , \end{aligned} \tag{B.47}$$

where the variables a_1 through a_4 represent constants to be determined. The derivatives of the displacement equations will be used in solving for these constants, and are given by

$$\begin{aligned} w_1' &= a_1\,k_1\,e^{k_1\,x-i\omega t} + a_2\,k_2\,e^{k_2\,x-i\omega t} \ , \\ w_2' &= a_3\,k_3\,e^{k_3\,x-i\omega t} + a_4\,k_4\,e^{k_4\,x-i\omega t} \ , \end{aligned} \tag{B.48}$$

$$\begin{aligned} w_1'' &= a_1\,{k_1}^2 e^{k_1\,x-i\omega t} + a_2\,{k_2}^2 e^{k_2\,x-i\omega t} \ , \\ w_2'' &= a_3\,{k_3}^2 e^{k_3\,x-i\omega t} + a_4\,{k_4}^2 e^{k_4\,x-i\omega t} \ , \end{aligned} \tag{B.49}$$

$$\begin{aligned} \dot{w}_1 &= -i\omega e^{-i\omega t}\left(a_1\,e^{k_1\,x} + a_2\,e^{k_2\,x}\right) \ , \\ \dot{w}_2 &= -i\omega e^{-i\omega t}\left(a_3\,e^{k_3\,x} + a_4\,e^{k_4\,x}\right) \ , \end{aligned} \tag{B.50}$$

$$\begin{aligned} \ddot{w}_1 &= -\omega^2 e^{-i\omega t}\left(a_1\,e^{k_1\,x} + a_2\,e^{k_2\,x}\right) \ , \\ \ddot{w}_2 &= -\omega^2 e^{-i\omega t}\left(a_3\,e^{k_3\,x} + a_4\,e^{k_4\,x}\right) \ . \end{aligned} \tag{B.51}$$

There are several boundary conditions that allow us to solve for the unknown constats. First, the amplitude of the incoming wave, a_1, is known, so that

$$a_1 = c \ . \tag{B.52}$$

Second, displacement compatibility at the horns left hand boundary, $x = 0$, requires that

$$e^{-i\omega t}\,(a_1 + a_2 - a_3 - a_4 = 0) \quad . \tag{B.53}$$

Third, equilibrium is maintained at $x = 0$ requires that

$$e^{-i\omega t}\,(a_1\,k_1 + a_2\,k_2 - a_3\,k_3 - a_4\,k_4 = 0) \quad . \tag{B.54}$$

Finally, and the stress at the right end of the horn is zero, so that

$$a_3\,k_3\,e^{k_3\,l_2 - i\omega t} + a_4\,k_4\,e^{k_4\,l_2 - i\omega t} = 0 \quad . \tag{B.55}$$

Using the boundary conditions to solve for the constants a_1 through a_4 gives

$$a_1 = c \quad , \tag{B.56}$$

$$a_2 = -\frac{a_1\left(k_3\,k_4 - k_3\,k_4\,e^{l_2\,(k_3-k_4)} - k_4\,k_1 + k_3\,e^{l_2\,(k_3-k_4)}k_1\right)}{k_3\,k_4 - k_3\,k_4\,e^{l_2\,(k_3-k_4)} - k_4\,k_2 + k_3\,e^{l_2\,(k_3-k_4)}k_2} \quad , \tag{B.57}$$

$$a_3 = -\frac{a_1\,k_1 + a_2\,k_2}{k_3\left(-1 + e^{l_2\,(k_3-k_4)}\right)} \quad , \tag{B.58}$$

$$a_4 = \frac{(a_1\,k_1 + a_2\,k_2)\,e^{l_2\,(k_3-k_4)}}{k_4\left(-1 + e^{l_2\,(k_3-k_4)}\right)} \quad . \tag{B.59}$$

Once the coefficients of the solution were found, MATLAB's `freqresp` function was used to numerically evaluate the response to a given input wave.

B.4 Comparison of the Models

Here a comparison is made between the consistent mass model and the wave equation solution for some simply shaped reflectors, or acoustic horns. Figures B-6, B-7 and B-8 show some sample comparisons. Also included in the figures is the solution obtained from a lumped mass model that was used briefly but discarded due to obvious flaws. The consistent mass finite element model matches the wave equation solution quite well, even with elements nearly half the length of wavelength being propagated.

Although the consistent mass finite element model matches the other 1-D mathematical models well, it proves less accurate in more complex multidimensional systems. Figure B-9 shows a comparison of simulated and actual results from an experiment in which a brass

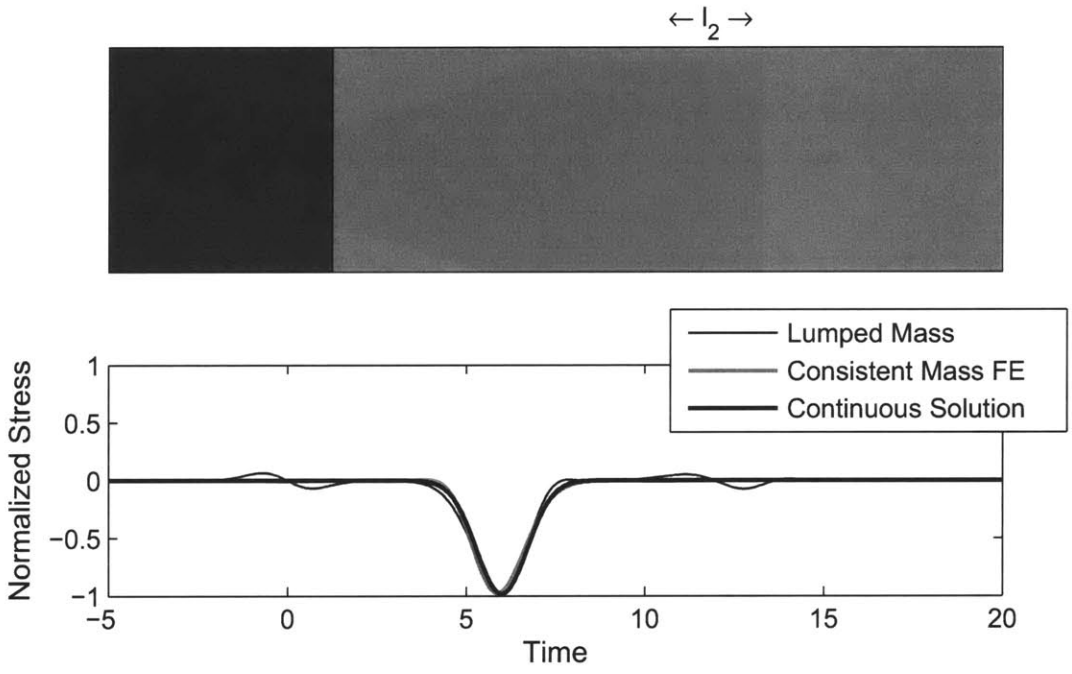

Figure B-6: Stress at the material boundary ($x = 0$) caused by the reflection of an extensional gaussian pulse off the free end of the second rod. The pulse was centered at $x = 0$ when $t = 0$. All displayed data is non-dimensional. Obvious defects caused by the element size are visible in the lumped mass (Lumped Mass) simulation. The number of elements is 10.

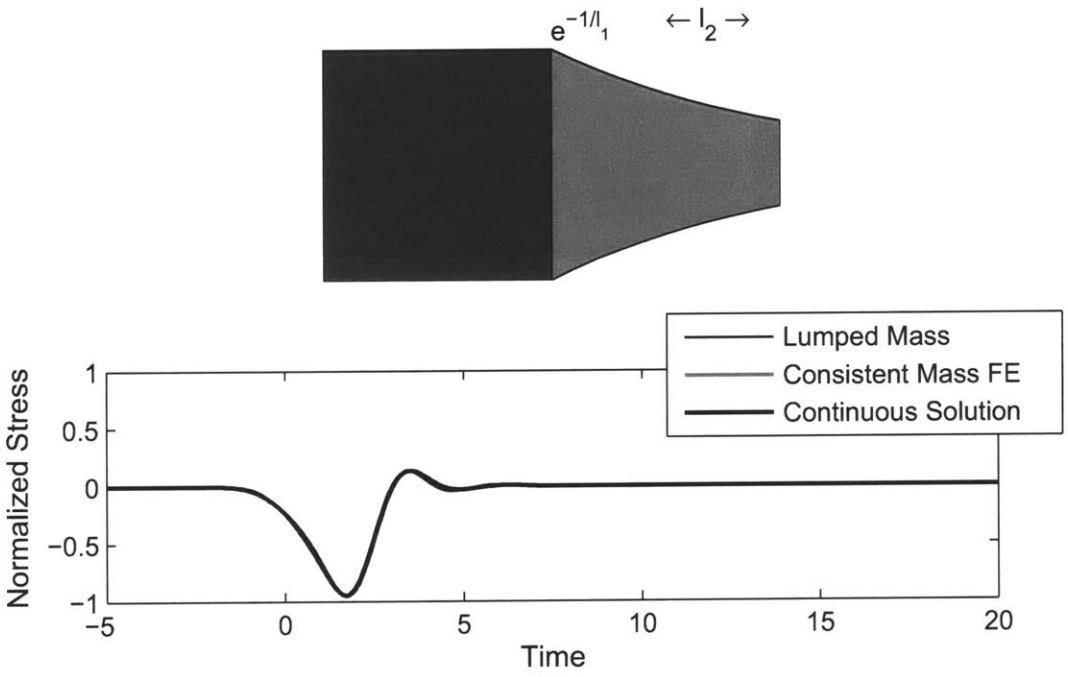

Figure B-7: Stress at the material boundary ($x = 0$) caused by the reflection of an extensional gaussian pulse off the exponential horn. The pulse was centered at $x = 0$ when $t = 0$. All displayed data is non-dimensional. Defects caused by the element size are visible in the lumped mass (Lumped Mass) simulation. The number of elements is 10.

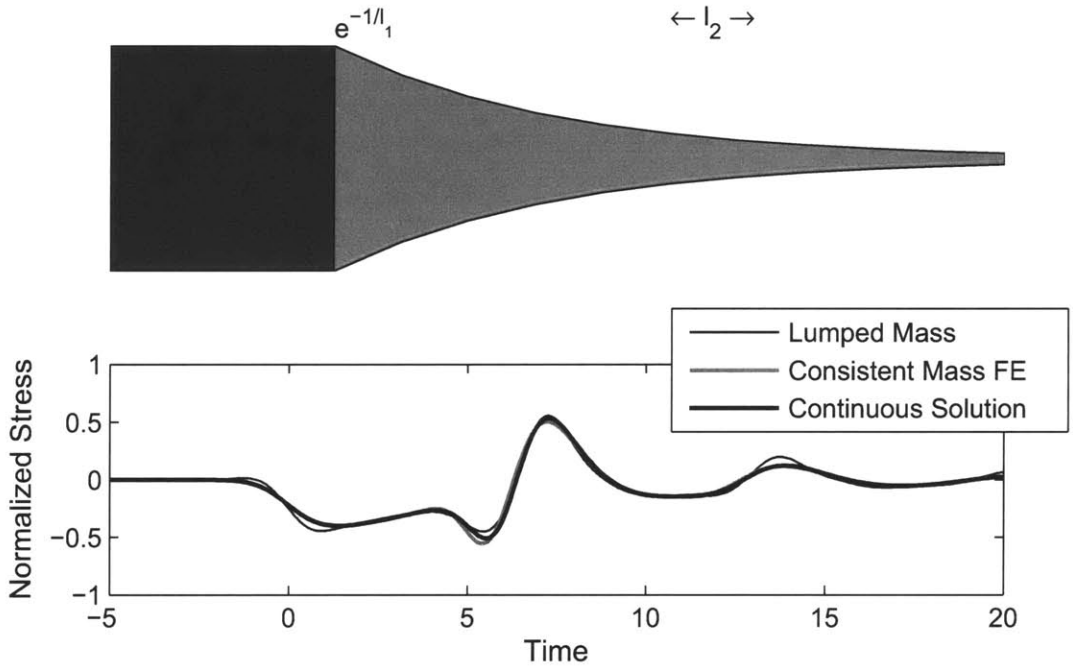

Figure B-8: Stress at the material boundary ($x = 0$) caused by the reflection of an extensional gaussian pulse off the exponential horn. The pulse was centered at $x = 0$ when $t = 0$. All displayed data is non-dimensional. Small defects caused by the element size are visible in the consistent mass finite element (Consistent Mass FE) solution. The number of elements is 10.

dummy crystal replaced the actual FSMA. It was thought that removing the FSMA would linearize the system and allow it to be modeled accurately. However, it can be seen from the results that the simulation is still quite different from the actual stress measurement, due to three dimensional effects no captured by the one dimensional models.

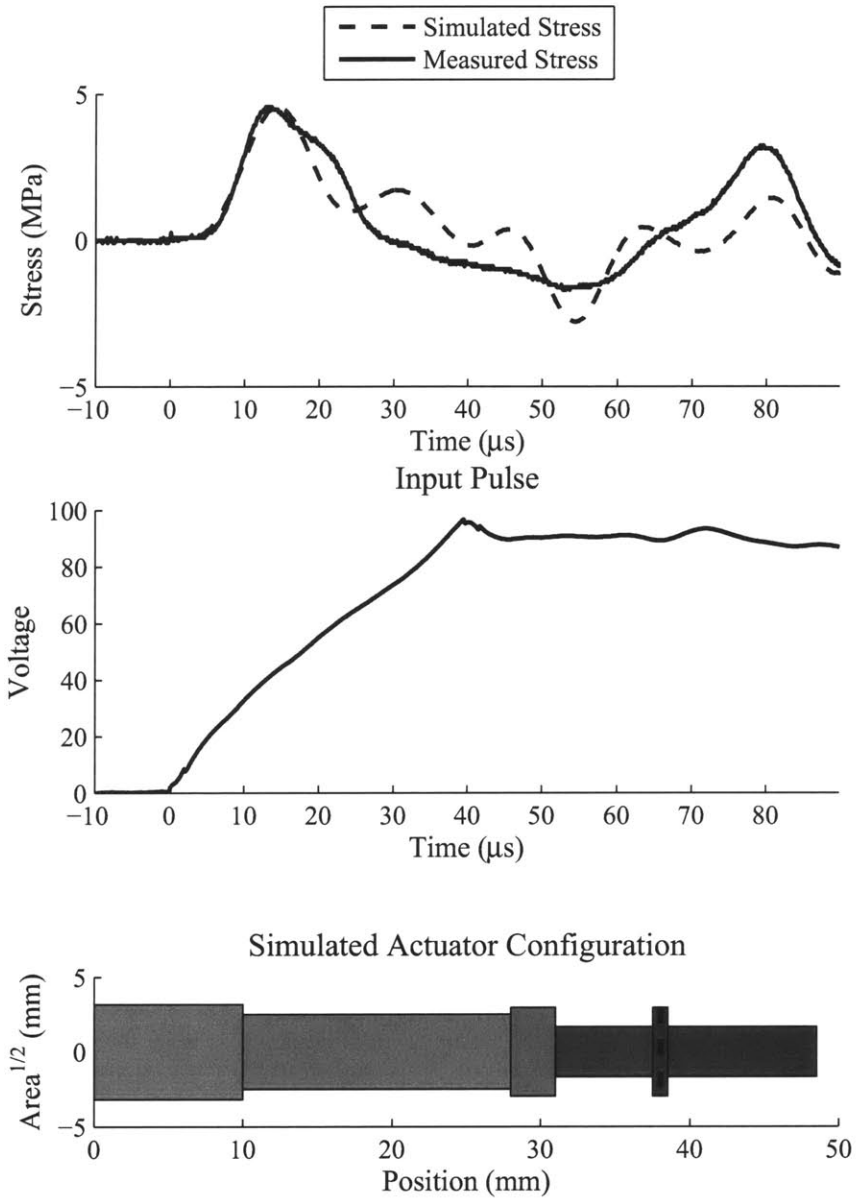

Figure B-9: Comparison of a consistent mass finite element simulation and measured stress data from a dummy actuator configuration. The vertical dotted line in the lower chart shows the position from which the simulated stress was taken. The materials of the system from left to right are: brass, piezoelectric stack, brass, epoxy (not visible), brass, epoxy (not visible), piezoelectric sensor, epoxy (not visible) and brass. Note that the simulation used an adjustable calibration factor to match the height of the first stress peak.

Appendix C

Supplemental Figures

This appendix contains data referenced in Chapter 3 and used to generate some of the figures in Chapter 4. Section C.1 shows the bidirectional actuation data discussed in Section 3.2. Section C.2 shows the strain counterparts to the stress data shown in Section 3.4.2.

C.1 Free Actuation with Varying Input Parameters

This section shows a collection of experimental results collected with apparatus C1, which is shown in Figure C-1. Figure C-1 schematically shows where the measurements shown in this section were taken. The pulse shapes (piezoelectric input pulses and stress pulses) were measured prior to actuation; compressive pulses through a compressed crystal and tensile pulses through a mostly extended crystal. The strain curves were taken from the second cycle in a set of continuous bidirectional actuation cycles.

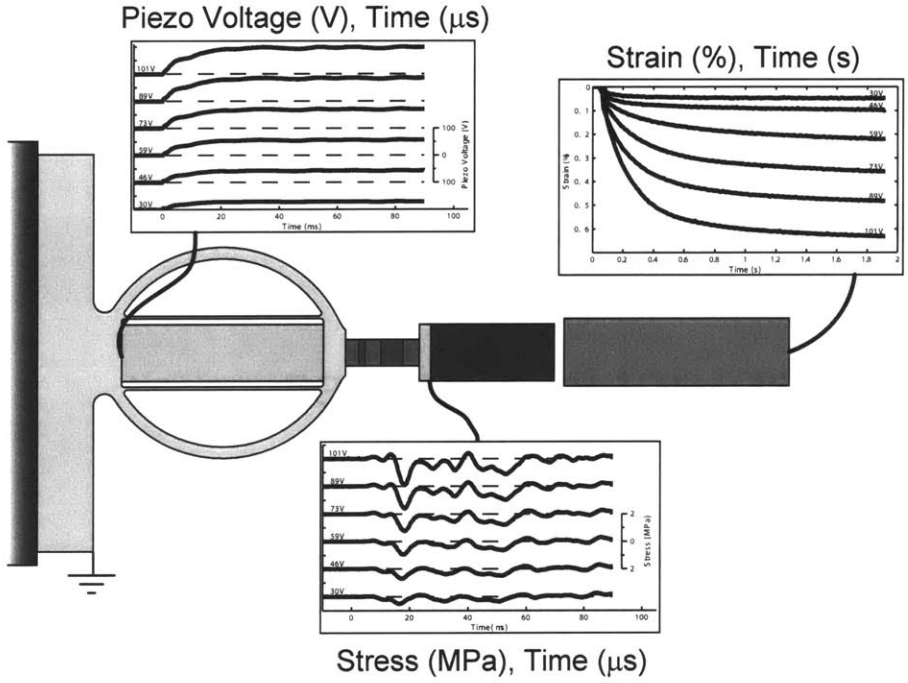

Figure C-1: Schematic representation of apparatus C1. The smaller inset figures indicate where the measurements shown in Section C.1 were taken.

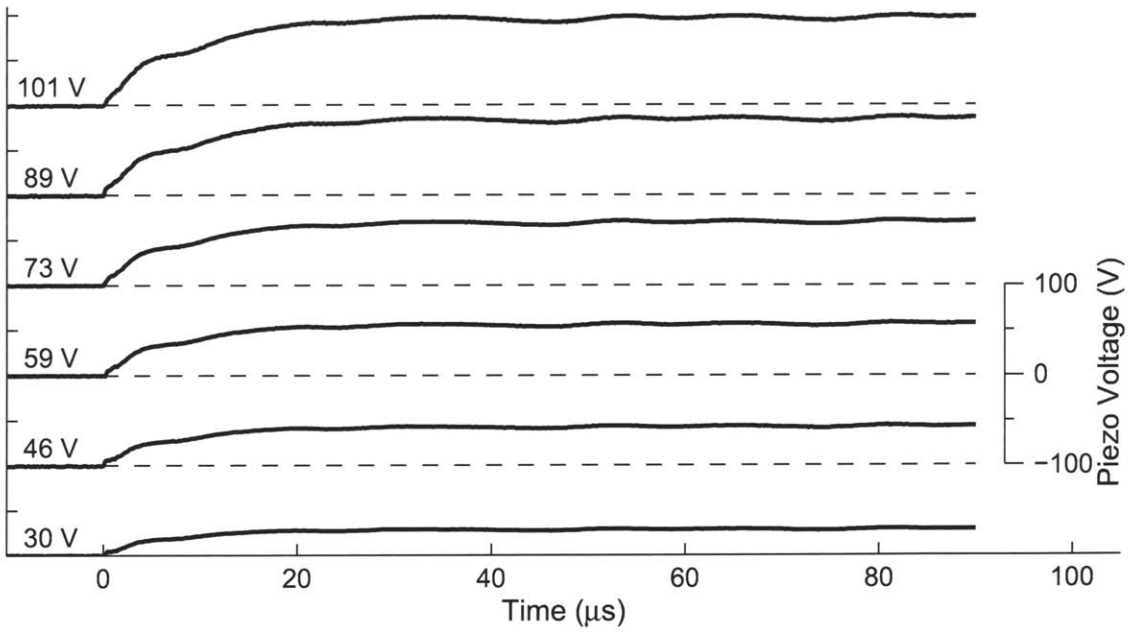

Figure C-2: Compressive input pulses for apparatus C1, with varying power supply voltages. Gate voltage was 12 V (full on), repetition rate 100 Hz.

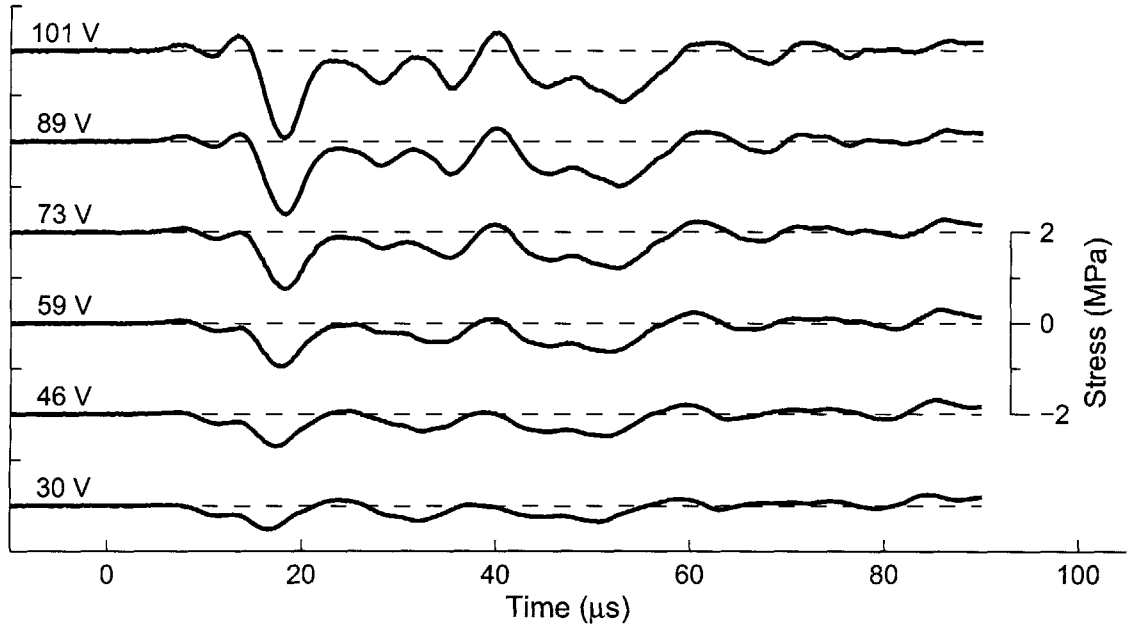

Figure C-3: Compressive stress pulses for apparatus C1, with varying power supply voltages. Gate voltage was 12 V (full on), repetition rate 100 Hz. The stress was measured when the FSMA crystal was fully compressed. Stress calculated from piezoelectric sensor voltage.

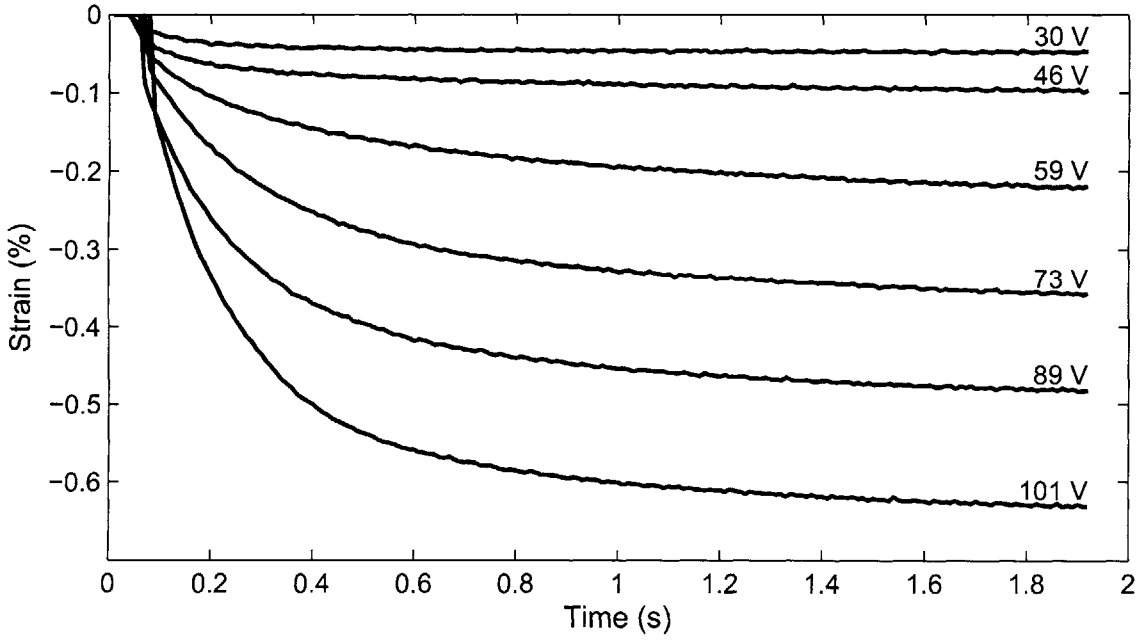

Figure C-4: Compressive actuation strain for apparatus C1, with varying power supply voltage. Gate voltage was 12 V (full on), repetition rate 100 Hz.

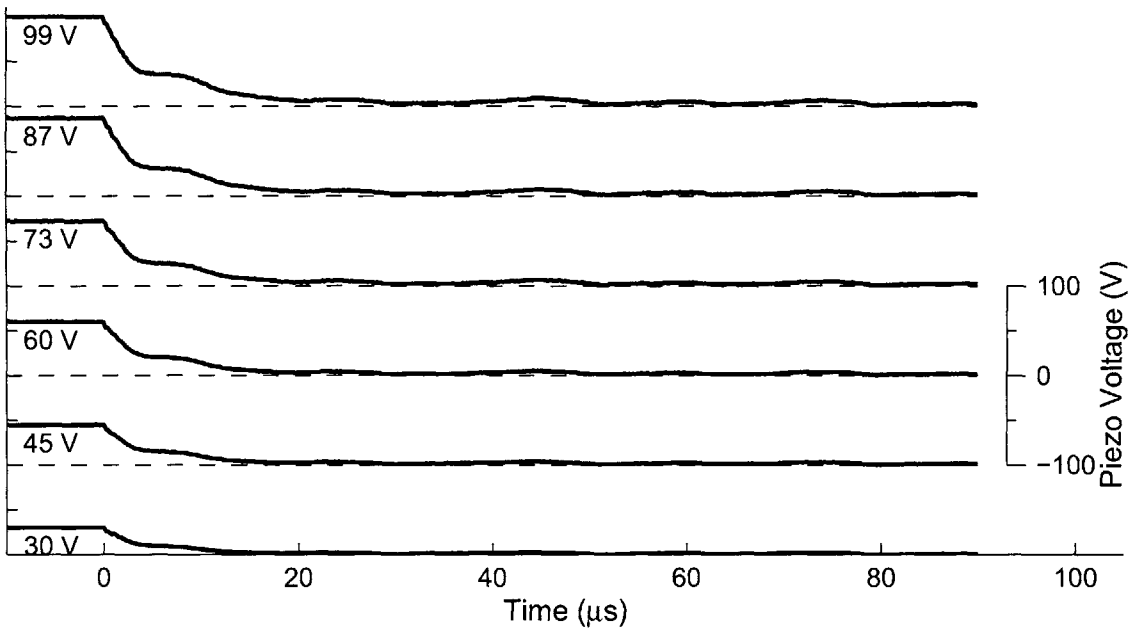

Figure C-5: Extensional input pulses for apparatus C1, with varying power supply voltages. Gate voltage was 12 V (full on), repetition rate 100 Hz.

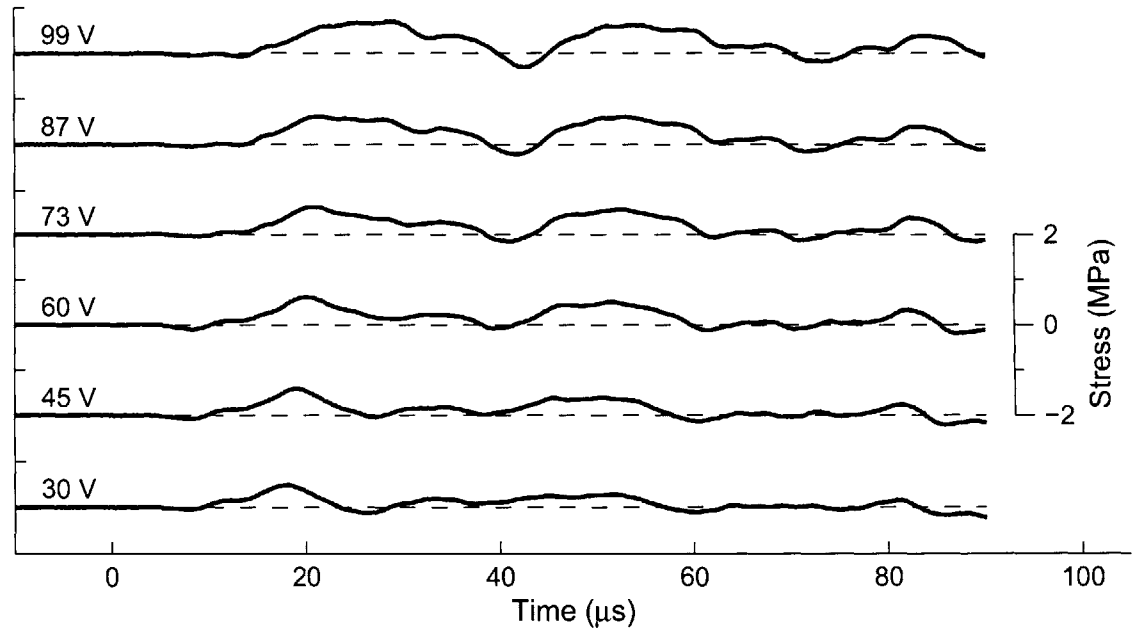

Figure C-6: Extensional stress pulses for apparatus C1, with varying power supply voltages. Gate voltage was 12 V (full on), repetition rate 100 Hz. The stress was measured when the FSMA crystal was fully compressed. Stress calculated from piezoelectric sensor voltage.

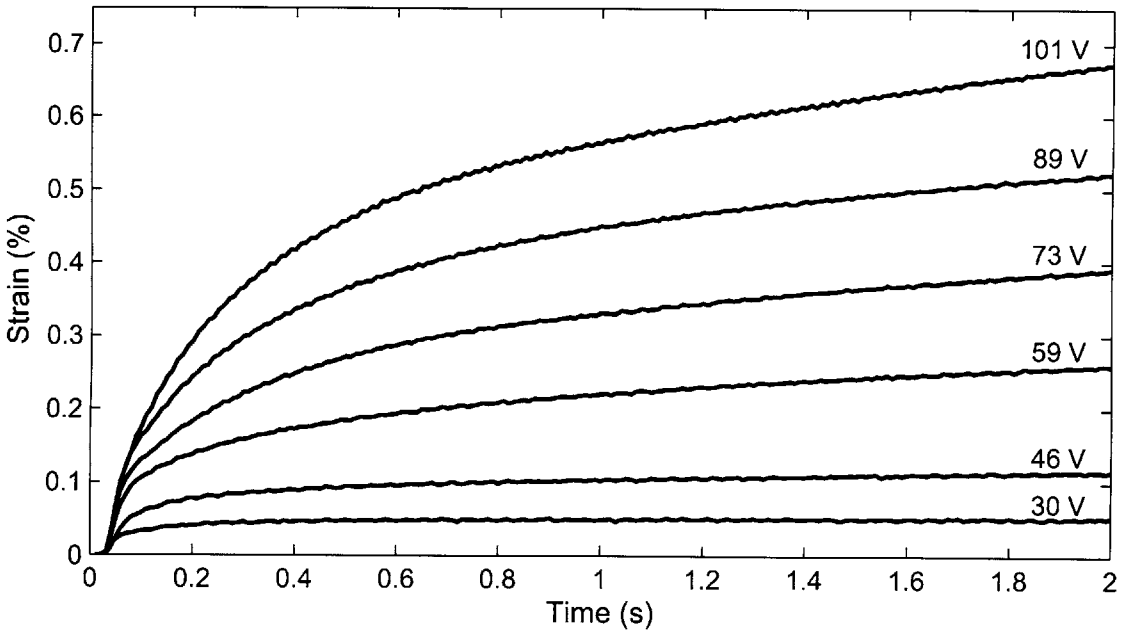

Figure C-7: Extensional actuation strain for apparatus C1, with varying power supply voltage. Gate voltage was 12 V (full on), repetition rate 100 Hz.

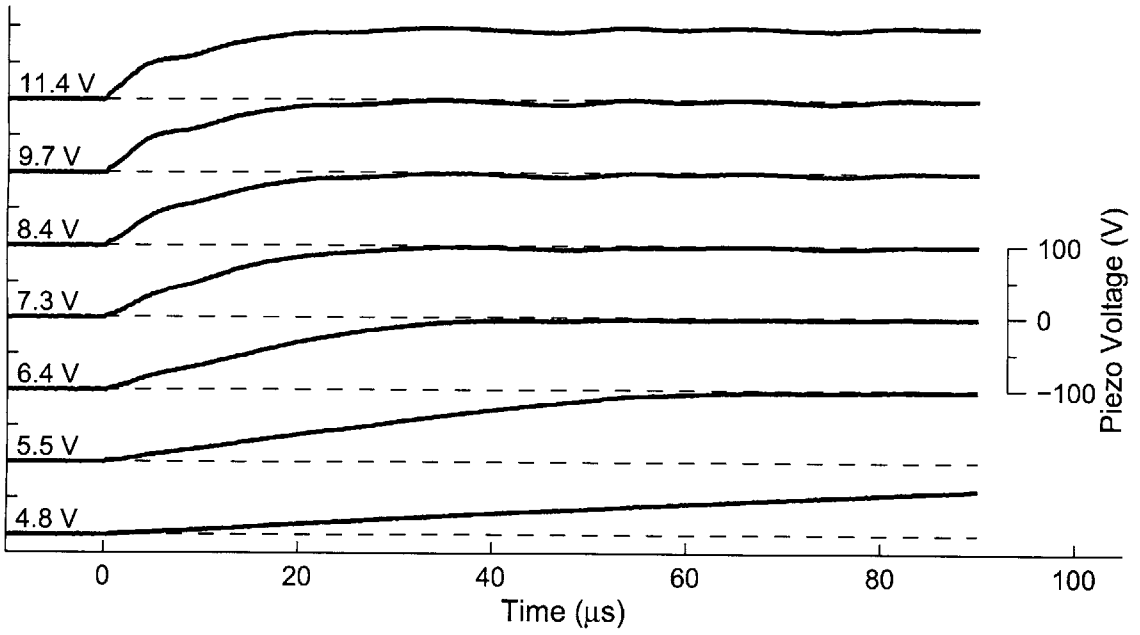

Figure C-8: Compressive input pulses for apparatus C1, with varying gate voltages. Power supply voltage was 100 V, repetition rate 100 Hz.

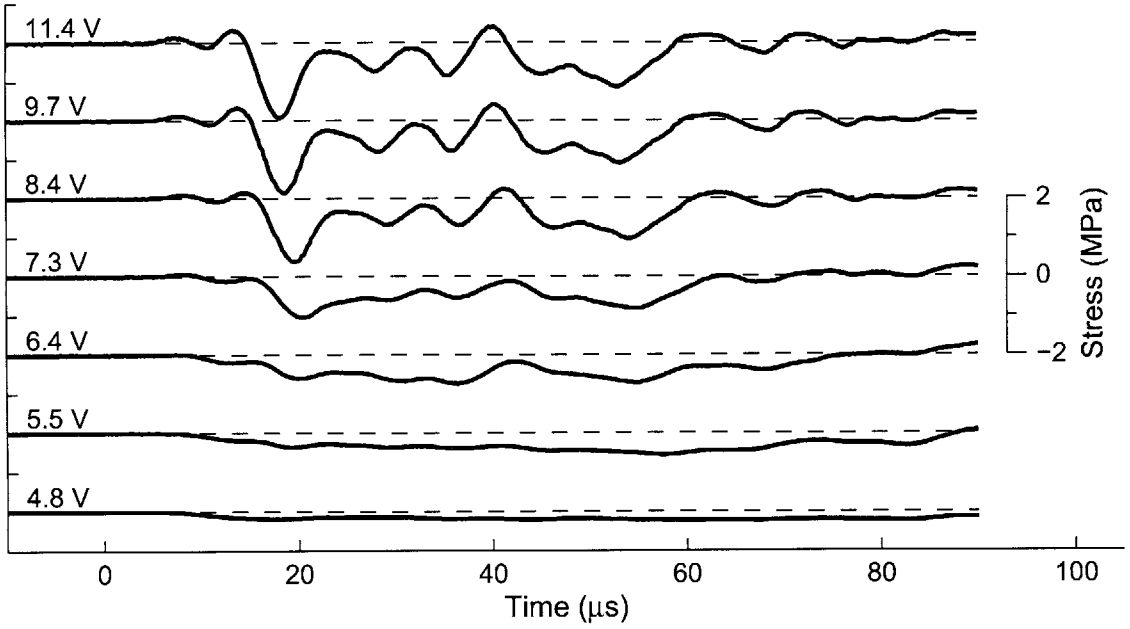

Figure C-9: Compressive stress pulses for apparatus C1, with varying gate voltages. Power supply voltage was 100 V, repetition rate 100 Hz. The stress was measured when the FSMA crystal was fully compressed. Stress calculated from piezoelectric sensor voltage.

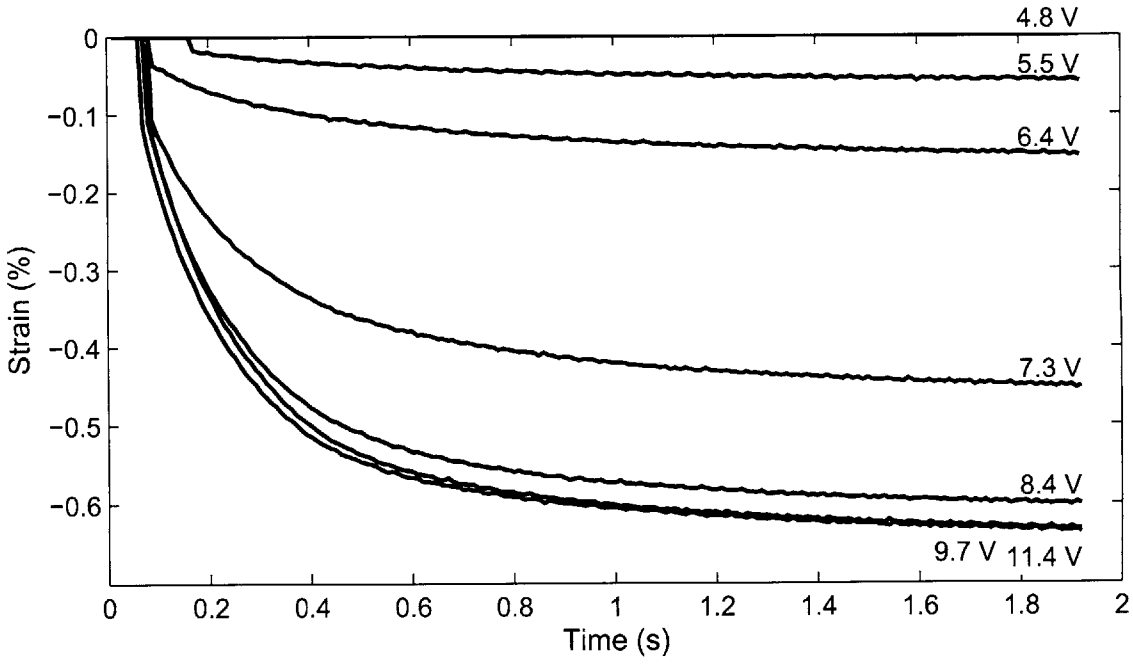

Figure C-10: Compressive actuation strain for apparatus C1, with varying gate voltage. Power supply voltage was 100 V, repetition rate 100 Hz.

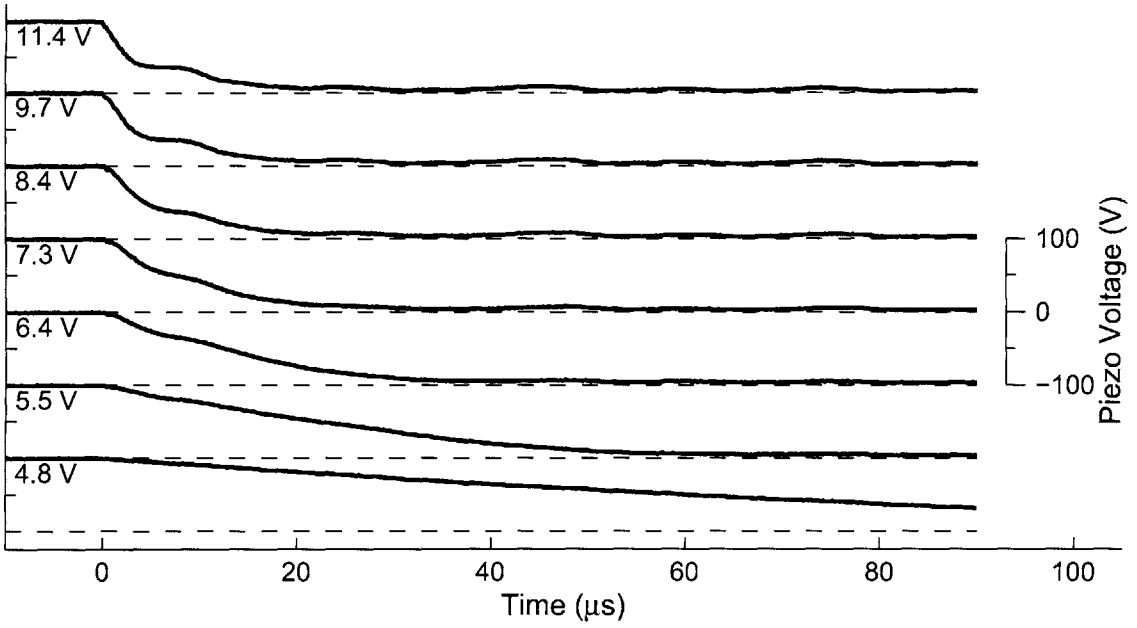

Figure C-11: Extensional input pulses for apparatus C1, with varying gate voltages. Power supply voltage was 100 V, repetition rate 100 Hz.

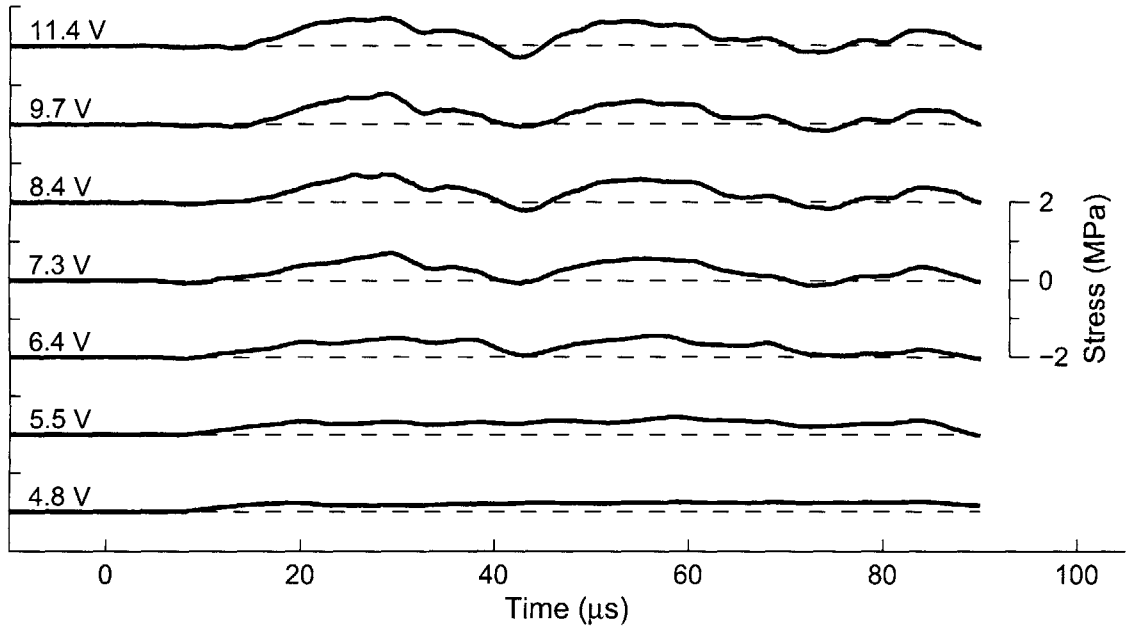

Figure C-12: Extensional stress pulses for apparatus C1, with varying gate voltages. Power supply voltage was 100 V, repetition rate 100 Hz. The stress was measured when the FSMA crystal was fully compressed. Stress calculated from piezoelectric sensor voltage.

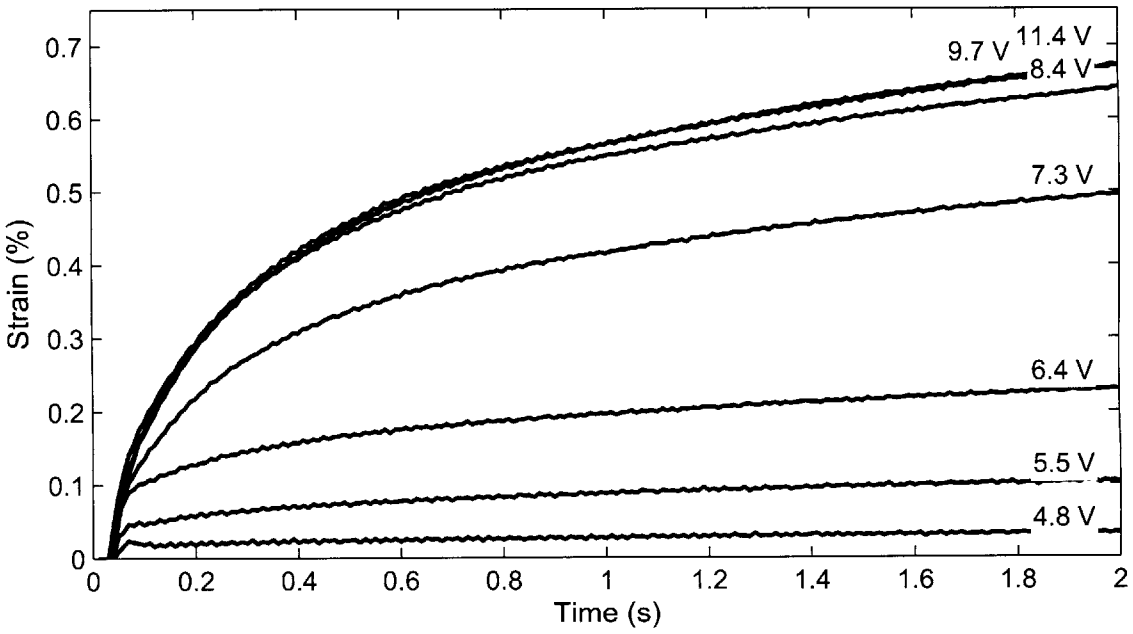

Figure C-13: Extensional actuation strain for apparatus C1, with varying gate voltage. Power supply voltage was 100 V, repetition rate 100 Hz.

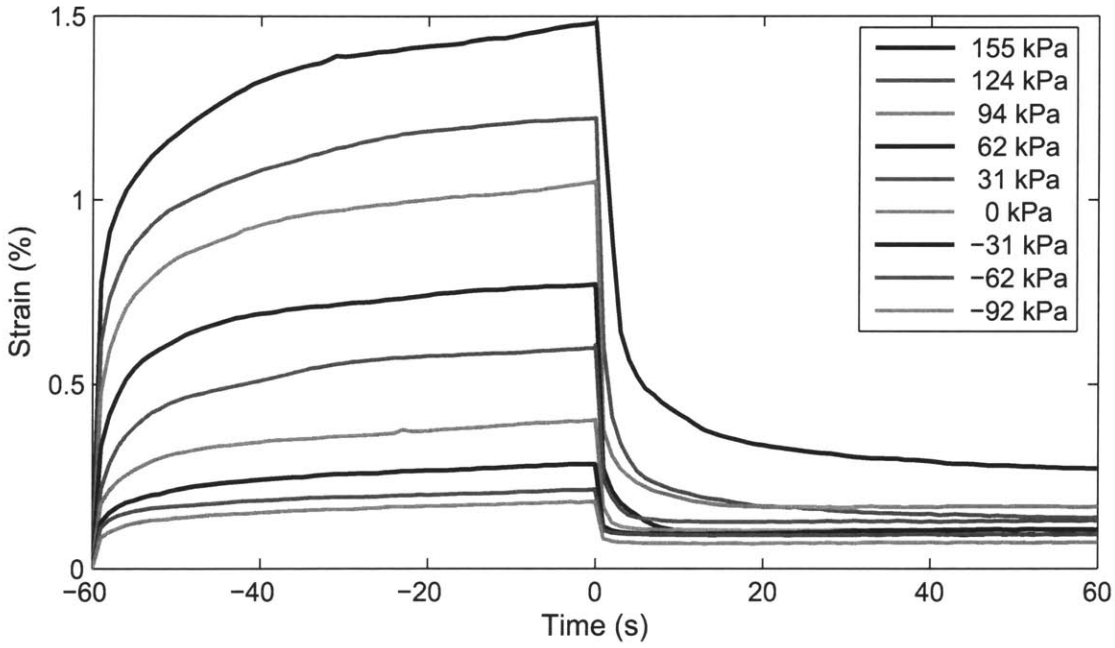

Figure C-14: Actuator strain versus time for a variety of prestresses using flexure B4, stiffness = 17.9 N/mm. The legend indicates the prestress values, measured before actuation begins. Each actuation test began with a fully compressed crystal. V = 100 V, V_g = 12 V, f_R = 50 Hz.

C.2 Actuation Strain Versus Actuator Prestress and Load Stiffness

The figures in this section show the strain measured during the actuation cycles shown in Figures 3-21 through 3-25. They do not show independent data, as the strains were calculated using the spring constant of the flexure being actuated against. The displacement measured using the ADE3800 displacement meter correlates well with the calculated strain. However, it is much more noisy that the strain gauge measurements shown here.

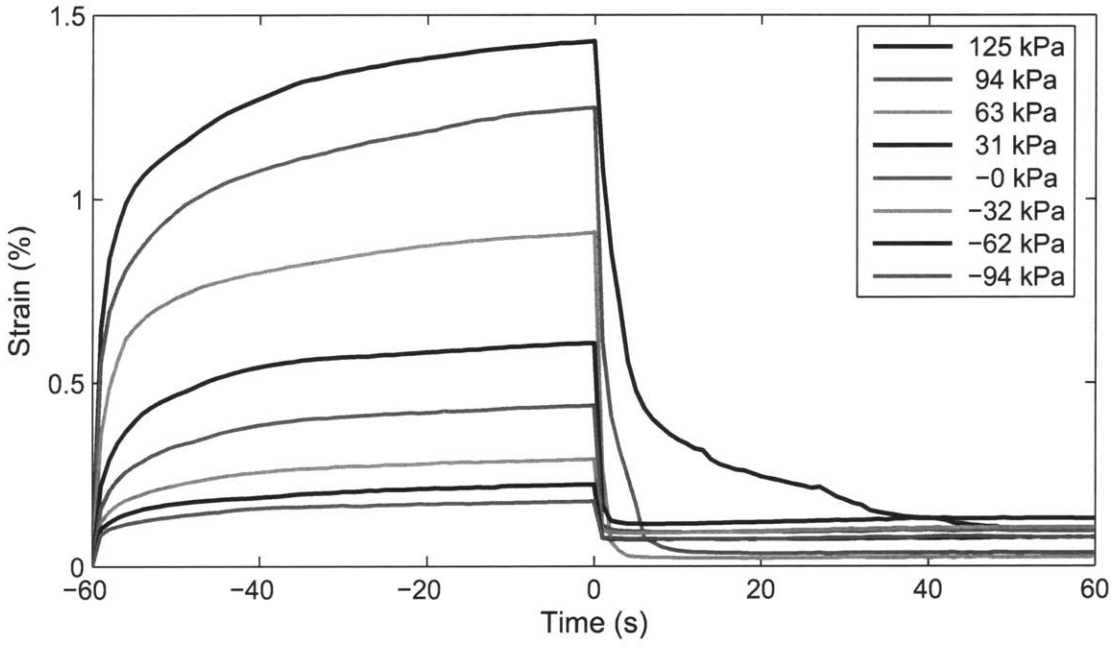

Figure C-15: Actuator strain versus time for a variety of prestresses using flexure B4, stiffness = 15.0 N/mm. The legend indicates the prestress values, measured before actuation begins. Each actuation test began with a fully compressed crystal. V = 100 V, V_g = 12 V, f_R = 50 Hz.

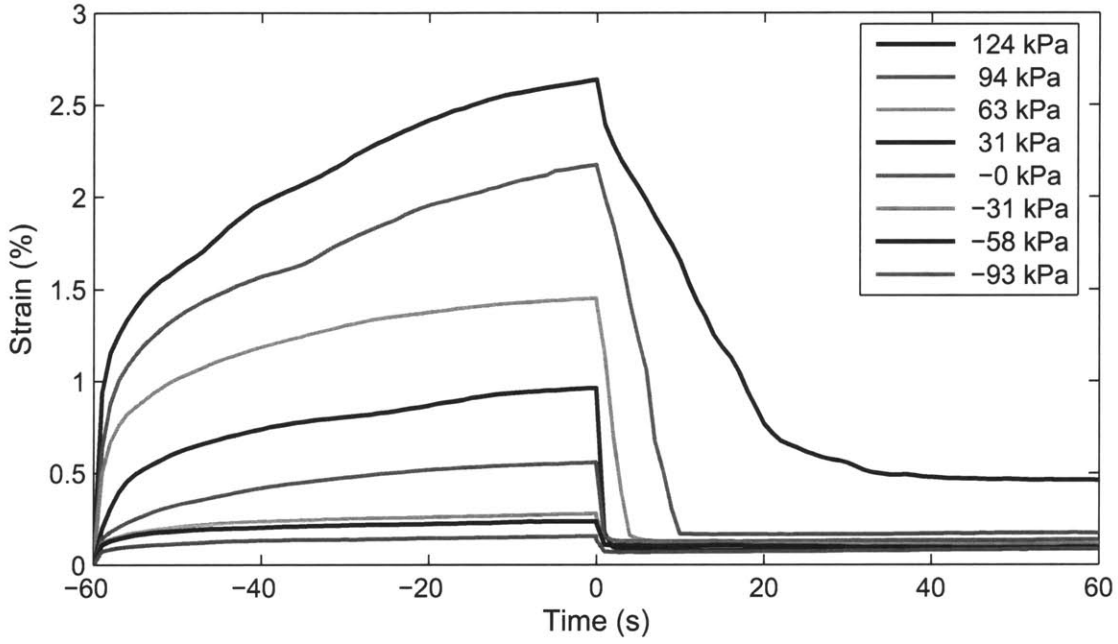

Figure C-16: Actuator strain versus time for a variety of prestresses using flexure B4, stiffness = 7.49 N/mm. The legend indicates the prestress values, measured before actuation begins. Each actuation test began with a fully compressed crystal. V = 100 V, V_g = 12 V, f_R = 50 Hz.

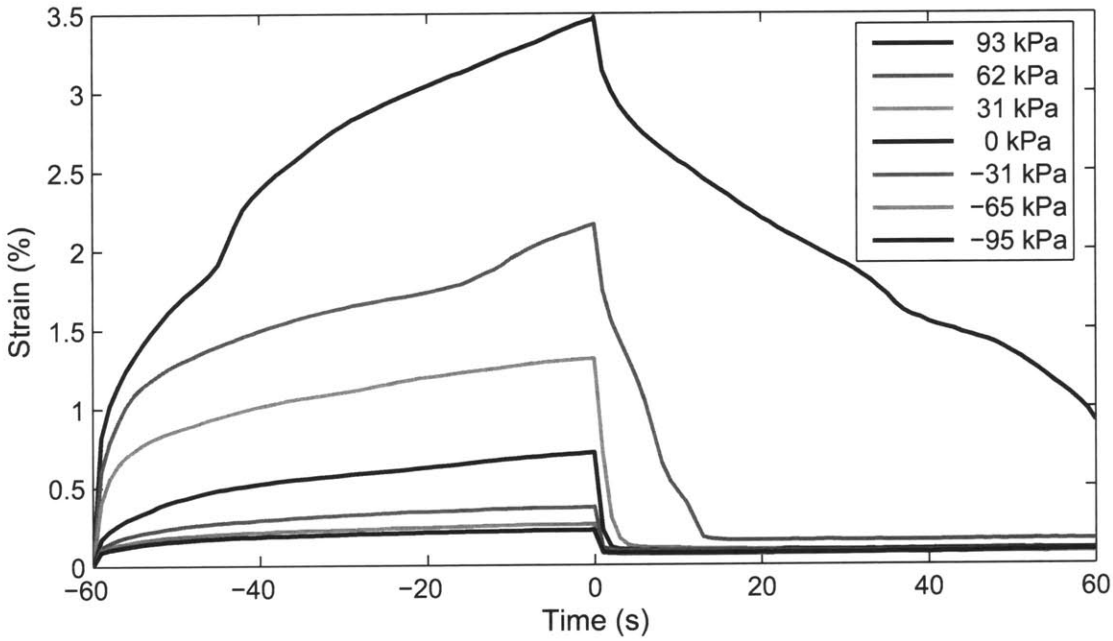

Figure C-17: Actuator strain versus time for a variety of prestresses using flexure B4, stiffness = 3.80 N/mm. The legend indicates the prestress values, measured before actuation begins. Each actuation test began with a fully compressed crystal. V = 100 V, V_g = 12 V, f_R = 50 Hz.

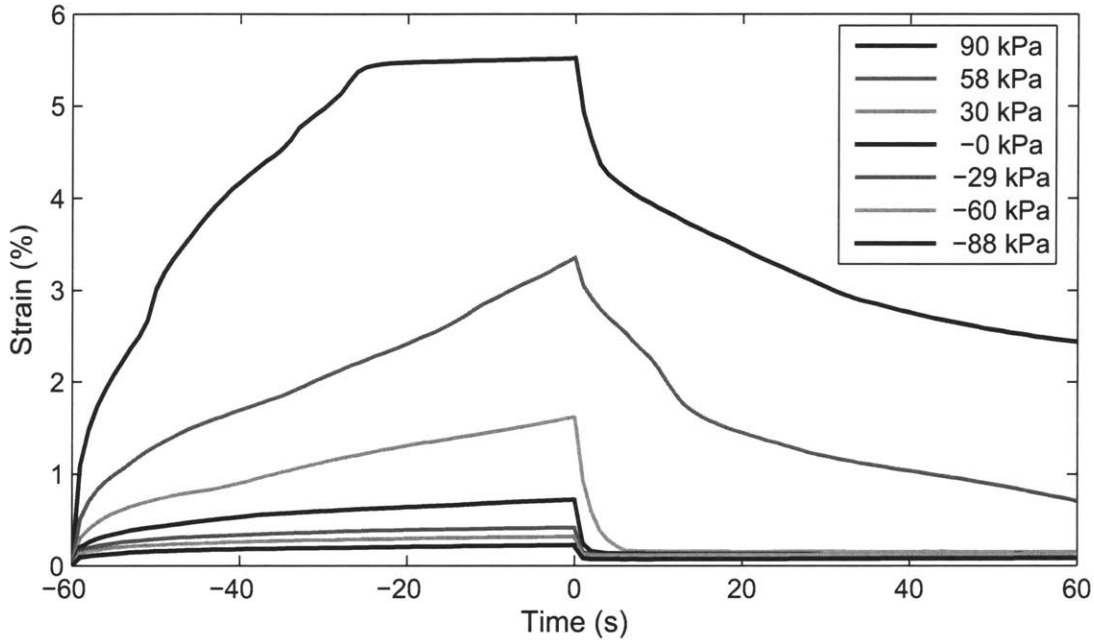

Figure C-18: Actuator strain versus time for a variety of prestresses using flexure B4, stiffness = 1.88 N/mm. The legend indicates the prestress values, measured before actuation begins. Each actuation test began with a fully compressed crystal. V = 100 V, V_g = 12 V, f_R = 50 Hz.

Bibliography

[1] A. Sozinov, A. A. Likhachev, N. Lanska, and K. Ullakko, "Giant magnetic-field-induced strain in NiMnGa seven-layered martensitic phase," *Appl. Phys. Lett.*, vol. 80, pp. 1746–1748, 2002.

[2] M. A. Marioni, R. C. O'Handley, and S. M. Allen, "Pulsed magnetic field-induced actuation of Ni–Mn–Ga single crystals," *Appl. Phys. Lett.*, vol. 83, pp. 3966–3968, 2003.

[3] C. P. Henry, D. Bono, J. Feuchtwanger, S. M. Allen, R. C. O'Handley, H. Dorn, J. Rule, and S. Yoshikawa, "Ni–Mn–Ga AC engineering properties," *J. Phys. IV France*, vol. 112, pp. 997–1000, 2003.

[4] D. E. Hodgson, M. H. Wu, and R. J. Biermann, *Metals Handbook*, vol. 2, ch. Shape Memory Alloys, pp. 897–902. ASM International, 1990.

[5] C. Rice, *Encyclopedia of Smart Materials, Volumes 1-2*, ch. Shape Memory Alloys, Applications, pp. 921–936. John Wiley & Sons, 2002.

[6] S. J. Murray, M. A. Marioni, S. M. Allen, R. C. O'Handley, and T. A. Lograsso, "6% magnetic-field-induced strain by twin-boundary motion in ferromagnetic Ni–Mn–Ga," *Appl. Phys. Lett.*, vol. 77, pp. 886–888, 2000.

[7] S. J. Murray, M. A. Marioni, A. M. Kukla, J. Robinson, R. C. O'Handley, and S. M. Allen, "Large field-induced strain in single crystalline Ni-Mn-Ga ferromagnetic shape memory alloy," *J. Appl. Phys.*, vol. 87, pp. 5774–5776, 2000.

[8] K. Ullakko, J. K. Huang, C. Kantner, R. C. O'Handley, and V. V. Kokorin, "Large magnetic-field-induced strains in Ni_2MnGa single crystals," *Appl. Phys. Lett.*, vol. 69, pp. 1966 – 1968, 1996.

[9] R. C. O'Handley, "Model for strain and magnetization in magnetic shape-memory alloys," *J. Appl. Phys.*, vol. 83, pp. 3263–3270, 1998.

[10] M. A. Marioni, *Pulsed Magnetic Field-Induced Twin Boundary Motion in Ni–Mn–Ga.* PhD thesis, Massachusetts Institute of Technology, Cambridge, MA, 2003.

[11] C. P. Henry, *Dynamic Actuation Properties of Ni–Mn–Ga Ferromagnetic Shape Memory Alloys.* PhD thesis, Massachusetts Institute of Technology, Cambridge, MA, May 2002.

[12] C. P. Henry, P. G. Tello, D. Bono, J. Hong, R. Wager, J. Dai, S. M. Allen, and R. C. O'Handley, "Frequency response of single crystal Ni-Mn-Ga FSMAs," in *Proceedings of SPIE, Smart Structures and Materials 2003* (D. C. Lagoudas, ed.), vol. 5053, pp. 207–211, 2003.

[13] M. A. Marioni, S. M. Allen, and R. C. O'Handley, "Nonuniform twin-boundary motion in Ni–Mn–Ga single crystals," *Appl. Phys. Lett.*, vol. 84, pp. 4071–4073, May 2004.

[14] AdaptaMat Ltd., "Commercial Ni–Mn–Ga product information." `http://www.adaptamat.com/products/`; Accessed December 16, 2004.

[15] B. W. Peterson, J. Feuchtwanger, J. M. Chambers, D. Bono, S. R. Hall, S. M. Allen, and R. C. O'Handley, "Acoustic assisted, field-induced strain in ferromagnetic shape memory alloys," *J. Appl. Phys.*, vol. 95, pp. 6963–6964, 2004.

[16] V. V. Rubanik, V. V. Klubavich, and V. V. Rubanik Jr., "The ultrasound initiation of SME," *J. Phys. IV France*, vol. 112, pp. 249–251, 2003.

[17] SRI International, "Active material comparison tables/charts." `http://ndeaa.jpl.nasa.gov/nasa-nde/lommas/eap/actuators-comp.pdf`; Accessed January 16, 2005.

[18] J. F. Nye, *Physical Properties of Crystals*, ch. IV, VII, pp. 68–81, 110–130. Oxford Science Publications, 1985.

[19] Piezo Systems, Inc., "Commercial piezoelectric actuator properties." `http://www.piezo.com/`; Accessed January 28, 2004.

[20] L. Dai, J. Cui, and M. Wuttig, "Elasticity of austenitic and martensitic NiMnGa," in *Proceedings of SPIE, Smart Structures and Materials 2003* (D. Lagoudas, ed.), vol. 5053, pp. 595–602, 2003.

[21] L. Dai, J. Cullen, and M. Wuttig, "Intermartensitic transformation in a NiMnGa alloy," *J. Appl. Phys.*, vol. 95, no. 11, pp. 6957–6959, 2004.

[22] M. Mitrovic, G. P. Carman, and F. K. Straub, "Response of piezoelectric stack actuators under combined electroc-mechanical loading," *Internaition Journal of Solids and Structures*, vol. 38, pp. 4357–4374, June 2001.

[23] Knowles et al., "Patent no.: US 6,465,936 B1." United States Patent, Oct 2002.

[24] H. Kolsky, *Stress waves in solids*, ch. 7, pp. 170–171. New York: Dover, 1963.

[25] D. Hull and D. J. Bacon, *Introduction to Dislocations*, ch. 6. Dislocations in Other Crystal Stuctures, p. 125. Pergamon Press, 1984.

[26] W. G. Johnston and J. J. Gilman, "Dislocation velocities, dislocation densities, and plastic flow in lithium fluoride crystals," *J. Appl. Phys.*, vol. 30, pp. 129–137, 1959.

[27] C. P. Henry, J. Feuchtwanger, D. Bono, R. C. O'Handley, and S. M. Allen, "AC magnetic field-induced strain of single crystal Ni–Mn–Ga," in *Proceedings of SPIE, Smart Structures and Materials 2002*, (San Diego, USA), 2002.

[28] D. Hadfield, *Permanent Magnets and Magnetism.* John Wiley & Sons, 1962.

[29] R. C. O'Handley, *Modern Magnetic Materials*, ch. 13, pp. 470–476. New York: John Wiley & Sons, Inc., 2000.

[30] M. McCaig and A. G. Clegg, *Permanent Magnets in Theory and Practice.* John Wiley & Sons, 1987.

[31] J. Hong, K. S. Michael, and M. S. Patrick, "Feedback control of a family of nonlinear hysteretic systems," in *Proc. Second IFAC Sym. on Nonlinear Control Design*, pp. 63–68, June 1992.